Measurement of the Top Quark Mass in the All-Hadronic Top-Antitop Decay Channel Using Proton-Proton Collision Data from the ATLAS Experiment at a Centre-of-Mass Energy of 8 TeV

by

Thomas G. McCarthy
B.Sc. Honours, Trent University, Peterborough, Ontario, 2005
B.Ed., Queen's University, Kingston, Ontario, 2006
M.Sc., Carleton University, Ottawa, Ontario, 2010

A thesis submitted to the
Faculty of Graduate and Post Doctoral Affairs
in partial fulfillment of the requirements for the degree of
Doctor of Science

Ottawa-Carleton Institute for Physics
Department of Physics
Carleton University
Ottawa, Ontario, Canada
September, 2015

Abstract

A measurement of the top quark mass (m_{top}) is presented using top quark candidates reconstructed from the jets in all-hadronic $t\bar{t}$ decays. The analysis makes use of the full ATLAS dataset collected over the 2012 period at a centre-of-mass energy of $\sqrt{s} = 8$ TeV and with a total integrated luminosity of $\int Ldt = 20.6$ fb^{-1}. A five-jet trigger, together with an offline cut requiring five central jets with a transverse momentum of at least 60 GeV, was used to preselect candidate signal events. A series of selection cuts are subsequently employed to increase the signal fraction in data events, motivated by both measured data and simulation. These cuts, as well the analytic χ^2 reconstruction algorithm to designate which jets are to be used to reconstruct the top quarks, aim to select those events and candidate top quarks deemed most consistent with an all-hadronic $t\bar{t}$ decay topology. The most discriminating cut involves the output of a b-tagging algorithm employed to identify jets suspected as having been initiated by a bottom-type quark – a key signature of top quark decays.

The measurement is made using a one-dimensional template method, in which a series of distributions are produced for an observable sensitive to the top quark mass by using simulated signal samples with varying input m_{top} values. The ratio of the three- to two-jet invariant masses of candidate top quark - W boson pairs is selected as the m_{top}-sensitive observable, as it is less susceptible to uncertainties arising from the jet energy scale, thereby reducing the corresponding systematic uncertainty on m_{top}. The contributions from backgrounds, including the dominant QCD multi-jet production but also $t\bar{t}$ events with at least one leptonic W boson decay, are estimated using a mix of simulation and data-driven methods.

The final measurement is made *via* a binned χ^2 minimization procedure which takes into account uncertainties in the bin contents from the measured data as well as uncertainties in the parameterization for both signal and background shapes.

The final measured value is found to be $m_{top} = 174.29 \pm 0.52$ (stat) $\pm$ 1.03 (syst) GeV, consistent both with recent LHC measurements in the same and orthogonal decay channels and the current world average. The fraction of background events within the range of the final distribution, measured simultaneously, is found to be $F_{bkgd} = 0.517 \pm 0.015$ (stat)$\pm$0.075 (syst).

Acknowledgements

Many thanks to my supervisor Gerald Oakham for his patience, his absolute trust, and his unwavering support throughout my years at Carleton. You were the calm and steady voice of reason, and were always there when I needed you. Whenever I had any doubts, I knew I could count on you to support me 100% of the time. Thank you.

A great deal of thanks also to the various members of Carleton's ATLAS group present throughout my M.Sc. and Ph.D. programs for all the feedback and fruitful discussions. In particular I wish to thank Manuella Vincter for her support in promoting outreach work, and Alain Bellerive for sharing his expertise in statistics. To the ATLAS graduate students who have been with me over the years, thanks for the many chats, the coffee breaks, and of course the arguments we got into over assignments earlier in our program – likely where we learned the most.

To Teresa Barillari, Sven Menke, Andi Wildauer and the members of the HEC group at the Max Planck Institute for Physics in Munich: my year in Germany was certainly a defining time for me, and working with your group and the time I spent in Bavaria marked the highlight of my program. I can't thank you enough for everything. A particular thank you to Gerald, to Sven and to Teresa for providing me with this opportunity.

Thanks also to my family: to my parents Richard and Marilyn for always supporting me in whatever decision I made, whether personal or professional, and to my siblings Brian, Matthew & Kathy. I really appreciate you all being there for me since I started my M.Sc. program.

I would also like to acknowledge the generous support of the Natural Sciences and Engineering Research Council of Canada.

Contents

List of Tables

List of Figures

Glossary of Terms

ATLAS **A** **T**oroidal **LHC** Apparatus

BSM **B**eyond the **S**tandard **M**odel

BR **B**ranching **R**atio

CERN European Centre for Nuclear Research

CMS **C**ompact **M**uon **S**olenoid

EM **E**lectro**m**agnetic (Weighting Scale for Energy Clusters, *cf.* LCW)

EMEC **E**lectro**m**agnetic **E**nd **C**ap

FCAL **F**orward **Cal**orimeter

HEC **H**adronic **E**nd **C**ap

JES **J**et **E**nergy **S**cale

JVF **J**et **V**ertex **F**raction

LAr **L**iquid **Ar**gon

LCW **L**ocal **C**luster **W**eighting (Weighting Scale for Calorimeter Energy Clusters, *cf.* EM)

LHC **L**arge **H**adron **C**ollider

MPI **M**ultiple **P**arton **I**nteraction

MV1(c) **M**ulti**v**ariate b-Tagging Algorithm

(N)NLO (**N**ext-to-)**Next**-to-**L**eading **O**rder

PDF **P**arton **D**istribution **F**unction[†] or **P**robability **D**ensity **F**unction[†]

PLC **P**arton-**L**evel **C**orrection

QCD **Q**uantum **C**hromo**d**ynamics

QFT **Q**uantum **F**ield **T**heory

[†]More than one definition is used for **PDF** but the meaning should be clear from the context.

Chapter 1

Introduction

At the time of writing, the recent triumph marked by the discovery of the Higgs boson [1] – the final and crucial piece of the Standard Model of Particle Physics – remains palpable. Great milestones in physics such as this are important in allowing scientists to find their bearings, to discount those theories consequently rendered unsound, and to chart a course toward the next big discovery. And yet a confirmation of the existence of the Higgs boson has, perhaps expectedly, spawned a series of further questions to be answered.

The Standard Model describes, with great precision, the laws which seem to govern our universe at the smallest scale. The model is regularly vindicated and continues to be tested to its limits in a variety of ways and through a multitude of experiments. In every instance thus far the model emerges unscathed. Yet gaping holes in our understanding of the universe persist: the origin of dark matter, the root of cosmic expansion, the reason for the observed matter-antimatter asymmetry, the possibility of the compositeness of quarks and leptons – questions a particle physicist strives, as ever, to answer. The presence of such holes suggests that the theory encompassed by the Standard Model may constitute only a low-energy approximation – a small piece in a larger, more comprehensive theory of nature.

The top quark mass has a seminal role in the theory of elementary particle physics. It has been, and continues to be, measured in different ways, and using a variety of techniques. Its precise value is an important fundamental parameter to measure in its own right, but moreover its value could have even further implications as to the ultimate stability of the universe [2].

A precision measurement of the top quark mass has the potential to bridge several gaps in our understanding by helping to constrain a number of proposed theoretical models which would require the existence of new and yet unobserved particles with kinematic dependences on the value of the top quark mass. The aim of making such a measurement is to do no more and no less than to take us an additional step in the direction of acquiring a better knowledge of our universe at its most fundamental level and the laws that dictate its evolution. As the heaviest of all known fundamental particles, the top quark sits as a beacon on the frontier of our known

understanding of the universe – the nearest-mass neighbour to a number of theorized but yet unobserved particles currently being searched for at the high-energy frontier.

At the time of writing, the experiments at CERN's **Large Hadron Collider** (LHC) are transitioning to the next phase of data collection as the accelerator begins colliding oppositely directed beams of protons with an even higher centre-of-mass energy. In this new chapter of collider physics, new results and limits on alternative theories or extensions to the Standard Model could be observed on a very short timescale; these results will dictate the future direction and design of collider physics machines and experiments. Hints of other new physics phenomena may additionally emerge in the coming months or years, and analyses involving top quark signatures may very well herald their discovery. It is an exciting time for experimental top quark physics!

The analysis presented in this thesis represents, at the time of writing, the precision top quark mass measurement in the all-hadronic $t\bar{t}$ channel performed using the largest dataset from any collider experiment.

The chapter breakdown following this introduction is as follows: **Chapter 2** sets the context of the present analysis – describing what is currently known about the top quark, its role as the heaviest fundamental particle in the Standard Model, and motivating the need for a precision measurement of its mass in the all-hadronic $t\bar{t}$ channel. A detailed description of the detector and relevant physics formulae are provided in **Chapter 3**. **Chapter 4** is dedicated to the physics objects referred to as jets – their role as the manifestations of quarks in ATLAS, the way in which they are reconstructed from energy deposits in the detector's calorimeters, and how they can be used to build the mass-sensitive observables to probe the properties of the top quark. The kinematics of all-hadronic $t\bar{t}$ signal events, together with descriptions of associated background processes, are presented in **Chapter 5**. **Chapter 6** outlines the algorithm employed as a means to reconstruct candidate top quarks from their constituent pieces; it also provides benchmarks for performance for such algorithms in general. **Chapter 7** presents a comprehensive list of the event selection cuts used to select candidate signal events and suppress contributions from the otherwise overwhelming background. **Chapter 8** describes the concept of a template method in the context of a mass measurement, and outlines the manner of extracting an m_{top}-dependent parameterization of an observable sensitive to the top quark mass for all-hadronic $t\bar{t}$ signal events. The corresponding parameterization for the combined backgrounds follows in **Chapter 9**, together with a description of the data-driven technique used to estimate the QCD multi-jet background shape. The framework for extracting a measurement of the top quark mass is laid out and described in **Chapter 10**, along with the nominal result obtained and an estimate of its statistical uncertainty. The sources of systematic uncertainty on the measurement of m_{top} are enumerated and described in detail in **Chapter 11**. Finally **Chapter 12** summarizes the full results of the measurement and offers some concluding remarks and an outlook.

Chapter 2

Theoretical Background

2.1 The Standard Model of Particle Physics

Four fundamental forces – the electromagnetic, the strong, the weak nuclear, and the gravitational force – are believed to govern the interactions between all known fundamental particles in the observed universe. Of these four forces, all but the gravitational are encompassed in the framework of the Standard Model of Particle Physics. In this model, the fundamental particles are grouped based on their properties, analogously to the layout of the periodic table of the elements. The matter particles – the quarks and leptons – are spin $\frac{1}{2}$ fermions in the context of Dirac theory. The gauge bosons – the photon, the W^+, W^- and Z, and the eight gluons – have integral spin values and mediate the forces *via* interactions between each other and with the matter particles. An additional boson, the Higgs, can be added to this latter group. Though not a mediator of one of the fundamental forces, the Higgs boson plays an integral role in the process of **Electroweak Symmetry Breaking** (EWSB) responsible for the generation of the masses of the matter particles.

Figures 2.1 and 2.2 depict the Standard Model fermions and bosons, respectively. All particles are shown in groups, and the three different generations of the fermions are highlighted by the use of different shades. The charge, mass and quantum mechanical spin are summarized in these figures[1]. To each of the fermions, save perhaps the neutrinos[2], there corresponds an oppositely charged anti-particle with many similar properties including the quantum mechanical spin and mass. The anti-particles themselves are not shown explicitly in the figure, but their inclusion is implied.

[1]The convention adopted in the present analysis is to work in units such that $c = \hbar = 1$. All values listed in the figures are measured values from the **Particle Data Group** (PDG) summary tables [3], with the exception of the Higgs Boson mass in Figure 2.2, which comes from a combined ATLAS and CMS measurement [4].

[2]Should neutrinos turn out to be majorana particles they will be their own anti-particles.

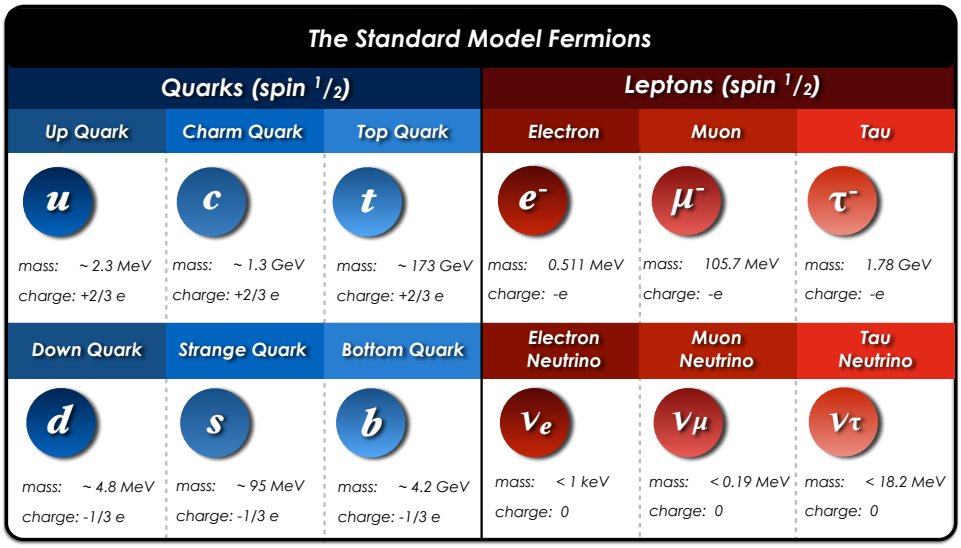

Figure 2.1: The quarks and leptons making up the fermions of the Standard Model.

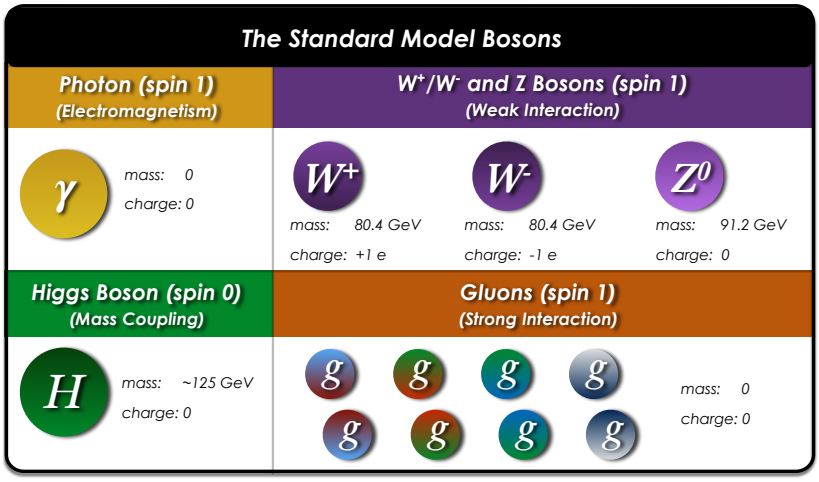

Figure 2.2: A summary of the various Standard Model gauge bosons, including the force mediators for the electromagnetic, strong and weak nuclear forces. The Higgs boson, which is involved in the generation of the masses of the matter particles *via* EWSB, is also included.

2.2 The Top Quark

2.2.1 Role in the Standard Model

Speculation on the existence of the third-generation, positively charged weak-isospin doublet partner of the bottom quark – the top – came in 1997, shortly after the discovery of the bottom quark itself [5]; the bottom quark was discovered as a result of the observation of a series of heavy baryons and mesons suggesting the existence of quarks with masses beyond those of the up, down, charm and strange quarks [6]. The observation, nearly twenty years later, of pairs of top quarks[3] produced *via* the strong interaction in p-$\bar{p}$ collisions was made jointly by the $D0$ and CDF collaborations [7] [8]; this was subsequently followed in 2006 by evidence, again by the $D0$ collaboration, of single top quark production mediated by charged weak-current interactions, with the subsequent observation confirmed by both Tevatron experiments in 2009 [9–11]. The centre-of-mass energy of the Tevatron at the time of the single top discovery was $\sqrt{s} = 1.96$ TeV. The protons accelerated by the LHC and involved in the collisions at the centre of the ATLAS detector considered for the present analysis each have an energy of $E_p = 4$ TeV, leading to a total centre-of-mass energy of $\sqrt{s} = 8$ TeV.

In the recent years since the LHC has been the world's highest-energy centre for collider physics, vast numbers of top quarks have been produced allowing for the measurement of the properties of what is now the heaviest of all known fundamental particles. As many as five million top quarks were produced, either singly or in $t\bar{t}$ pairs, in the centre of the ATLAS detector during the 2012 data-collection period; the LHC can consequently be referred to as a veritable top factory. While only a minor fraction of those top quarks produced ultimately end up being reconstructed as signal top quark candidates in the various analyses due to the efficiency of triggering and event selection requirements, substantial numbers of them remain to fill the final distributions of interest. Indeed, the recent years have witnessed a paradigm shift in many top quark-related measurements as systematic uncertainties now become dominant over statistical uncertainties.

2.2.2 Production Mechanisms

In high-energy collider physics, two useful quantities that determine the event rates for a given process are the luminosity and the cross-section. The luminosity is intrinsically an accelerator-dependent quantity and is a measure of the rate at which high-energy collisions occur. Units for the instantaneous luminosity, denoted as L, are $\mathrm{cm}^{-2} \cdot \mathrm{s}^{-1}$. One can also speak of the integrated luminosity, $\mathcal{L}$, which is simply the intantaneous luminosity integrated over a selected period of time. In general then, the instantaneous and integrated luminosities are related *via*:

[3] Pairs in this case implies a top-antitop quark pair, often abbreviated as $t\bar{t}$.

$$\mathcal{L} = \int L dt \tag{2.1}$$

The cross-section is rather a process-dependent quantity, denoted by σ, and represents, in a sense, a measure of the statistical probability of a particular process occurring. It has dimensions of area and is typically quoted in units of μb, nb or pb (micro- or nano-, or picobarns) where one barn is equal to 10^{-24} cm^2. In the case of the proton-proton collisions at the centre of the ATLAS detector, the production cross-sections depend on the partonic centre-of-mass energy $\sqrt{\hat{s}}$ available as a result of the inelastic scattering of parton[4] constituents from two oppositely directed protons[5]. The calculation of production cross-sections for a particular process of interest is necessarily an approximation to a given level of desired precision[6] and involves the addition of a large number of possible interactions *via* the perturbative machinery of **Quantum Field Theory** (QFT) [12]. It should be emphasized that in order to produce heavier particles, such as top quarks, it is necessary that the energy available, $\sqrt{\hat{s}}$, be above a production threshold, dictated by the rest mass(es) of the particle(s) to be produced.

For the generic process $pp \to X$, the number of expected events to be produced as a result of collisions over the relevant time interval is dictated by the relation:

$$N_X = \mathcal{L}\sigma_{pp\to X} \tag{2.2}$$

Figure 2.3 shows the peak instantaneous luminosities measured at ATLAS over the three years of the Run I data-collection period. The largest value can be seen to be approximately 8×10^{33} cm$^{-2} \cdot$ s^{-1} or, equivalently, 0.008 pb$^{-1} \cdot$ s^{-1}.

Provided there is sufficient energy in the hard-scatter event resulting from a *p*-*p* collision, *i.e.* provided $\sqrt{\hat{s}} \gtrsim 2m_{top}$ where m_{top} is the top quark mass, it becomes kinematically possible to produce a top and anti-top quark pair. The dominant production mechanism at the LHC involves a **gluon-fusion** process – the interaction of two gluons, each originating from one of the colliding protons – and mediated by the exchange of either a third gluon *via* a triple gluon coupling in an **s-channel** interaction, or a virtual quark in a **u-** or **t-channel** interaction[7]. Alternatively, a valence quark from one proton annihilates with an anti-quark from the other proton, thereby producing a $t\bar{t}$ pair mediated by the exchange of a virtual gluon, either *via* an

[4]The term **parton** refers to the constituents of the proton and is therefore used as a general term to denote either a quark or a gluon.

[5]For the scattering of two partons, labelled 1 and 2, each with momentum fraction x_1 and x_2 of their respective protons, the centre-of-mass energy available will not be $\sqrt{s} = 8$ TeV, but rather $\sqrt{\hat{s}}$ where $\hat{s} = x_1 x_2 s$.

[6]Theoretical calculations are commonly performed at **Next-to-Leading** or **Next-to-Next-to-Leading Order** (NLO or NNLO).

[7]The Mandelstamm variables s, t and u arise in $2 \to 2$ scattering processes (though not limited to such cases) and correspond to different permutations of four-momentum transfers between the incoming and outgoing bodies involved. In the present context they are used to differentiate between graphical representations of the interactions in the form of Feynman diagrams. For more information see, for example, [12], [14] or [3].

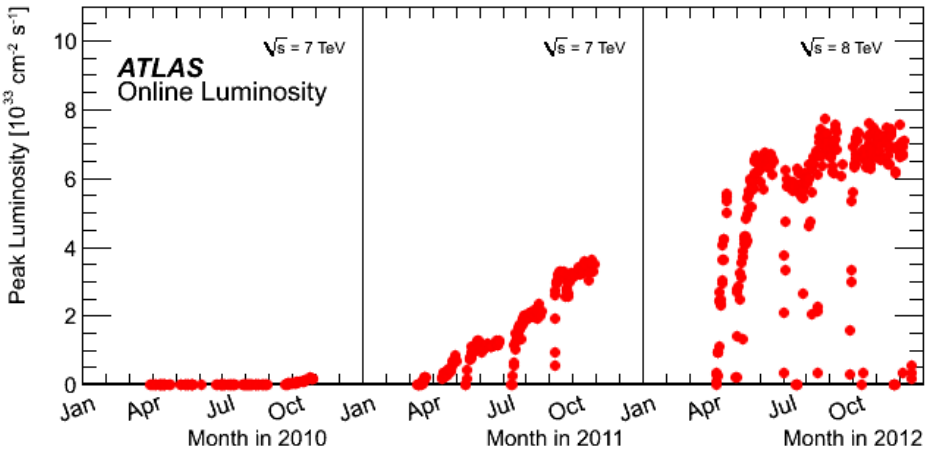

Figure 2.3: The measured peak instantaneous luminosities at ATLAS during Run I [13].

s- or t-channel, in a process referred to as **quark-antiquark annihilation**.

Both the gluon-fusion and quark-antiquark annihilation processes are possible at the LHC, though their relative contributions depend on the energy available in the scattering process [3]. During 2012 ATLAS data-taking at a centre-of-mass energy of $\sqrt{s} = 8$ TeV, the contribution from gluon-fusion production of $t\bar{t}$ pairs was roughly eight times larger than that from the $q\bar{q}$ annihilation process for reasons that will become clear in what follows.

2.2.3 The Partonic Structure of the Proton

An understanding of the composite nature of a proton is of paramount importance in the study of processes from hadronic collider interactions. The partonic (quark and gluon) structure of the proton has been studied extensively, and is described in the framework of the so-called **Parton Distribution Functions** (PDFs) [3]. These functions, measured by data *via* lepton-nucleon scattering experiments, mathematically describe the expected fractional contribution from each flavour of parton in the makeup of the proton, evaluated in a particular energy regime. This fact is important, as it is the interactions between the individual partons, and not the protons as a whole, which are relevant to the production mechanisms for $t\bar{t}$ pairs in a given collison event [15,16]. Figure 2.4(a) shows an example of the measured CT10 parton distribution functions of the proton which were used during the production of the simulated signal samples used in this analysis[8].

The total probability of selecting a parton of any flavour in the proton is subject to the normalization constraint:

[8]The all-hadronic $t\bar{t}$ signal process will be described in detail in Chapter 5.

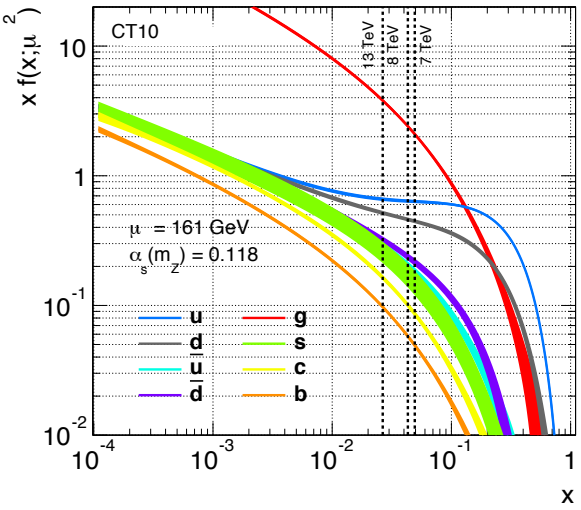

(a) Examples of the CT10 proton parton distribution functions (PDFs) employed in this analysis, describing the probability a particular parton type with fraction x of the incoming proton momentum being involved in a given hard-scattering process. The particular PDFs shown as a function of x are evaluated at a factorization scale $\mu = 161$ GeV. The various coloured lines correspond to different parton flavours. The widths of the lines correspond to uncertainties in the values of $xf_i(x;\mu^2)$ for parton flavour i. The meaning of the three dotted vertical lines is explained in the text.

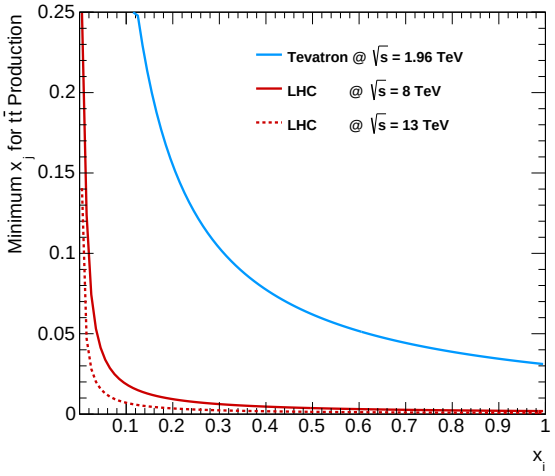

(b) Top quark pair production thresholds, represented by the minimum required momentum fraction of one parton as a function of the momentum fraction of the other, presented for three different hadron collider configurations. Note that lines represent thresholds only – production of $t\bar{t}$ pairs would also be possible at any values of (x_i,x_j) above the corresponding lines. The reference value of the top quark mass is taken to be $m_{top} = 172.5$ GeV.

Figure 2.4: Sample distributions illustrating the concept of the proton PDFs as well a representation of the $t\bar{t}$ production theshold for three hadron collider scenarios.

$$\sum_i \int_0^1 x f_i(x;\mu^2) dx = 1 \tag{2.3}$$

where the sum is performed over all parton flavours. The partonic structure of anti-protons such as those involved in the p-$\bar{p}$ Tevatron collider differ from those of protons, but similar such PDFs exist in either case. Concerning the quark-related makeup of the protons involved in the LHC collisions, in order to yield a final state $|uud\rangle$ and satisfy baryon conservation, a necessary requirement is that:

$$\int_0^1 \left(f_i(x;\mu^2) - \bar{f}_i(x;\mu^2)\right) dx = \begin{cases} 2 & \text{when } i = u \\ 1 & \text{when } i = d \\ 0 & \text{when } i = s, c, b, t \end{cases} \tag{2.4}$$

In the above equation the index i denotes the particular quark flavour, and the forms of $f_i(x;Q^2)$ and $\bar{f}_i(x;\mu^2)$ are meant to highlight parton distribution functions for a given quark flavour and its associated anti-quark flavour, respectively.

Figure 2.4(b) illustrates the role of the centre-of-mass energy of a hadron collider, notably in the context of the threshold requirement for the production of a $t\bar{t}$ pair, namely: $\sqrt{\hat{s}} = 2m_{top}$. This requirement can be expressed in terms of the two proton momentum fractions, x_i and x_j for partons i and j, as a requirement that x_i and x_j satisfy:

$$x_i x_j = \frac{4m_{top}^2}{s} \quad \text{or} \quad x_j = \left(\frac{2m_{top}}{\sqrt{s}}\right)^2 \frac{1}{x_i} \tag{2.5}$$

This value of x_j is plotted as a function of x_i for different values of $\sqrt{s}$ corresponding to three different hadron collider configurations. One can clearly observe that the product $x_i x_j$ can be substantially lower in the case of the LHC compared with the Tevatron, particularly during Run II conditions at a higher centre-of-mass energy, while still satisfying the threshold requirement for $t\bar{t}$ production. With such low momentum fractions and in light of the parton distribution functions of the colliding protons shown in Figure 2.4(a), the probability of an interaction involving a gluon pulled from the parton sea far exceeds that of a quark or anti-quark.

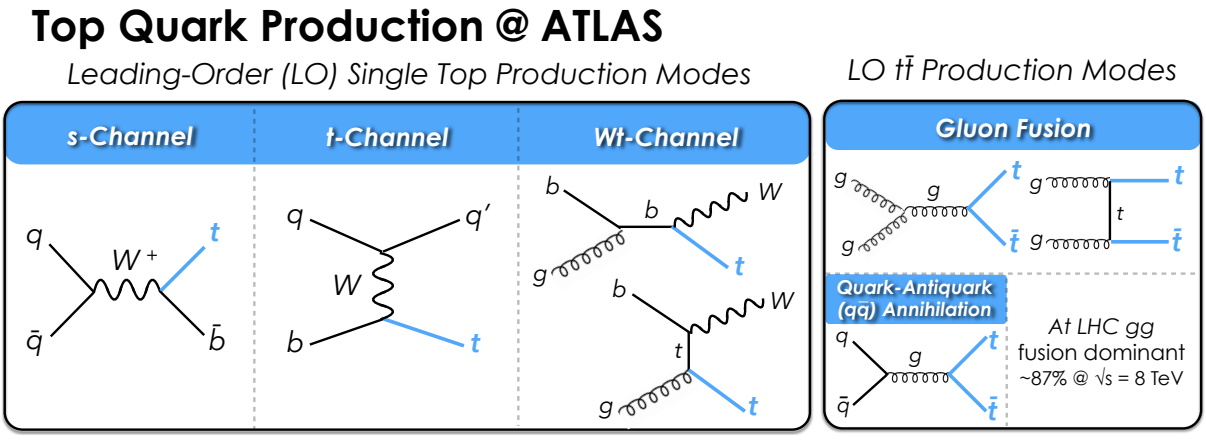

Figure 2.5: The dominant production modes of top quarks at the LHC.

By the same reasoning, the gluon-fusion process can be expected to play an even more significant role as the available energy in the collision increases. The dotted vertical lines in the

plot of Figure 2.4(a) show the values of x required to produce a $t\bar{t}$ pair in the case that both momentum fractions are equal, *i.e.* in the case where $x_i = x_j$. From Equation 2.5 these have values given by $x = 2m_{top}/\sqrt{s}$. The values shown correspond to the two Run-I centre-of-mass energies of the LHC ($\sqrt{s}$ = 7 and 8 TeV) and that for the initial Run-II data-taking period ($\sqrt{s}$ = 13 TeV). In this case a top quark mass of m_{top} =172.5 GeV is assumed. An inspection of the lines confirms that at a higher centre-of-mass energy the $t\bar{t}$ production threshold becomes significantly lower relative to the total $\sqrt{s}$ = 13 TeV available in the collisions; one can conclude that during Run II data-taking only a very small relative fraction of the $t\bar{t}$ pairs will be expected to be produced *via* $q\bar{q}$ annihilation – gluon-fusion is far more likely to occur in a given interaction as the gluons in the colliding protons are more accessible for interactions.

In the case of the Tevatron experiments, where p-$\bar{p}$ collisions allow for the quark-antiquark annihilation mechanism from valence quarks alone, it is rather the $q\bar{q}$ annihilation process which dominates the production of $t\bar{t}$ pairs.

It should be highlighted that at LHC energies, the $t\bar{t}$ production threshold is so low relative to the total energy available in a typical interaction that the $t\bar{t}$ pairs are often produced with a significant boost[9]; this has implications in the strategies used in the offline reconstruction of top quark candidates.

Figure 2.5 illustrates some leading-order production modes of top quarks at the LHC experiments such as ATLAS. The dominant production mechanisms for both single top quarks and top quark pairs are shown [17].

A recent measurement of the total inclusive $t\bar{t}$ production cross-section was made in the dileptonic ($e\mu$) channel by ATLAS[10], specifically searching for events with oppositely charged high-p_{T} electrons and muons[11] [18]. The analysis resulted in a measured value of $\sigma_{t\bar{t}} = 242.4 \pm 1.7$ (stat) $\pm$ 5.5 (syst) $\pm$ 7.5 (lumi) $\pm$ 4.2 (E_{beam}) pb, using the $\sqrt{s} = 8$ TeV dataset[12]. This value is consistent with recent theoretical NNLO and NNLL Standard Model predictions [19–22]. From this value of $\sigma_{t\bar{t}}$, together with the instantaneous luminosity shown in the plot in Figure 2.3, one can estimate that at peak instantaneous luminosity during the 2012 data-collection period, as many as two pairs of top quarks were produced per second.

The total production cross-section for $t\bar{t}$ pairs in ATLAS can be expressed in the form [23]:

$$\sigma_{pp\to t\bar{t}}\left(\sqrt{s}, m_{top}\right) = \sum_{i,j=q,\bar{q},g} \int dx_i dx_j f_i(x_i,\mu^2) f_j(x_j,\mu^2) \times \hat{\sigma}_{ij\to t\bar{t}}\left(\rho, m_{top}^2, x_i, x_j, \alpha_{\mathrm{S}}(\mu^2), \mu^2\right) \quad (2.6)$$

[9]The **boost** of a particle is a measure of its energy relative to its rest mass. For a particle with mass m and energy E the boost is characterized by the familiar Lorentz factor $\gamma = E/m$.

[10]The decay channels of $t\bar{t}$ pairs will be outlined in detail later in the chapter.

[11]The transverse momentum p_{T} will be defined in the following chapter.

[12]The uncertainties (lumi) and (E_{beam}) in the measured value of the cross-section correspond to uncertainties in the total collected integrated luminosity and the LHC beam energy, respectively.

where the sum is taken over all possible subprocesses, each evaluated at an energy scale μ; the indices ij can therefore represent gg (gluon fusion) or $q\bar{q}$ (quark-antiquark annihilation), but also the less dominant qg or $\bar{q}g$ production modes of $t\bar{t}$ pairs. The cross-section for a given subprocess, $\hat{\sigma}_{ij\to t\bar{t}}$, is expressed as a function of several variables including $\rho = \frac{4m_{top}^2}{\sqrt{\hat{s}}}$ and the strong coupling constant α_S. A higher top quark mass results in a larger production threshold; the cross-section can consequently be expected to decrease. The presence of the top quark mass in this expression suggests that the inclusion of higher-ordered corrections to this expression and the reduction of overall additional uncertainties could allow for an indirect measurement of the top quark mass to be made from that of an inclusive cross-section $\sigma_{t\bar{t}}$ measurement alone[13].

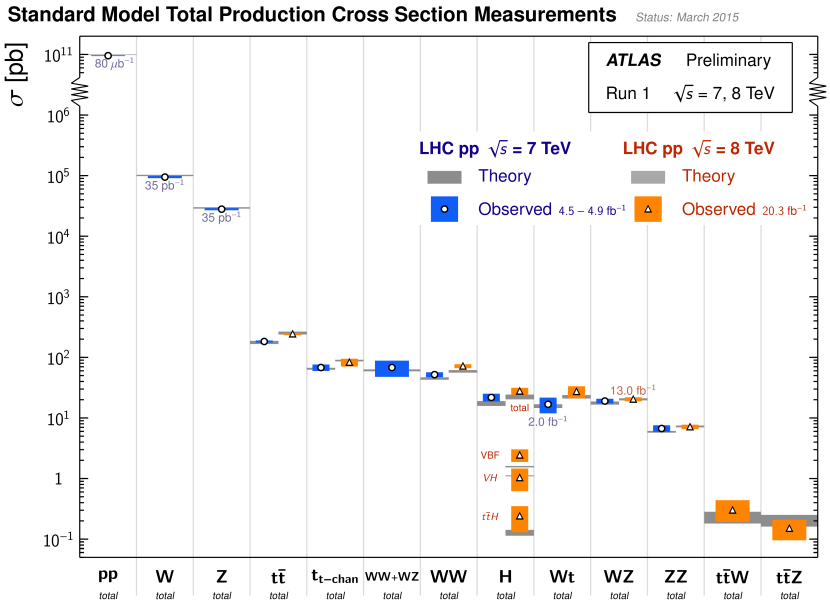

Figure 2.6: A selection of the production cross-sections for a selection of processes of interest at ATLAS. Shown are both theoretical values and those measured at LHC centre-of-mass energies of either $\sqrt{s} = 7$ TeV (in blue) or $\sqrt{s} = 8$ TeV (in orange). The widths of the bands denote the total uncertainty on the particular values. The numerical values listed beside each point correspond to the total integrated luminosity of the dataset used in performing the measurement [25].

For the sake of comparison the inclusive production cross-sections for a selection of processes of interest at ATLAS are shown in the plot in Figure 2.6, showcasing the relative production rates of $t\bar{t}$ pairs compared with other Standard Model processes. Shown are both the theoretical values, overlaid with recent measurements made using ATLAS Run I data at both $\sqrt{s} = 7$ TeV

[13]Such a measurement was made with early ATLAS data based on the results of a cross-section measurement, obtaining a total precision on m_{top} of approximately 5% [24].

and $\sqrt{s} = 8$ TeV.

From the plot one can observe the inclusive W and Z boson production cross-section to be two to three orders of magnitude above that of $t\bar{t}$ pairs – evidence of the large role played by these processes as backgrounds in several analyses, particularly those involving single top quarks produced *via* the electroweak interaction where signal and background signatures are difficult to distinguish from one another. The dominant production mode of single top quarks at the LHC is *via* a t-channel production mode, which one can also note from the plot to be a few times smaller than the total $t\bar{t}$ production cross-section; top quarks are produced more often in pairs at the LHC than singly. The fact that $t\bar{t}$ production is quite large compared to many other Standard Model processes of interest at the LHC results in $t\bar{t}$ production serving as a significant background process to the signal processes in a number of physics analyses. This is also true for many **Beyond the Standard Model** (BSM) type theories, where $t\bar{t}$ processes represent the largest proportion of background event.

The results of various LHC measurements of the inclusive $t\bar{t}$ cross-section, as well as a combination from measurements made from the Tevatron experiments, are highlighted in the plot in Figure 2.7[14]. All measurements can be seen to be consistent with the Standard Model predictions. The ATLAS-only results for single top quark production cross-section measurements, all in agreement with the Standard Model, can be seen in Figure 2.8.

[14]The $t\bar{t}$ **differential production cross-section** has also been measured – the production cross-section as a function of several detector observables – using ATLAS $\sqrt{s} = 7$ TeV data [26].

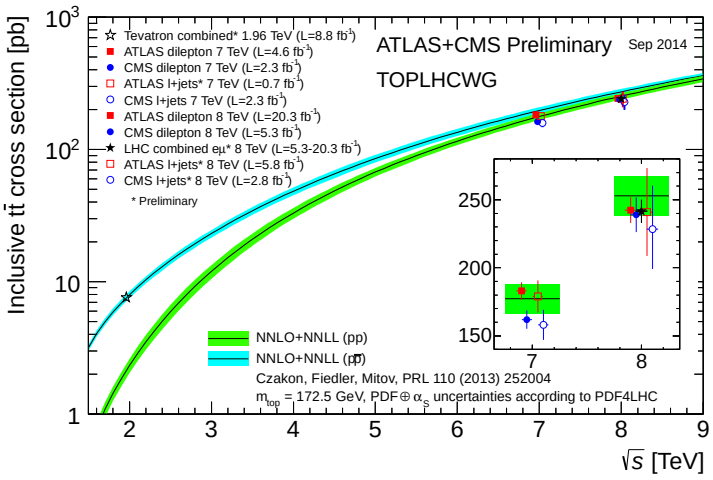

Figure 2.7: Summary of recent top quark pair production measurements, $\sigma_{t\bar{t}}$, shown as a function of centre of mass energy $\sqrt{s}$. Theoretical values are indicated by solid lines, with uncertainties represented by coloured bands. The inset figure, with the y-axis no longer on a logarithmic scale, shows an enlarged view of the two sets of measurements from the LHC experiments [27].

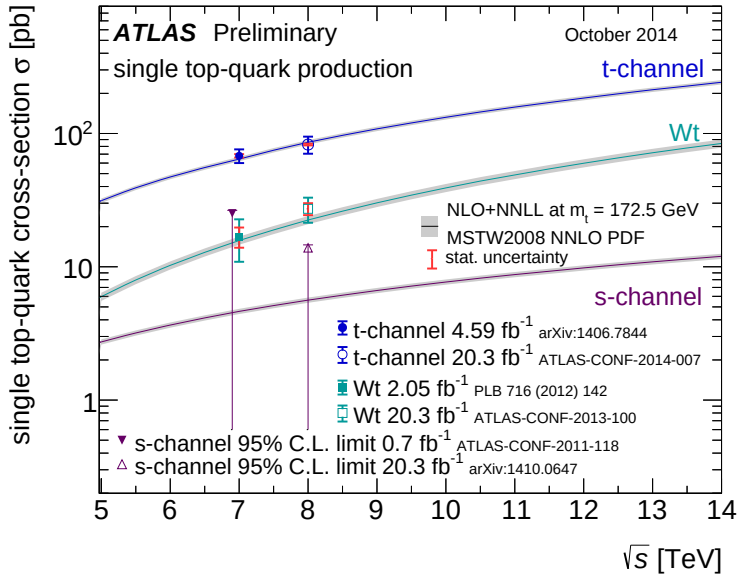

Figure 2.8: Summary of recent ATLAS single top quark cross-section measurements, σ_t, shown as a function of centre of mass energy $\sqrt{s}$. Theoretical values are indicated by solid lines, with uncertainties represented by coloured bands. Shown separately are the three production modes for single top quarks: t-channel, s-channel, and the Wt associated production channel [27].

2.2.4 Decay Modes

Once produced, top quarks will nearly always decay *via* $t \to Wb$, with the Standard Model **branching ratio** (BR) for such a process (as compared with other top quark decay channels) being greater than 99%; the CKM[15]-suppressed BR($t \to Ws$) is at the per mil level and BR($t \to Wd$) an order of magnitude below that[16] [23]. The decay of a $t\bar{t}$ pair will therefore nearly always result in an intermediate state $W^+bW^-\bar{b}$.

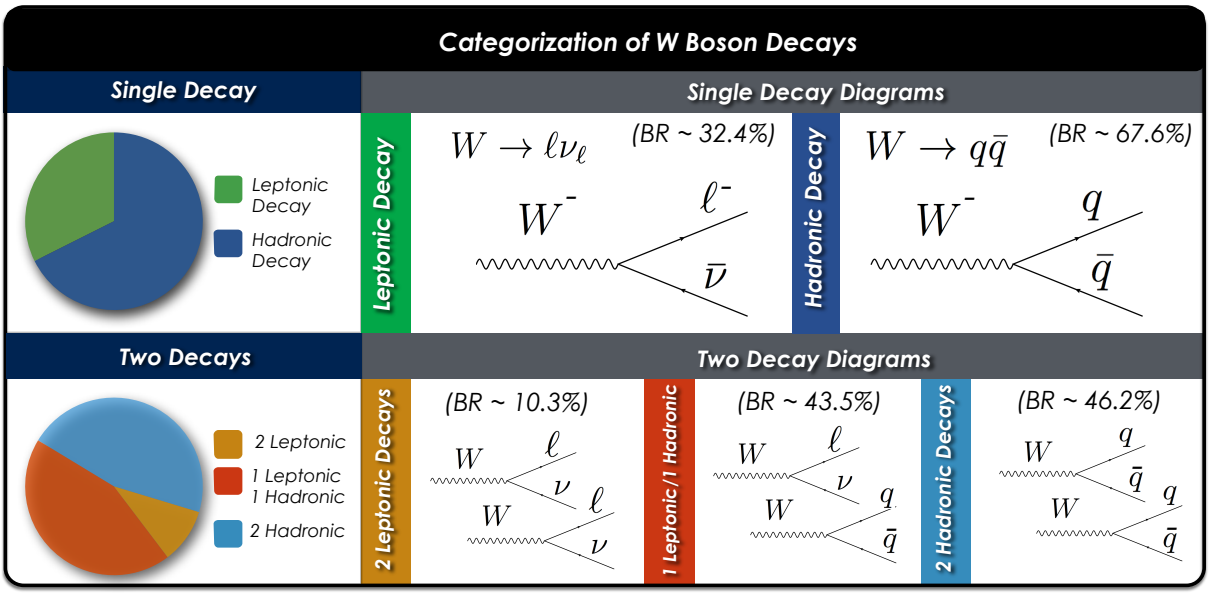

Figure 2.9: A depiction of the leptonic and hadronic decays of a real Standard Model W boson, as well as pie charts illustrating the fractional decay categorizations in the case of a single or pair of W bosons. Values quoted are from [23].

The W bosons, in contrast, are less partial to a single particular decay mechanism as in the case of the top quark decays; a W boson will either decay leptonically (with a decay of the type $W \to \ell\nu$) or hadronically (*via* $W \to q\bar{q}$). Measurements have found the respective branching ratios for each of these processes to be 32.4% and 67.6%, in agreement with Standard Model theoretical predictions. Since there are two W bosons in each $t\bar{t}$ decay, three unique decay scenarios present themselves: both W bosons decay leptonically, both decay hadronically, or a decay of each type occurs. The decay channels of the $t\bar{t}$ pairs are thus characterized by the subsequent decays of the two W bosons and are designated, respectively, as the **dileptonic**

[15]The values of the **Cabibbo–Kobayashi–Maskawa** matrix effectively represent the mixing of quark between the various generations and flavours. For more information refer to the Particle Data Group summary [3].

[16]The strength of the vector-minus-axial-vector (V-A) charged-current Wtb vertex in the Standard Model is given by $\left(-i\frac{g}{\sqrt{2}}V_{tb}\gamma^\mu\frac{1}{2}(1-\gamma_5)\right)$, where V_{tb} is the corresponding term in the CKM quark-mixing matrix.

channel, the **all-hadronic or fully hadronic** channel, and the **semileptonic** or **lepton+jets** ($\ell + jets$) channel.

Figure 2.9 illustrates the decay mechanisms of the Standard Model W boson, with pie charts depicting the branching ratios of the leptonic and hadronic W-decays, as well as the categorizations involving a pair of W bosons (or equivalently, top quarks). The values of the branching ratios of $t\bar{t}$ pairs are summarized explicitly in Table 2.1.

Table 2.1: A summary table of the dominant decay channel classifications for top-antitop quark pairs including the associated branching fraction for each channel. Values quoted are from [23].

Decay Channel	Process	Branching Ratio [%]
Dileptonic	$t\bar{t} \to W^+bW^-\bar{b} \to \ell\nu b\ell\nu\bar{b}$	10.3%
Semileptonic	$t\bar{t} \to W^+bW^-\bar{b} \to q\bar{q}b\ell\nu\bar{b}$	43.5%
All-Hadronic	$t\bar{t} \to W^+bW^-\bar{b} \to q\bar{q}bq\bar{q}\bar{b}$	46.2%

Each of these three $t\bar{t}$ decay topologies presents their own set of both advantages and disadvantages from an experimental point of view. It should be noted that although in principle the branching ratios for the dileptonic and semileptonic channels include all possible lepton flavours, in the case of W bosons decaying *via* $W \to \tau\nu_\tau$, the subsequent decays of the tau particles are often more difficult to identify, and in general the term *lepton* in 'lepton+jets' is taken to correspond only to electrons and muons (*i.e.* $\ell = e, \mu$ only).

Dileptonic $t\bar{t}$ Channel

The dileptonic $t\bar{t}$ channel is characterized by extremely low backgrounds, which consist primarily of cases of fake or misidentified leptons [28]. The presence of two high-energy, non-interacting neutrinos makes it difficult to infer their respective four-vector quantities from the missing energy in the detector. Consequently a full event reconstruction of the $t\bar{t}$ system is not possible; an over-constrained set of equations is often used to infer the neutrino energies. The low branching ratio also results in limited statistics for this channel.

Semileptonic $t\bar{t}$ Channel

In the semileptonic or ℓ+jets $t\bar{t}$ channel, an ambiguity arises in terms of which of the two bottom-quarks[17] are to be associated with which reconstructed W boson – an issue referred to

[17]It is in fact a reconstructed object referred to as a jet which is associated with each bottom-type quark in ATLAS. This will be the topic of Chapter 4.

as **combinatorics** – though when the correct association is made, the hadronically decaying top quark[18] can then be fully reconstructed. The ability to trigger on the high-p_{T} lepton allows for the use of a so-called **tag-and-probe** technique: the leptonically decaying top quark is identified *via* the high-p_{T} lepton which helps to identify a candidate signal event, whereas the hadronically decaying top quark is fully reconstructed, thereby offering a reconstructed object with a strong sensitivity to the top quark mass. A comparatively larger branching ratio also gives the semileptonic channel a source of statistical leverage over the dileptonic channel due to the larger number of potential candidate events. The background contributions are larger than in the dileptonic channel but remain small. It should be noted that the most precise determination of the top quark mass by means of a single measurement was performed in this channel [29].

All-Hadronic $t\bar{t}$ Channel

Among the advantages of the all-hadronic channel – the channel of interest for the present analysis – are the fact that it offers the largest branching ratio as well as the ability to fully reconstruct the $t\bar{t}$ system due to the absence of any final-state neutrinos[19]. The drawbacks of an all-hadronic final state are however significant, with the primary challenges being the presence of a considerable QCD multi-jet background and the heightened effect of combinatorics – ambiguity in the assignment of reconstructed objects to the six final-state quarks in order to reconstruct the two separate top quark candidates. These difficulties and the way in which they are addressed are discussed in detail in Chapters 5 and 6.

Figure 2.10 shows leading-order diagrams for both the initial decay mode of the top quark *via* $t \to Wb$, as well as the three $t\bar{t}$ decay topologies outlined above.

For any top quark-related analysis, it is important to make separate measurements, whenever meaningful to do so, in all three orthogonal decay topologies – dileptonic, semileptonic and all-hadronic – for several reasons. Firstly, separate measurements in each channel are an important test of the consistency of the Standard Model – the top quark mass and the inclusive $t\bar{t}$ cross-section measured in all three channels should not differ with any significance[20]. Also, the signal and background processes in each channel differ, and each measurement is consequently affected by systematic uncertainties either from different sources or from the same sources in varying

[18]The term **leptonically decaying** or **hadronically decaying** top quark refers to the subsequent decay mode of the W boson. A hadronically decaying top quark therefore decays *via* $t \to Wb \to bq\bar{q}$, whereas a leptonically decaying top quark decays *via* $t \to Wb \to b\ell\bar{\nu}_{\ell}$.

[19]Final-state neutrinos in this case corresponds only to neutrinos produced in the initial hard-scatter process from at least one leptonically decaying W bosons.

[20]For $\sigma_{t\bar{t}}$ measurements, the determination of the total cross-section is inferred using the known branching ratio for the particular decay topology used in the analysis. This allows for a direct comparison of the measured values of $\sigma_{t\bar{t}}$ made in different decay channels.

proportions; this point furthermore provides an incentive to ultimately perform a combination of these measurements, since a difference in backgrounds leads to minimally correlated systematic uncertainties, which will ultimately allow for a smaller overall uncertainty. Lastly, while the precision in one channel may prove far superior to the others in one set of circumstances, this ordering in sensitivity is by no means fixed and could depend on a variety of variables such as the type of collider, the centre-of-mass energy, or several detector-related features of the experiment itself; it is therefore important to have benchmark measurements made in even the weakest decay channel, for the purpose of future comparison.

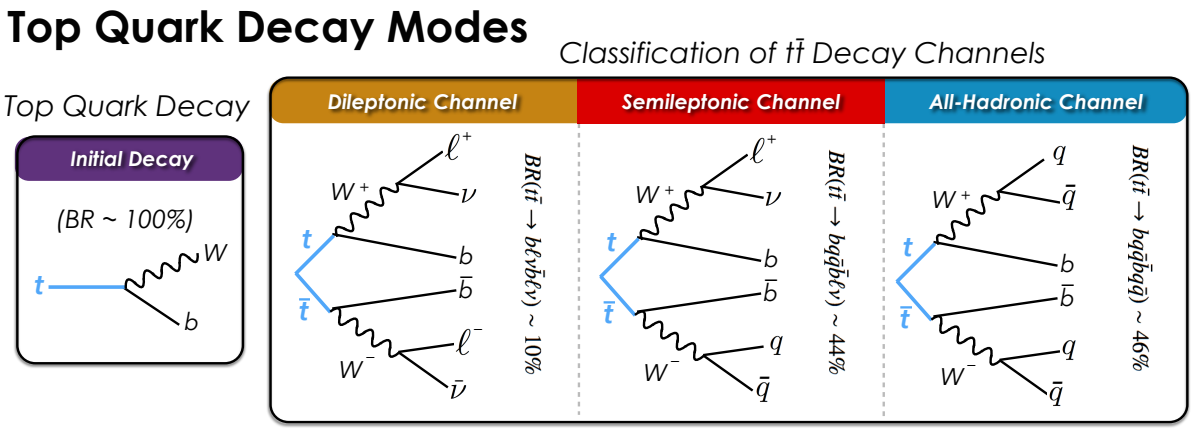

Figure 2.10: The decay of a single Standard Model top quark and the three decay topologies of $t\bar{t}$ pairs, together with their corresponding branching ratios.

2.2.5 Properties

Several of the notable properties of the top quark follow from its large decay width, Γ_{top}. This can be calculated within the Standard Model from a number of leading- and next-to-leading-order decay diagrams; neglecting terms of order m_b^2/m_{top}^2 and $(\alpha_S/\pi)M_W^2/m_{top}^2$ and higher, the full width can be approximated as [23]:

$$\Gamma_{top} \approx \frac{G_F m_{top}^3}{8\pi\sqrt{2}} \left(1 - \frac{M_W^2}{m_{top}^2}\right)^2 \left(1 + 2\frac{M_W^2}{m_{top}^2}\right) \times \left[1 - \frac{2\alpha_S}{3\pi}\left(\frac{2\pi^2}{3} - \frac{5}{2}\right)\right] \tag{2.7}$$

Based on the current knowledge of the top quark mass, the width can be evaluated using the above expression. The value of Γ_{top} can in turn be used to estimate the top quark lifetime ($\sim 1/\Gamma_{top}$), which has a value on the order of 10^{-24} s. Having a lifetime on this scale means that top quarks do not hadronize – form bound meson or baryon states – before they decay. Early proposals of searches for bound toponium states such as $t\bar{t}$ decaying *via* $t\bar{t} \to \gamma\gamma$ were made [30], but no such bound states have been observed[21].

This inability to hadronize also sets the top aside from the other quarks; several of the bare properties of the lighter quarks are either inaccessible or simply have little meaning once they form a bound state. The spin and polarization of a top quark, on the other hand, becomes directly accessible *via* the examination of its decay products, notably the electron and muon in leptonic top quark decays[22], as this information is not washed out from strong interaction effects resulting from hadronization. A multitude of analyses exploit this unique property of top quarks to make detailed measurements of spin correlations and W polarization measurements in $t\bar{t}$ decays[23]. No statistically significant deviations from Standard Model predictions have been observed so far.

Analyses were also carried out using ATLAS data to look for mass differences between the top and anti-top quarks, as a test of the CPT invariance theorem [33]. In another analysis, made in the ℓ+jets channel, an exotic top quark charge of $Q_t = -4/3$ was ruled out, rather favouring the Standard Model $Q = +2/3$ prediction [34].

Figure 2.11 highlights but a selection of some of the roles the top quark plays in a variety of Standard Model processes; many analyses are based on diagrams such as these, where the presence of new, BSM physics signals could most prominently reveal themselves.

[21] It should be noted that exotic, as-of-yet-undiscovered heavier particles such as the Z', theorized to decay *via* $Z' \to t\bar{t}$ could still exist; their presence would therefore give rise to a peak in the invariant $t\bar{t}$ mass spectrum, though this is to be distinguished from a true bound $t\bar{t}$ state.

[22] The term leptonic decays in this sense corresponds to the final-state leptons produced as a result of the decay of the intermediate W boson from the top quark decay.

[23] See for instance [31] and [32].

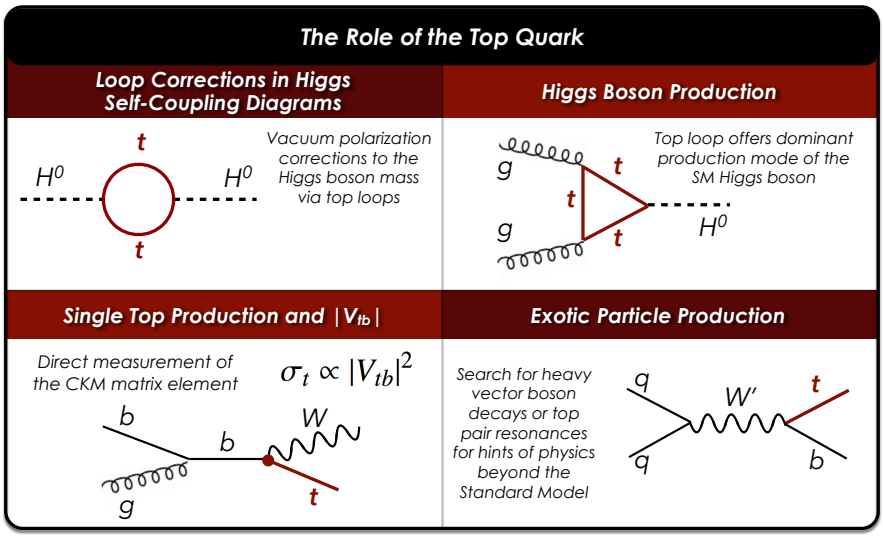

Figure 2.11: Illustrations of some representative ways in which the top quark plays a role in production or decay diagrams. The value of m_{top} has either direct or indirect consequences on any measurements made in these contexts.

2.2.6 Mass

Of the properties of the top quark, the mass, m_{top}, plays a particularly important role in the interactions of elementary, high-energy particles, with a value near the electroweak symmetry-breaking scale.

Having the largest mass of all known fundamental particles, the top quark consequently has the largest coupling to the Standard Model Higgs boson, and thus plays a prominant role in its production mechanisms, such as the gluon-fusion Higgs production mechanism *via* a top quark loop. Furthermore, exotic or BSM particles could manifest themselves principally *via* decays to top quarks.

Definition of the Top Quark Mass

The use of a template method in the present analysis, which constructs a series of so-called template distributions of an m_{top}-sensitive observable for a number of discrete values of the top quark mass, consequently defines the measured value m_{top} as the input mass in the generation of the Monte Carlo samples. This definition is standard for the majority of m_{top} analyses in ATLAS similarly employing a (one- or multi-dimensional) template method for the m_{top} measurement[24].

[24]See for instance the $\sqrt{s} = 7$ TeV ATLAS top quark mass measurements made in the dileptonic and ℓ+jets channels, employing a one- and three-dimensional template method for the extraction of m_{top}, [35] and [36], respectively. In addition a measurement of the top quark mass was performed by the ATLAS collaboration by

Note however that there is an intrinsic ambiguity on the exact definition of the top quark mass, and that the difference between m_{top} using the above definition and that of the top quark pole mass can be expected to be $\mathcal{O}(\Lambda_{QCD})$ or approximately 200 MeV [39].

The final figures in this chapter, Figures 2.12 and 2.13, summarize some of the results of various measurements of m_{top} by the four leading experiments capable of making such a measurement: ATLAS and CMS (LHC) and CDF and D0 (Tevatron) [40]. Figure 2.13 shows some of the most recent ATLAS and CMS public results at the time of writing, some of which supersede the earlier measurements as indicated in the figure. Also shown in both figures is the most current world average value[25] of $m_{top} = 173.34 \pm 0.76$ GeV, derived from a linear unbiased estimation technique which aims to take into account conservative estimates of the statistical and systematic correlations between individual measurements[26]. The more recent resuts have yet to be included in an updated world combination.

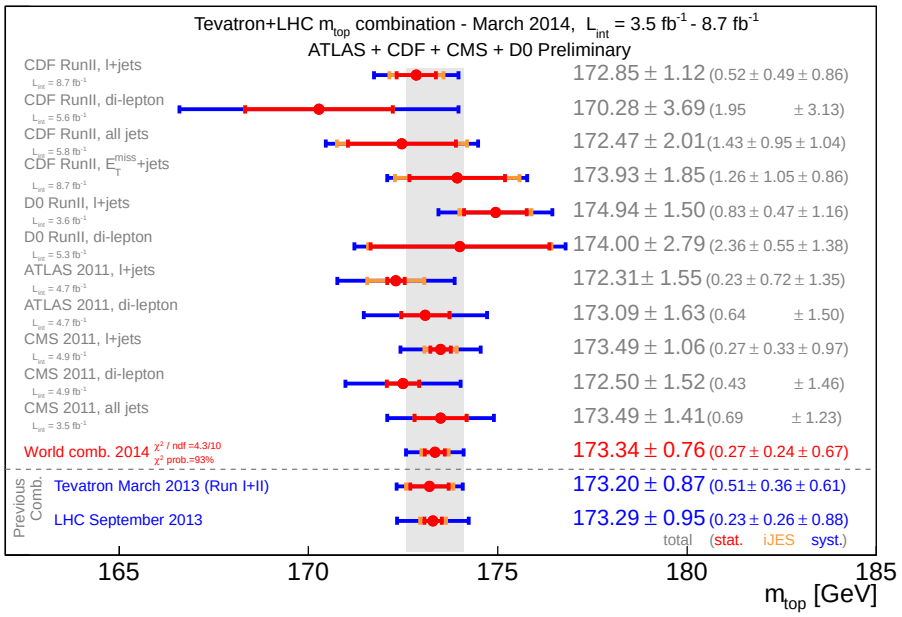

Figure 2.12: Summary plot of recent top quark mass measurements made at the leading LHC (ATLAS and CMS) and Tevatron (CDF and D0) experiments [40].

searching in data for topologies with enhanced contributions from single top quark production [37]. For the results of an ATLAS measurement of the top quark pole mass, see [38].

[25] Note that the value from this world combination does not yet include all of the most recent measurements of the top quark mass, notably the most precise measurement from a single analysis as previously mentioned [29].

[26] For more information on this **Best Linear Unbiased Estimate** (BLUE) method, see [41].

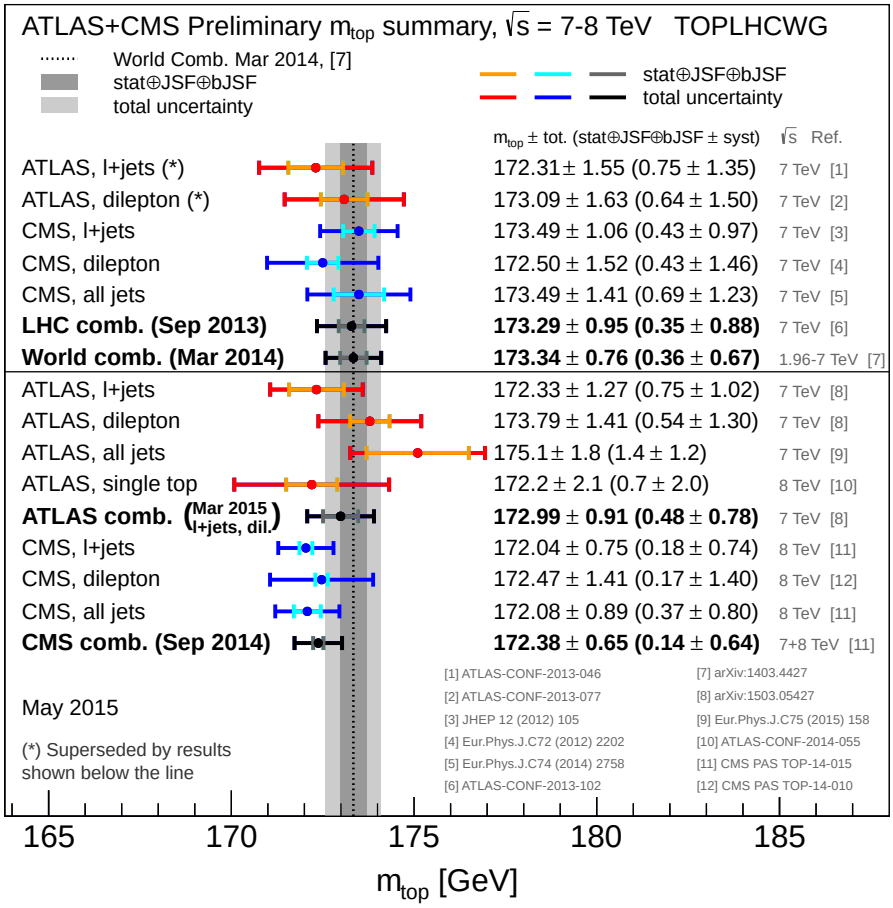

Figure 2.13: An updated summary plot of some of the more recent top quark mass measurements performed at the two LHC experiments [40].

Chapter 3

The ATLAS Experiment

3.1 CERN and the Large Hadron Collider

The Large Hadron Collider (LHC) [42], the host of two of CERN's flagship experiments, ATLAS and CMS, accelerates oppositely directed beams of protons which cross at the designated positions coinciding with the centres of the respective detectors. Large, powerful dipole magnets are used to steer the beams through an ultra high-vacuum beam pipe around their 27 km circular paths. During the 2012 data-taking period approximately 1380 individual bunches of protons, each consisting of approximately 1.6×10^{11} protons, were circulated in each beam, with adjacent bunches separated by 50 ns[1]. An arrangement of multipole magnets are used to confine the proton bunches at the centre of the beam pipe.

3.2 The ATLAS Detector

The ATLAS detector is a large, multi-purpose detector, designed to study a variety of interesting particle physics phenomena. The detector is situated at one of the beam-crossing points of the LHC ring, geographically on the French-Swiss border near the Jura Mountains, and approximately 100 m underground. The multi-layered structure of the detector provides nearly full solid-angle coverage around the p-p interaction point, and allows for the direct measurement of the energies and momenta of a multitude of particle types. As the various fundamental particles leave different signatures in each of the detector's subcomponents, these measurements allow a reconstruction of the interaction events which in turn allows for an understanding of the fundamental interactions of interest that result from the partonic hard-scattering process.

[1]These values differ from the original experimental design as well the values used in Run II, which began roughly at the time of writing and where 25 ns bunch-spacing was used with approximately 2508 bunches per ring. For a more complete description see the High-Energy Collider Parameters summary table in [3].

This chapter outlines the basic purpose and design of the subcomponents of ATLAS with a particular focus on the calorimeter system due to its particular relevance to the analysis described in this thesis. Figure 3.1 presents an overview of the ATLAS detector, highlighting the location of its various subcomponents. For more detailed information the reader is referred to [43].

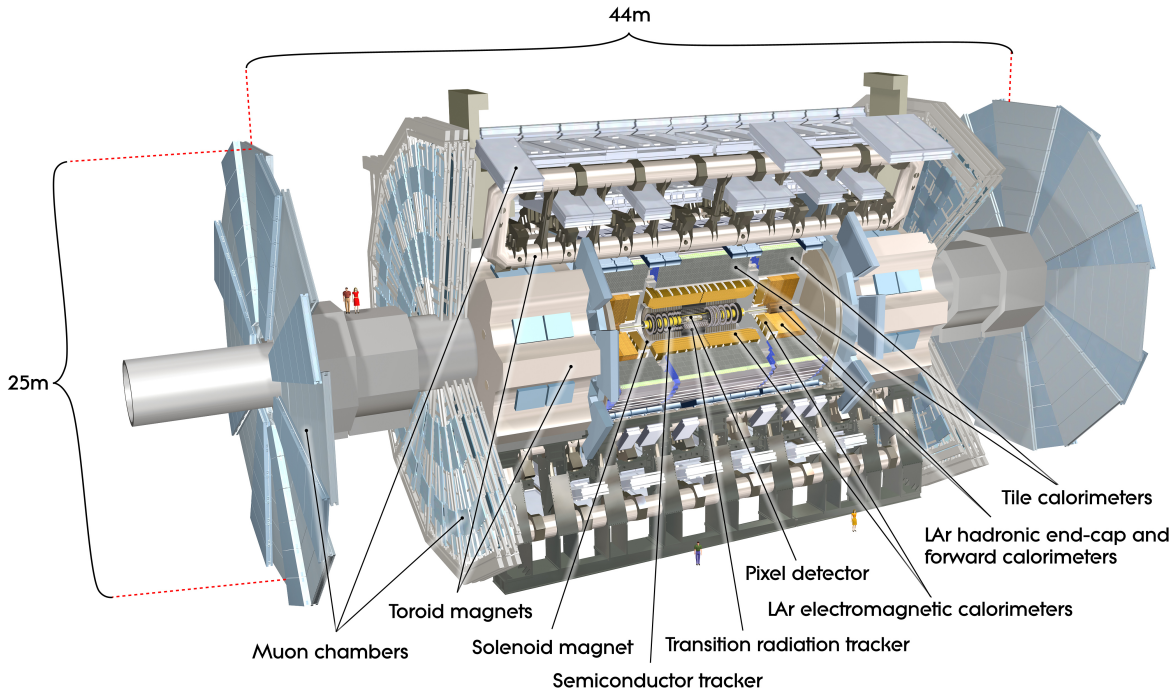

Figure 3.1: A cutaway view of the ATLAS detector highlighting its various components.

3.2.1 Coordinate System and Useful Collider Physics Formulae

A right-handed coordinate system is used in ATLAS with the main interaction point at the centre of the detector definining the origin. The positive x-direction is chosen to point from the interaction point to the centre of the LHC ring, some 4.3 km from the origin. The positive y-direction is selected to point vertically upward. Finally the $\hat{z}-$direction is defined along the beam pipe such that $\hat{x} \times \hat{y} = \hat{z}$.

Owing to the symmetry of the detector, it is useful to introduce a set of cylindrical coordinates (θ, ϕ, z) which can be used to define any position in three-dimensional space in the

laboratory frame. Here θ and ϕ refer to the standard polar and azimuthal angles, respectively[2]. A useful quantity in collider physics to describe the kinematic properties of an object with four-momentum $p^\mu = (E, p_x, p_y, p_z)$, mass m, angular coordinates (θ, ϕ) and speed $\beta = p/E$ is the **rapidity**, defined as:

$$y = \frac{1}{2} \ln \frac{E + p_z}{E - p_z} \quad \text{or} \quad y = \frac{1}{2} \ln \frac{1 + \beta \cos\theta}{1 - \beta \cos\theta} \tag{3.1}$$

The rapidity is a convenient Lorentz-invariant quantity with the distinct advantage that a boost in the z-direction[3] results in a translation in rapidity-space such that $y \to y' = y + y_b$, where $y_b = \ln[\gamma(1 + \beta)]$. Here γ is the usual Lorentz factor given by $\gamma = E/m$. Another useful relation between such quantities is that $\tanh y = \beta \cos\theta$.

High momenta in the transverse (x-y) plane are generally correlated to hard-scatter events of interest, and consequently the **transverse momentum**, $p_\mathrm{T} = \sqrt{p_x^2 + p_y^2}$, becomes a relevant quantity. Similarly, the **transverse energy** E_T is defined by $E_\mathrm{T}^2 = E^2 - p_z^2 = p_\mathrm{T}^2 + m^2$.

For massless particles, where $E = |\vec{p}|$, the rapidity can be replaced by the **pseudorapidity**:

$$\eta = \frac{1}{2} \ln \frac{|\vec{p}| + p_z}{|\vec{p}| - p_z} = -\ln\left(\tan\frac{\theta}{2}\right) \tag{3.2}$$

The pseudorapidity is often used in collider physics as an approximation for the rapidity y, provided the mass of the particle is small such that $E \approx |\vec{p}|$.

The **invariant mass** of any four-vector object with energy E and momentum $|\vec{p}|$ is defined as:

$$m = \sqrt{E^2 - |\vec{p}|^2} \tag{3.3}$$

For any two objects with four-momenta p_1^μ and p_2^μ, the invariant mass of their four-vector sum, $m_{1,2}$, is given by:

$$m_{1,2}^2 = (p_1^\mu + p_2^\mu) \cdot (p_{\mu,1} + p_{\mu,2}) = m_1^2 + m_2^2 + 2\,(E_1 E_2 - \vec{p_1} \cdot \vec{p_2}) \tag{3.4}$$

Using the above expression and following some algebra, a similar expression may be written for the invariant mass of a three-body system[4]:

$$m_{1,2,3}^2 = (p_1^\mu + p_2^\mu + p_3^\mu) \cdot (p_{\mu,1} + p_{\mu,2} + p_{\mu,3}) = m_{1,2}^2 + m_{1,3}^2 + m_{2,3}^2 - m_1^2 - m_2^2 - m_3^2 \tag{3.5}$$

[2]The angle θ is measured with respect to the positive z-axis, and ϕ is defined as the angle from the positive x-axis in the direction of the positive y-axis.

[3]For such a boost, E and p_z are transformed *via* $E \to E' = \gamma(E + \beta p_z)$, and $p_z \to \gamma(p_z + \beta E)$.

[4]The invariant mass can also recognizably be written for a generalized n-body system, and can be expressed in its most basic form *via* the relation: $m_{1,2,\ldots,n}^2 = (\sum_{i=1}^n p_i^\mu) \cdot (\sum_{j=1}^n p_{j,\mu})$

Re-expressing the four-momenta coordinates *via* $p_i^\mu = (p_{T_i}, y_i, \phi_i, m_i)$ for $i = 1, 2$ and letting $\beta_T = p_\mathrm{T}/E_\mathrm{T}$, the two-object invariant mass may be written alternatively, by modifying Equation 3.4, as:

$$m_{1,2}^2 = m_1^2 + m_2^2 + 2E_{T_1}E_{T_2}\left(\cosh\left(y_2 - y_1\right) - \beta_{T_1}\beta_{T_2}\cos\left(\phi_2 - \phi_1\right)\right) \tag{3.6}$$

This allows for some useful relations between the quantities presented thus far:

$$E = E_\mathrm{T}\cosh y, \qquad p_z = E_\mathrm{T}\sinh y, \qquad \beta_z = \tanh y \tag{3.7}$$

In the low-mass approximation where $E \approx |\vec{p}|$, these relations become:

$$E = |\vec{p}| = p_\mathrm{T}\cosh\eta, \qquad p_z = p_\mathrm{T}\sinh\eta, \qquad \beta_z = \tanh\eta \tag{3.8}$$

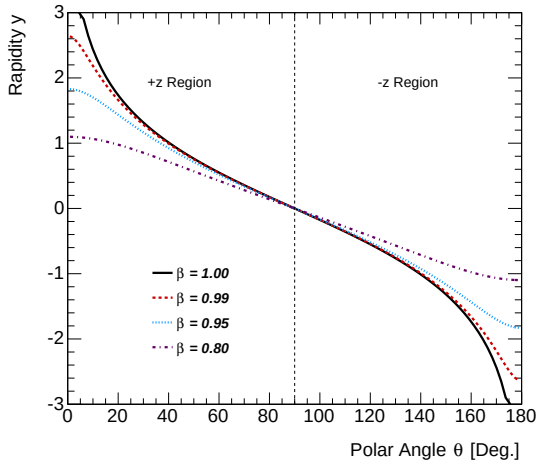

(a) The rapidity y, shown over the polar angle range of the ATLAS detector for a variety of $\beta = p/E$ values. Note that the $\beta = 1.00$ line coincides with the definition of the pseudorapidity η and is associated with particles travelling at the speed of light. y tends to $\pm\infty$ in the direction of the p-p beamline axis.

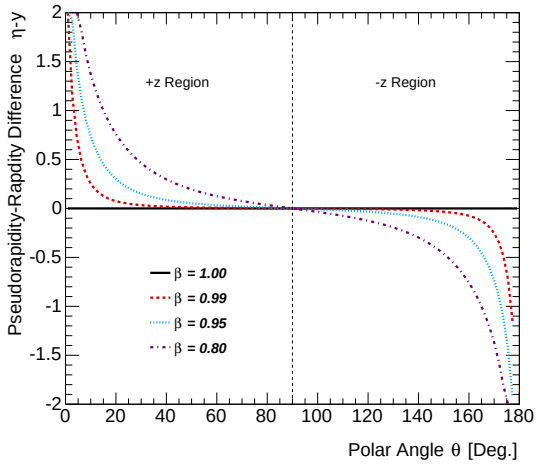

(b) The difference between the pseudorapidity and the rapidity as a function of polar angle, illustrating the bias in using the pseudorapidity for massive particles.

Figure 3.2: The (a) rapidity and (b) scale of the approximation in using the pseudorapidity over the rapidity, both shown for a variety of β values.

The plots in Figure 3.2 illustrate the range of typical y and η values, as well as their difference, as a function of the more familiar polar angle θ. It should be noted that the present analysis restricts itself to central objects with $\eta \in [-2.5, 2.5]$. Figure 3.2(b) in particular makes clear

the difference between the rapidity and pseudorapidity; in the central region of the detector the difference is minimal, but in general one can observe the trend that $|\eta| > |y|$ always, and that the difference between the two becomes enhanced as $E \to m$.

Since there is a one-to-one correspondence between the value of η and the laboratory-frame polar angle θ, a particle's measured angular position together with knowledge only of its transverse energy can therefore be used to infer its total energy. This is recognizably true only in the case that $\frac{m}{E} \sim 0$, but provided $m \ll E$, it provides a reasonable approximation.

As has been shown above, angular separations between particles play an important role in the context of invariant mass calculations. Furthermore they can be used as a means to aid in the discrimination between signal and background events, due to differences in normalized shapes of several key variables. As such, a quantity ΔR is often used in this analysis as a measure of the angular separation between two objects in η-ϕ space. The quantity is defined as:

$$\Delta R = \sqrt{(\Delta\eta)^2 + (\Delta\phi)^2} \qquad \text{(where } \Delta\eta = \eta_1 - \eta_2 \text{ and } \Delta\phi = \phi_1 - \phi_2\text{)} \tag{3.9}$$

In summary, two variables, the transverse momentum (p_{T}) and the separation in η-ϕ space between two objects (ΔR), are used throughout the analysis and their importance here is highlighted as they differ from the more familiar 3-momentum $\vec{p}$ and polar and azimuthal coordinates θ and ϕ. The advantage of employing the transverse momentum is due to the fact that in any hard-scatter interaction, the total momentum in the z-direction is unknown[5] whereas in the transverse (x-y) plane initially there is very little net momentum, and zero net momentum on average; large transverse momenta are therefore indicative of deeply inelastic scattering events of interest. Making use of both the pseudorapidity and azimuthal angular coordinates for the various objects in a given event is more useful for probing the underlying kinematics.

3.2.2 Interaction of Particles with Matter

The interaction of particles with matter constitutes an extensive field of study. Many useful references are available on this topic and the reader is referred to *e.g.* [3, 44, 45]. The primary energy deposition mechanism of interest for high-energy particles interacting with the ATLAS detector involves, in some form, the ionization of electrons from atomic nuclei in the various detector components[6]. Ultimately the energy deposited by particles or their decay products allows for the reconstruction of ionization tracks in the case of charged particles or energy clusters in the detector calorimeters. Both tracks and energy clusters are subsequently used to

[5] The momenta of both incoming protons are known in the z-direction, but the interaction itself involves the partons – the proton constituents – and these may in general have any fraction of their respective proton's total momentum in the z-direction.

[6] Note that ionization is but one of the possible energy deposition mechanisms for high-energy particles. The relative contribution from ionization (and other mechanisms) in general depends on the type of interacting particle, the particle's electric charge and energy, and the material the particle is incident upon.

infer properties of the particles of interest such as their energies or momenta.

3.2.3 Overview of the Various Detector Components

In what follows, a brief summary is provided for each of the parts of the ATLAS detector. Additional information for each detector subcomponent is available in a number of sources, including the full ATLAS detector paper [43]. A particular focus is placed in this section on the calorimeter system, responsible for the energy measurement of high-energy, interacting particles, due to its relevance to the all-hadronic $t\bar{t}$ final state considered in this thesis.

3.2.4 Inner Detector

The innermost region of the ATLAS detector consists of the Pixel detector, the **Semi-Conductor Tracker** (SCT) detector and the **Transition Radiation Tracker** (TRT). The high-granularity Pixel and SCT detectors allow for high-precision measurements of the positions of charged particles as they travel through the tracker region in order to reconstruct trajectories. This information is subsequently used to determine particle momenta and to reconstruct primary and secondary vertices – the projected intersections of charged-particle tracks which identify the position in space at which a particle of interest decayed to two or more particles, as well as the position of the primary partonic interaction for a given event. The large solenoidal magnet surrounding this inner region provides a nominal 2 T field which bends the paths of such charged particles, thereby facilitating a high-precision momentum measurement. The TRT utilizes layers of gas-filled straw tube elements to further enhance the measurements of particle tracks, offering an improvement in the momentum resolution; the TRT also provides electron identification *via* a measurement of transition radiation which is complimentary to that from the calorimeter system. Tracking information is only available for charged particles and only within the pseudorapidity range $|\eta| < 2.5$.

The nominal p_{T}-dependent resolution for the inner detector is required to satisfy[7]:

$$\sigma_{p_{\mathrm{T}}}/p_{\mathrm{T}} = 0.05\%\ p_{\mathrm{T}}\ \oplus\ 1\% \tag{3.10}$$

The relative p_{T} resolution can thus be seen to degrade with increasing momentum – straighter tracks result in a larger uncertainty in the saggita measurement which impacts the measured value of the transverse momentum.

[7]For a detailed summary of the alignment and performance of the inner detector and tracking system during the 2012 data-collection period, refer to [46].

3.2.5 Electromagnetic and Hadronic Calorimeters

The ATLAS calorimeter system surrounds the inner detector and tracking region, and is subdivided into a **Liquid Argon**-based (LAr) calorimeter and a surrounding tile calorimeter, both of which are classified as sampling calorimeters. As can be seen in the schematic in Figure 3.3, both the LAr and Tile calorimeter systems consist of alternating layers of sampling and absorbing materials and together provide near-hermetic coverage surrounding the interaction point. The calorimeter system serves to provide a high-precision measurement of the energies deposited by interacting particles in the detector media, as well as to provide full containment of the showers initiated by high-energy particles. The LAr-based calorimeters use alternating regions of liquid argon and tungsten or copper as the active and absorbing materials, respectively. In the case of the tile barrel calorimeter, steel is chosen as the absorbing material and scintillating tile as the active medium. The novel accordion-shaped design of the **electromagnetic barrel** (EMB) calorimeter layers allows for full azimuthal coverage in the pseudorapdity range $|\eta| < 1.475$.

Three separate cryostats house the LAr electromagnetic barrel, the **electromagnetic endcaps** (EMEC) and **hadronic endcaps** (HEC). The purpose of the cryostats is to maintain near-constant temperatures for the active liquid argon medium. The higher-radiation, far-forward regions are each served by **forward calorimeter** (FCAL) modules, housed in the same cryostats as the EMEC and HEC.

The levels of granularity in the calorimeter systems vary, with the smallest base unit of measurement in a calorimeter referred to as an individual **readout channel** or **cell**. The second layer of the electromagnetic barrel offers the finest granularity of $\Delta\eta \times \Delta\phi = 0.025 \times 0.025$[8]; this has been selected for optimum performance of reconstructed electron and photon objects in the central region. The granularity is increased to $\Delta\eta \times \Delta\phi = 0.1 \times 0.1$ in the tile barrel. A total of approximately 170k individual readout channels make up the combined LAr calorimeters, and there are 10k channels for the tile barrel and extended barrel calorimeters.

In contrast with the momentum measurements from the inner detector, the fractional energy resolution is optimal for particles with high energy. The nominal resolution requirements for the different calorimeter components vary, and were designed to satisfy[9]:

$$\begin{aligned}
\sigma_E/E &= 10\%/\sqrt{E} \oplus 0.7\% \quad \text{(Electromagnetic Calorimeters for } |\eta| < 3.2\text{)} \\
\sigma_E/E &= 50\%/\sqrt{E} \oplus 3.0\% \quad \text{(Hadronic Calorimeters for } |\eta| < 3.2\text{)} \\
\sigma_E/E &= 100\%/\sqrt{E} \oplus 10\% \quad \text{(Forward Calorimeters for } 3.1 < |\eta| < 4.9\text{)}
\end{aligned}$$

[8]Note that $\Delta\eta$ is a dimensionless quantity, and $\Delta\phi$ is measured in radians.

[9]See reference [47] for a summary of the performance of the ATLAS liquid argon calorimeters (EMB, EMEC, HEC, FCAL) over the first three years of data-collecting, as well as a selection of highlighted physics results relying on optimal calorimeter performance.

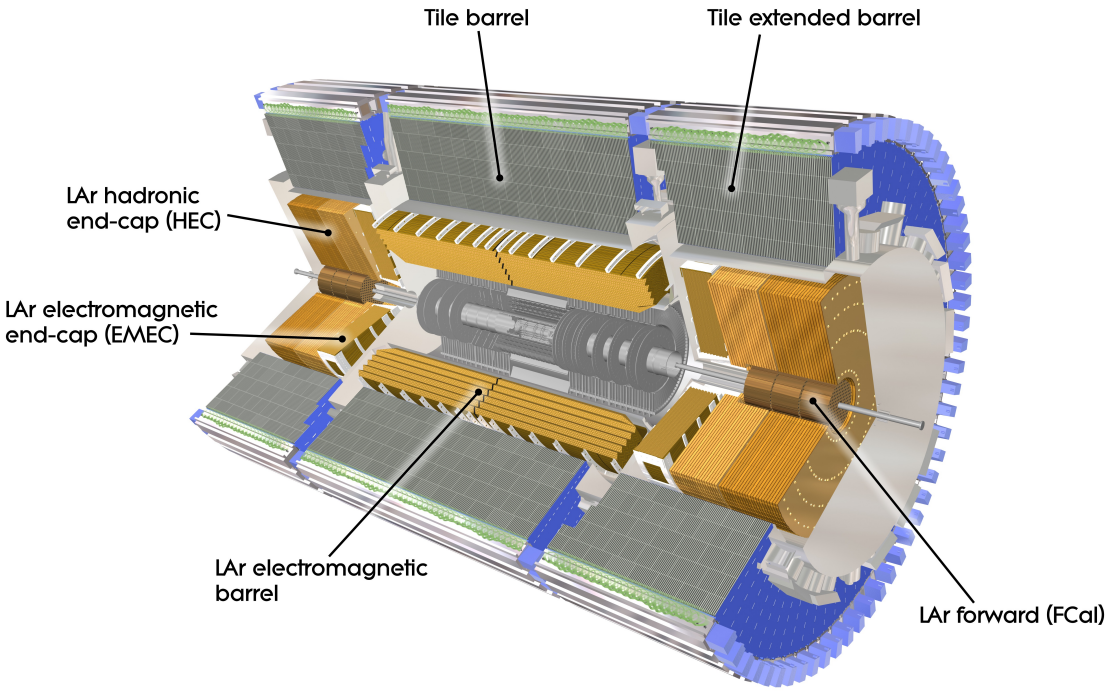

Figure 3.3: A cutaway view of the ATLAS electromagnetic and hadronic calorimeter system.

Pile-Up Effect

The term **pile-up** in the context of energy measurement within ATLAS refers to additional, unwanted energy deposits which adversely affect the final desired measurement, predominantly *via* the degradation of the energy resolution. Pile-up is often classified as having originated from either in-time or out-of-time effects. **In-time pile-up** refers to the presence of multiple interactions per beam crossing in addition to those from the hard-scatter interaction of interest; it is a direct and necessary consequence of the increased luminosity in a collider such as the LHC. **Out-of-time pile-up** refers to additional energy deposits in the calorimeters due to interactions from a previous bunch crossing. An optimization to reduce the effects of pile-up based on data-taking conditions is not trivial: increasing the LHC bunch spacing to mitigate the effects from out-of-time pile-up leads to a decrease in statistics; an increase in sampling times also brings about an increase in electronics noise.

Two physical observables sensitive to the amount of in- and out-of-time pile-up are the number of identified primary vertices, N_{PV}, and the average number of interactions per bunch crossing, denoted by $\langle\mu\rangle$. Though the time interval between adjacent proton bunches in the LHC

ring is constant, the bunches themselves travel in so-called 'bunch trains' – a series of successive bunches which is subsequently followed by a number of empty bunches; interactions between protons from the leading bunches in a train will therefore be subject to a minimal contribution from out-of-time pile-up, compared with those in the middle of the trains; this offers a means by which in- and out-of-time pile-up effects can be differentiated from one another.

Means to suppress the contributions from pile-up in the reconstruction of physics objects and calibration techniques are employed when possible, and are validated by the comparison of data and simulation. It is also customary for analyses to display several measured variables as a function of N_{PV} and $\langle\mu\rangle$ in order to investigate and display their expected sensitivities to pile-up.

Topological Clustering of Readout Channels

Individual readout channels or cells are grouped together by what is referred to as a **topological clustering algorithm**, which performs successive clustering starting with a number of input or **seed** cells. Such an algorithm is meant to limit the unwanted contributions due to random fluctuations or noise and contributions from pile-up activity unrelated to the process of interest. Seed cells are identified based on a predesignated signal-to-noise ratio by requiring the energy of a candidate seed cell to exceed a threshold of $|E_{cell}| > 4\sigma_{noise}$; all cells satisfying such a criterion are classified as seeds.

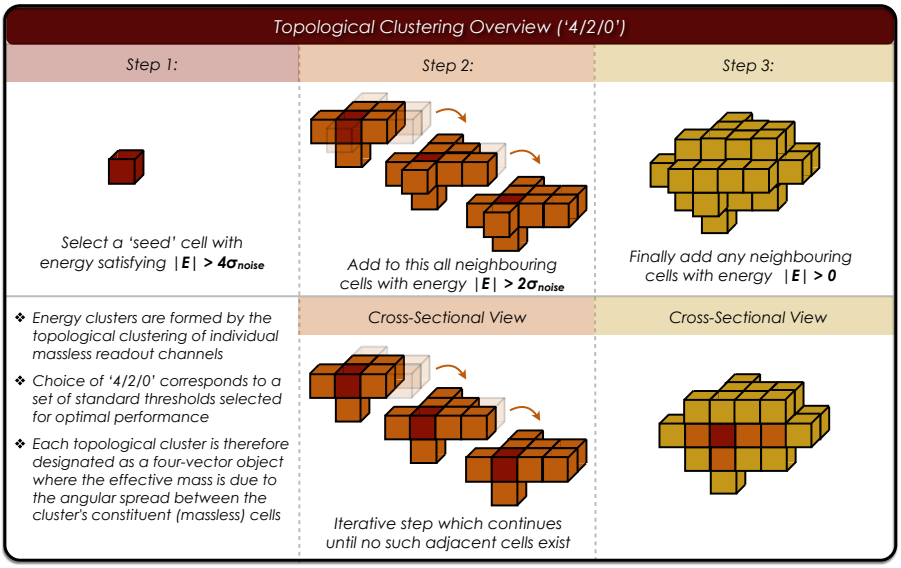

Figure 3.4: An illustration of the process of forming topological energy clusters from individual readout channels using the 4/2/0 seed and noise thresholds - the default used in ATLAS analyses at $\sqrt{s}$= 8 TeV centre of mass energy.

The next step adds to the proto-cluster any adjacent[10] cells satisfying $|E_{cell}| > \mathbf{2}\sigma_{noise}$. Such a process is repeated iteratively and the cluster continues to grow until there are no adjacent cells to add. As a final step, any cells on the cluster's periphery, *i.e.* those adjacent to any cell in the cluster, are added to the cluster[11]. The series of **4/2/0** thresholds, corresponding to the energies of seed/neighbour/periphery cells relative to the noise, were optimized based on dedicated studies performed on simulated data, and were adopted to be the default for ATLAS analyses [48]. The iterative formation of topological energy clusters is illustrated in Figure 3.4.

These energy clusters thus form the baseline for the energy measurements; they become the inputs to the subsequent reconstruction of electron and photon objects as well as hadronic jets as will be outlined in the following chapter.

Local Hadronic Calibration

The **energy response** of a calorimeter refers to the fraction of so-called 'visible' energy read out by the calorimeter system relative to the true energy of the incident particle initiating the formation of energy clusters; an ideal calorimeter will have an energy response that is linear and will be calibrated to unity based on a series of isolated beam tests, validated by comparisons between simulation and data. The ATLAS calorimeters were calibrated using a series of such tests [49–52]. The nominal calibration of a calorimeter is performed based on electromagnetic energy deposits such that the difference between the average measured energy and the true energy of deposits electromagnetic in nature – those as a result of interactions of electrons and photons with the material in the detector – is very small. A significant fraction of hadronic energy deposit mechanisms differ from those that are purely electromagnetic in nature. In general the ratio of the measured energy, following calibration, and true energy for hadronic energy deposits is less than unity. The hadronic energy response and resolution of a calorimeter improve with energy.

The term **Local Hadronic Calibration** or **Local Cluster Weighting** (LC or LCW) refers to the weighting of energy clusters based on their measured properties, particularly *via* a variety of cluster moments, selected for their power to discriminate between energy deposits which are hadronic or electromagnetic in nature. Hadronic energy deposits, for instance, tend to have a lower energy density and are more likely to be situated at greater depths in the calorimeter layers [44]. The goal of local hadronic calibration is to bring the final hadronic response of the calorimeter closer to that of electromagnetic clusters. Out-of-cluster and dead material corrections are also included in order to improve energy linearity and resolution. Clusters deemed to be electromagnetic in nature are unaffected, whereas those clusters consistent with hadronic deposits are scaled up by an energy-dependent factor. The decision is based on the

[10] The identification of neighbouring cells is performed based on the cell positions in three-dimensions.

[11] In this step there is an implicit requirement of $|E_{cell}| > \mathbf{0}\sigma_{noise}$, though in general this threshold may take other values.

output of a neural net with the various cluster moments as the inputs [53]. Following the application of these correction factors, the energy clusters are said to be at the hadronic scale (LCW scale).

An alternative to such an approach is to simply take the cluster energies as they are, and ultimately apply an object-level energy or p_{T} correction to the final physics object of interest; in this case the cluster energies are said to be left at the electromagnetic scale (EM scale).

In ATLAS, both the LCW and EM scaling of clusters are viable options offering comparable performance, and the optimal choice on a global level is not always clear, though many studies have been carried out to compare the performance of the missing transverse energy in the ATLAS detector based on different calibration schemes [54]. The selection of LCW compared with EM is consequently left as an analysis-dependent choice. In the case of the present analysis, the LCW option was selected as the preferred scheme; energy clusters calibrated at the LCW scale were selected to be used for the subsequent reconstruction of hadronic jets – the focus of the following chapter.

3.2.6 Muon Spectrometer

The peripheral region of the ATLAS detector consists of the enormous muon spectrometer system, in which toroidal magnetic fields bend the trajectories of muons as they travel beyond the calorimeters, allowing for a measurement of their momentum complementary to that of the inner detector. The momentum measurements are made by means of high-precision tracking chambers – three layers of monitored drift tubes acting in concert with forward cathode strip chambers in the more forward region. The muon spectrometer employs its own set of triggers and covers the pseudorapidity range $\eta \in [-2.4, 2.4]$, though momentum measurements are possible in a range satisfying $|\eta| < 2.7$. The nominal momentum resolution in the muon spectrometer is required to satisfy $\sigma_{p_{\mathrm{T}}}/p_{\mathrm{T}} = 10\%$ for transverse momenta up to 1 TeV.

3.2.7 Particle Signatures in ATLAS

Figure 3.5 summarizes the interactions of some common particles with the various subcomponents of the ATLAS detector. Solid black regions denote detector components insensitive to the passage of the respective particle. The associated anti-particles are implied for all relevant particles. **Electrons** leave ionized particle tracks in the inner portion of the detector and deposit the bulk of their energy in the electromagnetic calorimeter system. The half-coloured contribution from **photons** in the inner detector is meant to reflect the fact that while **unconverted photons**, being electrically neutral, remain invisible to the detector, **converted photons** in contrast – leading to an e^+e^- pair – leave tracks allowing their presence to be inferred. **Muons** interact only faintly in the electromagnetic and hadronic calorimeters, depositing relatively small amounts of their energy *via* ionization; their contribution in this portion of the table is con-

sequently muted to highlight this fact. Both **charged** and **neutral hadrons**, which include protons and neutrons, respectively, are primarily produced as a result of the hadronization of quarks and gluons. Only electrically charged hadrons leave tracks in the inner detector, whereas all hadrons will leave the vast majority of their energy in the calorimeters. **Neutrinos** can be treated as invisible to all regions of the ATLAS detector due to their vanishingly small interaction cross-sections; in certain cases however, their presence can be inferred using missing transverse energy measurements. Due to the importance of quark signatures in the context of this analysis, the following chapter is devoted entirely to the manifestation of quarks in the ATLAS detector.

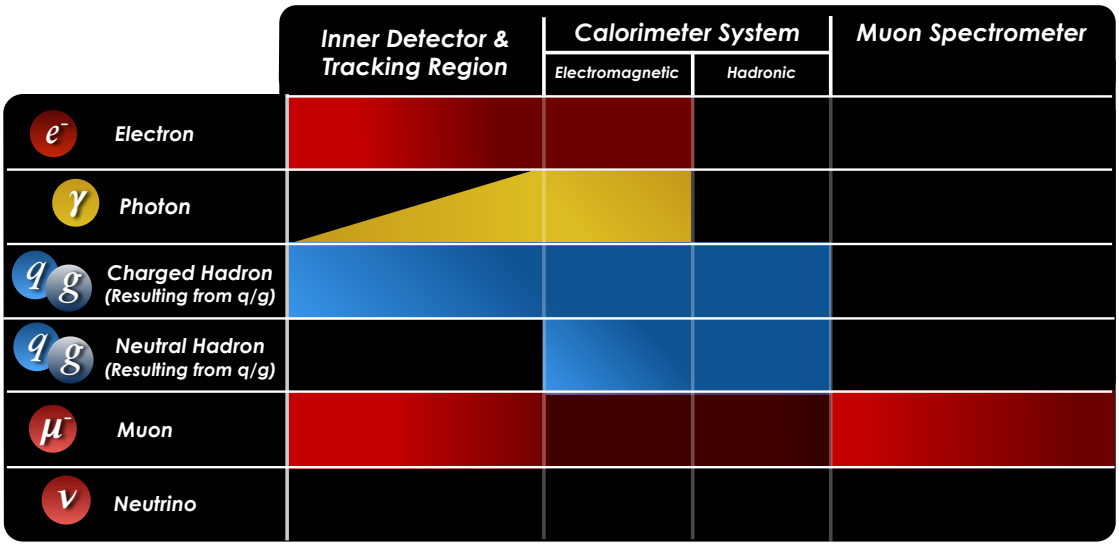

Figure 3.5: A summary of the ways in which long-lived particles interact with different subcomponents of the ATLAS detector. Though photons do not directly leave tracks in the inner detector, those which have converted to e^+/e^- pairs – so-called conversion photons – consequently leave their trace *via* such charged particles. Muons interact, but only very minimally, in the ATLAS calorimeter system; the corresponding entry in the table is lightened to highlight this fact. Both charged and neutral hadrons are formed during the hadronization process often initiated by a quark or a gluon.

It should be recognized that the decay of any particles prior to the transition from one detector component to the next could result in slight deviations from the table[12]. Electromagnetic and hadronic showers initiated by particles as they traverse the calorimeters are predominantly contained within the calorimeter volumes; muons and neutrinos are therefore the only Standard

[12]A neutral π^0 hadron, for example, while not directly detected within the inner detector, usually decays *via* $\pi^0 \to \gamma\gamma$; the subsequent conversion of one of the photons to an e^+e^- pair would consequently be expected to leave tracks in the inner detector.

Model particles expected to contribute with any significance in the makeup of particles travelling as far as and beyond the muon spectrometer system.

3.2.8 High-Level Trigger System

ATLAS makes use of a graduated trigger system made up of three incremental levels, in order to keep data recording rates to a manageable level from the incredible number of potential hard-scatter candidates produced from proton-proton collisions at the centre of the detector.

The first-level trigger (L1) consists of a hardware-based system designed to identify candidate events and suspected **regions of interest** (ROIs) using a subset of detector information. The L1 trigger items are passed by satisfying designated p_{T} and isolation requirement thresholds. The L1 trigger is designed to keep the event rate to below 75 kHz; a failure to reach these rates results in the application of trigger **prescale** values which keep only a subset of some events so as to reach the designed rate.

The high-level trigger system, encompassing the final two levels (L2 and EF or **E**vent **F**ilter), is software based and includes additional offline p_{T} and isolation requirements to be satisfied for an event to be considered. The final event recording rate is required to be below 300 Hz [43, 55].

3.2.9 ATLAS 2012 Dataset

The present analysis makes use of the full statistics available from the proton-proton collision events recorded in 2012 at a centre of mass energy of $\sqrt{s} = 8$ TeV. The evolution of the integrated luminosity collected by ATLAS as a function of time is shown in Figure 3.7(a) with a total cumulative value of approximately $\mathcal{L} = 20.3$ fb^{-1}, recorded over the full year and which passed the required data-quality standards[13].

LHC beam conditions were optimized in order to allow for high rates of collisions at the beam crossing point. As a result the so-called **average number of interactions per bunch crossing**, $\langle\mu\rangle$, was higher than in previous such running conditions. This can be seen in the plot in Figure 3.7(b), which shows the same integrated luminosity divided into bins of $\langle\mu\rangle$, separately for both 2011 and 2012 data-taking. Figure 3.6 shows an event display from a candidate $H \to ZZ^* \to e^+e^-e^+e^-$ event selected from the $\sqrt{s} = 8$ TeV dataset. The rightmost portion of this figure shows a number of reconstructed vertices along the z-axis in the ATLAS coordinate system. These vertices correspond to multiple p-p interactions occurring in the same bunch crossing. The more pronounced red and blue lines, associated with the reconstructed electron candidates, are shown to eminate from only one of these vertices, which is identified as the primary vertex in the event.

[13] An uncertainty of approximately 2.8% was evaluated for the total integrated luminosity [56].

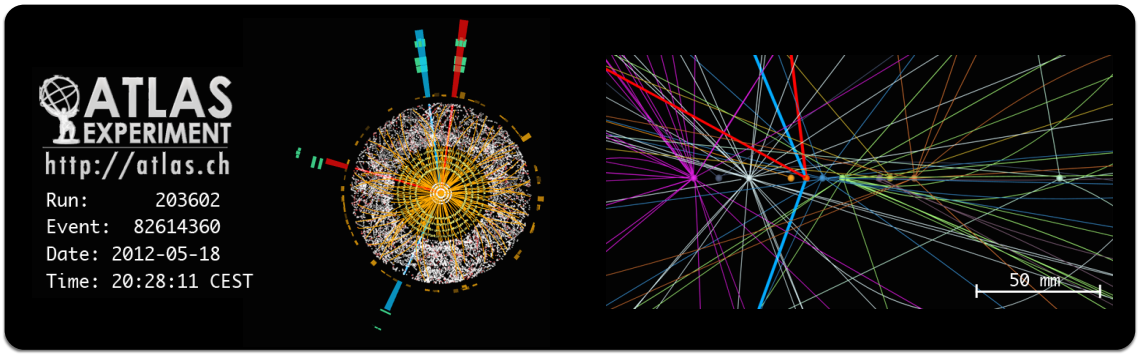

Figure 3.6: A candidate Higgs event display for the process $H \rightarrow ZZ^* \rightarrow e^+e^-e^+e^-$ from the $\sqrt{s}$= 8 TeV ATLAS dataset. The rightmost figure shows a large number of identified vertices in the event. From the event's primary vertex the four reconstructed electron objects are also highlighted (two in blue, two in red). The central image shows the ϕ (or x-y) plane centered on the primary vertex and merged over the full η range in order to visualize the interactions from these reconstructed objects in the transverse plane. Shown are both hits in the innermost tracking region of the detector and energy deposits in the calorimeters. The interactions of particles in the ATLAS detector as a result of the remaining vertices would contribute to the in-time pile-up for the event [57].

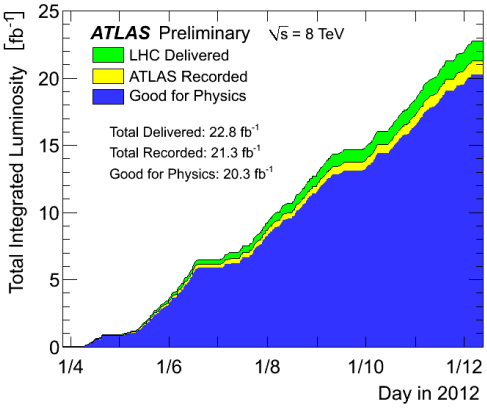

(a) Integrated luminosity collected by ATLAS as a function of time.

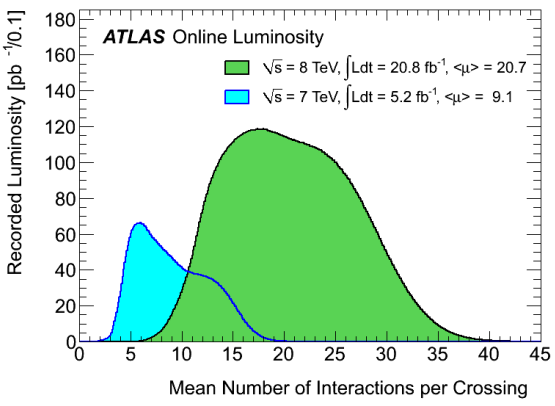

(b) The average number of interactions per bunch crossing.

Figure 3.7: Plots showing (a) the data collected over the course of the 2012 period and (b) the average number of interactions per proton-proton bunch crossing. Both plots are taken from [13].

Chapter 4

Quarks & Jets

4.1 Quark Signatures in ATLAS

The production of any quarks in a hard-scattering interaction at the centre of the ATLAS detector is inferred from characteristic signatures exhibited in the various detector components by the particles produced as a result of a hadronization or showering process. These signatures are predominantly in the form of charged-particle tracks in the inner region of the detector or of calorimeter energy deposits. The latter is of primary interest for this analysis.

Bare quarks are found only to exist in bound hadronic, colour-neutral states – a property which is referred to as quark confinement. The final-state quarks produced in p-p collisions immediately form charged or neutral hadrons and are therefore not detected themselves. Though no analytic form exists to describe such partonic showering and hadronization processes, many models successfully describe their properties. The end result is a collimated spray of high-energy hadrons which either travel through the various regions of the detector, or decay to lighter particles (ultimately leading to lighter leptons, neutral and charged pions and photons) which themselves do so. As the hadrons or their decay products travel through the detector calorimeters their energy is deposited through a variety of mechanisms in localized regions of the detector. These energy deposits can be reconstructed to infer the properties of the given quark (or gluon) produced in the hard-scatter event.

The focus of the present chapter is that of such **jets** – the manifestations of quarks in the ATLAS detector. Jets are created by means of the four-vector addition of a number of conglomerate energy clusters[1]. In this sense a jet is not meant to represent a physical object; rather, it is the representation of a more fundamental particle which is not able to be reconstructed directly. A quark's four-vector quantities and other properties are thus inferred from those of

[1]So-called **track jets** can similarly be defined based on the interactions of charged particles in the inner detector region and stemming from the same hadronization process. For the present analysis however, it is calorimeter jets which are of primary interest.

its associated reconstructed jet.

Similarly to quarks, gluons form hadrons *via* parton showers, and ultimately leave their footprint in the form of showers of charged tracks and energy deposits. Although subtle differences between quark- and gluon-initiated jets exist, both types of particles manifest themselves in a similar way. In this way the term 'jet' is meant to refer to the reconstructed object used by ATLAS physicists to probe the properties of deeply inelastic scattering events in which at least one quark or gluon is produced in the hard-scatter process of interest[2].

4.2 The Anti-k_T Jet Reconstruction Algorithm

A **jet reconstruction algorithm** is employed to reconstruct the four-vector objects referred to as jets given a collection of input energy clusters. A number of such algorithms are available, and these can generally be subdivided into two classes: geometric or **cone-type** algorithms and **sequential recombination-type** algorithms. The anti-k_T algorithm used in this analysis is of the latter type. It is the standard jet reconstruction algorithm employed by the majority of $\sqrt{s} = 8$ TeV ATLAS analyses [59].

The Anti-k_T Algorithm

The anti-k_T algorithm sequentially groups together calorimeter energy clusters, and begins with the merging of higher-p_{T} objects. This is in contrast to the k_T algorithm which begins by merging together softer objects. The input to the algorithm for a given event is the set of all topologically constructed energy clusters in the detector's calorimeters. In this analysis these energy clusters are corrected using derived LCW weights based on several cluster moment variables as mentioned in Section 3.2.5.

For the purposes of the anti-k_T algorithm, a metric d_{ij} is used to define the distance between two objects with indices i and j, and where d_{ij} is given by:

$$d_{ij} = \min\{k_{Ti}^{-1}, k_{Tj}^{-1}\}\Delta R_{ij}/R \tag{4.1}$$

In the above expression, k_{Ti} is the transverse momentum (p_{T}) of object i, and ΔR_{ij} a measure of the angular separation[3] between two objects in the ATLAS coordinate system where:

$$\Delta R_{ij}^2 = (y_i - y_j)^2 + (\phi_i - \phi_j)^2 \tag{4.2}$$

[2]See for example [58], where a multivariate technique was employed in order to build a quantity useful in discriminating quark- from gluon-initiated jets.

[3]Note that this differs slightly from the definition of ΔR presented earlier, though for massless objects the definition is identical. The present definition using the rapidity y rather than pseudorapidity η is used exclusively for the anti-k_T algorithm presented in this chapter.

The term R is a user-defined parameter. The default value of R employed for the present analysis is $R = 0.4$, whereas larger values such as $R = 1.0$ are typically chosen for boosted topologies in which a single, large-radius jet is reconstructed, in an effort to encompass the majority of the energy deposits. Though it is tempting to visualize a cone-shaped region with an angular radius of $R = 0.4$ to define the confines of a given jet, it would be misleading to do so; given the sequential recombination nature of the anti-k_T algorithm, not all clusters within the geometrical confines of an angular area satisfying $\Delta R < 0.4$ necessarily become constituents of the final jet. The size of the R parameter is nevertheless correlated to the geometric size of a reconstructed jet – larger values of R will reconstruct jets encompassing a larger effective volume in the calorimeters.

With the definition of d_{ij} above, the anti-k_T algorithm begins by first calculating, for each possible energy cluster pairing ij, the value of d_{ij} from Equation 4.1, as well as the distance between each individual cluster and the beamline – a quantity defined by $d_{iB} = k_{T,i}^{-1}$. The minimum of all values of d_{ij} and d_{iB} is then identified for all pairs of clusters. In the case that the minimum is found to be one of the distance terms d_{ij}, the two corresponding clusters are merged together by means of a four-vector sum. The process is repeated iteratively until such time as no more clusters remain to be merged together; at any point in the procedure that d_{iB} is found to be the minimum value for some cluster i, that cluster is classified as a jet and is removed entirely from the list. Eventually no such clusters will remain; all clusters will have been replaced by the merged and higher-energy objects referred to as jets. Ultimately only those jets above a certain p_{T} threshold will be considered in a given event. This threshold is also common to the majority of ATLAS analyses with the $\sqrt{s} = 8$ TeV dataset and is chosen to be 20 GeV.

4.3 Levels of Jet Reconstruction

The **level** of reconstruction of a jet defines the type of objects from which a jet object is reconstructed, and the manner in which such reconstruction is performed. The anti-k_T algorithm to be presented in Section 4.2 is the way that this reconstruction is performed for data events, but alternate levels or definitions of jets are possible for simulated events. Comparisons between various levels allow for the development of understanding in the context of several detector-related effects which can affect the ultimate performance of jet reconstruction for a given analysis. Figure 4.1 outlines the various levels of reconstruction – from the idealized concept of parton-level jets to the fully reconstructed jets employed in the analysis of data events. What is meant by each of these levels is described below.

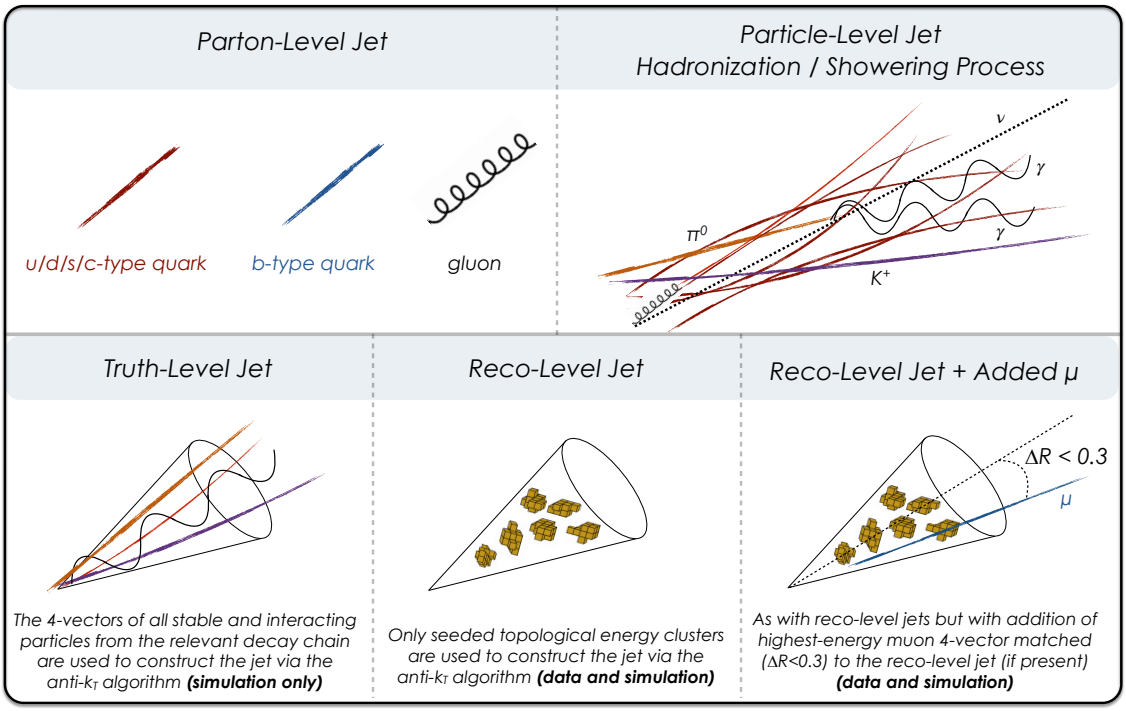

Figure 4.1: Illustration of jets reconstructed at various levels as explained in the text. The parton- and particle-level jets correspond to true physics objects, whereas the truth- and reconstructed-level jets are reconstructed to infer the properties of the associated physics objects.

Parton- and Particle-Level Jets

At its most fundamental level, a parton itself – a quark or a gluon as the case may be – may be thought of as an idealized jet. From the truth record of a simulated sample, one has access to the four-vector coordinates $(p_{\mathrm{T}}, \eta, \phi, E)$ which define the parton-level jet object[4]. For the present case only the six principal quarks from the $t\bar{t}$ decay products are considered, though early on in the stages of the analysis some preliminary studies were performed based on gluons, in order to understand the kinematics, based on simulation, of gluon-initiated jets. **Parton-level jets** therefore represent an idealized and unattainable – albeit illustrative – upper limit for what could be achieved were it possible to probe the hard-scatter process to an arbitrarily high level of precision.

The next level of complexity involves **particle-level jets**, which serve primarily as a pedi-

[4]It should be pointed out that it is more customary to express four-momentum coordinates as (E, p_x, p_y, p_z). The non-standard form $(p_{\mathrm{T}}, \eta, \phi, E)$ is written here due to the fact that the variables are more commonly employed in collider experiments. Both forms nonetheless uniquely define the energy and three-momentum coordinates of a given object.

gogical tool in the development of the concept of a jet; particle-level jets can be thought of as the collective four-vector sum of all associated particles down the decay chain belonging to the initial quark or gluon of interest, assuming such information to be available.

Truth-Level Jets

Not far from the concept of particle-level jets, **truth-level jets** are similarly constructed from particles associated with the parton of interest, though only the subset of stable particles, and crucially those visible to the ATLAS calorimeters, are included. Stable in this case is taken to mean particles with lifetimes satisfying $\tau > 10$ ps. Truth-level jets therefore characterize the ideal level of performance attainable from the calorimeter-level information. As they rely on truth-record quantities, truth-level jets, like parton- and particle-level jets, are able to be reconstructed only in simulated events. To reconstruct truth-level jets, the four vectors of all stable, interacting particles are grouped together by means of the anti-k_T clustering algorithm with the same R parameter choice as above, though here it is the four-vectors of the actual particles that are used in the reconstruction as opposed to those of energy clusters.

Reconstruction-Level Jets

The anti-k_T jet reconstruction algorithm, as described above, is employed to sequentially group together topologically clustered energy readout cells in order to produce the final category of jet objects: **reconstruction-level** (or simply **reco-level**) **jets**. The topological energy clusters used as inputs for the algorithm are those described in Section 3.2.5. As no truth-record information is employed in this process, reconstruction-level jets may be constructed in an identical fashion in both simulated and data events.

Reconstruction-Level Jets with Added Muon Four-Vectors

Finally, the four-vectors of muon objects[5] which are matched to reconstruction-level jets are added to the associated jet four-vector in an effort to correct for the often significant energy lost due predominantly to certain types of heavy-flavoured quark decays. Such decays are classified as **semileptonic b-quark decays** and are mediated by a virtual W boson[6]. These types of decays are depicted in Figure 4.2, and it can be reocgnized that in the case of a final-state neutrino and muon, only a minimal amount of energy will be expected to be deposited in the detector's calorimeters from the muon. It is for such cases that it is advantageous to add the

[5]Muon objects are to be defined in Chapter 7 prior to introducing the event selection cuts employed to select candidate signal events.

[6]The semileptonic b-decays referred to here are not to be confused with the semileptonic $t\bar{t}$ decay classification; the latter refer to the decay channels of the two *real* W bosons produced from the top quark decays directly.

muon's energy back to the reconstructed jet should such a match exist. In the contrasting case of **hadronic b-quark decays**, one expects a minimal loss in the resulting detected energy.

It is recognized that semileptonic bottom-quark decays are also possible with lepton flavours other than muons, such as $b \to W^* c \to \ell \nu_{\bar{\ell}} c$ where $\ell = e, \tau$[7]. For either of such cases, the neutrino will escape the detector undetected, but the lepton's energy – with the exception of a further leptonic τ decay – will largely be absorbed by the detector's calorimeters. Since muons interact only minimally in the calorimeters, only the muonic decays of bottom-type quarks are targeted and corrected for in this way – they represent cases in which one expects a significant amount of otherwise undetected energy due to semileptonic quark decays[8].

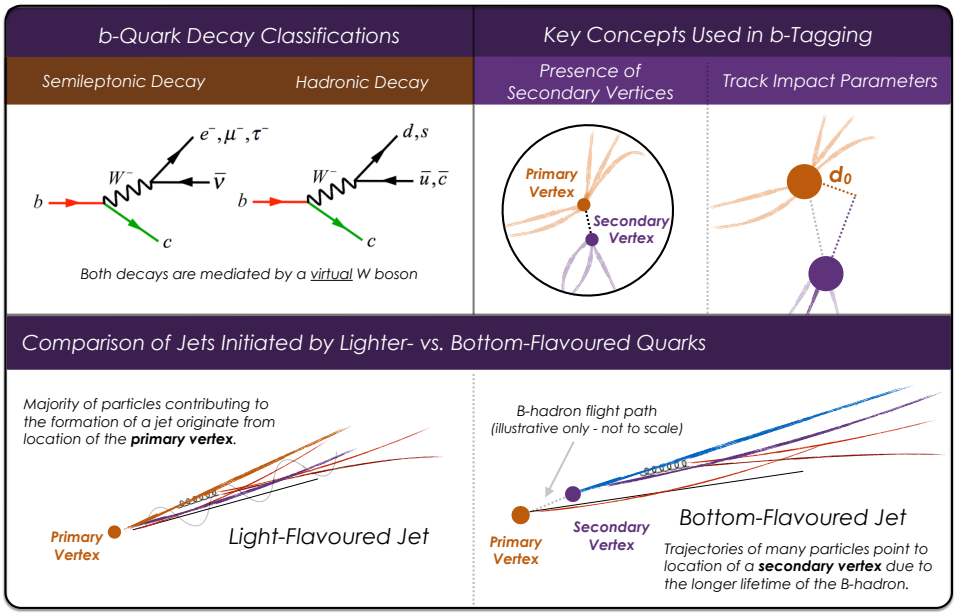

Figure 4.2: Illustration of key concepts used in the identification of b-quark initiated jets *via* b-tagging algorithms. In the upper left are shown the two leading-order decay channels for bottom-type quarks. The upper right image shows two key ingredients used in the various b-tagging algorithms: the presence of secondary vertices in the inner detector and the impact parameter from reconstructed track-level objects relative to the primary vertices. The difference between primary and secondary vertices are illustrated in the lower portion of the figure.

In the event that more than one reconstructed muon is matched to the same jet, only the highest-energy muon is added to the jet. Note that, as illustrated in Figure 4.1, the same

[7]Furthermore it can be recognized that semileptonic c-quark decays are possible from the decays of c-quarks originating from the *real* hadronically decaying W bosons.

[8]In the description above it is recognized that c-type quarks in the final state $\ell \nu_{\bar{\ell}} c$ can themselves subsequently decay *via* the same process involving a virtual W boson. Such a process is referred to as a cascade-type decay. Adding a matched muon's energy and momentum back to an associated reconstructed jet will also recognizably be expected to compensate for energy losses due to cascading decays.

requirement of $\Delta R(\mu,\text{jet}) < 0.3$ is used in order to constitute a match between objects.

The improvement from adding muons to jets will be further motivated in Section 4.5.3. It is employed in this analysis for the purposes of assignment of jets to the top quark candidates, which will be described in detail in Section 6.4.2, as well as in building the final observables to extract the measurement of the top quark mass. It will be shown that this correction improves the precision in the final measurement by a modest but significant amount.

4.4 Jet Flavour and Tagging

4.4.1 Jet Flavour

The flavour of a reconstructed jet is meant to correspond to the flavour of quark or gluon having initiated the hadronization process leading to the reconstructed jet. In the categorization of the quark flavours, the term **light** is meant to correspond to up-, down-, and strange-type quarks. The charm- or bottom-type quarks are referred to as **heavy** quark flavours for this analysis, though at times the charm-type quarks will be grouped together with the other light flavours when bottom-type quarks are meant to be distinguished from any other-flavoured quarks. In the case of ambiguity this will be explicitly stated. For simulated events, in which one has access to truth-record information from the initial hard-scatter process, a quantity referred to as the **jet-quark matching efficiency**, $\varepsilon_{j,q}$, will be defined as the fraction of jets which have been both reconstructed and matched to a truth-record quark from the initial hard-scatter process, relative to all such quarks in the central region of the detector ($|\eta| < 2.5$). Those quarks falling outside the fiducial detector region considered cannot be expected to lead to a jet being reconstructed within such a region, and are therefore not included in this calculation. The jet-quark matching efficiency is thus defined as:

$$\textbf{Jet-Quark Matching Efficiency:} \quad \varepsilon_{j,q} = \frac{\#\text{ of hard-scatter quarks in } |\eta| < 2.5 \text{ matched to a jet}}{\#\text{ of all hard-scatter quarks in } |\eta| < 2.5} \tag{4.3}$$

The subscript j,q denotes 'jet' and 'quark' respectively, and is simply meant to distinguish this from other efficiencies in the analysis. It should be recognized that $\varepsilon_{j,q}$ is a flavour-dependent quantity; it is evaluated separately for each particular quark flavour.

Figure 4.3 shows the jet-quark matching efficiency for simulated signal $t\bar{t}$ events as a function of the quark pseudorapidity. It can be observed that $\varepsilon_{j,q}$ is greatest for bottom-flavoured jets, in part due to the fact that the bottom-type quarks in $t\bar{t}$ events are more often produced at higher energies and are thus more likely to initiate hadronic showers of sufficiently high energy that a high-p_{T} jet will be reconstructed[9].

[9] As in the case of muon objects, the definition of jet objects will be summarized in Chapter 7.

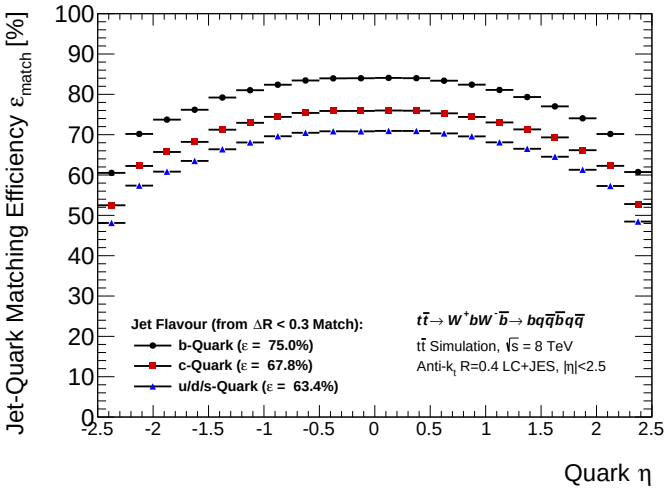

Figure 4.3: The jet-quark matching efficiencies as evaluated from simulated all-hadronic $t\bar{t}$ events. The various marker shapes and colours represent the different quark flavours or the jets associated to these quarks: b-type quarks (**black**), c-type quarks (**red**), and other lighter-type (u/d/s) quarks (**blue**), with inclusive values for the overall matching efficiencies shown in brackets. The efficiencies were evaluated prior to the application of event selection cuts aside from the selection requirements on the reconstructed jets.

The jet-quark matching is performed by requiring $\Delta R < 0.3$ between the two candidate objects[10]. In the case of a successful match, the jet flavour is thus assigned based on that of the matched quark. While the bottom-flavoured quarks are plotted separately, the up-, down-, and strange-type quark flavours are grouped and displayed together, and sometimes with the inclusion of charm-type quark flavours, though the latter are also displayed on their own for reasoning that will be explained below.

Given the jet flavour information, stacked distributions of the jet energy, mass[11] and pseudorapidity were produced, and are shown in Figure 4.4, illustrating the flavour decomposition of the jets. The distributions are filled from the same signal events used to produce the plots in Figure 4.3.

Quantitatively, since roughly a third of the final-state quarks in an all-hadronic $t\bar{t}$ sample can be expected to be $b/\bar{b}$-type quarks[12], one should expect to observe twice the number of jets initiated by lighter-type (u/d/s/c) quarks as b-type quarks in signal events. Indeed upon taking into account the cumulative values of the jet-quark matching efficiencies for the respective flavours, it is found that, as expected:

$$\frac{N_{q-jets}}{N_{b-jets}} = \frac{f_q \ \frac{1}{\varepsilon_{j,q}}}{f_b \ \frac{1}{\varepsilon_{b,j}}} \approx 2 \tag{4.4}$$

[10]Here it is noted that ΔR once again refers to the angular separation in $\eta - \phi$ space, *i.e.* $\Delta R = \sqrt{\Delta\eta^2 + \Delta\phi^2}$, as there is a potential ambiguity due to the R parameter employed by the anti-k_T algorithm in the reconstruction of jets. The definition here is to be implied by default throughout this thesis.

[11]The invariant mass of a jet, as in the case of any four-vector object, is the difference in quadrature between that object's energy and momentum, namely $m = \sqrt{E^2 - p^2}$.

[12]A minimal number of events with CKM-suppressed decays of the type $W^+ \rightarrow c\bar{b}$ or $W^- \rightarrow \bar{c}b$ are also to be expected.

where f_q is the fraction of all light-flavoured jets, and f_b the fraction of bottom-flavoured jets, evaluated from the integrals of the respective distributions.

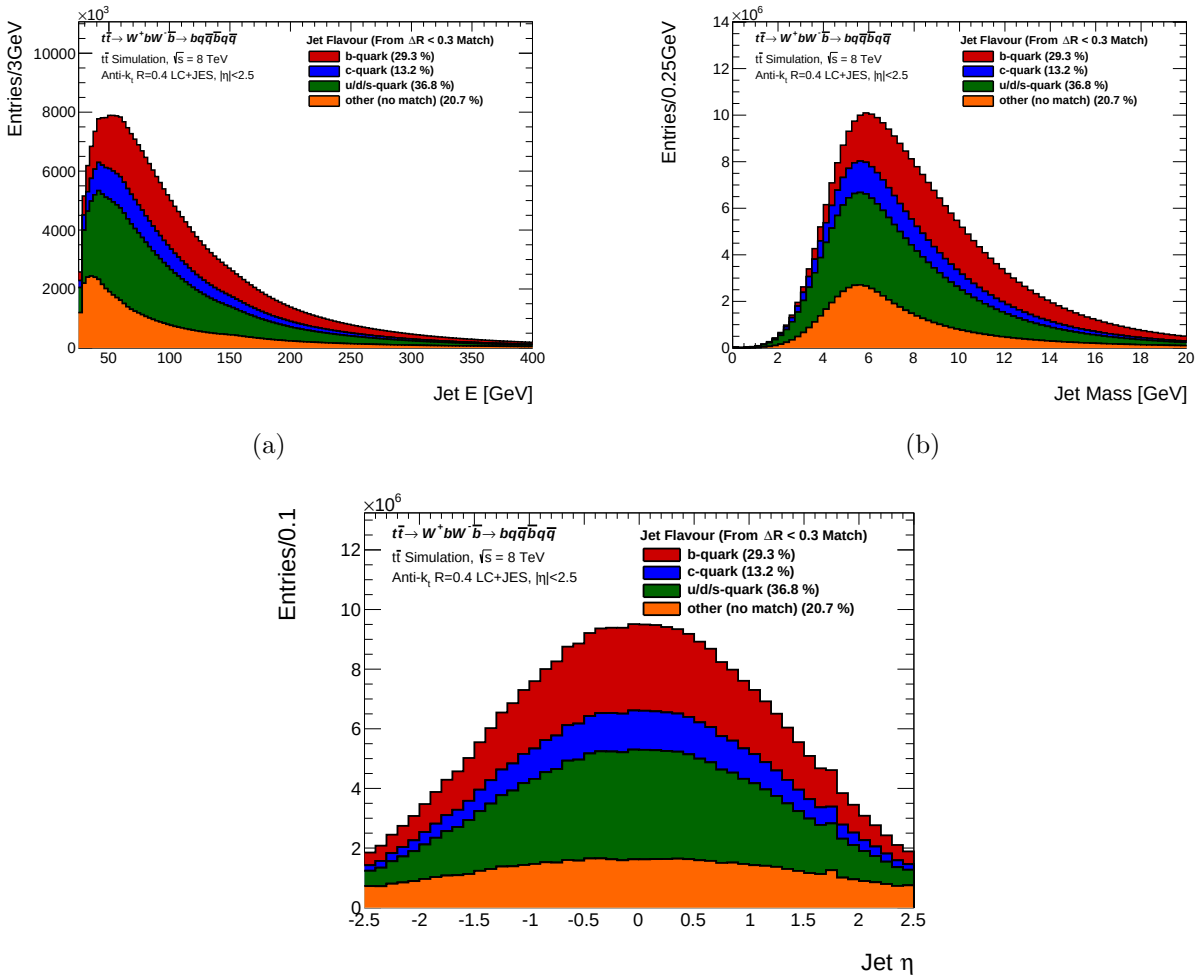

Figure 4.4: Stacked histograms from simulated signal events showing distributions of (a) jet transverse momentum, (b) jet mass and (c) jet pseudorapidity, decomposed into jet flavours based on matches to truth-record quarks from top and anti-top quark decays.

In the flavour-decomposed distributions in Figure 4.4, the orange-filled histograms correspond to jets which were not matched to any of the six quarks from the hard-scattering process; they are assumed to have been initiated by gluons, though strictly there was no ΔR match to a truth-record object . The gluons themselves can be produced as a result of colour radiation from

the quarks or from higher-ordered $t\bar{t}$ production diagrams. It should be emphasized however that a non-matched jet does not necessarily imply the presence of a true gluon, nor will the presence of a true soft gluon necessarily lead to the reconstruction of a unique jet.

4.4.2 b-Tagging Efficiencies and Rejection Rates

The ability to identify or **tag** a jet initiated by a bottom-type quark is of prime importance in $t\bar{t}$ analyses which have a pronounced fraction of jets initiated by bottom-type quarks [60]. This identification proves a particularly useful tool in the all-hadronic topology where tagging helps to characterize the event. A failure to employ any such tagging techniques in this analysis would result in an overall signal fraction so low that a signal peak would be scarcely discernible, if at all, over the immense QCD multi-jet background.

The lifetimes of hadrons containing a bottom-type quark are generally much longer than those of other hadrons; since bottom hadrons are produced from the hadronization of a bottom-type quark, this gives rise to a number of distinguishing properties exhibited by b-quark initiated jets, such as the presence of secondary vertices displaced with respect to the primary vertex. A multivariate technique can exploit these properties and discriminate between those jets initiated by bottom- *vs.* lighter-flavoured quarks. The use of such a discrimination process, commonly referred to as **b-tagging**, is a common tool used in flavour physics analyses and for searching for signal events with high bottom-flavoured jet multiplicities such as top quark events.

The **b-tagging efficiency** for a particular quark flavour provides a measure of the performance of a b-tagging algorithm. It is defined *via* the following expression:

$$\textbf{b-Tagging Efficiency:} \quad \varepsilon_{b-tag} = \frac{\text{\# of jets of a given flavour tagged as b-jets}}{\text{\# of all same-flavoured jets}} \tag{4.5}$$

A related quantity is the **rejection rate** R_{b-tag}, given by:

$$\textbf{b-Tagging Rejection Rate:} \quad R_{b-tag} = \frac{\text{\# of all jets of a given flavour}}{\text{\# of same-flavoured jets mistagged as a b-jet}} \tag{4.6}$$

One can recognize that $R_{b-tag} = 1/\varepsilon_{b-tag}$. The rejection rate, like the b-tagging efficiency and jet-quark matching efficiency, is a flavour-specific quantity, defined for each quark flavour[13]. It is primarily, however, to be used in the context of the lighter quark flavours only – a measure of the rate at which light-flavoured jets are incorrectly tagged as having originated from the

[13]It should be noted that despite the 'b' in the subscript for R_{b-tag} and ε_{b-tag}, these quantities do not involve any bottom-type quarks or jets in the case that they are being evaluated for other flavours – in such cases no bottom-type quarks or jets appear in either the numerator or denominator. The 'b' is present simply in light of the fact that the tagging is of primary use to identify bottom-flavoured jets.

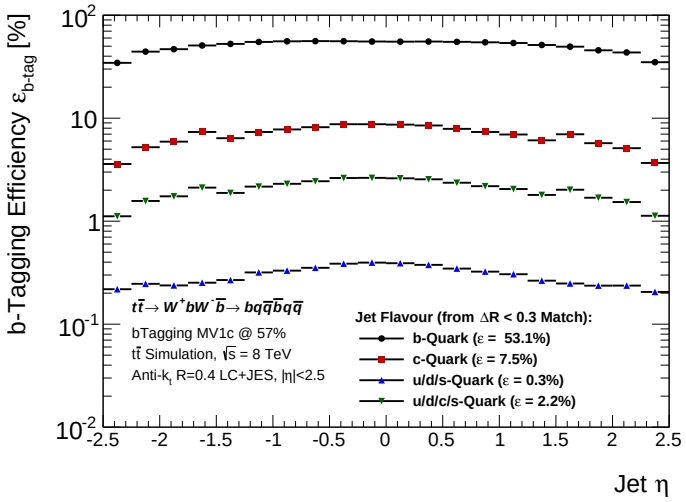

Figure 4.5: The b-tagging efficiencies for the MV1c b-tagging variable at the selected 57% efficiency working point. The values were evaluated from simulated all-hadronic $t\bar{t}$ events. The various marker shapes and colours represent the different quark flavours or the jets associated to these quarks: b-type quarks (**black**), c-type quarks (**red**), and other lighter-type (u/d/s) quarks (**blue**), with inclusive values for the overall efficiencies shown in brackets. The b-tagging efficiencies were evaluated prior to the application of event selection cuts aside from the selection requirements on the reconstructed jets.

hadronization of a bottom-type quark. Recognizably the same fiducial region of $|\eta| < 2.5$ applies to the quarks in the context of this definition; this is clear from the fact that only matched jet-quark pairs are included in the evaluations of both ε_{b-tag} and R_{b-tag}.

The b-tagging tool employed in this analysis is named **MV1c**, and is based on a multivariate approach referred to as a neural net. This approach makes use of a number of input observables with a strong sensitivity to identify bottom-quark-initiated jets, such as those depicted in Figure 4.2, ultimately returning a single output value which can be translated to a probability of a positive match. The neural net is trained on simulated samples of events containing a mix of jets truly initiated by bottom-type quarks, and those initiated either by gluons or other-flavoured quarks. A similar such tool simply referred to as **MV1** is also available and is widely used in ATLAS analyses – the difference being that the inclusion of the c in the name indicates that the samples used for the neural net training include a higher fraction of jets initiated by charm-type quarks. Since the lifetimes of hadrons containing charm-type quarks can also be long, even if not as long as the bottom-type quarks, jets initiated by charm-type quarks are far more likely to be mistagged as a b-jet compared with jets of other flavours; it is for this reason that the rejection rates for c-quark-initiated jets are evaluated separately.

The ideal b-tagging algorithm will have both a high b-tagging efficiency for true b-quark-initiated jets and a high light-flavour rejection rate. Striking the optimal balance between the two is challenging and is often analysis-dependent, based on the types of background processes. The production of W and Z bosons in association with jets can often give rise to the presence of charm-quark initiated jets in the final state; to suppress the potential contribution from this background, the MV1c algorithm was selected for the analysis.

A number of **working points** are available for flavour-tagging tools such as MV1c, where the working point refers to a reference b-tagging efficiency value as evaluated on a sample of

Table 4.1: Summary of the overall jet-quark matching efficiencies and b-tagging efficiencies for various quark flavours in simulated all-hadronic $t\bar{t}$ signal events. The numbers were derived using reconstructed jets and truth-record quarks from the simulated Monte Carlo sample. Also shown is the b-tagging rejection rate R_{b-tag} as defined in the text. For the b-tagging related quantities, the c-type quarks are listed both as combined with the u/d/s-type and alone as they lead to the largest number of jets mistagged as b-jets.

Quark Flavour	ε_{match} [%]	ε_{b-tag} [%]	R_{b-tag}
b-type	75.0	53.1	1.89
c-type	67.8	7.5	13.3
u/d/s-type	63.4	0.3	333.3
u/d/c/s-type	/	2.2	45.5

simulated ℓ+jets $t\bar{t}$ events. The working point for the present analysis is at the 57% efficiency point[14]. The b-tagging efficiencies can be validated by the identification of dileptonic $t\bar{t}$ events in both data and simulation, where the backgrounds are low and the jet flavour decomposition is well known [60, 61]. Differences between data and simulation are resolved by means of so-called **b-tagging scale factors** which are applied on an event-by-event basis[15]. The b-tagging efficiency as a function of reconstructed jet η is shown in Figure 4.5. The plot was produced using the same signal events as those in Figure 4.3.

Table 4.1 summarizes the inclusive values of ε_{match}, ε_{b-tag}, and R_{b-tag} for each jet flavour, evaluated using the same simulated all-hadronic $t\bar{t}$ signal events.

4.5 Jet Energy Response and Resolution

The **response** of a quark- or gluon-initiated jet is meant as a measure of how closely on average the energy or p_{T} of a reconstructed jet matches that of some reference object. The reference object conventially corresponds to the truth-level jet associated[16] with the reco-level jet. This is predominantly of interest in the context of calorimeter performance. In this case however it is also illustrative to measure the response relative to the associated quark having initiated the jet (in the case of jets initiated by the hard-scatter quarks in simulated $t\bar{t}$ events.).

[14] In Appendix C.7 a comparison in performance is provided between this and alternate choices for the b-tagging variable and efficiency working point.

[15] Refer to Appendix B.2 for information on how these scale factors are applied. Uncertainties in the b-tagging scale factors are taken into account and are propagated to the final uncertainties on the measured value of m_{top}. This will be discussed in Chapter 11.7.6.

[16] Here associated is taken to mean matched in ΔR in the same way that the jet flavour is determined.

4.5.1 Jet Energy Response Relative to Quarks

Though there is no way of knowing the true energy of a quark or gluon, nor is it possible to distinguish with certainty between a light-quark-initiated jet from a gluon-initiated jet, samples of simulated $t\bar{t}$ events can nevertheless be used to estimate the expected responses for various parton types as a benchmark for performance for various jet calibration schemes.

Distributions of the quantity E^{reco}/E^{quark} can be produced from Monte Carlo events, where E^{reco} refers to the energy of the reco-level jet, and E^{quark} to that of its associated quark based on the jet flavour assignment. As such, only matched jet-quark pairs are used in filling these distributions. Ideally this ratio has a value of unity, though due to a number of physics- and detector-related effects, the distributions can be expected to have some natural width. A variety of additional mechanisms give rise to a low-response tail. A double Gaussian parameterization provides a reasonable description of the shape of these distributions. The term **jet energy response**[17] here is defined as the fit parameter for the first Gaussian mean[18] returned by means of a least-squares fit.

$$\mathcal{R} = \left\langle \frac{E^{reco}}{E^{quark}} \right\rangle \tag{4.7}$$

The fractional **jet energy resolution** $\sigma(E)/E$ is defined as the width parameter corresponding to the same Gaussian. It is often plotted as a function of the true energy and conventionally a fit is then performed based on a standard parameterization which typically describes this shape, though no such fit is used in this analysis.

While the jet energy response relative to quarks allows for the development of intuition with regards to the mapping between quark- and reco-level jets, the response itself is not strictly employed in the present analysis and is shown solely for illustrative purposes[19].

4.5.2 Jet Energy Response Relative to Truth Jets

The jet energy response and fractional resolution relative to a truth-level jet is defined and calculated analogously, with the replacement of $E^{quark} \to E^{truth}$. In this case the denominator corresponds to the energy of the truth-level jet matched to the reco-level jet, though the jet

[17] In this case one may speak of the p_{T} or the energy response; here the latter is implied by default.

[18] The first mean corresponds to the narrower Gaussian at a higher value of E^{reco}/E^{quark}.

[19] In some $t\bar{t}$ analyses, however, such responses are used by means of so-called **transfer functions** which map reconstructed four-vector quantities to parton-level ones. This can be useful in kinematic likelihood fits for the event reconstruction, to be discussed in Chapter 6, and particularly in cases where there is a high probability of correct jet-quark assignments in the reconstruction of the $t\bar{t}$ system. Such an approach suffers consequently from some uncertainties due to the fact that this relies and is based on simulation alone. An iterative parton-level correction was investigated for this analysis but was not ultimately used to correct the energy of the jets. This method, though not adopted for the final analysis, is detailed Appendix E.

flavour is still taken from the matched parton. Though the low-response tail is not as pronounced as in the case of the response relative to quark energies, it is still appropriate to use a double-Gaussian parameterization to describe the resulting distribution (E^{reco}/E^{truth}), and the jet energy response in this case is again defined to be the mean parameter for the narrower, higher-response Gaussian from the resulting fit.

Since non- or minimally interacting particles such as neutrinos and muons are not taken into account in the term in the denominator, the energy response relative to truth-level jets is a quantity more often of interest in the context of jet reconstruction since it represents the upper limit in performance, attainable only for the case of an optimally calibrated calorimeter system.

Shown in Figure 4.6 is a selection of representative plots from simulated all-hadronic $t\bar{t}$ events. They corresponding to bottom-flavoured jets based on ΔR matches to truth-record bottom quarks. The energies of the reconstructed jets are compared to those of their associated quarks in Figures 4.6(a) and 4.6(c); in Figures 4.6(b) and 4.6(d) they are compared to their associated truth-level jet energies[20].

The resulting responses and fractional resolutions from the fits shown, as well as those for other flavours of jets, are summarized in the plots in Figure 4.7, which are shown as a function of energy. Note that the points corresponding to the jet energy response and fractional resolution relative to partons in the case of gluon-flavoured jets are not shown owing to the fact that the truth-record information for the gluons was not stored; they were identified as gluon-flavoured jets by default in the case of no match to a truth-record quark from the top quark decays.

[20]One can note, particularly in Figure 4.6(b), that the fitting range does not cover the full range of the distribution. The reason is due to limited statistics in the lower-reponse tail of the distribution which leads to an artificially diminished number of entries in that region. Even in the case that the calorimetric response were truly Gaussian, the fact that there is a sharp minimum threshold in the energy of truth-level (and reconstruction-level) jets in the numerator without a corresponding threshold for the quark energy in the denominator would lead to an asymmetric distribution. This arises only in the lower-energy bins. It is again highlighted that these fits have no bearing on the analysis and are illustrative only.

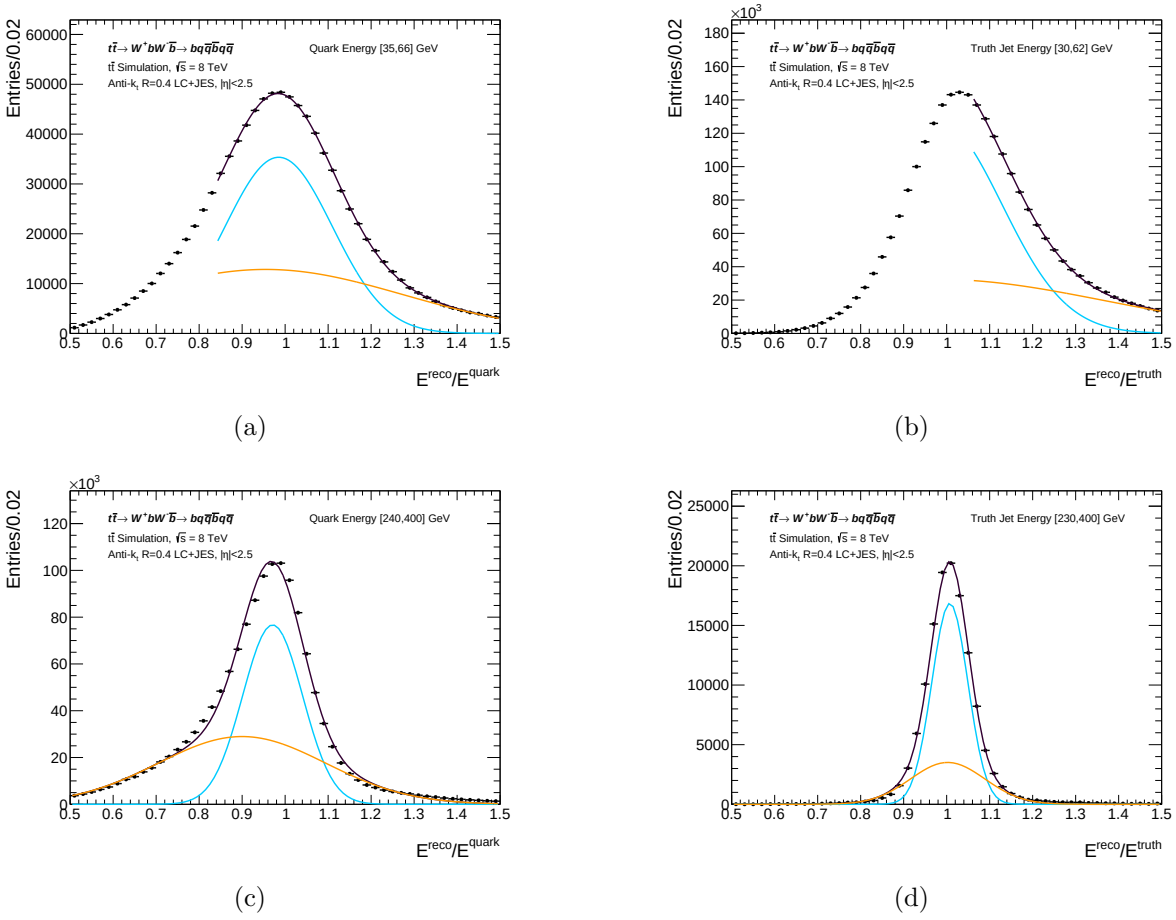

Figure 4.6: Representative plots produced in order to evaluate the jet energy response and fractional jet energy resolution, shown here for bottom-flavoured jets in simulated signal samples. The flavour of the jets was identified from ΔR matches to truth-record quarks from the initial hard-scatter process with only minimal selection cuts applied. The plots in (a) and (b) show the energy response relative to the matched quark energy and truth jet energy respectively, and correspond to low-energy jets in the ranges indicated. Plots (c) and (d) are analogous plots for high-energy jets. The solid lines correspond to the fitted shapes: the higher- (blue) and lower-response (orange) Gaussians, and the sum of the two (magenta).

A more complete set of distributions similar to those in Figure 4.6, but for different parton flavours, can be seen in Appendix D. The extracted parameters from the fits in these additional plots are used to set the values of the points in the plots shown in Figure 4.7.

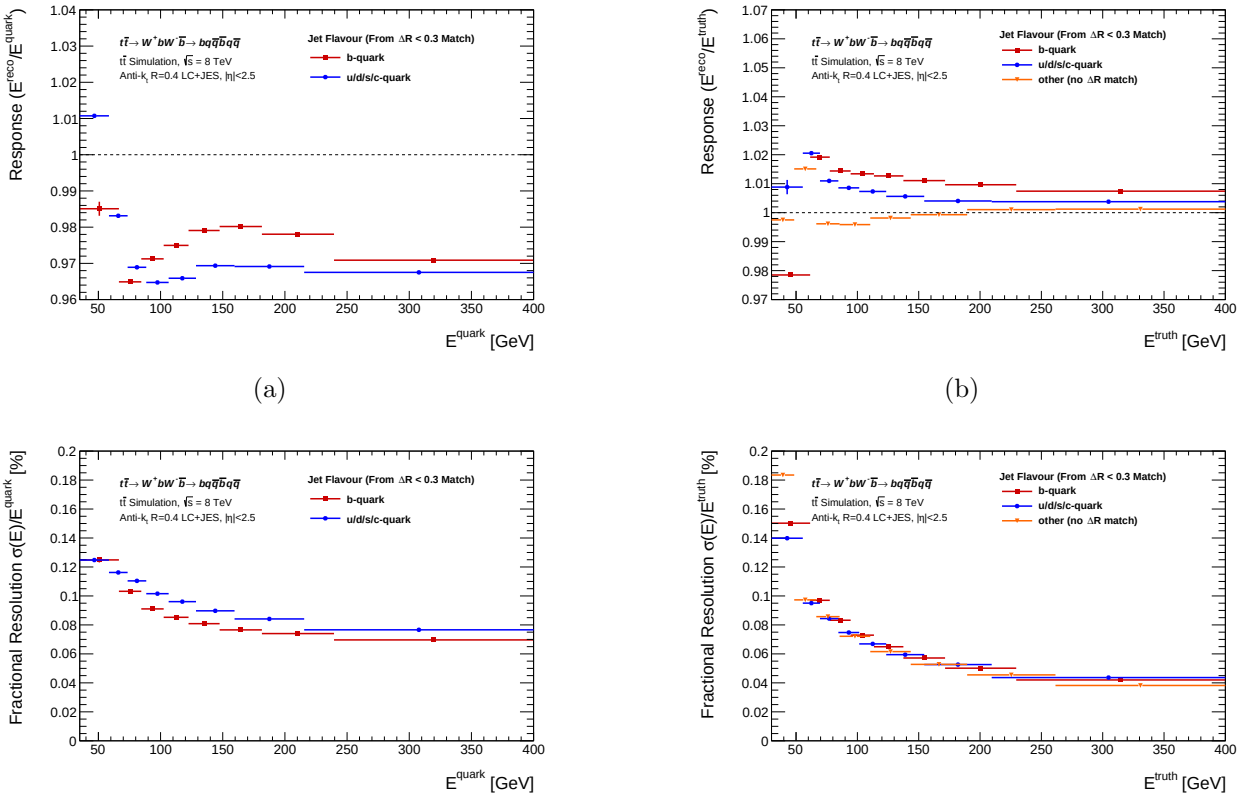

(a) (b)

(c) (d)

Figure 4.7: The jet energy response (a) relative to quarks $\langle E^{reco}/E^{quark} \rangle$ and (b) relative to truth-level jets $\langle E^{reco}/E^{truth} \rangle$ for reconstructed jets in simulated signal samples. Also shown is the fractional energy resolution for both cases in (c) and (d), respectively. The flavour of the jets was identified from ΔR matches to truth-record quarks from the initial hard-scatter process.

4.5.3 Semileptonic Quark Decays and Matched Muons

It is illustrative to decompose the distributions such as those shown in Figure 4.6 into three cases, depending on the presence or non-presence of matched reconstructed muons to the jets[21]:

1. Jets with no matched reconstructed muon present
2. Jets with a matched reconstructed muon present
3. Jets with a matched reconstructed muon present and added back to the jet four-vector

The resulting normalized distributions for these three cases, for quarks in a single but representative energy range, are shown in Figure 4.8(c). The distributions are filled solely for bottom-flavoured jet-quark pairs, since the energy loss due to semileptonic quark decays is most prominent for this flavour. Such normalized distributions highlight the fact that the presence of matched muons is indicative that a semileptonic decay of one of the bottom-flavoured hadrons has occurred – in addition to the minimally interacting muon, at least one (non-interacting) neutrino should also have been present, which will typically carry away a significant fraction of the energy that would otherwise be attributed to the jet. The addition of the reconstructed muon four-vector to that of the jet can be observed to qualitatively improve the overall energy response and resolution of such jets.

This qualitative result is confirmed quantitatively in the plots shown in Figure 4.8(a) and 4.8(b). It can be seen that the addition of reconstructed muons to the jets improves both the energy response and fractional energy resolution for those jets over the full range of energies considered. A similar but less pronounced improvement was observed for lighter-flavoured jets, where the dominant contribution would be expected to be from charm-flavoured jets.

Based on the results of this study, it was decided to adopt the prescription of adding the highest-energy matched muon to the reconstructed jets in the analysis. The plots in Figure 4.8 were produced using only bottom-flavoured jets, but the addition of muon four-vectors to jets was used for all reconstructed jets independently of their flavour[22]. The effect on other-flavoured jets is less significant, particularly since the fraction of jets with a candidate muon match for non-bottom-flavoured jets is significantly lower, as can be seen in Table 4.2.

[21] An angular separation $\Delta R(\mu,\text{jet}) < 0.3$ is required to define a positive match.

[22] The flavour information for reconstructed jets in data is not known. In addition it was found that it was best to avoid introducing correlations from b-tagging by applying this procedure only for the case of b-tagged jets since this could adversely affect the background estimation technique, which will be introduced in Chapter 9.

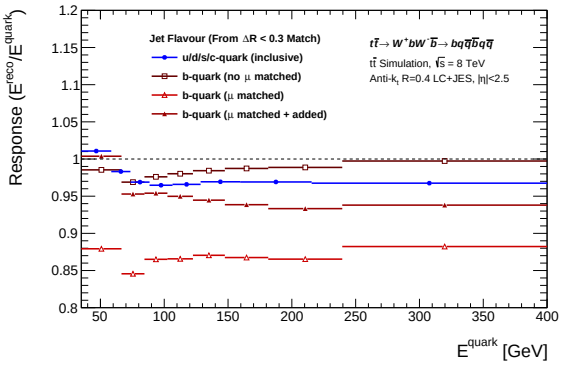

(a) Energy response

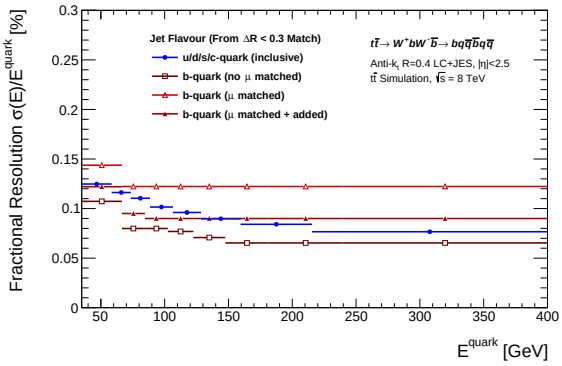

(b) Fractional energy resolution

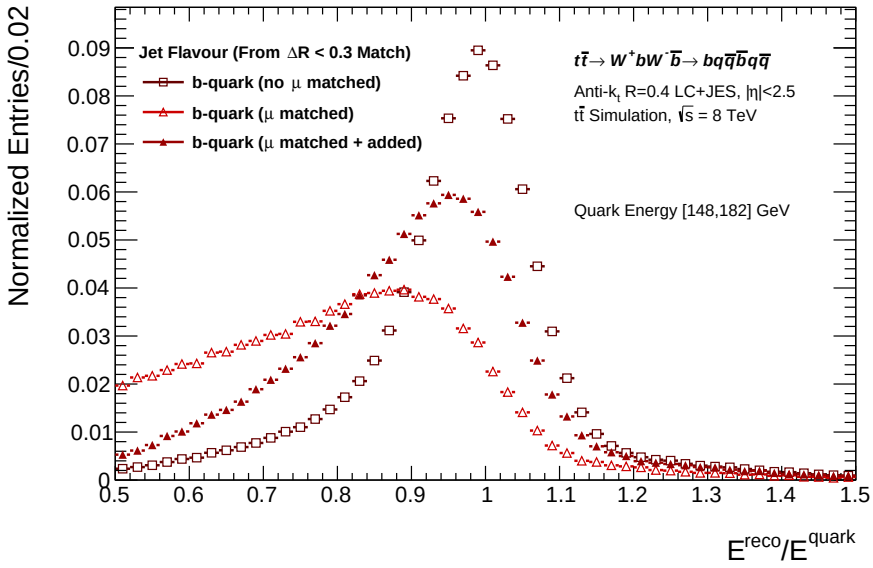

(c) Normalized shapes of the E^{reco}/E^{quark} distributions

Figure 4.8: Distributions showing the effect of semileptonic decays on the energy response and fractional resolution of bottom-flavoured jets relative to the quark energies. The semileptonic decay is inferred by the presence of a reconstructed muon ΔR-matched to a reconstructed jet as described in the text. The lower figure (c) shows normalized distributions of the quantity E^{reco}/E^{quark} for a representative range of bottom-flavoured quark energies. The values for the plots in (a) and (b) are based on the fits to distributions similar to that shown in (c). These base distributions and fits can be seen in Appendix D.2.

The improvement in the jet energy resolution was shown to lead to a slightly reduced overall statistical uncertainty on the final measurement, since it leads to an improvement in resolution

Table 4.2: The fraction of reconstructed jets with a matched reconstructed muon within $\Delta R < 0.3$. Numbers are quoted separately for jets of different flavours based on ΔR matches to truth-record quarks. The numbers were evaluated using simulated all-hadronic $t\bar{t}$ events with only minimal event selection applied.

Jet Flavour (from $\Delta R < 0.3$ Match)	Fraction of Jets with Matched Muon [%]
b-Quark	16.1
u/d/s/c-Quark	4.2
Gluon (No Matched Quark)	4.3
Inclusive	7.5

for the observable sensitive to the top quark mass which will be used in the final measurement; this should become more clear in the following chapters[23].

4.6 Standard Corrections to Reconstructed Jets

A series of corrections are applied to jet four-vector objects prior to their being used in the analysis. These corrections are standardized for all ATLAS top quark analyses employing events from the 2012 $\sqrt{s} = 8$ TeV dataset. A more detailed description of these corrections and the way in which they are derived from and applied to jets in both $\sqrt{s} = 7$ and 8 TeV analyses can be found here [62, 63].

4.6.1 Area and Offset Corrections Due to Pile-Up Activity

The unwanted contributions from pile-up activity in the calorimeter can greatly impact the p_{T} response and resolution of reconstructed jets. It was found that the **effective area of a jet** (A), together with a measure of the median p_{T} density (ρ) in an event allow for an effective means to suppress the contributions from pile-up. Due to the anti-k_T jet reconstruction algorithm being a sequential clustering-type algorithm rather than an algorithm involving fixed cone-shaped jet boundaries, the area encompased by a jet is not well defined. The effective jet area must therefore be estimated by means of adding so-called 'ghost' clusters with negligible but non-zero energy prior to the anti-k_T clustering step; these ghost clusters are then added to a jet in order to estimate the area of the jet [64].

[23] At the time of writing, studies are planned to investigate and further validate this procedure by investigating any potential systematic shift associated with uncertainties in the b-quark fragmentation which could lead to a countervailing effect and offset any gains in precision. For the present time however, the muons are added to the jets as it leads to an improvement in precision of the overall result.

In addition, a flat offset correction is subtracted from the p_{T} of the jet based on the **Number of Primary Vertices** (N_{PV}) in the event and the **Average Number of Interactions per Bunch Crossing** $\langle\mu\rangle$. The corrected p_{T} of the jet is translated *via* $p_{\mathrm{T}} \to p_{\mathrm{T}}^{corr}$ where:

$$p_{\mathrm{T}}^{corr} = p_{\mathrm{T}} - \rho A - \alpha(N_{PV} - 1) - \beta\langle\mu\rangle \tag{4.8}$$

The values of α and β are derived separately for jets constructed with LCW- and EM-calibrated clusters. Their values are validated from data using di-jet events in which the p_{T} of the jets are known within some uncertainty.

4.6.2 Origin Correction

A jet origin correction is employed in order to adjust the jet axis such that it points to the primary vertex in an event as opposed to the centre of the ATLAS coordinate system (0,0,0). This is performed by redefining the position of each of the constituent energy clusters to point to the primary vertex and subsequently repeating the anti-k_T jet reconstruction. This adjustment changes the angular position of the jet and thus improves the jet angular resolution, but has a negligible effect on the jet energy or transverse momentum.

4.6.3 Absolute Jet Energy Scale (JES) Correction

The **Jet Energy Scale** (JES) corrections used by ATLAS are calibrations applied to jet four-vectors which are derived and validated from measurements of the p_{T} response of jets relative to truth-level jets from both simulation and *in situ* techniques[24]. In the evaluation of the JES correction using simulated events, jets are required to be matched to truth-level jets. Based on large samples of such isolated, truth-matched jets, a series of energy- or p_{T}-dependent and η-dependent correction factors (c) can be derived from simulation and validated with data *via*:

$$c = \mathcal{R}^{-1} = \left\langle \frac{E^{reco}}{E^{truth}} \right\rangle^{-1} \tag{4.9}$$

As these correction factors were derived using di-jet samples, which have higher fraction of gluon-initiated jets, and since the responses of the various flavours of jets have been shown to differ in Figure 4.7(b), the final energy response is not expected to be unity for $t\bar{t}$ events even after such corrections have been applied to the jet four-vectors. It nevertheless brings the energy and p_{T} response of the reconstructed jets far closer to unity by correcting for out-of-cluster and dead material contributions, as well as the energy contributions invisible to the calorimeters.

[24]The derivation and application of an alternative, analysis-specific correction to the jet p_{T} was also pursued, but was not adopted for the final analysis. Additional information is provided in Appendix E.

It should be noted that different JES corrections are available for both LCW and EM calibrated jets. These correction factors are smaller in the case of the former where the hadronic weights applied to clusters already brings the energy response of the jets closer to unity.

4.6.4 Global Sequential Calibration

The **Global Sequential Calibration** (GSC) of jets is a residual correction designed to improve the overall p_{T} resolution and reduce the uncertainty in the response of the jets due to the jet flavour. The calibration applies a correction to jets as a function of E, p_{T}, η and an additional jet property such as the overall angular spread of the tracks associated to a particular jet. These corrections are then derived and applied sequentially for each such property of the jets [65].

4.6.5 Residual In-Situ Correction

Finally, a residual *in situ* correction can be applied to jets based on studies of the jet response in events exploiting a good p_{T} balance between a jet and some recoiling reference object such a photon or Z boson. Different types of such p_{T}-balance events are sensitive to different jet p_{T} regimes; such residual corrections can therefore be derived to be able to cover large regions of kinematic phase space.

4.6.6 Summary of Jet Corrections

The goal of all the corrections described above is to have calibrated jet four-vectors with a response as close as possible to unity relative to truth-level jets. Uncertainties in this response are largest at higher pseudorapidity and lower transverse momentum. As the four-vector energy, transverse momentum and mass are used to build variables which probe the kinematic quantities of the original quarks of interest, uncertainties in the JES tend to dominate the systematic uncertainties in precision mass measurements such as the present top quark mass measurement.

Chapter 5

All-Hadronic $t\bar{t}$ Signal and Associated Background Processes

5.1 All-Hadronic $t\bar{t}$ Signal Processes

In all-hadronic $t\bar{t}$ events a top-antitop quark pair is produced in the inelastic scattering of two partons at the centre of the ATLAS detector, and each of the top quarks subsequently decays to a three-quark final state. The full production and decay for such a process is therefore of the form[1]:

$$pp \to t\bar{t} \to W^+bW^-\bar{b} \to q\bar{q}bq\bar{q}\bar{b}$$

A leading-order Feynman diagram for the all-hadronic signal process is displayed in Figure 5.1. In this figure, the six-quark final state is emphasized, and particularly the fact that two of these quarks are expected to be bottom-type quarks. As detailed in Chapter 4, the six quarks themselves will lead to the production of charged tracks and of energy deposits in the calorimeter system; in an ideal case these processes will result in a unique jet being reconstructed for and associated to each quark. As is clear from the diagram shown, the $t\bar{t}$ pairs are produced *via* a strong-interaction coupling.

5.1.1 Simulated Monte Carlo Datasets

There are four primary steps leading to the production of simulated datasets which can be compared to the measured data from the detector and which are then made available to the

[1]Note that with the labelling shown it is not important to make explicit the flavour of the four quarks resulting from the decays of the two hadronically decaying W bosons. It is implied that the $q\bar{q}$ flavours will be of the correct type so as to preserve charge in the $W^+ \to q\bar{q}$ or $W^- \to q\bar{q}$ decays. Two flavour-explicit examples of all-hadronic decays are $t\bar{t} \to W^+bW^-\bar{b} \to c\bar{s}bd\bar{u}\bar{b}$ and $t\bar{t} \to W^+bW^-\bar{b} \to u\bar{d}bs\bar{u}\bar{b}$.

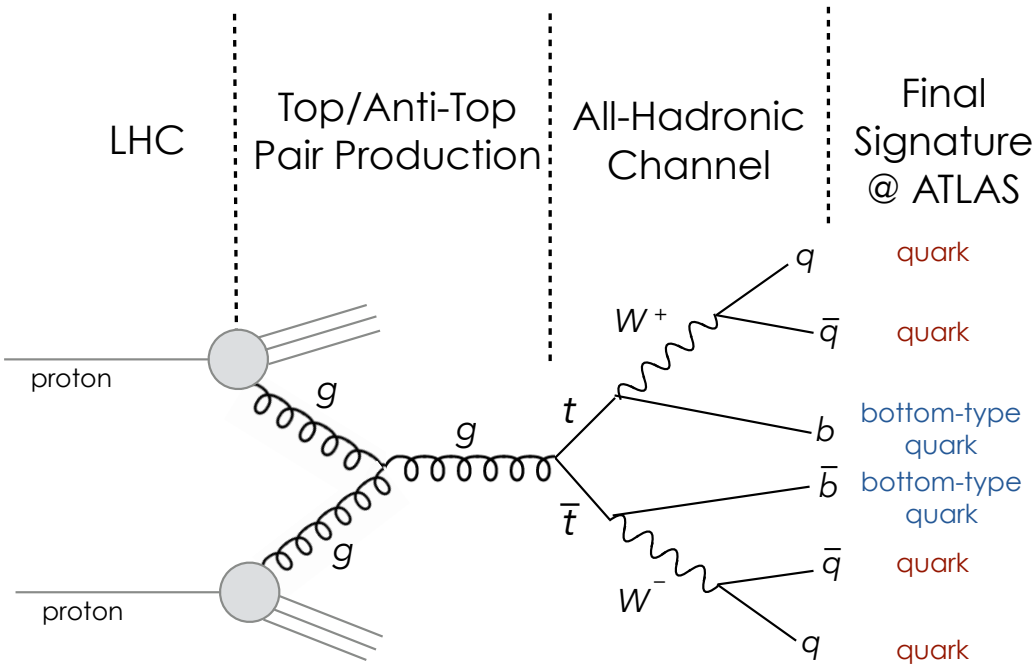

Figure 5.1: A leading-order diagram for the production and all-hadronic decay of a $t\bar{t}$ pair *via* quark-antiquark annihilation. Shown are the two initial protons involved in the hard-scatter interaction, the fusion of a pair of gluons to produce a $t\bar{t}$ pair *via* an s-channel interaction also mediated by a gluon, the all-hadronic decay characterized by the $W \to q\bar{q}$ decay of both W bosons, and ultimately the final six-quark signature of signal events [17].

ATLAS collaboration: **generation**, **simulation**, **digitization** and **reconstruction**. Monte Carlo datasets will often be referred to simply as simulated, but with all steps implied.

For the majority of the plots to be shown in this thesis, the simulated all-hadronic $t\bar{t}$ dataset used corresponds to 60M events generated using Powheg interfaced with Pythia 6.4 in order to model the parton showering and the hadronization [66–68], as well as the modelling of the **underlying event** – the activity, predominantly in the far-forward (high $\pm z$) regions of the detector, resulting from partonic remnants of the interacting protons aside from those involved in the hard-scattering interaction. The Perugia P2012 tune sets the values of the tunable Pythia parameters [69]. The central set of CT10 proton parton density functions are used for the generation of the events[2], with an input generator-level top quark mass of 172.5 GeV.

The simulation step is performed by means of a so-called **fast-simulation**, which is abbre-

[2]Refer to Section 2.2.3.

viated as AFII and is based on a parameterized description of the ATLAS detector[3] [72].

Hits in the various components of the detector, based on the simulation step, are subsequently digitized, and as a final step the reconstruction is performed identically to that used for data events by running through the full reconstruction, ultimlately yielding a number of reconstructed tracks and calorimeter energy deposits for each event.

Truth-record information such as the flavour, Monte Carlo particle ID number, and four-vector quantities are available for the top and bottom quarks, as well as the W bosons and their decay products. In some cases, additional particles along the decay chain are made available which can provide insight to motivate the choices made in the analysis from truth-level studies based on simulation.

A detailed summary of all simulated datasets used in the analysis, including additional signal and background datasets used to evaluate a number of systematic uncertainties, is provided in Appendix B.1.

5.1.2 Kinematics of All-Hadronic $t\bar{t}$ Events

A number of kinematic plots for different key variables can be produced for simulated signal events which allow for the development of a familiarity with the topology of all-hadronic $t\bar{t}$ events. When contrasted with normalized shapes of the relevant background events, these kinematic plots assist in the identification of those variables providing the highest level of signal-to-background discrimination which can be employed in event selection cuts. The event selection for this analysis is presented in detail in Chapter 7. In this section the focus is to be placed on distributions of signal events only.

Depedendence of Event Kinematics on Centre-of-Mass Energy

As highlighted in Section 2.2.2, the production threshold of a $t\bar{t}$ pair is twice the mass of the top quark, roughly$\sqrt{\hat{s}} \approx 350$ GeV. Due to the composite nature of the interacting protons, although the value of $\sqrt{s}$ of the p-p interaction is fixed at 8 TeV, it is the actual momentum fractions carried by each of the respective partons involved in the hard-scatter process, and not the momentum of the composite protons themselves, for which this threshold is relevant. In the case that $\sqrt{\hat{s}} = \sqrt{x_1 x_2}\sqrt{s} \gg 350$ GeV, the residual energy beyond that required for the production manifests itself in the boost of the top and anti-top quarks.

[3]The name fast simulation is due to the fact that the simulation of the interactions of generated particles in the various components of the detector is performed by means of a parameterized ATLAS detector response as opposed to using the full GEANT4 simulation [70,71]. These approximations greatly reduce the computing time required for the simulation; this reduction comes, however, with a moderate level of degradation of or greater uncertainty in performance.

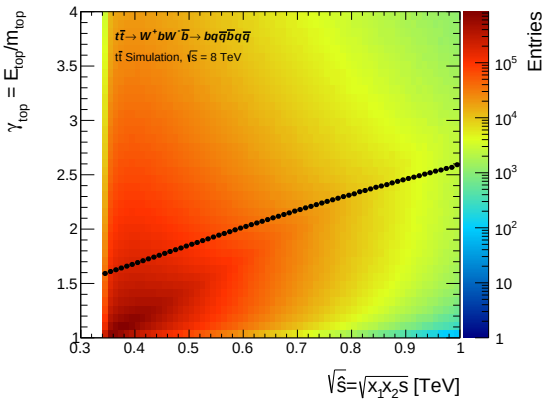

(a) Dependence of the top quark boost γ_{top} on the centre-of-mass energy of the partonic interaction $\sqrt{\hat{s}}$

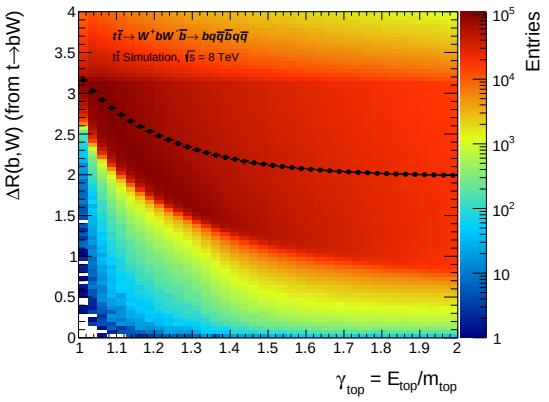

(b) Angular ΔR separation between W-b quark pairs from the (anti-)top quark decays

Figure 5.2: Two-dimensional histograms showing sensitivities of truth-record quantities to the energy involved in the parton-parton scattering process. The average values for each of the bins along the x-axis are denoted by the black markers. Corresponding RMS values are included as error bars on these points but are negligible. The $t\bar{t}$ production threshold is visible in the cutoff at approximately $\sqrt{\hat{s}} = 350$ GeV in the distribution in (a).

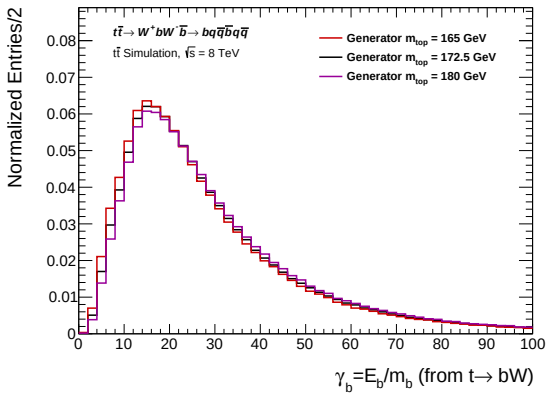

(a) Boost of bottom-type quarks originating from the decay of a top quark from the truth record.

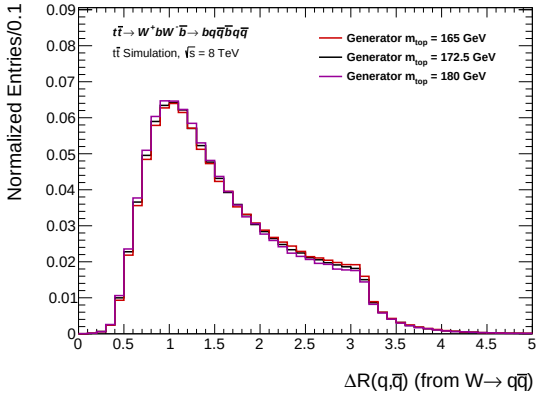

(b) The angular separation ΔR between the $q\bar{q}$ pair produced as a result of the hadronic W boson decay.

Figure 5.3: Normalized distributions of (a) the boost of the bottom-type quarks and (b) the dimensionless angular separation ΔR between $q\bar{q}$ pairs, both shown for three different values of the input generator m_{top} in simulated $t\bar{t}$ events from 8 TeV p-p collisions.

This trend is demonstrated clearly in the plot in Figure 5.2(a) which shows, for simulated all-hadronic $t\bar{t}$ signal events, the top quark boost ($\gamma = E/m$) as a function of the centre-of-mass energy of the parton-parton interaction ($\sqrt{\hat{s}}$). The values of the momentum fractions carried by the two partons of interest, x_1 and x_2, are available from the truth record of the simulated samples. The distributions were filled twice per event – once for each top- and anti-top quark. One can note a roughly linear trend: the larger the energy available in the collision, the higher the boost of the top quarks.

These higher boosts in turn produce higher boosts for the top quark decay products – the hadronically decaying W bosons and the bottom-type quarks – resulting in reduced angular separations between these particles in the laboratory frame. This is demonstrated in the similar plot of Figure 5.2(b) showing the ΔR separation between each W-b pair as a function of the parent top quark boost. In such cases the W bosons and associated bottom-flavoured quarks are identified *via* the truth record from the simulated dataset, though one should expect a similar effect in reconstructed quantities assuming the association between truth-record and reconstructed object could be made correctly.

Dependence of Event Kinematics on the Top Quark Mass

The value of m_{top} itself can lead to similar effects: the larger the value of the top quark mass, the greater the difference in mass between top quarks and their decay products. A larger value of m_{top} can thus be expected to produce W bosons and bottom-type quarks with higher boosts as they will have higher energies relative to their rest mass.

The relative number of $t\bar{t}$ pairs produced can be expected to decrease for larger values of m_{top}, since a larger value of m_{top} will result in a smaller relative fraction of events with sufficient energy in the partonic interaction to meet the $t\bar{t}$ production threshold. The diminished overall $t\bar{t}$ production rates notwithstanding, the boosts of the W and bottom-type quarks from the top decays then act as probes to the true value of m_{top}. Indeed, it is through m_{top} dependences such as this that a series of m_{top}-dependent template distributions can be built in order to infer the true top quark mass from data, as will be described in Chapter 8.

In addition to the nominal 60M signal events, a number of simulated datasets consisting of all-hadronic $t\bar{t}$ events were produced for a number of discrete values of m_{top} in an effort to gauge this depedendence. A total of seven such simulated datasets were produced with m_{top} values from 165 to 180 GeV, spaced at even 2.5 GeV intervals. In all cases a fast simulation was employed, similarly to the nominal 60M signal dataset. Figure 5.3(a) highlights the dependence of the bottom-quark boost on the value of m_{top} and it can be seen that higher values of m_{top} result in higher values of the boost. Similar plots were produced for the boost of the W bosons and were seen to exhibit the same trend though with a slightly lessened effect since $m_W \gg m_b$.

In a similar way to the effect on the angular separation between the top quark decay products caused by the partonic centre-of-mass energy $\sqrt{\hat{s}}$, it can be seen in Figure 5.3(b) that the angular

separation between the $q\bar{q}$ pairs from the W decay also has an m_{top}-dependence. Due to the sequential clustering nature of the anti-k_T algorithm, this physical effect can have an impact on the jet reconstruction in a given event – the energy deposits from the $q\bar{q}$ pair are closer in ΔR space, and cross-talk can consequently exist between two candidate jets during their reconstruction. The invariant masses of the resulting reconstructed W bosons can therefore be affected by and are sensitive to the top quark mass, though the effect is small.

It should be emphasized that the plots in Figures 5.3(a) and 5.3(b), produced using all-hadronic $t\bar{t}$ signal samples with different m_{top} values, differ from the previous distributions in that they were filled only with events passing a number of pre-selection criteria. These cuts were applied during a slimming process solely as a means to reduce the overall size of the simulated datasets at an intermediate stage when running the analysis framework; further event selection cuts would eventually be applied. The application of these pre-selection cuts were therefore applied solely for a intermediate reduction in the overall file sizes of simulated samples, but their application has consequences on the kinematic distributions. Events used to fill the distributions in Figures 5.3(a) and 5.3(b) were required to have six reconstructed jets in the central (*i.e.* $|\eta| < 2.5$) region[4], which gives rise to the sharp cutoff in Figure 5.3(b) for separations around $\Delta R(q, \bar{q}) \approx 3$, whereas no such dropoff would be expected in the absence of any event selection. The plot nevertheless demonstrates the sensitivity of the kinematic quantity $\Delta R(q, \bar{q})$ to the top quark mass. It is this aspect that is important here rather than the actual values.

Detector Acceptance-Related Effects

As an example to highlight the expected differences between quark-level distributions and reconstruction-level distributions which can exhibit detector-related effects, the plots shown in Figures 5.4(a) and 5.4(b) show two-dimensional distributions in η-ϕ space of bottom-type quarks from the truth record and the reconstructed jets tagged as b-jets, respectively. The value $\eta = 0$ corresponds to the x-y plane, and it can therefore be noted that the bottom-type quarks from (anti-)top quark decays in signal events tend to be reconstructed in the central region of the ATLAS detector. Values of $|\eta| = 2.5$, corresponding to the upper and lower cutoffs of the plot, also mark the extent of the inner detector tracking region. In order to be able to take advantage of the flavour tagging algorithms presented in Chapter 4 by tagging jets initiated by bottom-type quarks, this analysis concerns itself only with those jets within this range.

[4]A description of a good reconstructed jet object will be described in Section 7.2.1.

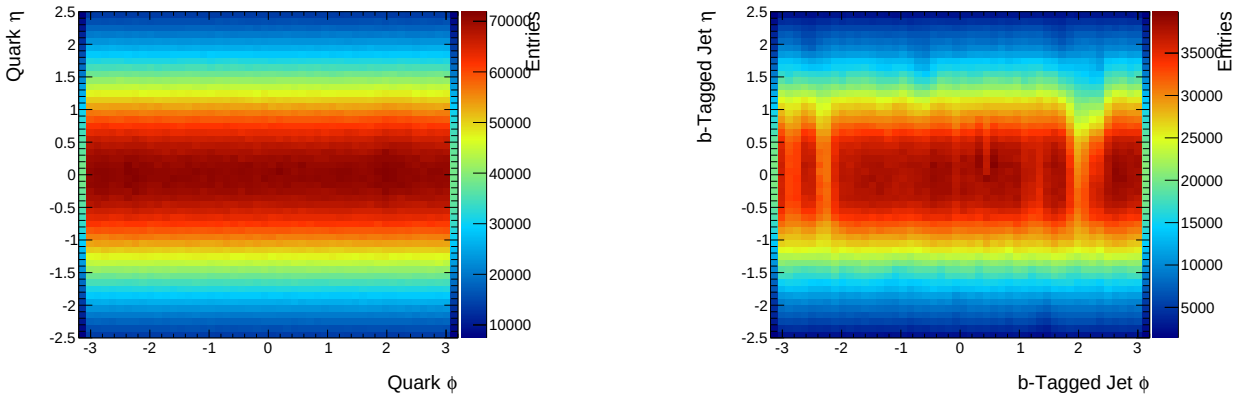

(a) Truth-record bottom-type quarks from the top quark decays of the type $t \to Wb$.

(b) Reconstructed jets b-tagged with the MV1c algorithm at the 57% efficiency working point.

Figure 5.4: Two-dimensional $\eta - \phi$ histograms of (a) bottom-type truth-record quarks and (b) b-tagged jets. The distributions are produced with the baseline all-hadronic $t\bar{t}$ signal sample.

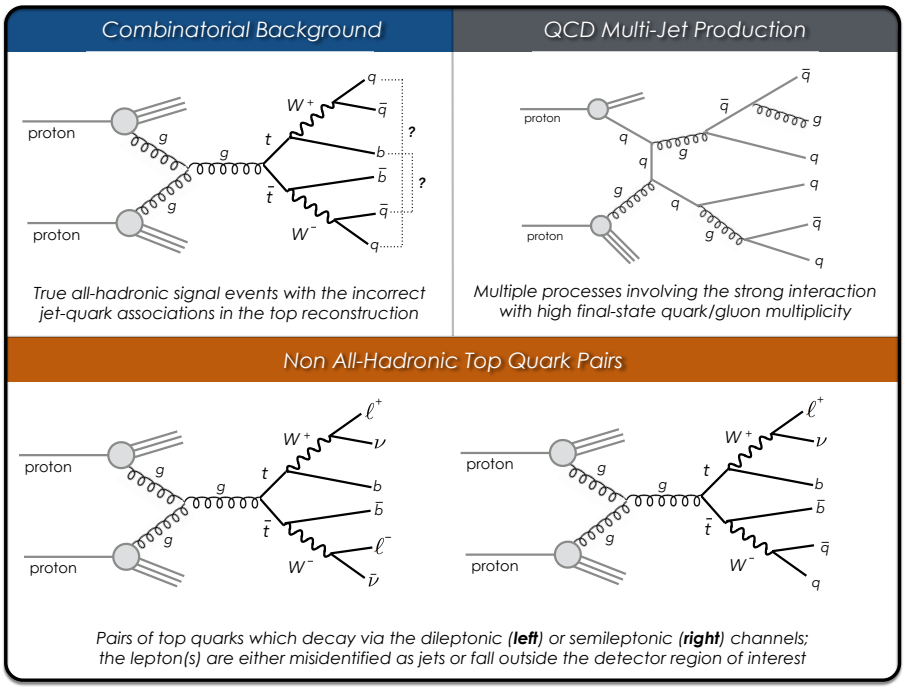

Figure 5.5: Leading-order diagrams for the various backgrounds to the all-hadronic $t\bar{t}$ channel.

The asymmetries exhibited in Figure 5.4(b), in contrast to Figure 5.4(a), reflect a modelling of detector inefficiencies and dead regions during data-taking – to mimic as closely as possible the average conditions present during the collection of the true data in 2012 running conditions[5].

5.2 Background Processes

One advantage of the all-hadronic $t\bar{t}$ channel is the fact that only a small number of relevant background processes exist which can mimic signal events and which must therefore be considered for this analysis. Though the number of relevant backgrounds to consider is small, their scale is such that analyses in the all-hadronic channel have the largest contribution from background processes of any of the $t\bar{t}$ decay channels.

In what follows, the three relevant sources of background to analyses of all-hadronic $t\bar{t}$ decays are described in turn, namely: QCD multi-jet production, non all-hadronic $t\bar{t}$ decays, and the combinatorial background arising from true signal events. Examples of leading order diagrams for each of these processes are presented in Figure 5.5.

5.2.1 QCD Multi-Jet Production

The dominant source of background to the signal process is that of QCD multi-jet production, consisting of a multitude of production modes all characterized by a high jet multiplicity similar to all-hadronic $t\bar{t}$ events.

Though QCD events can be similar to signal events in the number of reconstructed jets, small differences exist in both the kinematics and identified flavour of the jets in the events, as well as differences in the topologies of reconstructed objects. These differences can therefore be exploited through a series of topological cuts in order to preferentially reject QCD events, thereby increasing the relative fraction of signal $t\bar{t}$ events in data. Due to the enormous QCD multi-jet production cross-section and the strong cuts that will be employed, only a minute fraction of simulated QCD background events pass the stringent event selection. The measurement of the top quark mass presented in this thesis relies on the bin contents of one-dimensional histograms, as will be described in subsequent chapters. The contributions from simulated QCD multi-jet events in such histograms would then need to be scaled up significantly according to the integrated luminosity of the 2012 dataset prior to being used for the estimation of the background. Scaling the small numbers of entries up by such a large scale would serve to enhance statistical fluctuations. This would greatly limit the sensitivity of a measurement

[5]It should be highlighted that such simulation is performed independently of the present analysis; the plots shown employ a negligible number of upstream selection cuts and thus represent the true kinematic shapes of the simulated data. Similar features were observed in other simulated $\sqrt{s} = 8$ TeV samples including some Higgs $H \to ZZ^* \to \ell\ell\ell\ell$ and SuperSymmetry (SUSY) samples.

performed using data, but which relies on the shapes of these simulated QCD distributions for the background. This limitation motivates the need for a data-driven estimation for both the shape and normalization of the QCD multi-jet background for the final-state observable of interest.

In addition, in order to raise the signal fraction in data to a level sufficiently high that signal peaks can be identified, the overwhelming majority of true signal events in data will have to be rejected, thereby reducing the statistical leverage of the all-hadronic channel compared to other $t\bar{t}$ decay channels.

An example of a typical leading-order Feynman diagram for QCD multi-jet production is shown in the upper-right portion of Figure 5.5. A variety of such multi-jet diagrams are possible – any diagram resulting in a sufficiently high number of gluons or quarks in the final state which can lead to six or more jets being reconstructed. With at least six reconstructed jets and no high-p_{T} isolated leptons, these multi-jet events would contain the basic ingredients required to fake an all-hadronic $t\bar{t}$ signal event.

5.2.2 Non All-Hadronic $t\bar{t}$

An inspection of the values in Table 2.1 which was presented earlier in Chapter 2 and lists the branching ratios of the three $t\bar{t}$ decay channels, reveals that more than half of those Standard Model $t\bar{t}$ pairs produced in ATLAS result in a final state signature in which one or both of the W bosons from the $t \to Wb$ process decays leptonically *via* $W \to \ell\nu_{\ell}$. Such events are referred to as semileptonic and dileptonic $t\bar{t}$ events, respectively, and they are to be referred to collectively here as non all-hadronic $t\bar{t}$ events. Examples of leading-order production diagrams for both the semileptonic and dileptonic $t\bar{t}$ channel can be seen in Figure 2.10 as well as Figure 5.5.

Although the final-state signature of such non all-hadronic $t\bar{t}$ events differs from their all-hadronic counterparts, the leptons can be wrongly reconstructed or misidentified, and the events thus miscategorized as true candidate signal events. This is particularly the case due to the fact that such processes nonetheless exhibit the presence of two jets inititated by bottom-type quarks – a telltale signature of $t\bar{t}$ decays which is more difficult to mimic in the case of other background proceses, notably that of QCD multi-jet production.

5.2.3 Combinatorial Background from Signal Events

A third significant source of background consists of true, hadronically decaying $t\bar{t}$ pairs in which at least one of the top quarks, or its associated W boson, has been reconstructed from the incorrect constituent pieces. As will be presented in the following chapter, the reconstruction of candidate top quarks involves the four-vector addition of jets associated with the final-state quarks from the initial hard-scatter process. Since one has no way of knowing *a priori* which of these jets are to be associated with which candidate top quark, it follows that in a number

of events the wrong constitutent pieces will have been added together to reconstruct the top quarks candidates. Such events cannot therefore be rejected, although the following chapter outlines a algorithm which aims to minimize the number of cases of wrongly reconstructed $t\bar{t}$ pairs. The distinction between true signal and combinatorial events will be described in more detail in the following chapter, but it should be emphasized that such a distinction between the two can only be made with truth-record information from the simulated datasets. Such truth information can also be used to assess the probability that the correct jet-quark associations will be made.

With a greater number of jets in the final state compared with the semileptonic $t\bar{t}$ channel the ambiguity over which jets to assign to the two top quark candidates is heightened, and the combinatorial background in all-hadronic $t\bar{t}$ analyses therefore plays a much more significant role than it does in semileptonic analyses.

Chapter 6

Top Quark Reconstruction

6.1 Jet-Quark Assignment in Reconstruction Algorithms

As described in Chapter 3 energy clusters in the calorimeter are formed by means of a topological clustering algorithm which groups together individual read-out channels[1]. Jets are subsequently assembled from these energy clusters using the anti-k_T jet construction algorithm described in Section 4.2. In the same way, top quark candidates themselves must then be reconstructed from these jets. This chapter describes the way in which this reconstruction is performed.

In a true signal event with two fully hadronic top quark decays, the six quarks in the final state will typically, but not always, initiate a hadronic shower of energy - a hadronic jet - as described in Chapter 4. Even in true all-hadronic signal events however, the radiation of gluons from the quarks or effects during the hadronization process can produce additional, unwanted jets which are difficult to distinguish from the six jets of interest[2].

Conversely, a number of situations can lead to cases with fewer than six jets being observed in signal $t\bar{t}$ events: at least one of the quarks of interest could either be produced such that it travels in a direction outside of the selected kinematic region; alternatively the jet it initiates may either fail to meet certain selection criteria, or it may simply be too low in transverse momentum p_{T} and consequently fails to pass the requisite thresholds.

It is therefore only in an ideal case that six well reconstructed jets will be present in a given event, and that these six jets were indeed each initiated by a unique one of the six quarks from the initial inelastic scattering process of interest.

Since one cannot know *a priori* which true particle initiated each of the jets reconstructed in a particular event, it can be recognized that one of the primary challenges of the all-hadronic

[1] Refer to Section 3.2.5.

[2] As mentioned in Section 4.1, some techniques have been shown to be somewhat successful in distinguishing quark- from gluon-initiated jets, just as b-tagging techniques can help to identify a jet initiated by a bottom-type quark [58].

$t\bar{t}$ channel lies in the difficulty of correctly assigning the final jets to the six quarks produced in the two top-quark decays. Such an assignment must however be made in order to reconstruct both the hadronically decaying W bosons and the top quarks.

The goal of a **top reconstruction algorithm** is to define a process by which the n jets in a given event, of which n_b are assumed to be b-tagged as described in Section 4.4.2, are assigned to the six primary quarks.

Before describing the algorithm selected for the present analysis, it is useful to enumerate the unique ways to reconstruct, for a given event, a pair of top quark candidates, where each top quark candidate is itself reconstructed from the four-vector sum of three individual jets. The number P of unique permutations given n jets of which n_b are b-tagged can be expressed by:

$$P_{n,n_b} = \begin{cases} \binom{n-n_b}{2-n_b}\binom{n-2}{2}\binom{n-4}{2}, & n \geq 6 \text{ and } 0 \leq n_b \leq 2 \quad \text{(with the b-tagging requirement)} \\ \binom{n}{2}\binom{n-2}{2}\binom{n-4}{2}, & n \geq 6 \quad \text{(without the b-tagging requirement)} \end{cases} \tag{6.1}$$

In the above, $\binom{n}{r} = \frac{n!}{(n-r)!r!}$ is the number of unique ways to select r elements out of n distinct elements. The **first term** represents the number of ways to select two jets to be associated to the two bottom-type quarks from the top decay; no distinction is made between the top or anti-top quark. A b-tagging requirement may be enforced in the form of a veto, whereby permutations are rejected in the case that a non-tagged jet is assigned to one of the b-quark positions[3]. In the case that $n_b > 2$ and such a b-tagging requirement is imposed, the first term $\binom{n-n_b}{2-n_b}$ is replaced by $\binom{n_b}{2}$. The **second term** represents the number of ways to select two jets of the remaining $n-2$ to be associated with one top quark candidate, and similarly the **third term** the number of remaining $n-4$ jets to be associated to the light quarks with the second top quark candidate. It should be noted that the final term is exactly one in the case that $n = 6$ since there are no remaining choices to be made. Furthermore the number of possible permutations to consider in the $n_b = 0$ case is always identical to the number of permutations to consider without a strict b-tagging requirement. Table 6.1 shows values of P_{n,n_b} for typical values of n and n_b, both with and without the b-tagging requirement.

Here it should be noted that a two-fold ambiguity arises in the assignment of the jets to the decay products of each of the hadronically decaying W bosons. From the values of the CKM matrix[4] comes the fact that hadronically decaying W bosons typically decay to $q\bar{q}$ pairs where $q = u, d, s$ or c. Though such jets cannot be distinguished from one another, it is in fact not necessary to do so – it is sufficient that a reconstructed W boson candidate be comprised of

[3]No such b-tagging veto is applied in the analysis, but it was considered and investigated for a time. For completeness the value n_b is left in the expression in Equation 6.1. The application of such a b-tagging veto is discussed in the concluding remarks and outlook in Chapter 12.

[4]The values of the **Cabibbo–Kobayashi–Maskawa** matrix effectively allow for the mixing of quark between the various generations and flavours. For more information refer to the Particle Data Group summary [3].

Table 6.1: Summary of the number of unique possible permutations, with and without the use of b-tagging, to reconstruct two top quark candidates each from three jets and to further select from each top quark candidate the two jets to be associated to the W boson candidate. The number of permutations are shown for a selection of different jet multiplicities in an event.

Number of Jets		# of Unique Permutations P_{n,n_b}	
n	n_b	w/ b-Tagging Requirement	w/o b-Tagging Requirement
6	1	30	90
6	2	6	90
7	1	180	630
7	2	30	630
8	2	90	2520
9	2	210	7560
10	2	420	18900

two selected jets, in any order. Similarly, it is not important to identify which of the two top quark candidates are associated to the top *vs* the anti-top quark in the event[5]. This fact is helpful in reducing the number of unique permutations to consider, though as Table 6.1 shows, the number of permutations to consider remains formidable even in the $n = 6$ case, particularly when the b-tagging requirement is not employed.

The proliferation of jet-quark permutations makes clear the fact that it becomes increasingly difficult for a top reconstruction algorithm to select the correct permutation in signal events with a large number of jets.

It is also important to highlight the fact that in QCD multi-jet events, for which there is no correct jet-quark association given that there are no real top quarks, a larger jet multiplicity provides more flexibility in being able to fake a signal event – there are a sufficiently large number of permutations to choose from and at least one such configuration will be nearly indistinguishable from a signal $t\bar{t}$ event. Additional kinematic knowledge of true signal events will also have to be used in parallel to separate the signal from background events in such cases.

[5]Analyses have been performed in the semileptonic $t\bar{t}$ channel in which the charge of the lepton is used to make such distinction in an effort to measure the top *vs.* anti-top quark mass difference $\Delta m_{top} = m_t - m_{\bar{t}}$, though for the present analysis it is assumed that this difference is exactly zero as predicted by CPT invariance – an exact symmetry of nature which at present has not been shown to be violated. For more information see [73].

6.2 Levels of Top Quark Reconstruction

Top quark and W bosons, due to their extremely short lifetimes, do not travel any significant distance; they consequently do not themselves leave tracks or deposit energy in the calorimeters of the ATLAS detector. In this sense they must be reconstructed from objects associated to their decay products. In the case of the all-hadronic channel this corresponds to the jets constructed by means of the anti-k_T algorithm.

A top quark candidate is a four-vector object with **energy**, **momentum**, **pseudorapidity** η, and **azimuthal angle** ϕ as measured in the ATLAS coordinate system. It is reconstructed *via* the four-vector sum of its constituent pieces, each of lower energy than the reconstructed top quark. The types of objects used in this four-vector sum determine the **level** of top quark reconstruction, analogously to the various levels of jet reconstruction described in Chapter 4.

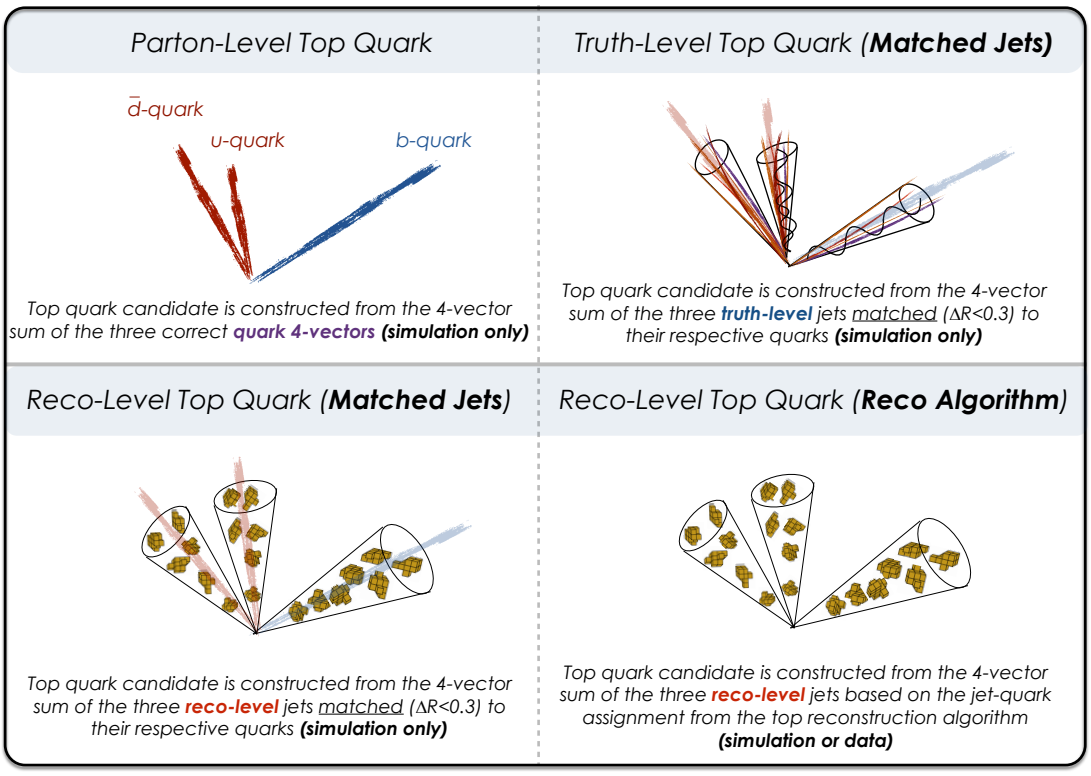

Figure 6.1: An illustration depicting the difference between quark-level and jet-level reconstruction of a top quark. Only the option depicted in the lower right is a viable option in the case of data since it does not rely on truth-level information, though the other options are useful in measuring the performance of a given reconstruction algorithm.

A **parton-level top quark**, as illustrated in Figure 6.1, involves the four-vector addition of the three original quark four-vectors from the process $t \to bq\bar{q}$. It can be thought of as the purest way in which a top quark (or an anti-top quark) can be constructed as no energy is lost due to reconstruction or detector effects. The next level of reconstruction of top quarks involves the four-vector addition of the three jets associated to each of the quarks. This association can be performed either *via* ΔR matching to the truth-record objects by requiring $\Delta R(\text{quark}, \text{jet}) < 0.3$ for a match, or, as is done at the analysis level, by means of a top reconstruction algorithm. Jet-level top quark reconstruction can therefore further be divided into different classes, corresponding to the jet object definitions depicted in Figure 4.1: **truth-level top quarks** using truth-level jet four-vectors to reconstruct a top quark, or **reco-level top quarks** using reco-level jet four-vectors. The reconstruction levels described above for reconstructed top quarks can be applied analogously to reconstructed W bosons.

Both parton- and truth-level top quark reconstruction rely on truth-record information and are therefore not feasible as a means to reconstruct top quarks in data where such knowledge is not available. Such reconstruction is only possible using simulated data. These categories of reconstructed top quarks nonetheless provide a benchmark of performance for different reconstruction algorithms, as will be described in Section 6.3.

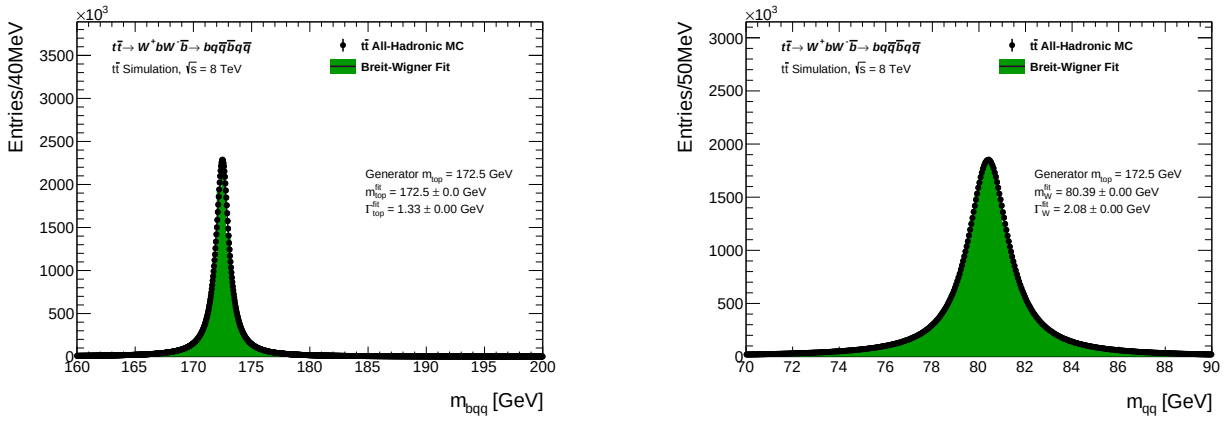

(a) Quark-level invariant $m_{bq\bar{q}}$ distribution.

(b) Quark-level invariant $m_{q\bar{q}}$ distribution.

Figure 6.2: Distributions of the invariant masses of reconstructed (a) top quarks and (b) W bosons, where the objects are reconstructed from the truth-record quark four-vectors.

Figure 6.2 shows the invariant mass distributions of parton-level top quark and W boson candidates reconstructed from the quarks themselves in simulated signal events. Only a small number of standard pre-selection cuts are applied to events used to fill these histograms[6]. Such invariant mass distributions depict the upper limit on the performance that could be achieved.

[6] see Section 7.4.2

The width visible in the distributions is an intrinsic physical property of the fundamental particles and entirely separate from the resolution inherent in and introduced by any detector used in performing a measurement such as the ATLAS calorimeter. Non idealized calorimeter deposits as well as uncertainties from the modelling of parton showering, hadronization and fragmentation processes, limit the ability to produce such ideal distributions from reconstruction-level quantities. Furthermore, non-linearity and resolution in the energy measurements from the calorimeter system will also necessarily broaden such distributions.

In addition to such energy response and resolution effects, a combinatorial background arises from true signal events which have been incorrectly reconstructed due to the wrong jet-quark assignment. For distributions of such combinatorial background events, no such resonant peak should be present; the invariant mass distributions will nevertheless have a characteristic shape dictated by the top reconstruction algorithm and modified as a result of the application of event selection cuts.

The following section will outline the classifications of correctly and incorrectly reconstructed objects in the context of signal events, in order to be able to contrast the shapes of correctly reconstructed signal events from combinatorial background events.

6.3 Reconstruction Purity in Simulated Signal Events

In what follows, some benchmarks for performance for top quark reconstruction algorithms are introduced; these are defined in the context of simulated all-hadronic $t\bar{t}$ signal events where truth-record information related to the six primary quarks is available.

Provided a given truth-record top quark has any three jets uniquely matched to its decay products[7], the reconstruction is said to be **correct** if the three jets selected by the reconstruction algorithm truly correspond to the jets matched to the three quarks, modulo the interchange of the two jets assigned to the hadronically decaying W boson since the distinction here is not made[8]. If at least one of the jets selected by the algorithm is not one of the three jets matched to the quarks, the top quark reconstruction is classified as **incorrect**. A third case exists for any reconstructed top quark candidate for which at least one quark is not matched uniquely to a reconstructed jet; in such cases it is not meaningful to speak of correct or incorrect jet-quark assignment, and the reconstruction assignment for the top quark is simply classified as **non-matched**. As introduced earlier in the chapter, a large number of these cases will come about when at least one of the quarks falls outside of the kinematic region of interest, or if the energy of the quark is sufficiently low that its associated protojet candidate fails to meet the requisite

[7] As in the classification of jet flavours presented in Chapter 4, a reconstructed jet is deemed to be **matched** to a truth-record quark in a simulated event if the angular separation between the two objects satisfies $\Delta R < 0.3$.

[8] It is, however, necessary to distinguish between the two top quarks for the event: in order to be correct, the three jets must be assigned to the three quarks from a single parent top or anti-top quark.

energy or quality thresholds necessary to constitute a good reconstructed jet. The three classes are depicted in Figure 6.3.

The **reconstruction purity** is defined as:

$$\mathcal{P}_{reco} = \frac{\#\text{ of correctly reconstructed top quarks}}{\#\text{ of correctly + incorrectly reconstructed top quarks}} \tag{6.2}$$

The analogous classifications exist for the reconstructed W boson candidates, though there it matters only that the two jets, ordered either way, be selected to reconstruct a given W boson in order that the reconstruction be classified as correct[9]. It should be emphasized that the distinction between correct and incorrect permutations in the reconstruction is made with the knowledge of four-vector information of the six quarks from the truth record, *i.e.* the quarks from the top and anti-top quark decays. As such $\mathcal{P}_{reco}$ is a quantity which can only be calculated when such truth information is available. A reconstruction algorithm with a high reconstruction purity will be expected, however, to perform well with data events in which no such truth information is accessible.

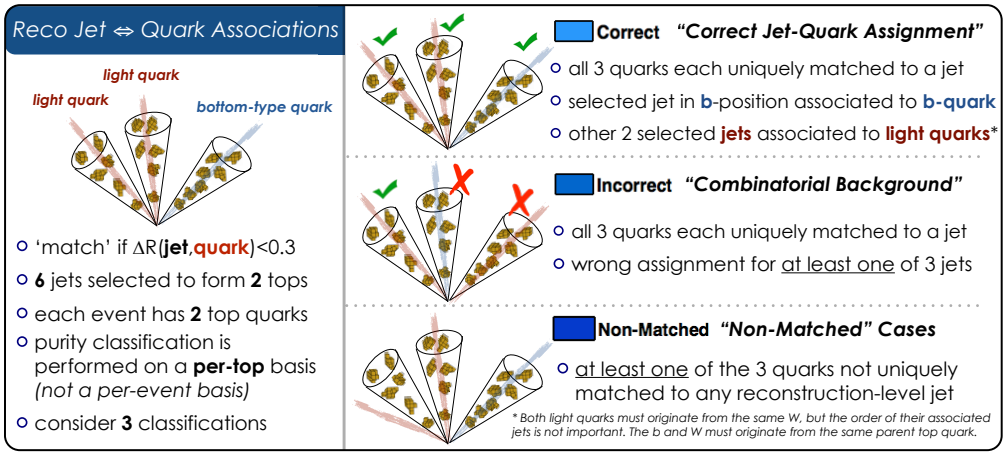

Figure 6.3: An illustration summarizing the three categories for determining a given algorithm's reconstruction purity - a measure of how often the correct permutation of jets is selected.

6.4 Event Reconstruction Using a χ^2 Minimization

There are two leading and conventional types of event reconstruction algorithms to consider, each employing the minimization of a χ^2 variable. Each exploits the known kinematic properties

[9]To be specific, each of the two light jets must be associated to the correct W boson (either W^+ or W^-), though no distinction must be made between the two jets, nor is it important to identify which of the reconstructed W bosons is a W^+ and which is a W^-. This is the same as in the case of the top and anti-top quark.

of jets and the quarks which initiated them from all-hadronic signal $t\bar{t}$ events, and also where possible the known detector energy or p_{T} response, as measured from simulation.

The first type of reconstruction algorithm is a kinematic likelihood method – a maximum likelihood fit performed on each possible permutation of jets, taking advantage of the known W boson mass, and the pure lineshape of the hadronically decaying W bosons and top quarks from the hard-scatter process. A mapping from parton-level energies and momenta to the measurements that would be expected in real data due to detector-related effects are also employed. This type of algorithm has been demonstrated in a wide range of analyses to perform very well in assigning the correct jets to the quarks of interest in the event [74]. In addition, the energy of each of the jets can be adjusted on an event-by-event basis due to the known W boson mass which is used as a constraint in the fit. The strong performance of such an algorithm, however, comes at the cost of a formidable amount of computing time required to run over all events since a fit must be performed for each individual permutation in a given event.

An alternative type of algorithm which is widely popular due to its comparable performance and simplicity, but its less intensive use of computing resources, is an analytic χ^2 method [75]. This type of reconstruction algorithm similarly considers all possible permutations, but rather than performing a fit, the algorithm simply returns a single, analytically computed, χ^2 value for each permutation of jets[10]. The particular permutation resulting in the lowest χ^2 value out of all possible permutations in a given event is then selected in order to set the jet-quark associations. Low χ^2 values denote permutations of jets with a good compatibility with the all-hadronic $t\bar{t}$ topology. Studies to compare the performance of these two types of reconstruction algorithm in the same all-hadronic $t\bar{t}$ channel using $\sqrt{s} = 8$ TeV ATLAS data [75] show only a modest gain in performance by a likelihood fit-based reconstruction algorithm compared to the analytic χ^2 algorithm, despite requiring roughly four orders of magnitude more computing time. For this reason the analytic χ^2 algorithm was used for the present analysis.

It was seen in earlier studies using simulated data that the knowledge of the angular separations between jets and/or reconstructed quantities such as W boson or top quark candidates could also be exploited to further enhance the performance of this χ^2 algorithm[11]. Such an approach resulted in an increased reconstruction purity $\mathcal{P}_{reco}$. Additionally the b-tagging information could be exploited to favour permutations in which a b-tagged jet is associated to a bottom-type quark position or, alternatively, to veto permutations in which it is not. Unfortunately neither of these potential ameliorations, though they strengthen the performance of the analytic χ^2 method, could be used in reconstructing top quarks[12] due to the fact that their

[10] In this sense, it is not a minimization in the standard context of least-squares or likelihood fit since it is designed to select the minimal value from a number of discrete values rather than sweeping through a continuous range of parameter values as in a conventional least-squares minimization.

[11] Such studies were carried out in the context of the present analysis. In addition, similar studies were investigated by the analysis group involved in performing a measurement of the inclusive $t\bar{t}$ cross-section using all-hadronic $t\bar{t}$ events with 8 TeV dataset. For more information see [75].

[12] Such kinematic properties were however used for event selection cuts after the reconstruction to reject badly

presence introduces correlations which ultimately lead to incompatibilities with the background estimation technique to be described in Chapter 9.

6.4.1 Reconstruction χ^2 Definition

As mentioned, the background estimation method used in the present analysis is sensitive to the presence of unwanted correlations which can degrade its performance. For this reason it was found that the ideal ingredients to be used in order to reconstruct a robust χ^2 variable should consist solely of quantities such as the invariant masses of reconstructed objects. One expects that both reconstructed W boson candidates and top quark candidates will have a mass close to some reference value, determined from simulation and taking into account detector response and resolutions, and that their difference from this reference value should also be small.

The initial event reconstruction χ^2 is defined to be:

$$\chi^2 = \left(\frac{m_{b_1 j_1 j_2} - m_t}{\sigma_t}\right)^2 + \left(\frac{m_{b_2 j_3 j_4} - m_t}{\sigma_t}\right)^2 + \left(\frac{m_{j_1 j_2} - m_W}{\sigma_W}\right)^2 + \left(\frac{m_{j_3 j_4} - m_W}{\sigma_{m_W}}\right)^2 \tag{6.3}$$

In the above expression, b_1 and b_2 correspond to the two jets in the role of the bottom-type quarks from the (anti-)top quark decays for a given permutation. Of the four remaining jets, j_1 and j_2 are attributed to the hadronic W boson which, added together with jet b_1, form the four-vector object corresponding to the first reconstructed top quark candidate. Similarly, the four-vectors of the jets in positions j_3 and j_4 can be added together with that of the jet in position b_2 to reconstruct the second top quark candidate.

Although the reconstructed top quark candidates themselves should each be expected to have an invariant mass close to the true m_{top} value, the inclusion of these first two terms should be avoided for the purposes of the present analysis as it is m_{top} which one is trying to measure. As such the value of m_t in the above can be assumed to be the average of the two reconstructed top quark masses. By making the substitution $m_t = \frac{\left(m_{b_1 j_1 j_2} + m_{b_2 j_3 j_4}\right)}{2}$, the expression reduces to:

$$\chi^2 = \frac{1}{2}\left(\frac{m_{b_1 j_1 j_2} - m_{b_2 j_3 j_4}}{\sigma_t}\right)^2 + \left(\frac{m_{j_1 j_2} - m_W}{\sigma_{m_W}}\right)^2 + \left(\frac{m_{j_3 j_4} - m_W}{\sigma_{m_W}}\right)^2 \tag{6.4}$$

This modification then translates to a requirement that the difference between the two reconstructed top quark masses should be small. By making the further substitutions $\Delta m_{bjj} = m_{b_1 j_1 j_2} - m_{b_2 j_3 j_4}$ and $\sigma_{\Delta m_{bjj}} = \sqrt{2}\sigma_t$, the above equation can alternately be written in the form:

reconstructed objects and increase the fraction of true and well reconstructed signal top quarks in the final dataset. In this case no degradation in the performance of the background estimation technique was observed.

$$\chi^2 = \left(\frac{\Delta m_{bjj}}{\sigma_{\Delta m_{bjj}}}\right)^2 + \left(\frac{m_{j_1 j_2} - m_W}{\sigma_{m_W}}\right)^2 + \left(\frac{m_{j_3 j_4} - m_W}{\sigma_{m_W}}\right)^2 \tag{6.5}$$

A natural question arises as to why the reference m_W terms in the numerators of the second and third terms cannot also be replaced analogously by their average value as was done for the top quark masses. Though this can also be done, it was observed that having the two separate terms as above is a stricter requirement and leads to better performance – by including two separate terms the W bosons are more often reconstructed correctly.

A further constraint could be placed on the average invariant top quark mass m_t, since the form of the χ^2 variable in Equation 6.5 does not specifically disfavour permutations in which the average m_t value is far from the true value. Such cases could still result in a small χ^2 value; the constraint itself is on the difference Δm_{bjj} and there is nothing limiting the average value itself which could be extremely large or small. Preliminary studies showed a modest improvement by employing such a constraint, but in its application there is the potential for a resulting bias on the final measurement. It was consequently decided to avoid the use of such a constraint despite the potential gains it offers.

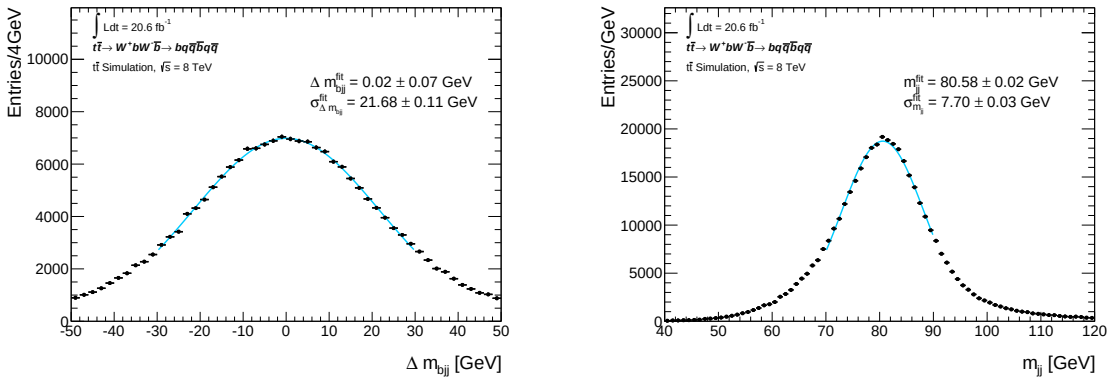

(a) Δm_{bjj} (b) m_{jj}

Figure 6.4: Distributions of the variables used to generate the reference terms m_W, σ_{m_W}, and $\sigma_{\Delta m_{bjj}}$ for the analytic χ^2 reconstruction algorithm. The distributions are filled using a subset of the simulated all-hadronic $t\bar{t}$ events as explained in the text. The truth-record information was used in order to have the correct jet-quark associations.

6.4.2 Detector Response and Resolution Reference Terms

In order to determine the reference terms m_W, σ_{m_W}, and $\sigma_{\Delta m_{bjj}}$ in Equation 6.5, distributions of each variable are filled, using as input the full set of simulated all-hadronic $t\bar{t}$ events. Events

are required to pass all event selection cuts, to be detailed in the following chapter, up to the point at which the reconstruction is performed[13]. Only the correct permutations are used for reconstructed top quark candidates, *i.e.* truth-record information is used in order to always select correctly reconstructed top quark candidates, thereby providing a true estimate of the response and resolution one would expect without combinatorial backgrounds; unmatched cases, as described in Section 6.3, are therefore discarded for this purpose.

A single Gaussian function is fitted to each of the distributions in Figure 6.4, and the resulting shapes based on the fitted parameters are shown in blue. The mean and width parameters from the Gaussian fits thus represent the expected response and resolutions of the reference variables in Equation 6.5 at the time the reconstruction will be performed. These values are considered fixed and are used throughout the analysis when performing the top reconstruction, notably in cases where one is not relying on the truth-record jet-quark associations as will be the case with both data and simulation in the nominal analysis. The mean of the Δm_{bjj} term is assumed to be zero. For the remaining reference terms appearing in Equation 6.5, the central W boson mass term (m_W) is assigned the value $m_{jj}^{fit} = 80.58$ GeV, the W boson width (σ_{m_W}) a value $\sigma_{m_{jj}}^{fit} = 7.70$ GeV, and the width term corresponding to the expected difference in reconstructed top quark masses $\sigma_{\Delta m_{bjj}}^{fit} = 21.68$ GeV.

In reconstructing the top quarks and W bosons, it was found that the addition of muons matched to each jet, where applicable, resulted in a modest improvement in the resolution of the invariant mass distributions[14]. The four-vector of the highest-energy muon matched to a given jet, by satisfying the requirement $\Delta R(\mu,\text{jet}) < 0.3$, is added to that jet's four-vector prior to running the top reconstruction algorithm[15]. The same modified jet four-vectors are then used to reconstruct the observables used for the m_{top} measurement.

The plots in Figures 6.5(a) and 6.5(b) show distributions of the numerators from the main terms of the χ^2 variable. Aside from any p_{T}-ordering bias in the jet-quark assignment, the final two terms in Equation 6.5 should be identical and the distribution shown in Figure 6.5(b) is therefore filled twice per event: one for each of the reconstructed W bosons. The final plot in Figure 6.5(c) shows the distribution of final χ^2 values for all events as defined in Equation 6.5 – the sum of the three individual terms.

[13]The particular cut referred to is C7 (see Section 7.4.8) – events must satisfy all of the selection cuts up to and including this cut.

[14]Refer to Sections 4.3 and 4.5.3 describing the addition of muons to jet four-vectors and the resulting effect on the jet energy response.

[15]See the final category of jet objects in Figure 4.1

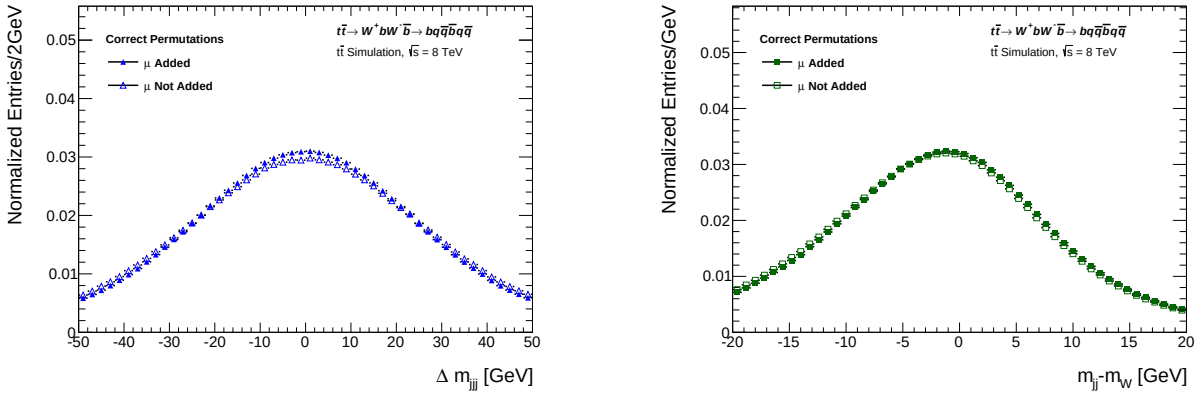

(a) (b)

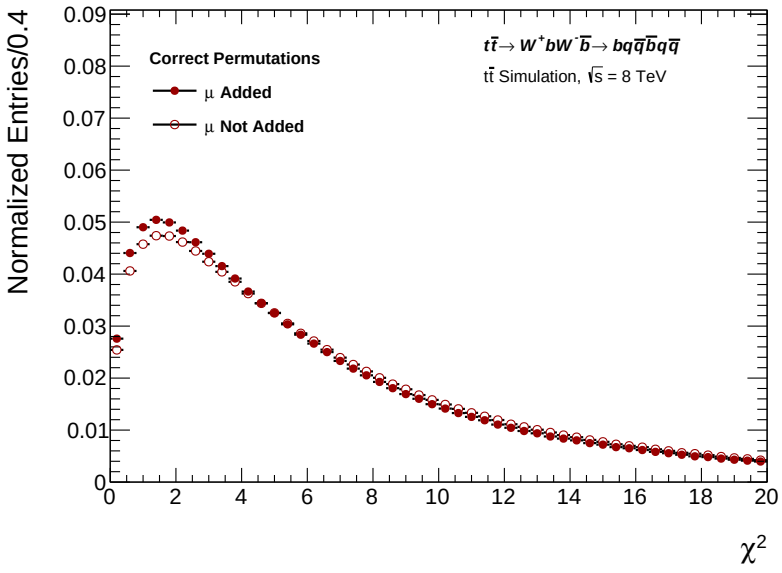

(c)

Figure 6.5: The numerators of the (a) first term and (b) combined second and third terms of the χ^2 variable. Distributions are filled only for signal events with the correct jet-quark assignment. The distributions show a comparison of the terms with and without the addition of the muon four-vectors to the jets. The sum of all three χ^2 terms is shown in (c).

6.4.3 Reconstruction Goodness of Fit Probability (P_{gof})

The χ^2 variable, as defined in Equation 6.5, is the sum of three squared terms, each consisting of a variable whose numerator is roughly expected to follow a Gaussian probability distribution. This allows the χ^2 variable to be re-expressed as a goodness of fit probability, P_{gof}, where

$$P_{gof} = 1 - F(\chi^2, 3) \tag{6.6}$$

In the above, $F(\chi^2, n)$ is the cumulative distribution function of a variable distributed according to a χ^2 probability distribution function with n degrees of freedom.

A one-to-one correspondence exists between a given χ^2 term and its associated P_{gof} value – any quality cut requiring a minimum value of P_{gof} therefore translates directly to a cut on a maximum value of χ^2_{min}. As such, the two values are often quoted together, recognizing their relation *via* Equation 6.6.

6.5 Performance of χ^2 Reconstruction on Signal Events

As a next step, the analytic χ^2 reconstruction method is again used to reconstruct top quark candidates from simulated signal $t\bar{t}$ events, though this time without relying on truth-record information in order to establish the true jet-quark associations. The same pre-selection cuts are applied, as is a further requirement that there be at least six jets in a given event. For all events satisfying these criteria, two top quark candidates are reconstructed for *all* of the possible permutations of the n jets in the event, where the number of distinct permutations was provided in Equation 6.1. For each unique permutation a particular χ^2 value will be returned, and the permutation resulting in the smallest χ^2 value[16] is the one selected[17]. No b-tagging information is used to veto or favour permutations when making the jet-quark assignment.

The same procedure of adding matched muon four-vectors to the reco-level jets is to be used when running the reconstruction on data events, and is thus applied here: the highest-energy muon matched to a given jet, if such a match exists, is added to the jet four-vector prior to running the χ^2 reconstruction algorithm.

[16] Another possibility is to retain all permutations, assigning a global weight of 1 for each event, but with each permutation receiving a fraction of this weight based on its P_{gof} value. While such an approach has been used in other contexts, the extremely large number of permutations has the effect of degrading the signal peak, as opposed to improving it. Adopting such an approach would also require an evaluation of the per-event correlations between individual permutations as they are constructed from the same set of jets which would be non-trivial. For both of these reasons only a single permutation is selected.

[17] Appendix C.5 shows some performance plots for the analytic χ^2 reconstruction algorithm for a number of representative simulated signal events with different numbers of jets.

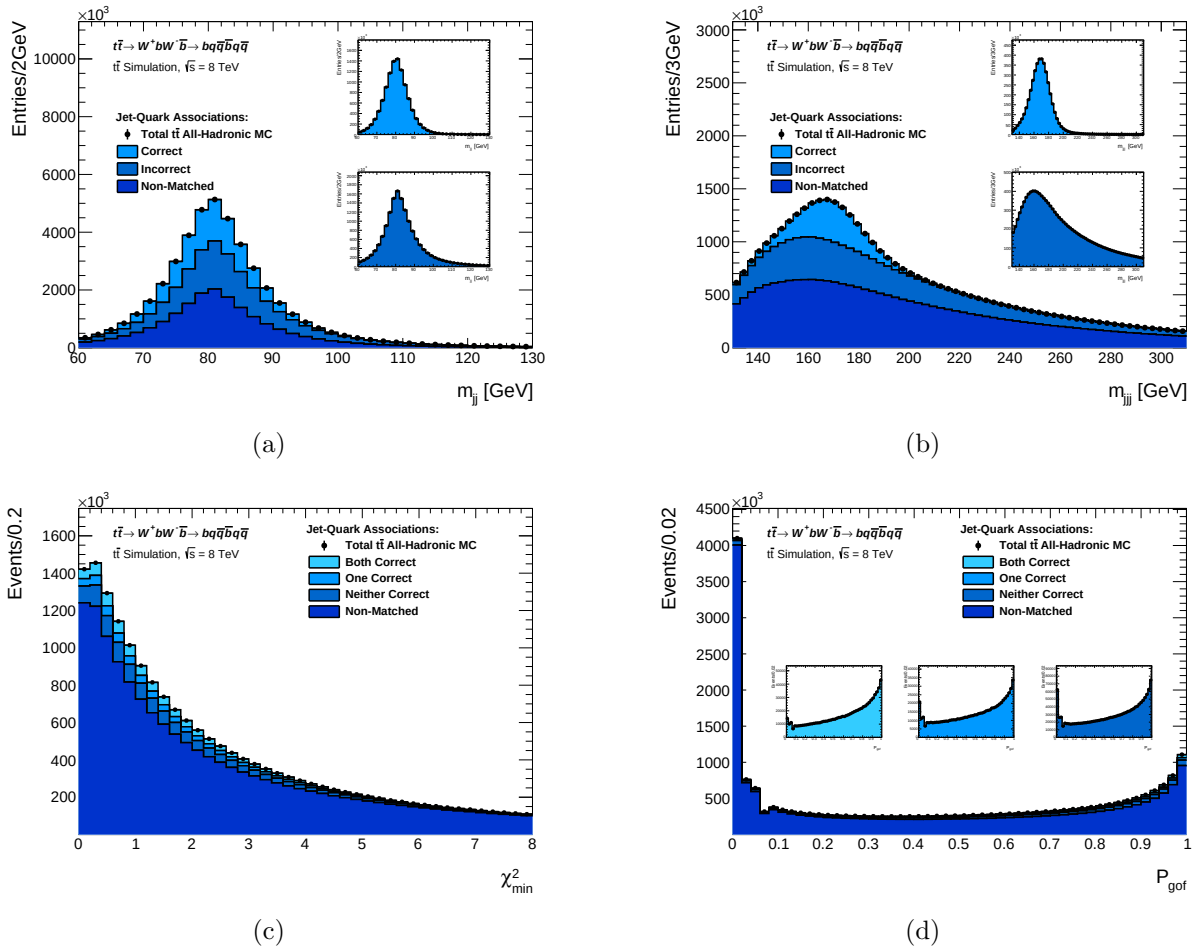

Figure 6.6: Distributions of the reconstructed invariant (a) m_{jj} and (b) m_{bjj} distributions with only pre-selection cuts applied. The main figure shows the three classifications of reconstruction purity represented by stacked histograms. Inset figures show the correct-permutation (upper) and incorrect-permutation (lower) distributions individually. Figures (c) and (d) show distributions of the minimum χ^2 for each simulated signal event as well as its corresponding goodness-of-fit value P_{gof}, respectively, where only pre-selection cuts have been applied. The distributions shown in the inset figures allow for a comparison of the individual shapes in the stacked distributions; in all cases the axis labels and horizontal range are unmodified from those in the main figure.

The distributions shown in Fig. 6.6(a) and Fig. 6.6(b) show the invariant mass distributions of reconstructed W boson and top quark candidates, respectively, based on jet-quark assignments corresponding to the minimal χ^2 permutation for each event. The distributions are stacked to highlight the correct, incorrect and unmatched cases, with totals shown as black markers. The upper and lower inset figures show the distributions of the correct and incorrect cases, respectively. It is worth noting that the incorrect cases – representing the combinatorial background – as well as the non-matched cases for the m_{jj} distribution peak in the same position as do the distributions corresponding to correct cases. This is a direct consequence of the fixed value chosen for the reference m_W value. The QCD multi-jet background can similarly be expected to exhibit such behaviour – even though there are no true W boson or top quarks to reconstruct in the case of QCD multi-jet events, the algorithm will return a permutation which looks the most like an all-hadronic $t\bar{t}$ event. In the case of the m_{jjj} distribution in Fig. 6.6(b) however, one can note the difference in the peak positions between the correct cases and the incorrect or non-matched cases[18]. The reconstruction purity $\mathcal{P}_{reco}$ is determined to be roughly 24.0% for reconstructed top quarks and 41.2% for reconstructed W bosons. Here the difference has partly to do with the stricter requirement on the fixed m_{jj} value for each of the two W candidates as opposed to the weaker difference term for the top quarks, but also the fact that a greater number of jet-quark associations are required to be correct in the case of the top quarks compared with the W bosons – one can have a correctly reconstructed W boson but fail to select the correct jet in the associated bottom-quark position; in contrast if a top quark is correctly reconstructed, then its associated W boson will necessarily be correctly reconstructed as well.

Finally Figures 6.6(c) and 6.6(d) show, for the same signal events, the distribution of the minimum χ^2 value together with its corresponding goodness-of-fit value, respectively. Although one can expect P_{gof} to follow a roughly uniform distribution in the case of only correct jet-quark associations due to the roughly Gaussian nature of its three composite terms, the non-uniform distribution visible in Figure 6.6(d) is a reflection of the fact that this is not so for the incorrect and non-matched cases. In addition the three terms in the χ^2 definition are not independent; the correlation will also lead to the non-uniformity of the P_{gof} distribution for the correct cases.

In the legends of both the minimum χ^2 and P_{gof} plots a fourth purity classification is shown which arises due to the fact that there are two reconstructed top quarks for each event. One can consequently consider the cases in which neither, strictly one, or both of the top quarks have the correct jet-quark assignments. If either of the reconstructed objects are classified as non-matched, the permutation classification for that event is similarly classified as non-matched.

[18]It should be highlighted that the term m_{bjj} has been replaced by m_{jjj} used earlier in the chapter. The reason has to do with the fact that there is no strict requirement that the third jet in each triplet must be a b-flavoured jet. In the earlier distributions such knowledge was obtained from the Monte Carlo truth record. It was decided to adopt this notation to avoid the suggestion that the invariant top quark mass distribution is formed by selecting one b-tagged jet and two non-tagged jets. While it is hoped that this will often be the case, there are many events for which it is not.

Additional event selection cuts, described in the following chapter, will further enhance the reconstruction purity $\mathcal{P}_{reco}$ by targetting incorrectly reconstructed top quarks while striving to keep those events in regions of phase space where correct jet-quark assignments are more often made.

6.6 Summary of Top Quark Decay and Reconstruction

Figure 6.7 provides a visual summary of the decay of a top quark, as well as the steps taken to reconstruct top quark candidates in the ATLAS detector in data events: from energy deposits in the calorimeters to fully reconstructed four-vector objects.

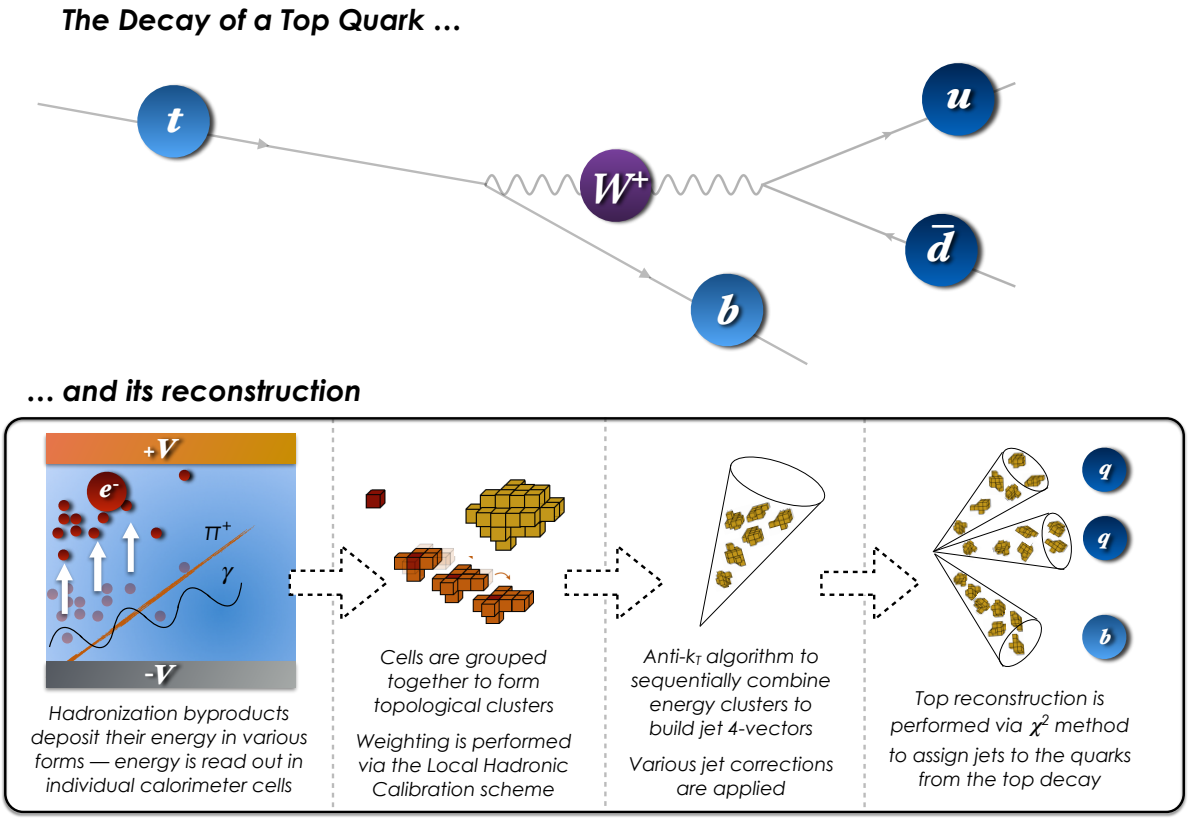

Figure 6.7: An illustration presenting the full reconstruction process, including (from **L-R**): various energy loss processes in the calorimeters (ionization of electrons in the liquid argon calorimeter shown here); reconstruction of energy topoclusters; jet reconstruction using the anti-k_T algorithm; χ^2 top reconstruction algorithm to build top quarks out of constituent jet four-vectors.

Chapter 7

Event Selection

7.1 Introduction

Although the combined branching ratios for the semileptonic and dileptonic $t\bar{t}$ channels are larger than that of the all-hadronic channel, there are more Standard Model $t\bar{t}$ pairs produced at ATLAS which decay to an all-hadronic or all-quark final state than there are $t\bar{t}$ pairs decaying to either of the other two decay channels individually.

In contrast with the other channels however, the lack of a high-p_{T} isolated lepton in the all-hadronic channel, and the resulting inability to trigger on it, gives rise to a large QCD multi-jet background with a final state signature very similar to that of all-hadronic $t\bar{t}$ events. In either of the other decay channels the requirement that there be at least one high-p_{T} isolated lepton immediately brings the QCD multi-jet background down to a manageable level. In dileptonic $t\bar{t}$ channel analyses for instance, in which one expects two oppositely charged high-p_{T} leptons and two bottom-quark-initiated jets, recent analyses demonstrated the ability to reduce the overall fraction of background events in the final distributions to the 1-4% level. In some semileptonic $t\bar{t}$ analyses at $\sqrt{s} = 8$ TeV analyzers have been able, through a series of event selection cuts, to yield background fractions at the 3% level[1]. In all-hadronic analyses the signal-to-background ratios are much higher as there are no characteristic high-p_{T} isolated leptons which can be used to identify candidate events.

Despite this difficulty, there are significant differences between the jet kinematics and event topologies in all-hadronic $t\bar{t}$ events as compared to those of QCD events. Such differences can be exploited in a series of event selection cuts which, while cutting away true signal events, are able to cut away an even greater relative fraction of QCD multi-jet events, thereby increasing the expected signal fraction. This, together with the large number of statistics provided by the

[1]See for instance the results from [76] and [18]. In these cases it should be highlighted that the composition of the background differs from that of all-hadronic events. The values quoted represent the sum of all non-signal contributions.

LHC, allows for a sizeable final number of selected candidate events with roughly equal expected contributions from both signal and background.

This chapter describes the full set of event selection cuts which are applied sequentially to both data and simulated Monte Carlo events, in order to yield the final distributions used to make the m_{top} measurement. A depiction of each of these event selection cuts is presented in Figure 7.1.

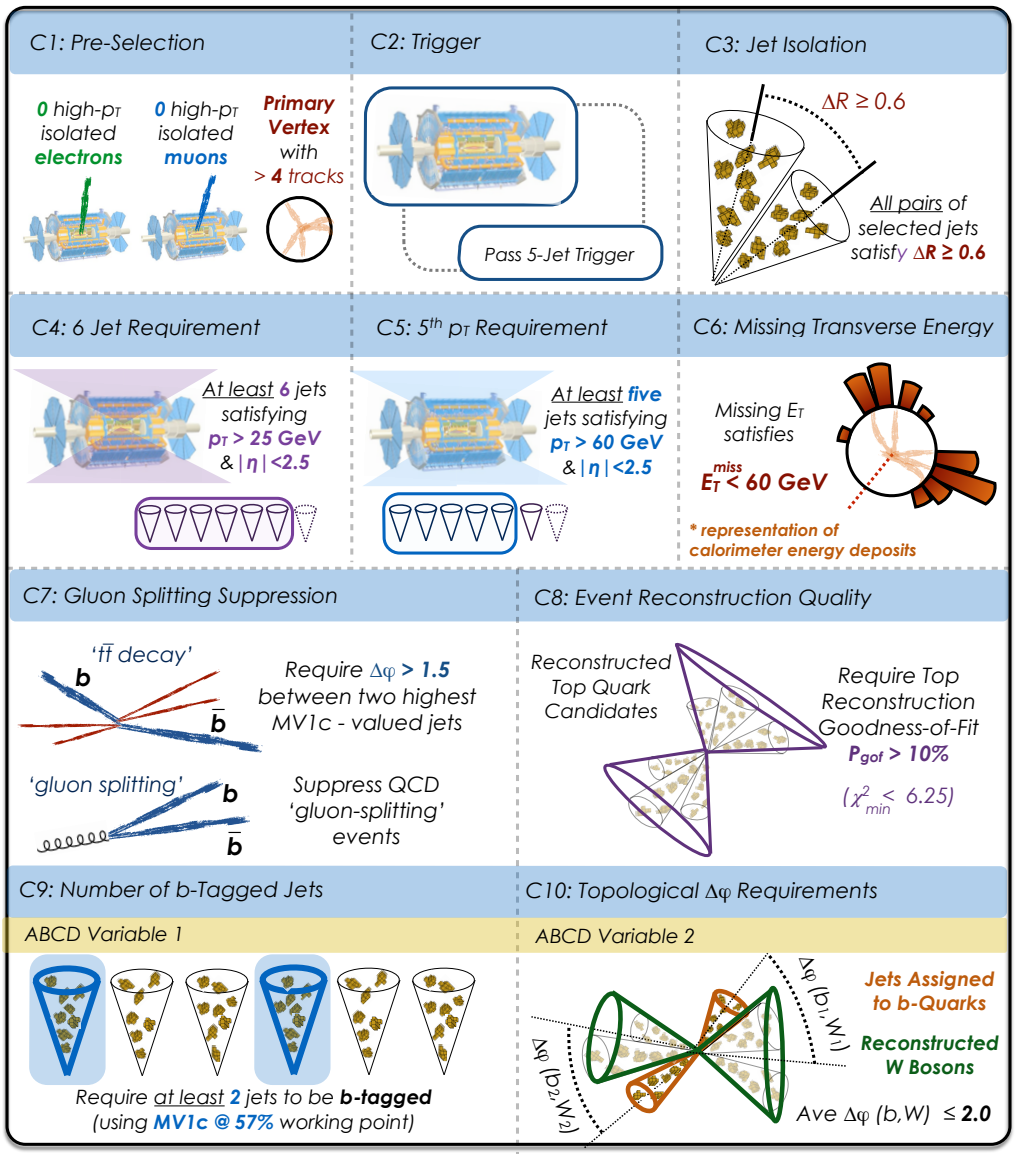

Figure 7.1: Illustration of event selection cuts from C1 through C10 as described in the text.

7.2 Object Definitions

Before describing each of the particular cuts, some physics object definitions are required. The definitions are based on standards adopted by the Top Physics Working Group within ATLAS, governing the majority of 8 TeV top quark-related analyses including but not limited to mass measurements[2]. The top quark mass measurements made using orthogonal[3] datasets, specifically those aiming to select $t\bar{t}$ pairs decaying semieptonically or dileptonically, use identical definitions of their physics objects.

7.2.1 Jets

The jets[4] included in the analysis are reconstructed from topologically clustered groups of read-out channels from the ATLAS calorimeter system, first weighted from their cluster moments as to whether the energy deposits are deemed of electromagnetic or of hadronic nature. The clusters are grouped to form jets based on the anti-k_T clustering algorithm with a distance parameter of $R = 0.4$. An *in situ* jet energy scale correction, derived using a set of events with similarly reconstructed and calibrated jets, though with a slightly differing flavour composition[5], is also applied to correct the jet energy and transverse momentum.

Jets are required to have a transverse momentum of at least 25 GeV. Below this value, the energy response and resolution of jets is degraded to such a level that they would diminish the performance capabilities of such a precision mass measurement. Only central jets within $|\eta| < 2.5$ are considered for the analysis.

In an effort to suppress the effects from the high-pileup environment at ATLAS, a **Jet Vertex Fraction**[6] (JVF) cut requiring $JVF > 0.5$ is imposed to suppress the contribution from jets originating from pile-up activity, as opposed to jets reconstructed as a result of a hard-scatter quark or gluon. The JVF cut was applied, as per the ATLAS recommendation, only to those reconstructed jets with $p_{\mathrm{T}} \leq 50$ GeV and within the tracking region of $|\eta| < 2.4$ [77].

In the event that the angular separation between a reconstructed jet and a reconstructed electron passing all quality criteria (to be described below) is within $\Delta R(e, jet) < 0.2$, the reconstructed jet is rejected; it is more probable in such cases that the shower deposits arising from a true, high-p_{T} isolated electron led to the seeding of clusters selected by the anti-k_T jet

[2]For further descriptions and motivations for the object definitions refer to [62, 63, 77, 78].

[3]The datasets are orthogonal in the sense that there is no overlap between events in the three channels, so no candidate events selected in one channel are selected for the other two channels.

[4]Recall the more thorough description of how jets are constructed from Chapter 4.

[5]The flavour composition refers to the fraction of quark- *vs.* gluon-initiated jets in a given sample.

[6]The jet vertex fraction is defined as the scalar p_{T} sum over all tracks associated to a particular jet *and* matched to the primary vertex divided by the scalar p_{T} sum over all tracks associated to the jet. A jet with a low JVF value implies that only a small fraction of its tracks are associated with the primary vertex, and it is therefore more likely to have been triggered as a result of pile-up activity in the calorimeter alone.

reconstruction algorithm.

7.2.2 Leptons (e/μ)

In this analysis **leptons** refer to reconstructed electrons or muons, or their anti-particle counterparts. It is important to make the distinction between high-p_{T}, isolated leptons produced in an initial hard-scatter process of interest and those leptons produced and associated with either heavy-flavour quark decays or as a result of a showering process, since the former can be a key signature of leptonically decaying $t\bar{t}$ pairs, particularly when identified in events with one or more b-tagged jes.

Though reconstructed lepton objects are treated on roughly equal footing for the purposes of the current analysis[7], electrons and muons leave strikingly different signatures in the detector and thus different definitions exist for the two types of reconstructed objects.

Electrons are reconstructed from energy deposits in the ATLAS calorimeters which lead to the formation of electromagnetic clusters. The clusters themselves are formed from the sum of longitudinal layers of electromagnetic calorimeter readout channels referred to as energy towers, with each tower encompassing a region in $\eta - \phi$ space with a granularity of $\Delta\eta \times \Delta\phi = 0.025 \times 0.025$. A sliding-window algorithm is employed using a window size of 3×5 towers; the algorithm identifies those seed towers satisfying a threshold $E_{\mathrm{T}} > 2.5$ GeV for the purposes of cluster reconstruction.

These electromagnetic clusters must then be matched to well reconstructed tracks, which originate from a region near the identified primary vertex for a given event, before they are able to be classified as reconstructed electron candidates. The electron candidates must be situated within the main tracking region of the detector, satisfying $|\eta| < 2.47$, with the exception that they not be within a so-called crack region from $1.37 < |\eta| < 1.52$. In this region, inactive detector materials such as cabling, as well as signal losses due to the transition region between two neighbouring parts of the calorimeter, result in degraded performance.

The requirement that the electrons be isolated is enforced by means of the following. The additional energy included in a conical region $\Delta R < 0.2$ surrounding the electron candidate must be less than 6 GeV, and in addition the scalar p_{T} sum of all tracks associated with the electron candidate within a similar region of $\Delta R < 0.3$, must also be below this threshold.

Finally, following the jet removal procedure described above, in the case of a jet-electron overlap, any remaining electrons within $\Delta R(e, jet) < 0.4$ of a reconstructed jet are themselves rejected – they are not considered as isolated lepton objects themselves as they are more likely to have stemmed from the hadronic activity leading to the reconstruction of the jet as opposed to a truly isolated electron from the hard-scattering process.

[7]Reconstructed muon four-vectors however, and not those of electrons, are employed for the purposes of increasing the top reconstruction purity as was explained in the preceding chapter.

Muon candidates must be identified both from tracks in the inner detector and from hits in the muon spectrometer. Successful candidates will have a transverse momentum satisfying $p_{\mathrm{T}} > 25$ GeV, and will necessarily be situated within the tracking limits of the muon spectrometer, namely $|\eta| < 2.5$.

The muon isolation requirement is enforced *via* a variable I^{μ}_{mini}, defined as:

$$I^{\mu}_{mini} = \sum_{i=1}^{N_{tracks}} \frac{p_{\mathrm{T}}^{track\ i}}{p^{\mu}_{\mathrm{T}}} \tag{7.1}$$

This isolation variable quantifies the amount of additional activity in a ΔR cone of p_{T}-dependent size around the muon candidate. Here the sum in Equation 7.1 is taken over all tracks situated within $\Delta R(\mu, \mathrm{track}) < R_{min}$, where the value of R_{min} defining the cone size depends inversely on the muon p_{T} and is given explicitly by $R_{min}(p^{\mu}_{\mathrm{T}}) = 10\ \mathrm{GeV}/p^{\mu}_{\mathrm{T}}$. The quantity $p_{\mathrm{T}}^{track\ i}$ denotes the transverse momentum of the particular track included in the sum. Furthermore, any muon candidates within $\Delta R < 0.4$ of a well reconstructed jet are not considered as isolated lepton candidates, similarly to the requirement on electron objects.

The isolation requirements imposed on either type of lepton candidates reduce the likelihood that electrons or muons originating either from a heavy-flavour quark decay, or as a result of the showering activity leading to the formation of a jet, will be identified as true hard-scatter leptons. This is important because events with identified high-p_{T} isolated leptons will be rejected to suppress the contribution of the non all-hadronic $t\bar{t}$ background.

7.2.3 Missing Transverse Energy ($E_{\mathrm{T}}^{\mathrm{miss}}$)

The missing transverse energy, denoted $E_{\mathrm{T}}^{\mathrm{miss}}$, is calculated as the vector transverse energy sum over all deposits in the calorimeter system; large values of the transverse missing energy calculated in this way suggest the presence of high-energy, non-interacting particles such as neutrinos travelling unimpeded through the detector, thereby giving rise to a large momentum imbalance in the transverse plane. The final value of the $E_{\mathrm{T}}^{\mathrm{miss}}$ depends on the reconstruction and calibration of energy clusters in the calorimeter.

A similar variable, $\sum E_{\mathrm{T}}$, can also be used to identify potential events of interest in proton-proton collisions. It is calculated as the scalar (as opposed to vector) E_{T} sum over all calorimeter energy deposits. The $\sum E_{\mathrm{T}}$ variable is however not used for the present analysis, and $E_{\mathrm{T}}^{\mathrm{miss}}$ is always taken to represent the vector sum.

7.3 Summary of Full Event Selection

Table 7.1 summarizes the evolution of the number of final event yields for both data and all-hadronic $t\bar{t}$ signal events – the later based on simulated Monte Carlo events – following each successive cut. Values are shown in thousands of events with corresponding uncertainties based on Poisson statistics. The same information is displayed in the form of a graph in Figure 7.2, in which solid, horizontal lines indicate the particular values following the cut which corresponds to that displayed on the horizontal axis. Solid black lines correspond to overall numbers of data events. The estimated numbers of all-hadronic $t\bar{t}$ signal events are depicted by the dark blue lines, and non all-hadronic $t\bar{t}$ background events by the orange lines. In both of these cases the values are derived from simulated Monte Carlo samples. The non all-hadronic $t\bar{t}$ background is not included in the nominal measurement, so values are not shown in Table 7.1, but are shown in the graph in Figure 7.2 for comparison.

The solid magenta line represents the estimated signal fraction $S/(S + B)$ expressed as a percent and with a scale shown on the right-hand side of the plot. The signal fraction is evaluated, following each cut, as the number of signal events (S) – evaluated from simulation and scaled to their theoretical cross-section – divided by the number of data events (S+B). The calculation of the estimated signal fraction includes the overflow and underflow bins outside of the plotting ranges which will be shown in the various distributions to be presented. The reconstruction purity for reconstructed W bosons and top quarks, as defined in Equation 6.2, is represented by the dashed red and light blue lines, respectively. The right-hand scale is also attributed to these reconstruction purities.

The top reconstruction is performed only following the cuts on the event-level quantities, with the $E_{\mathrm{T}}^{\mathrm{miss}}$ requirement (C6) being the final such cut; reconstruction purities prior to the $E_{\mathrm{T}}^{\mathrm{miss}}$ cut are therefore not available, and furthermore would be either misleading or meaningless prior to the six-jet requirement[8]. Here it can be seen that while all cuts have the detrimental effect of cutting signal events, they can all be seen to do at least one of following: reducing the fraction of background events (either non all-hadronic $t\bar{t}$, QCD multi-jet, or both) and thereby increasing the estimated signal fraction, or reducing the contribution from incorrectly reconstructed top quarks, in which case the reconstruction purities are increased.

[8]Note however that the reconstruction purity was quoted at an earlier stage in the event selection in the preceding chapter. In that case the top reconstruction was performed before all cuts on event-level quantities (following cut C4). When running the full analysis on both data and signal the reconstruction is performed following cut C6. For this reason the first reconstruction purity quoted in Table 7.1 is slightly larger than the value of 24.0% quoted in the previous chapter.

Table 7.1: A summary of the event yields following each of the individual event selection cuts, with values shown for both data (S+B) and all-hadronic signal events (S). The number of simulated signal events (S) are scaled to theoretical cross-section and integrated luminosity. The values of (S+B) are taken entirely from data. The estimated signal fractions are therefore derived from a mix of data and simulation. Also quoted is the top reconstruction purity ($\mathcal{P}_{reco}$), defined as the fraction of correctly reconstructed top quarks relative to the sum of both correctly and incorrectly reconstructed top quarks. These fractions are evaluated from simulation and based on the matching of jets selected for the reconstruction to truth-record quarks from the top quark decays. Values of $\mathcal{P}_{reco}$ are only defined for cuts following the top reconstruction step.

		Event Yields (in Thousands)		Signal Fraction & Reco Purity	
Cut	Description	Data (S+B)	All-Hadronic (S)	S/(S+B) [%]	$\mathcal{P}_{reco}$ [%]
C0	Initial	850450 ± 20	2384 ± 1	0.3 ± 0.0	/
C1	Pre-Selection	33476 ± 5	333.6 ± 0.6	1.0 ± 0.0	/
C2	Trigger	16110 ± 4	264.8 ± 0.5	1.6 ± 0.0	/
C3	Jet Isolation ($\Delta R < 0.6$)	7646 ± 2	152.1 ± 0.4	2.0 ± 0.0	/
C4	≥ 6 Central Jets, $p_{\mathrm{T}} \geq 25$ GeV	7646 ± 2	152.1 ± 0.4	2.0 ± 0.0	/
C5	5^{th} Jet $p_{\mathrm{T}} \geq 60$ GeV	3303 ± 1	57.6 ± 0.2	1.7 ± 0.0	/
C6	$E_{\mathrm{T}}^{\mathrm{miss}} < 60$ GeV	3021 ± 1	51.6 ± 0.2	1.7 ± 0.0	/
C7	$\Delta\phi$(Leading MV1c Jets) ≥ 1.5	1737 ± 1	33.9 ± 0.2	1.9 ± 0.0	31.8 ± 0.1
C8	Reconstruction $P_{gof} \geq 0.10$	425.8 ± 0.7	20.5 ± 0.1	4.8 ± 0.0	41.2 ± 0.1
C9	$N_{b-tag} \geq 2$	15.5 ± 0.1	5.97 ± 0.08	38.4 ± 0.6	45.3 ± 0.1
C10	$\langle \Delta\phi(b, W) \rangle < 2.0$	9.58 ± 0.10	4.08 ± 0.06	42.6 ± 0.8	59.3 ± 0.1

Figure 7.3 aims to highlight the individual power of each event selection cut in isolation. The solid lines correspond to the final values in the right-most bin of the plot in Figure 7.2 – they represent the final event yields for data and each $t\bar{t}$ process as well as the final signal fraction following all cuts. The dashed lines show the final event yields or estimated signal fraction in the case that the corresponding cut were omitted, but where all prior and subsequent cuts are still applied. The most striking of these is the requirement that there be at least two b-tagged jets in a selected event; the failure to include this cut would result in a final signal fraction of roughly 5%. The only cut which seems to have a detrimental effect on the signal fraction is the offline p_{T} cut of 60 GeV on the fifth jet, though as will be shown, such a cut is required on the 5^{th} jet p_{T} in order to be in the trigger efficiency plateau.

It should be noted that the final two event selection cuts C9 and C10 are unique in that they will be further employed as the two uncorrelated variables for the purposes of the background estimation which will be presented in Chapter 9.

Following the application of all event selection cuts, distributions of the final observables of interest can be produced, with the expectation that a signal peak will be clearly visible in the data distributions.

The total **signal efficiency** (ε_{signal}), evaluated from simulation, is defined as the fraction of weighted signal events passing all event selection criteria relative to the total initial number of weighted simulated signal events. The signal efficiency was found to have a value of approximately 0.2% – only two out of every thousand simulated all-hadronic $t\bar{t}$ events pass all selection requirements and are subsequently used to fill the final distributions of interest. This is significantly lower than the signal efficiencies attainable in the other $t\bar{t}$ decay channel analyses due to the tight selection cuts in the all-hadronic channel, though such stringent cuts are required in order to bring $S/(S+B)$ to a level sufficiently high so as to be able to clearly discern the signal above the otherwise dominant multi-jet background.

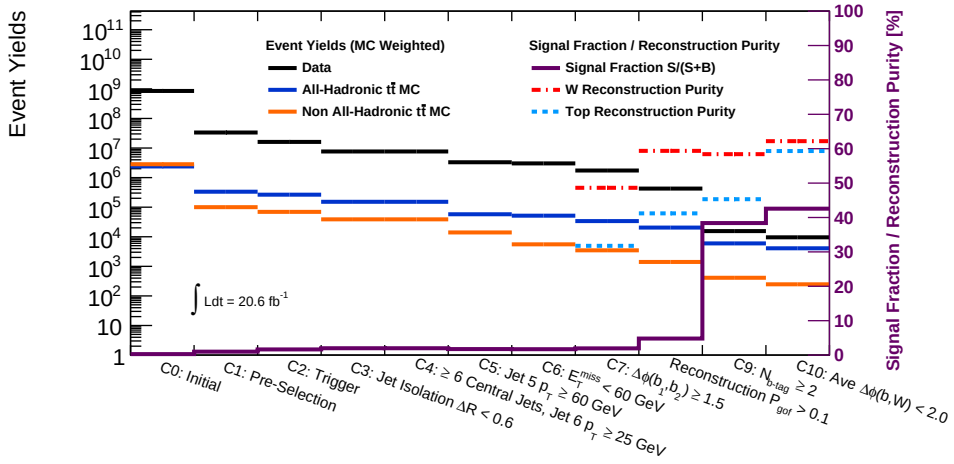

Figure 7.2: Summary of event yields for both signal and background processes following the application of each event selection cut. Dashed lines correspond to the top and W reconstruction purities, and the solid magenta line to the estimated signal fraction, as described in the text. The scale of the reconstruction purities and signal efficiency are shown on the right-hand axis.

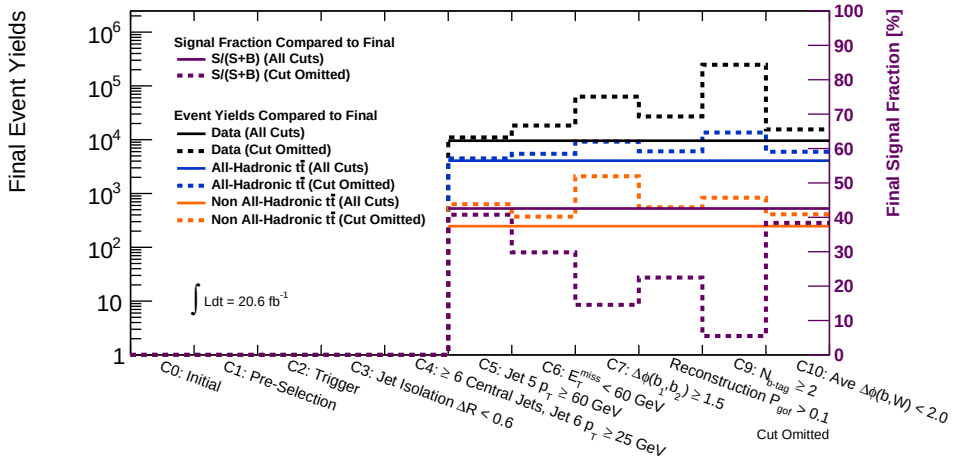

Figure 7.3: Summary highlighting the individual discriminating power of each event selection cut as described in the text. The solid lines correspond to the final event yields for each process, whereas dashed lines show the final event yields in the case that the corresponding cut were omitted.

7.4 Descriptions of Event Selection Cuts

7.4.1 Motivation Using Normalized Shape Comparisons

The event selection cuts are motivated by the distributions of Figure 7.4, which show the normalized shapes of several key discriminating variables for three relevant categories of events: all-hadronic $t\bar{t}$ signal events, non all-hadronic $t\bar{t}$ background events, and QCD multi-jet background events. The all-hadronic signal events are further split into two categories based on the jet-quark associations: events in which both reconstructed top quark candidates have the correct jet-quark associations and those for which at least one is incorrect, based on the classifications in Section 6.3. Signal events falling in the third permutation classification category of non-matched cases are not included for the purposes of filling these histograms.

All distributions were filled at an identical point in the event selection, specifically requiring events to satisfy cuts C1 through C4, to be described below. This point in the cut flow (C4) corresponds to a six-jet requirement, and it was selected solely for the purposes of the top reconstruction – six jets are required for it to be run with a meaningful output. With this requirement, the χ^2 top reconstruction algorithm can be executed in order to set the jet-quark associations and reconstruct the two top quark candidates for each event.

At this early point in the event selection, the data should still be expected to consist predominantly of QCD multi-jet events, with only a modest contribution (on the order of $\sim 2\%$) from $t\bar{t}$ signal events[9]. As such, the normalized shape of the data distributions can be expected to be representative of the QCD multi-jet background shapes. The value of 2% is made solely to validate the use of the data to infer the shapes of the QCD distributions and has no further effect on the analysis.

As additional cuts are made, these normalized shapes will change, as it is expected that there is recognizably some level of overlap between the cuts. The distributions as shown, frozen at a certain point in the cut flow, nonetheless provide the motivation for the cuts to be applied. By drawing the normalized distributions after each successive cut, although one would be able to observe the individual discriminating power of each sequential cuts, the signal contribution to the data events would get larger and larger, thereby rendering the assumption above less valid – the normalized shapes of the data distributions would no longer serve as a good reflection of the QCD multi-jet shape. A common point in the cut flow for all plots is used for this reason.

In what follows the individual event selection cuts are described step-by-step. In the context of the analysis framework and from a technical standpoint, only those events passing the first of such cuts denoted as a pre-selection (C1), which comprises a number of basic requirements, are included in the slimmed datasets stored locally and on which the main analysis is run.

[9]The signal contribution is estimated from the all-hadronic Monte Carlo samples normalized to their production cross sections and the total integrated luminosity for the 2012 dataset.

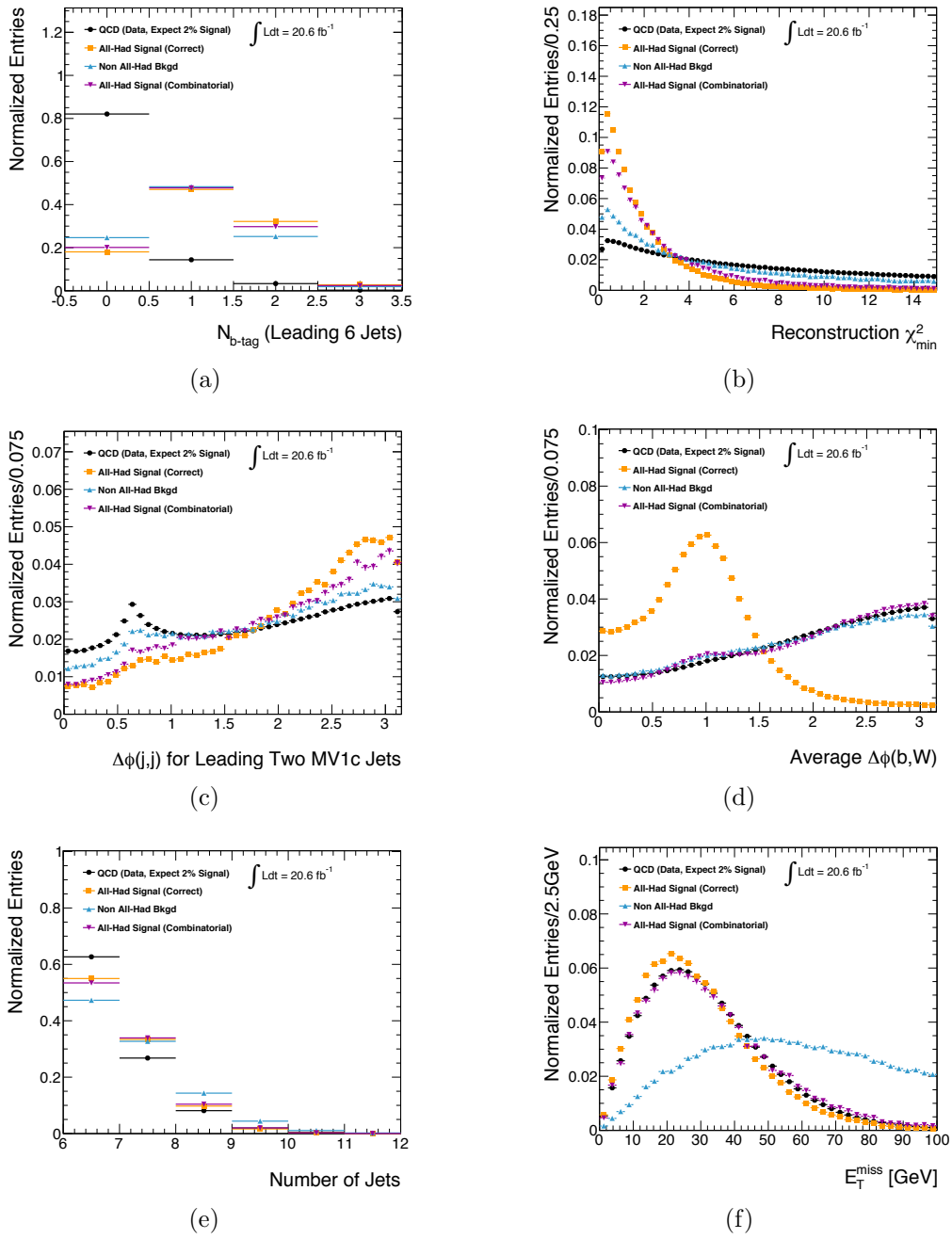

Figure 7.4: Comparisons of normalized distributions of several discriminating variables.

The exact cut values employed were determined by means of a series of optimization studies carried out at a later stage of the analysis. Such studies aimed to find the optimal tradeoff

between signal efficiency and signal fraction in the final distributions used for the measurement of the top quark mass – making tighter event selection cuts leads to a reduction in the overall statistics, thereby potentially increasing the statistical uncertainty, but also a higher concentration of signal events relative to background events which can improve the precision of the measurement. The selected cut values were found to yield the smallest overall uncertainty on the final measured value of m_{top} based on simulation. The uncertainties include those of statistical nature but also a number of sources of systematic uncertainty which will be presented in detail in Chapter 11.

7.4.2 Pre-Selection (C1)

Data events are required to correspond with a run included in the so-called **good run list**, thereby requiring a minimum set of standards to be satisfied with regards to detector performance during data-collecting. All events are further required to have a primary vertex with a minimum of five associated tracks, where the primary vertex in an event is defined as a vertex with the highest scalar p_{T}^2 sum for matched tracks. Events with one or more high-p_{T}, isolated leptons (electrons or muons as defined above) are vetoed, thereby forming an orthogonal dataset to that used in semileptonic or dileptonic $t\bar{t}$ analyses with $\sqrt{s} = 8$ TeV data where a requirement is made that there be at least one such lepton. The lepton objects are defined identically for ATLAS analyses of the three main $t\bar{t}$ decay channels.

Finally, events must pass at least one of the various unprescaled triggers considered for the analysis[10], including but not limited to that described in the following event selection cut.

7.4.3 Trigger and Offline p_{T} Requirement (C2)

The analysis makes use of a multi-jet trigger requiring at least five reconstructed jets with a p_{T} threshold of 55 GeV and pseudorapidities within $|\eta| < 3.2$ at the event filter level. Since event filter jets and those reconstructed offline employed in the analysis differ in their energy response, an offline p_{T} cut of 60 GeV on the fifth jet (in descending order of p_{T} for all the jets in a given event) is made in order to reach the trigger efficiency plateau region in the trigger turn-on curve visible in the plot in Figure 7.5. The plot was produced using the full set of ten million simulated all-hadronic $t\bar{t}$ signal events, and shows the trigger efficiency – the fraction of events satisfying the trigger requirement out of the total number of events – as a function of the fifth jet p_{T}. The jet isolation cut (C3), to be explained below, was the only significant cut also applied to produce the trigger efficiency plot; a failure to apply this cut yields a lower efficiency plateau value.

[10]The reason for the trigger requirement is in part a technical one – initially it was not clear which event filter trigger object would be selected for the analysis, and events firing any of the relevant triggers were kept beyond the slimming process in order to perform trigger efficiency comparison studies.

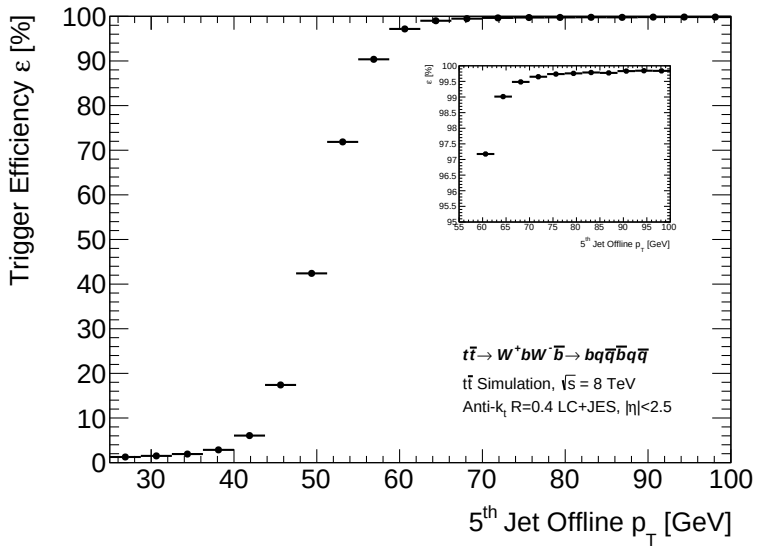

Figure 7.5: The trigger efficiency as a function of the 5^{th} jet offline p_{T}. The plot is filled using the full set of simulated MC all-hadronic $t\bar{t}$ signal events with only the jet isolation requirement (C3) cut applied. The inset figure shows a sub-range of the full plot beginning in the vicinity of the offline p_{T} cut selected for the analysis (C5); the horizontal and vertical axes represent the same quantities as in the case of the main figure. The values for the black markers were evaluated as the fraction of weighted signal events for which the trigger was fired divided by the total initial number of weighted events.

The five-jet trigger employed in the present analysis is denoted **EF_5j55_a4tchad_L2FS** following the naming scheme for ATLAS trigger items. The prefix **EF** corresponds to the fact that the trigger is at the event-filter level – the final stage in the three-level triggering system used by ATLAS. The **5j55** denotes the requirement of five jets above a p_{T} threshold of 55 GeV. This event-filter requirement was seeded by the requirement of four online L1 jets[11] satisfying $p_{\mathrm{T}} > 15$ GeV. The **a4tc** in the trigger name means that the trigger jets were reconstructed using an anti-k_T algorithm, with **had** to denote that the jets were calibrated at the hadronic scale *via* the weighting of their constituent energy clusters. Finally **L2FS** corresponds to a full calorimeter scan in contrast with only a partial or regional scan **PS** used by some trigger items.

A small number of alternative triggers were considered, including a b-jet trigger with a lower p_{T} threshold, and a marginally higher signal efficiency. It was decided to avoid such a trigger since its inclusion, particularly in regards to the b-tagging requirement, could introduce unwanted correlations which would adversely affect the performance of the background estimation method to be introduced in Chapter 9. The five-jet trigger selected represents the un-prescaled trigger with the lowest-p_{T} threshold of those available for 2012 data-taking.

7.4.4 Jet Isolation (C3)

An angular isolation cut requiring $\Delta R > 0.6$ between all possible pairs of jets was included in the event selection in order to ensure a flat plateau region in the trigger efficiency turn-on curve; the failure to include such a requirement was shown to have detrimental effects on efficiency, particularly at higher p_{T} values. When angular separations between jets are allowed to be

[11] Refer to the description of the ATLAS trigger system in Section 3.2.8.

smaller, a degree of cross-talk can occur during the reconstruction of nearby jets due to the potential to share constituents. This is to be avoided in the context of optimal energy response performance. Requiring the jets to be well isolated ensures a flat trigger efficiency above a certain threshold which does not decrease at higher transverse momentum.

7.4.5 Six Central Jet Requirement (C4)

The χ^2 reconstruction algorithm, which sets the jet-quark associations by identifying the permutation of jets which best matches the topology of all-hadronic $t\bar{t}$ events, requires a minimum input of six jets. As such, events are required to have six, well reconstructed jets above an offline p_{T} threshold of 25 GeV. Since the jets in $t\bar{t}$ events tend to be more central and since larger numbers of forward jets can be attributed to residual effects of pile-up in the forward region, the six jets are each required to be in the central region, by requiring $|\eta| < 2.5$, though this requirement was already in place in the object definition.

7.4.6 Five Central Jet and Offline p_{T} Requirement (C5)

In order to reach the plateau region of the trigger efficiency curve, described earlier and shown in Figure 7.5, an offline p_{T} requirement is placed on the fifth-leading jet ordered in p_{T}, requiring it to have a minimum transverse momentum of 60 GeV. The minimum p_{T} requirement of the sixth jet remains at 25 GeV. Employing such a cut has the detremental effect of cutting a large number of signal events with a fifth jet that fails to reach the p_{T} threshold of 60 GeV, though a roughly equal fraction of QCD background events are cut out in the process, thereby retaining a stable signal-to-background ratio.

7.4.7 Missing Transverse Energy (C6)

All-hadronic and non all-hadronic $t\bar{t}$ events are similar in that both are characterized by a high jet multiplicity, and both are expected ideally to have two jets initiated by bottom-flavoured quarks. Non all-hadronic events however exhibit two distinguishing features not present in all-hadronic $t\bar{t}$ events. The first feature is the presence of at least one high-p_{T} isolated lepton as previously mentioned; the requirement that there be no such leptons identified in an event greatly suppresses the contribution from such processes. The second feature of non all-hadronic events is a large amount of missing transverse energy due to the neutrino from the leptonic W decay. In the case that the lepton from a non all-hadronic event is misidentified as a jet or if it simply fails to satisfy the tight requirements of a lepton as per the object definition, the event can easily be expected to pass the selection up to this point. It is therefore important to make a cut on the missing transverse energy.

Figure 7.4(f) shows the normalized shapes of the $E_{\mathrm{T}}^{\mathrm{miss}}$ variable. One can clearly see the contrasting shape of non all-hadronic $t\bar{t}$ events which on average extend to far greater $E_{\mathrm{T}}^{\mathrm{miss}}$ values than in the case of other processes. A requirement is made that the event satisfy $E_{\mathrm{T}}^{\mathrm{miss}} < 60$ GeV, which significantly reduces the non all-hadronic $t\bar{t}$ background, while cutting away a minimal fraction of both the signal and QCD multi-jet events.

7.4.8 Gluon Splitting ($g \to b\bar{b}$) Suppression (C7)

In the rare case that a QCD multi-jet event contains a jet initiated by a bottom-type quark, it is often the result of gluon splitting *via* $g \to b\bar{b}$. Gluons are massless and bottom-type quarks have a mass of the order of 4.2 GeV [3]. If the gluons are at an energy that far exceeds the threshold energy to produce two bottom-flavoured quarks, the angular separation between the decay products can be expected to be small. Examination of the normalized shapes in Figure 7.4(c) showing the azimuthal separation between the two leading MV1c-ranked jets in an event, shows a more pronounced spike for QCD events at a separation of approximately $\Delta\phi(j,j) \sim 0.6$ which is likely the result of such $g \to b\bar{b}$ events. It should be noted that the jet isolation requirement (C3) was enforced prior to producing the normalized shapes in this figure, which is the reason for the apparent drop at lower $\Delta\phi$ values. This drop is present not only for the QCD events but for all processes.

In order to suppress contributions from the QCD multi-jet processes, the two leading b-tagged jets[12] are required to be separated in $\Delta\phi$ by more than 1.5. The choice of $\Delta\phi$ over ΔR was made in order to reduce the likelihood of introducing η-dependent correlations which could adversely affect on the background estimation method. Both variables however have similar discriminating power to separate signal and background.

7.4.9 Top Reconstruction Goodness of Fit (C8)

The analytic χ^2 minimization procedure presented in Chapter 6 aims to select the optimal permutation of six jets used to reconstruct the two top quark candidates for each particular event, as well as to designate which jets are to be associated to each of the W boson candidates. The method suppresses permutations in which the invariant masses of the two top quark candidates differ by a large amount, or in which the invariant mass of either of the two reconstructed W boson candidates differs greatly from the reference m_W value based on the expected detector response. Nevertheless, all events satisfying at least the six central jet requirement will yield a minimum χ^2 value, and will thus necessarily lead to two reconstructed top quark candidates, regardless of how large that minimum χ^2 value may be.

In order to place a quality cut on the minimum χ^2 obtained, one looks to the results of the χ^2 method performance on all-hadronic $t\bar{t}$ signal events from Section 6.5, where a particular χ^2

[12] *i.e.* the two jets with the highest MV1c value, regardless of whether or not they pass the b-tagged threshold

value was translated to a goodness-of-fit probability, P_{gof}, based on the fact that the χ^2 variable, in the case of correct jet-quark associations, can be expected to follow a χ^2 distribution with three degrees of freedom.

Events are required to have a goodness-of-fit probability of $P_{gof} > 10\%$ for the selected permutation, or equivalently a minimum χ^2 value satisfying $\chi^2_{min} < 6.2514$. Such a requirement rejects only a small number of events in which both top quarks were correctly reconstructed, whereas a significantly larger fraction of incorrectly reconstructed signal events lie in the upper tail regions of the minimum χ^2 distribution shown in Figure 7.4(b). In addition to the removal of many combinatorial background events, this cut further suppresses a comparatively larger fraction of QCD multi-jet events.

The requirement of this P_{gof} quality cut thereby requires events to have a topology consistent with that of all-hadronic $t\bar{t}$ events.

7.4.10 Number of Tagged Jets (C9)

Perhaps the most distinguishing signature of top quark decays is the presence of jets initiated by bottom-type quarks due to the branching ratio of very close to 100% for the top quark decay process $t \to Wb$. As such, $t\bar{t}$ events are often characterized by a higher number of b-tagged jets – two in an ideal case – whereas in QCD multi-jet events, the production of b-quark initiated jets is, by comparison, extremely rare.

Events are therefore required to have a minimum of two b-tagged jets in the central region, as identified by the MV1c b-tagging algorithm presented in Section 4.4.2. It is important to note that only jets up to the sixth jet, ordered in p_{T}, are considered for this requirement. The reason that no jets past the sixth jet are considered for this cut is due to a subtlety in the background estimation method to be outlined in Chapter 9. The inclusion of any jets in this sum, even those beyond the sixth jet ordered in p_{T}, introduces a correlation between the total number of tagged jets in an event and the overall jet multiplicity which would consequently not allow the jet multiplicity to be well modelled based on the employed background estimation technique.

Since the production cross-section for QCD multi-jet events is so large, although this b-tagging requirement cuts a sizeable fraction of the background, a significant number of such events remain. They will consist of multi-jets with true bottom-flavoured quarks due to processes such as gluon splitting, or lighter-flavoured quarks mis-tagged as b-jets.

7.4.11 Angular Separations of Reconstructed Objects (C10)

Although the present analysis searches for $t\bar{t}$ pairs which decay in the resolved regime, meaning that the boosts of the top quarks are sufficiently low that their decay products often initiate three fully resolved and isolated jets, correctly reconstructed signal top quarks often exhibit the quality that their associated W-b pair are relatively close in angular separation. A requirement is

placed on the average azimuthal separation between the constituents of the two reconstructed W-b pairs, namely to require that the average separation of such objects satisfy $\langle \Delta\phi(W, b) \rangle < 2.0$. Such a requirement limits the ability of reconstructed candidate $t\bar{t}$ pairs from QCD events or from wrongly reconstructed true $t\bar{t}$ pairs to fake correctly reconstructed signal $t\bar{t}$ pairs based solely on a sufficiently high P_{gof} value. The analytic χ^2 reconstruction algorithm selects jet-quark associations for a given event based on invariant mass quantities alone, so this kinematic cut aids to greatly suppress the contributions from all backgrounds as can be seen in Figure 7.4(d).

Chapter 8

Signal Templates of the $R_{3/2}$ Observable

8.1 Template Method Overview

The value of the top quark mass m_{top} was is present in expressions such as that for the total $t\bar{t}$ production cross-section, $\sigma_{t\bar{t}}$, shown in Equation 2.6. Its presence in this and other expressions illustrates the fact that the value of m_{top} plays an important role in dictating the final-state kinematics of all-hadronic $t\bar{t}$ signal events.

In light of this fact the true value of the top quark mass is required to generate simulated $t\bar{t}$ events that are most likely to provide the best agreement between data and simulation, the contributions from background notwithstanding. An equivalent statement is that the use of an incorrect value of the top quark mass for generating the simulated signal datasets would yield large disagreements between data and simulation in distributions of quantities most sensitive to the value of m_{top}. On the other hand it is precisely the value of the top quark mass that is to be measured; one cannot assume a top quark mass *a priori* with which ideal $t\bar{t}$ samples are to be generated. Indeed it is this very aspect that is exploited in employing a so-called **template method** to extract the value of m_{top}.

Template methods have proven to be an effective means to measure the top quark mass in a number of measurements, including several key analyses using $t\bar{t}$ events from ATLAS data in all three decay topologies [35, 36, 79]. In these analyses, samples of simulated signal events are produced for a discrete number of evenly spaced generator-level top quark masses in the vicinity of the current world average m_{top} value. In this way, it is possible to produce distributions of final-state observables for each $t\bar{t}$ signal sample – template distributions – each with a given input m_{top} value, and compare these in a quantitative way to the final distributions observed in data, thereby providing a means to gauge which interpolated value of m_{top} between the various generated samples exhibits properties most like those observed in the data.

Provided the top quark mass is the dominant unknown ingredient in the simulation process, one can treat any differences between the m_{top} samples as sensitivities to the top quark mass

and thus exploit such differences to infer the value of m_{top} from the data. The selection of an observable highly sensitive to the true value of m_{top} is thus an essential step in analyses employing a template method.

The present analysis makes use of seven simulated all-hadronic $t\bar{t}$ samples with m_{top} values spaced at even 2.5 GeV intervals from 165 to 180 GeV. The 172.5 GeV m_{top} sample, with a top quark mass closest to the current world average value, is taken as the nominal and central working point. A total of ten million simulated events were produced for this 172.5 GeV point (in addition to the 60M events used for the nominal simulated dataset), while four million events were simulated for each of the remaining six m_{top} points.

8.2 $R_{3/2}$ as the Top Quark Mass-Sensitive Observable

The three-jet invariant mass m_{jjj}, corresponding to the invariant mass of a given reconstructed top quark candidate is the obvious choice for an observable to determine the true top quark mass, given that the shape of the m_{jjj} distribution in signal events should exhibit a very strong sensitivity to the value of m_{top}. The m_{jjj} observable suffers, however, from a strong sensitivity to the uncertainties in the **Jet Energy Scale** (JES)[1] which will propagate to uncertainties in the final measurement of m_{top}: shifting the JES up or down will result in a significant corresponding upward or downward shift in the m_{jjj} distribution.

In an effort to mitigate this sensitivity to the JES systematic uncertainty, a different observable, $R_{3/2}$, was selected to build the signal templates for the purposes of performing the top quark mass measurement. The $R_{3/2}$ observable is defined as the ratio of the three- to two-jet invariant mass, namely:

$$R_{3/2} = m_{jjj}/m_{jj} \tag{8.1}$$

with the m_{jjj} and m_{jj} values corresponding to the invariant masses of associated top quark and W boson candidates, respectively. $R_{3/2}$ is thus defined for each reconstructed top quark - W boson pair and there are consequently two reconstructed $R_{3/2}$ values per event.

The $R_{3/2}$ observable has the advantage that uncertainties in the jet energy scale should be expected to largely cancel out due to a similar sensitivity in both the numerator and denominator, while the sensitivity to m_{top} remains similar to that of the m_{jjj} observable. The invariant W boson mass m_{jj} term in the denominator should be expected to depend only very weakly on the mass of the top quark – weakly in the sense that the kinematics for different top quark masses can lead to detector-related differences in the measured value of m_W, even though differences from the true value of m_W itself recognizably do not exist for differing values of m_{top}. Normalized distributions of the reconstructed $R_{3/2}$ observable filled using all events from a selection of

[1]For a reminder of the absolute JES correction to reconstructed jet four-vectors, refer to Section 4.6.3.

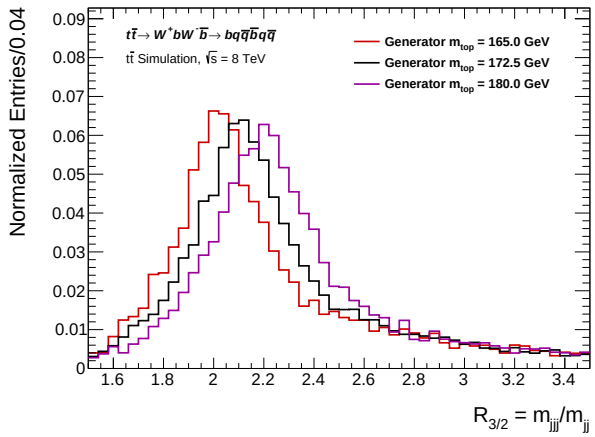

Figure 8.1: Normalized shapes of the reconstructed $R_{3/2}$ observable from simulated signal samples for three selected generator m_{top} input values. The distributions were filled twice per event following the application of all event selection cuts. A strong sensitivity to the top quark mass can be observed in the shapes of the distributions.

simulated signal datasets are shown in Figure 8.1. The generator value of the top quark mass in each of these samples ranges from 165 GeV to 180 GeV as shown in the accompanying legend. These distributions for $R_{3/2}$ are similar to those shown in Fig. 5.3 which were also produced in searching for potential observables with a strong sensitivity to m_{top}.

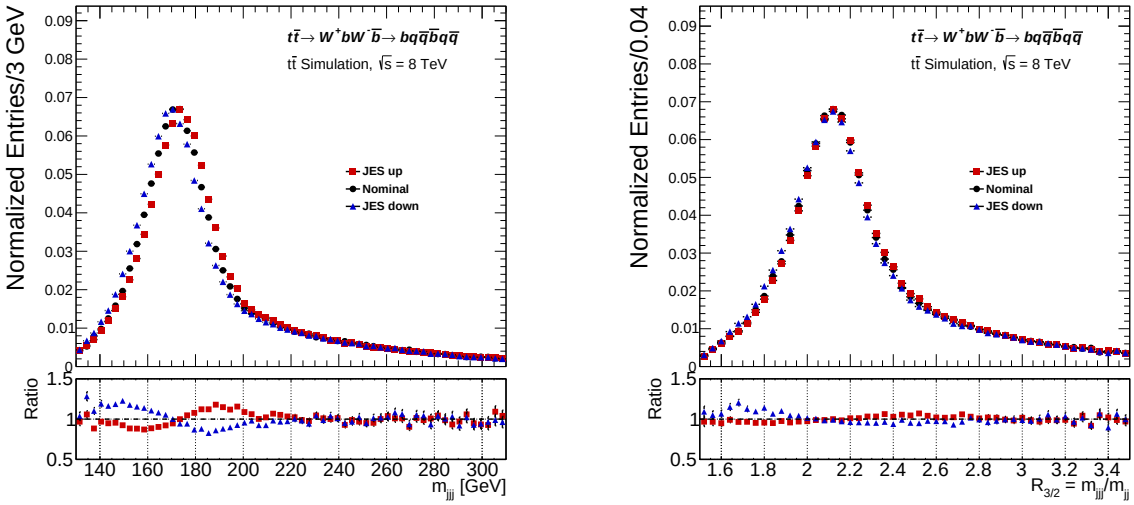

(a) Reconstructed m_{jjj}

(b) Reconstructed $R_{3/2}$

Figure 8.2: Sensitivity of the m_{jjj} and $R_{3/2}$ observables to a global upwards and downwards shift in the jet energy scale (JES). An upwards and downwards shift in this case corresponds to a 1-σ shift up or down respectively prior to the JES being applied to the reconstructed jet four-vectors, where σ in this case corresponds to the overall η- and p_{T}-dependent JES uncertainty. The ratio plots are produced for the up/down variations relative to the nominal case.

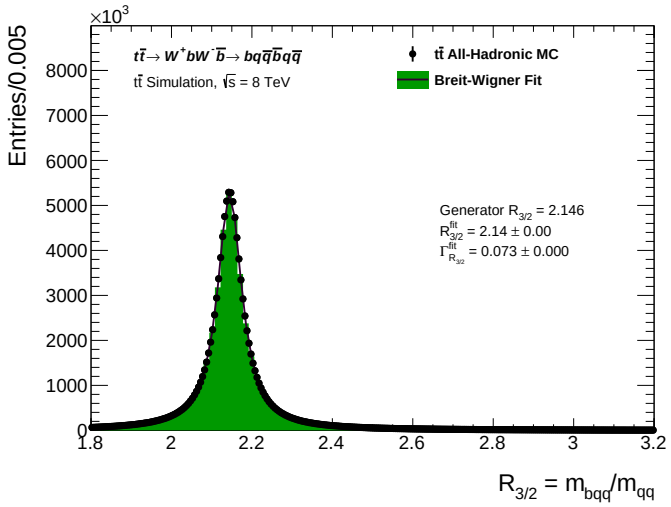

Figure 8.3: Distribution of the reconstructed $R_{3/2}$ observable for the nominal 60M fast-simulation signal samples with generator m_{top} = 172.5 GeV. In order to fill the distribution, the top quarks and W bosons were reconstructed from the quarks themselves from the truth record. Only minimal event selection cuts were applied.

In earlier studies both the m_{jjj} and $R_{3/2}$ observables were considered separately as candidates for the m_{top}-sensitive observable. The results of these studies, as well as the normalized distributions shown in Figures 8.2(a) and 8.2(b), confirm the hypothesis of the varying level of JES sensitivity for the two observables. The plots were produced using simulated signal events following the full event selection requirements. The global up and down shifts in these plots correspond to $p_{\mathrm{T}}-$ and η-dependent shifts in the absolute JES factor applied to correct the jet energy and momentum. In this case both the energy and momentum of each jet are scaled up or down by a modified factor of 1-σ based on the JES uncertainty for the η and p_{T} range corresponding to that particular jet . The identical set of simulated signal events were used in both the nominal and the shifted cases.

It is of the $R_{3/2}$ observable that signal template shapes are constructed for the various input top quark mass samples in this analysis. Since there are two candidate top quarks reconstructed for a given event, distributions of this observable are filled, as they were with m_{jj} and m_{jjj} variables, twice per event. The $R_{3/2}$ observable was previously used successfully in a top quark mass measurement made in the all-hadronic $t\bar{t}$ channel with ATLAS using the $\sqrt{s}$= 7 TeV data collected in 2011 [79].

8.3 Parameterization of $R_{3/2}$ Signal Template Shapes

One can speak of different levels of reconstructed $R_{3/2}$ values analogously to the categorizations of reconstruction levels of top quark candidates depicted in Figure 6.1. As the $R_{3/2}$ observable is constructed from the invariant mass ratio of a top quark and its associated W boson, the reconstruction level of each $R_{3/2}$ candidate is implied by the level of reconstruction of its associated top quark candidate.

A Breit-Wigner function provides a suitable parameterization for the parton-level $R_{3/2}$ distribution[2], as is shown in Figure 8.3.

Ultimately one is interested in the reconstruction-level distributions of the $R_{3/2}$ observable[3] where the invariant m_{jjj} and m_{jj} terms originate from the reconstructed top quarks and W bosons based on the jet-quark assignment from the top reconstruction algorithm presented in Chapter 6; this is comparable to what one might expect from data events without the presence of any background. Figure 8.4(a) shows the reconstruction-level distribution from simulated signal events and one should immediately be reminded of the purity decomposition distributions for m_{jj} and m_{jjj} which were shown in Figures 6.6(a) and 6.6(b); indeed, the distribution is constructed in an identical manner with the exception that in the present case, events were required to pass the full event selection prior to filling the histogram. Consequently there is a prominent increase in the fraction of correctly reconstructed objects compared with the earlier distributions for m_{jj} and m_{jjj} – a result of some of the event selection cuts employed exactly for this purpose.

The same $R_{3/2}$ distribution[4], but constructed from an indepdendent, smaller set of simulated signal events, is shown in Figure 8.4(b) with the major difference that rather than showing the permutation category decomposition, a fit is performed and the resulting parameterization – the sum of a Gaussian and a Landau function – overlaid both for the total function and its two constituent functions separately. The choice of the Gaussian and Landau functions is not physically motivated, nor are the two separate functions meant to represent the three permutation classifications; they were selected for the simple reason that they provide a reasonably good description of the combined shape of the $R_{3/2}$ observable following all event selection cuts[5].

[2]See for comparison the parton-level distributions of both m_{jjj} and m_{jj} in Figure 6.2

[3]In other words those for which a selection of normalized distributions were shown in Figure 8.1

[4]This second distribution shown in Figure 8.4(b) is very similar, but not identical, to the the distribution shown in Figure 8.4(a). The distribution in Figure 8.4(b) is filled using the 10M fast-simulation events used to build the signal templates of the $R_{3/2}$ observable whereas the distribution in Figure 8.4(a) is produced using the 60M signal events from the nominal sample. While both sets of simulated samples correspond to all-hadronic $t\bar{t}$ events, there are differences present in the simulation parameters. The lower-statistics sample is used in building the templates in order to match the same simulation parameter choices for the remaining six m_{top} samples.

[5]An initial attempt was made in order to find a functional form to describe each of the three permutation categories separately. This resulted in too many parameters and as a result the fitting procedure was prone to fluctuations in the final extracted parameter values despite the fact that this resulted in a good fit overall in the case of a successful minimization.

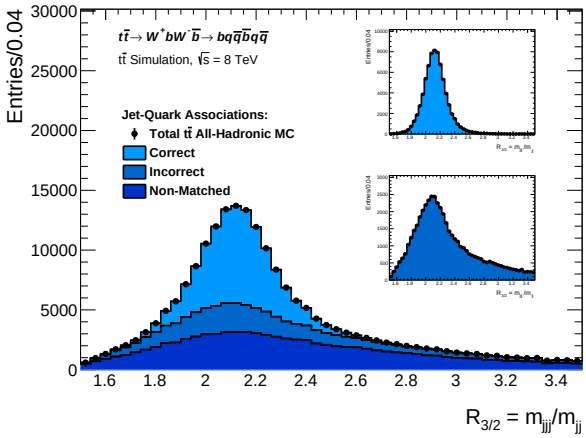

(a) Reconstructed-level $R_{3/2}$ distributions after full event selection has been applied. The three different permutation classifications, as defined in the text, are shown as stacked distributions. The upper and lower insets show the correct and incorrect permutation cases separately in order to compare their shapes; the axis labels and horizontal range are unmodified from the main figure.

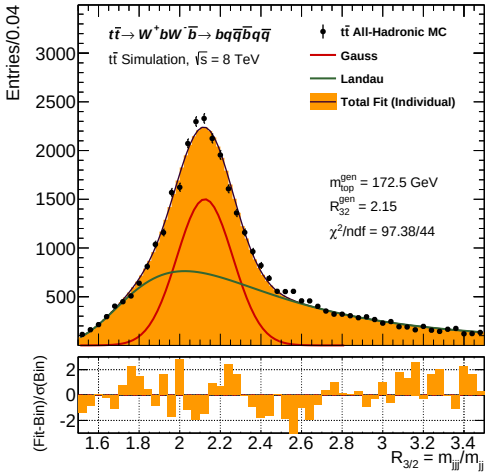

(b) Reconstructed-level $R_{3/2}$ distribution for the $m_{top} = 172.5$ GeV sample. Both matched and unmatched cases, as defined in the text, are shown as a single distribution as black markers. The total fit is shown in addition to the two-function decomposition.

Figure 8.4: Distributions of the reconstructed $R_{3/2}$ observable for the fast-simulation m_{top}= 172.5 GeV signal sample, where the top quarks and W bosons are reconstructed from jets based on the χ^2 event reconstruction. The distributions from simulated $t\bar{t}$ events in (a) and (b), described above, are similar, but were produced using different simulated datasets. In both cases the full set of event selection cuts were applied. The lower region in the right-hand plot shows the residuals for each bin – the difference between the fit and the bin content divided by the square root of the bin contents.

There are five parameters relevant to the sum of the Gaussian and Landau functions: the mean μ, and width σ of the Gaussian function (which will be designated by p_0 and p_1, respectively), the **most probable value** (MPV) μ_R and width σ_R of the Landau distribution which are relative to the Gauss terms[6] and are therefore designated as $p_0 \cdot p_3$ and $p_1 \cdot p_4$, respectively, and finally the Landau fraction f_L (p_2). A sixth parameter p_5, reflecting the overall normalization is included in the overall parameterization but is not relevant for the purposes of building a signal template shape.

The explicit functional form of the Gauss plus Landau parameterization is as follows, where

[6]The Landau MPV is relative to the mean of the Gaussian, such that the parameter p_3 is unique to the Landau shape, but is simpy a multiplicative factor; the full Landau MPV parameter is given by the product $p_0 \cdot p_3$. The width of the Landau is similarly defined to be a multiplicative factor relative to the width of the Gaussian.

the variable x corresponds to the $R_{3/2}$ observable:

$$\mu_S\left(x \mid \mathbf{p}\right) = \frac{p_5\left(1-p_2\right)}{p_1\sqrt{2\pi}} e^{-\frac{1}{2}\left(\frac{x-p_0}{p_1}\right)^2} + p_5 \cdot p_2 \; P_L(x \mid p_0 \cdot p_3, p_1 \cdot p_4) \tag{8.2}$$

In the above $P_L(x \mid m, \sigma)$ is meant to represent the normalized probability distribution for a Landau function[7] for the variable x with most probable value m and width parameter μ. To express this in an alternative manner, assuming $P_G(x \mid \mu, \sigma)$ to be the normalized probability distribution for a Gaussian function for the same variable x and with mean parameter μ and width parameter σ, Equation 8.2 can be written more simply as:

$$\mu_S\left(x \mid \mathbf{p}\right) = p_5\left(1-p_2\right) P_G(x \mid p_0, p_1) + p_5 \cdot p_2 \; P_L(x \mid p_0 \cdot p_3, p_1 \cdot p_4) \tag{8.3}$$

This highlights the role played by the Landau fraction parameter p_2 in dictating the relative contributions of the Gauss or Landau shapes. The same Gauss plus Landau fit is performed separately on the $R_{3/2}$ distributions generated from the remaining six m_{top} signal samples, and the distributions are shown, together with overlaid fit results, in the plots in Figure 8.5. In performing the least-squares fit, the bin position containing the maximum bin content is taken as the starting value of the Gauss mean parameter. Some loose constraints are placed on the parameter values in order to facilitate convergence in the minimization procedure.

[7]The Landau portion of the expression is not given explicitly. For an analytic expression see [80].

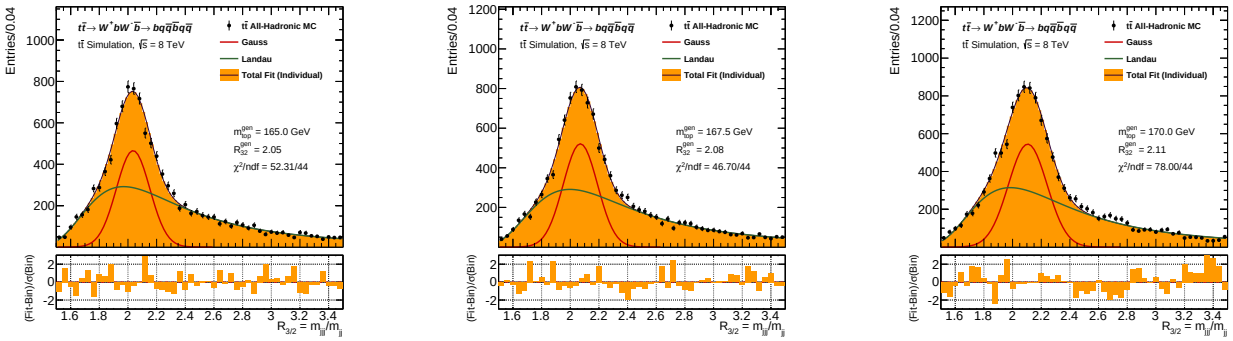

(a) $m_{top} = 165$ GeV

(b) $m_{top} = 167.5$ GeV

(c) $m_{top} = 170$ GeV

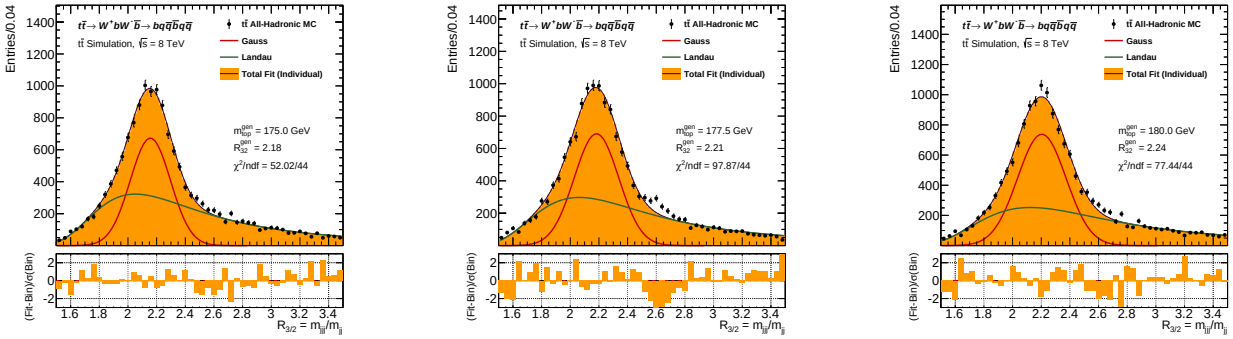

(d) $m_{top} = 175$ GeV

(e) $m_{top} = 177.5$ GeV

(f) $m_{top} = 180$ GeV

Figure 8.5: Reconstructed $R_{3/2}$ distributions from the remaining simulated samples with top quark masses in the range of 165-180 GeV. Fits are performed to each distribution individually.

8.4 Extracted Signal Template Parameters

8.4.1 Extracted Parameters from Individual Fits

The fits performed on the histograms shown in the plots in Figure 8.5 describe the shapes of the $R_{3/2}$ distributions reasonably well. There are some notable exceptions giving rise to the larger χ^2/ndf values quoted, but these are mostly due to residuals of bins away from the peak position. As a next step, a general signal template can be built whereby trends in the evolution of these shapes can be identified and exploited. In order to do this, each of the extracted fit parameters described above is plotted separately as a function of the input generator m_{top}. Such a plot is shown for the parameter corresponding to the mean of the Gaussian function in Figure 8.6 and a clear linear trend is observed. Similar plots for the remaining four parameters are shown in Figure 8.7, and it can be seen that it is a valid assumption to make that each of the shape parameters also depends linearly, to first order, on the value of m_{top}.

A least-squares or χ^2 fit is next performed separately to each of these five plots under the assumption of such a linear m_{top} dependence. An intercept and slope are extracted for each shape parameter; a particular value of m_{top} will therefore fix the value of each of the five shape parameters p_0 through p_4; in other words for fixed slope and intercept values, a given value of m_{top} will correspond to a unique point on the red fit line in the plot in Figure 8.6 and those in Figure 8.7. All of the slope and intercept parameters are denoted $\{a_i\}$, where i ranges from 0 to 9; evenly numbered subscripts denote intercept terms and oddly numbered subscripts the slope terms. In assuming such a linear dependence on m_{top}, the number of signal parameters is consequently doubled from five to ten though with the advantage that the dependence on m_{top} is now encompassed in this parameterization.

The mean of the Gaussian function can, for example, be expressed in the form:

$$p_0 = a_0 + a_1 \, (m_{top} - 172.5) \tag{8.4}$$

where a_0 is the intercept term evaluated at the $m_{top} = 172.5$ GeV point, and a_1 the corresponding slope term. In general then, parameter p_i is given by:

$$p_i = a_{2i} + a_{2i+1} \, (m_{top} - 172.5) \tag{8.5}$$

where i runs from 0 through 4.

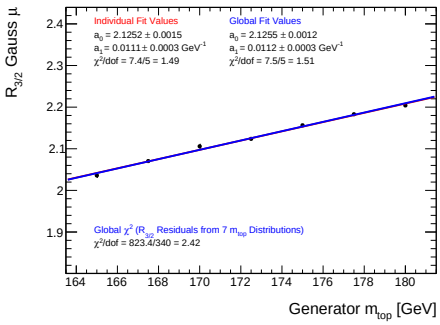

Figure 8.6: The Gaussian mean parameter for the seven $R_{3/2}$ distributions shown as a function of the generator m_{top}. The red line corresponds to the result of a fit to the seven points. The blue line corresponds rather to the slope and intercept parameters based on the global fit to be described in Section 8.4.2. As the results in both of these cases are similar, only the blue line is discernible.

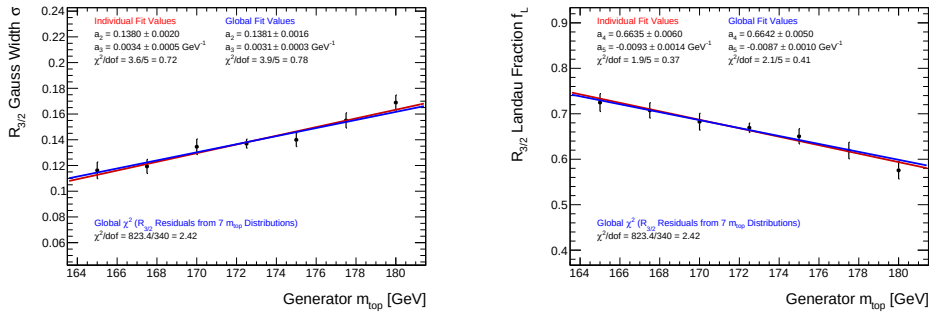

(a) p_1

(b) p_2

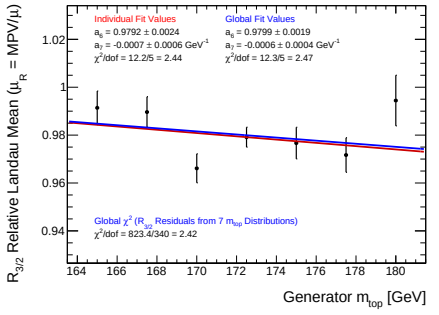

(c) p_3

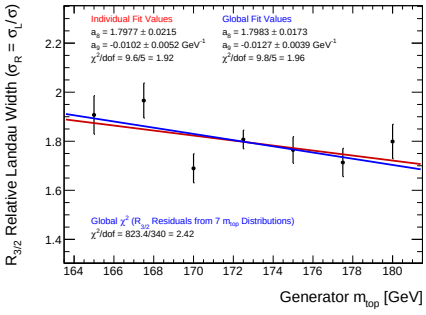

(d) p_4

Figure 8.7: The remaining parameter values from the signal shape fits to the $R_{3/2}$ distributions as a function of the generator m_{top} value. The plots correspond to the remaining four $R_{3/2}$ signal shape parameters and are analogous to that shown in Figure 8.6.

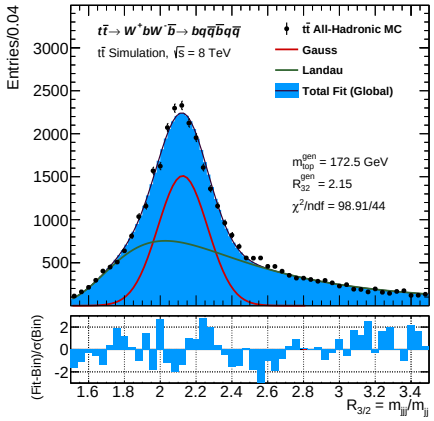

Figure 8.8: The reconstructed $R_{3/2}$ distribution with a shape determined from slope and intercept parameters $\{a_i\}$ from the global fit, interpolated for the particular value of $m_{top} = 172.5$ GeV.

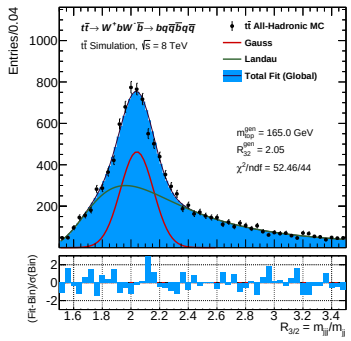

(a) $m_{top} = 165$ GeV

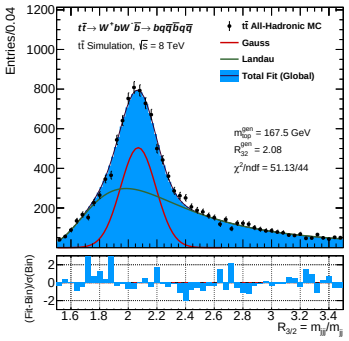

(b) $m_{top} = 167.5$ GeV

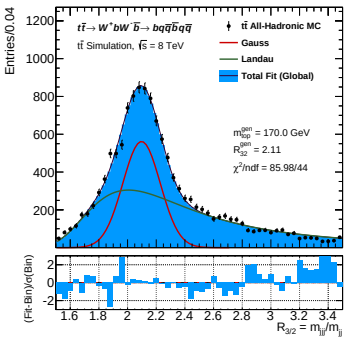

(c) $m_{top} = 170$ GeV

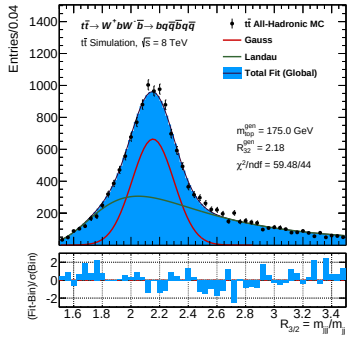

(d) $m_{top} = 175$ GeV

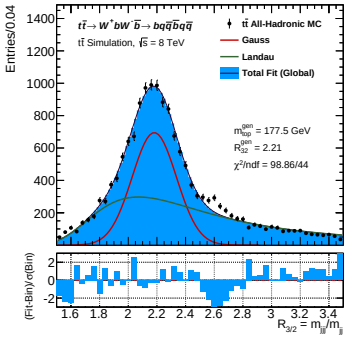

(e) $m_{top} = 177.5$ GeV

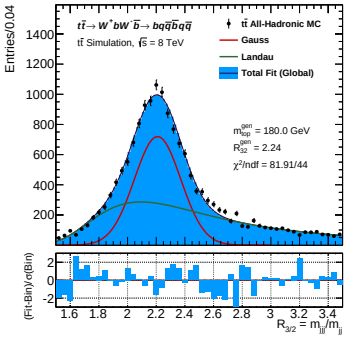

(f) $m_{top} = 180$ GeV

Figure 8.9: Distributions of reconstructed $R_{3/2}$ values with shape parameters are from the globally determined slope and intercept parameters $\{a_i\}$, based on the particular m_{top} value.

8.4.2 Extracted Parameters from a Global Fit

The individual linear fits described above properly account for the correlation between the slope and intercept values for each of the individual signal shape fit parameters, though in addition there should exist some non-zero level of correlation between all slopes and intercepts. Performing linear fits to each individual plot is a sensible first step, but the correlations between all fit parameters must also be taken into account to arrive at sensible values of the set of extracted parameters $\{\mathbf{a}\}$ which can be used to describe the full $R_{3/2}$ template shapes.

In order to account for these correlations, a global fit is performed to extract all ten slope and intercept values simultaneously. The resulting slope and intercept parameters from the individual linear fits are used as initial values in the global minimization. The global fit is performed *via* the minimization of a χ^2 variable defined as:

$$\chi^2 = \sum_{j}^{N_{samples}} \sum_{i}^{N_{bins}} \frac{\left(n_i^j - \mu_{s,i}^j\right)^2}{n_i^j} \tag{8.6}$$

where $N_{samples}$ is the number of different generator m_{top} samples, seven in total, and N_{bins} is the number of bins of the $R_{3/2}$ distribution. The value of N_{bins} was chosen to be 50. The n_i^j and μ_i^j terms represent the number of observed simulated entries and estimated number of entries from the parameterization, respectively, in bin i for the mass sample j. The $N_{samples} \times N_{bins}$ bin contents n_i^j thus represent, in effect, the data points for the purposes of the minimization.

The identical $R_{3/2}$ distribution for the 172.5 GeV m_{top} sample from the plot in Figure 8.4(b) is once again shown in Figure 8.8. The distribution is now displayed together with an overlaid shape described by the combined Gaussian and Landau functions but based now on the parameters from the global fit described above; the blue-filled distributions of the fits correspond to the set of five Gauss plus Landau shape parameters $\{\mathbf{p}\}$ interpolated from the blue lines in the plots in Figures 8.6 and 8.7 at an exact value of $m_{top} = 172.5$ GeV. Similar plots for the remaining six mass samples are shown in Figure 8.9.

Again the distribution and parameterized shape can be seen to be in relatively good agreement as can be observed from the residuals shown in the lower portion of the plots. While this may seem intuitive, it should be highlighted that using the same process of interpolating the five parameter values from the individual – rather than the global – linear fits yields a template shape which agrees very poorly with the $R_{3/2}$ distributions in all seven m_{top} samples[8]; this emphasizes the importance of proper treatment of correlations between the shape parameters.

[8] In other words, the parameters describing the $R_{3/2}$ shape can be interpolated from the red lines, rather than the blue lines, for the given m_{top} value and based on Figures 8.6 and 8.7. Since the first-order-polynomial fits, in the case of the red lines, were performed indepdently for each of the shape parameters, the resulting $R_{3/2}$ shape described differs greatly from the actual histogram bin contents.

8.5 Summary of Constructed Signal Templates

The extracted parameter values from both the individual and global fits to describe the signal $R_{3/2}$ shape are displayed in Table 8.1. The values in the two columns can be seen to agree within statistical uncertainties. Crucially however, the global fit takes into account that the dependence of each of the parameters on m_{top} are not independent. Moreover it allows for the extraction of a 10×10 covariance matrix, evaluated from the minimization procedure. This covariance matrix will subsequently play a small but important role in performing the final measurement. This will be presented in Chapter 10.

The end result is that a selected value of m_{top}, together with the fixed parameters $\{\mathbf{a}\}$, now sets the values of the parameters $\{\mathbf{p}\}$ and thus the normalized shape of the **probability density function** (PDF) for the signal $R_{3/2}$ distribution.

Table 8.1: Extracted fit parameters of the signal template shape of the $R_{3/2}$ observable. Shown are the values from both the individual and global fits. Evenly numbered subscripts correspond to the parameter values at $m_{top} = 172.5$ GeV (the intercepts), and oddly numbered subscripts correspond to parameter slopes *versus* m_{top}.

Parameter	Label	Individual Fit Value	Global Fit Value
p_0: Gauss Mean μ	a_0	2.1252 ± 0.0015	2.1255 ± 0.0012
	a_1	0.0111 ± 0.0003	0.0112 ± 0.0003
p_1: Gauss Width σ	a_2	0.1380 ± 0.0020	0.1381 ± 0.0016
	a_3	0.0034 ± 0.0005	0.0031 ± 0.0003
p_2: Landau Fraction f_L	a_4	0.6635 ± 0.0060	0.6642 ± 0.0050
	a_5	-0.0093 ± 0.0014	-0.0087 ± 0.0010
p_3: Landau MPV (Relative) μ_R	a_6	0.9792 ± 0.0024	0.9799 ± 0.0019
	a_7	-0.0007 ± 0.0006	-0.0006 ± 0.0004
p_4: Landau Width (Relative) σ_R	a_8	1.7977 ± 0.0215	1.7983 ± 0.0173
	a_9	-0.0102 ± 0.0052	-0.0127 ± 0.0039

Chapter 9

Background Modelling Using the ABCD Method

9.1 QCD Multi-jet Background Estimation

One of the greatest challenges in analyses searching for fully hadronic decays of $t\bar{t}$ pairs stems from the significant contribution of QCD multi-jet background events. Such events have a production cross-section several orders of magnitude greater than that of $t\bar{t}$ production and exhibit a final-state signature very similar to that of all-hadronic $t\bar{t}$ decays. While a series of selection cuts can be employed, as described in Chapter 7, to reduce the QCD background to a level comparable to that of all-hadronic $t\bar{t}$ signal events, there remains the difficulty of generating sufficient Monte Carlo statistics for these QCD background events. An incredibly small fraction of such simulated QCD events pass the stringent event selection cuts thereby requiring an impractically large number of generated events to be produced in order to yield meaningful and statistically significant final observable shapes and efficiencies for QCD multi-jet processes.

The production of a sufficiently large number of such simulated background events is computationally intensive and simply not feasible. It is however possible to determine the shape and normalization of the QCD multi-jet background for a given observable using a data-driven approach. The quantities of interest can be inferred in a particular region of phase space by making use of data events in an orthogonal region. Such a strategy is employed in the present analysis by means of a so-called **ABCD** method [81].

The goal of the ABCD method in the context of this analysis is to determine both the shape and the overall normalization[1] of the QCD multi-jet background in the final signal region (**SR**), for a variety of desired observables including but not limited to the $R_{3/2}$ observable, by

[1]The term **normalization** in this context is taken to mean the total number of background entries in the distribution of interest.

using events in different control regions (**CR**) with varying relative contributions of signal and background. The QCD mult-jet distributions for each variable are able to be derived in a fashion very different from the that in the analogous signal distributions, for which both the shape and normalization are derived from simulation alone. The final signal region corresponds to the region of phase space in which events from data are used to perform the final top quark mass measurement. The events in the control regions in contrast are used solely for the estimation of the QCD multi-jet background to be described in this chapter.

Figure 9.1 shows a two-dimensional plot of the estimated signal fraction S/(S+B) versus both the number of b-tagged jets[2] in the event and the average azimuthal separation between the reconstructed b-W pairs following the event reconstruction. It should be recalled that that these two variables constitute the final two event selection cuts as shown in Figure 7.1[3]. They were selected for the ABCD method in this analysis due to their strong discriminating power in separating signal from background events[4] and the fact that the number of b-tagged jets in an event is largely uncorrelated with the $R_{3/2}$ observable, with the importance of the latter requirement to be demonstrated in what follows.

The two-dimensional distribution was generated using all events, both signal and data, passing the full set of event selection cuts with the exception that no requirement was placed on the final two event selection cuts. The estimated signal fraction shown is evaluated as the ratio of signal events in a given region (S), based on simulated Monte Carlo signal $t\bar{t}$ events scaled to their theoretical cross-section, divided by the number of data events in that same region (S+B). One can note immediately from this plot that the largest signal fraction occurs for events with a large number of b-tagged jets and events in which the average angular separation between each reconstructed W boson candidate and its associated b-quark jet is small. In light of Figures 7.4(a) and 7.4(d) this fact should not be surprising.

The relative fraction of expected signal events in each of the four ABCD control regions can alternatively be presented in the form of pie charts, as is done in Figure 9.2. Table 9.1 defines the categorization of the four ABCD regions and similarly quotes the estimated signal fraction for each region, evaluated as before. The values of the estimated signal fractions shown in both Figure 9.2 and Figure 9.1, as well as those in Table 9.1, are the same.

[2]The number of b-tagged jets in a given event is determined by including only tagged jets within the leading six jets in the event, ordered in p_{T}.

[3]Refer also to the description of the event selection cuts in Section 7.4.

[4]Refer to the normalized distributions of several discriminating variables shown in Figure 7.4.

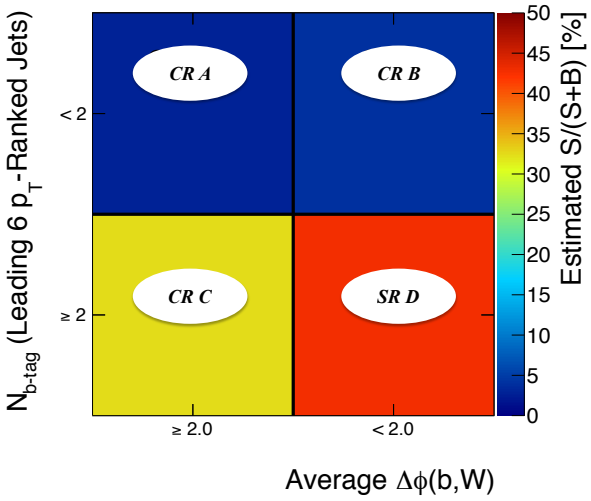

Figure 9.1: Two-dimensional plot of the estimated signal fraction, shown as a percent, as a function of the two final event selection cut variables, which are used to classify the three control regions (CR) and final signal region (SR) for the ABCD method used to estimate the multi-jet background.

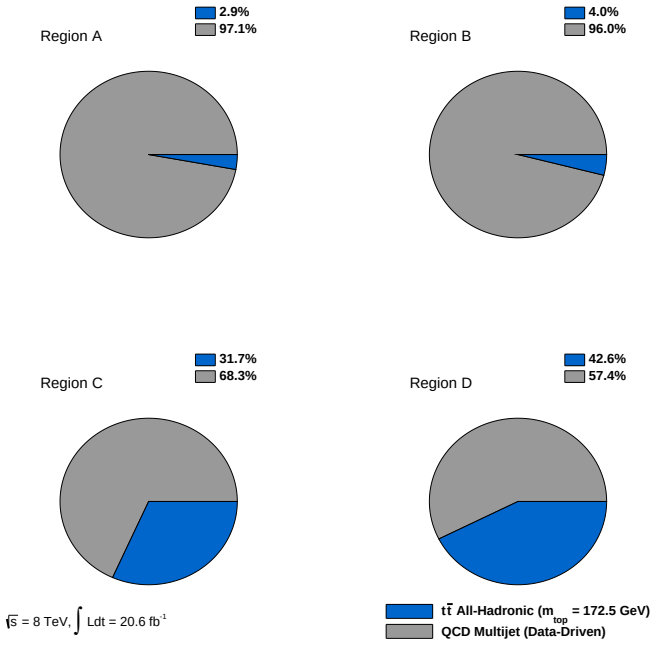

Figure 9.2: Pie charts displaying the estimated signal and background fractions in the four ABCD regions for the background estimation. Values are determined using both data and simulated signal events.

Table 9.1: Expected signal fractions in each of the four ABCD regions considered for the estimation of the QCD multi-jet background in signal region D. The signal fraction is estimated from the total number of reconstructed top quarks from simulated signal (S) and data (S+B) entries from the $R_{3/2}$ distribution in each particular region, including overflow and underflow bins.

ABCD Region and Definition			Estimated Signal Fraction
Region	N_{b-tag}	$\langle\Delta\phi(b,W)\rangle$	S/(S+B) [%]
CR A	<2	≥ 2.0	2.88 ± 0.03
CR B	<2	< 2.0	4.00 ± 0.03
CR C	≥ 2	≥ 2.0	31.66 ± 0.80
SR D	≥ 2	< 2.0	42.56 ± 0.77

The ABCD method operates under two primary assumptions. In what follows the $R_{3/2}$ observable is used as an example, but may be replaced by any particular variable of interest. The first assumption of the ABCD method is that the shape of the $R_{3/2}$ distribution for QCD multi-jet events does not change in moving from region B to D; that is, that the number of b-tagged jets in QCD events (up to the sixth jet ordered in p_{T}) is not correlated to the $R_{3/2}$ observable. The second assumption is that the two variables plotted on the axes of Figure 9.1 are themselves uncorrelated for QCD events.

In order to show that the correlation between the $R_{3/2}$ observable and the first ABCD variable (N_{b-tag}) is sufficiently small, a two-dimensional distribution is produced and shown in Figure 9.3(a). The bin contents for this distribution are set based on the number of data-minus-signal entries, such that they reflect the expected distributions for QCD multi-jet events. The correlation coefficient ρ is also quoted in the figure. For each N_{b-tag} bin each associated 1D distribution forming a column is normalized. The similarly constructed plot in Figure 9.3(b) shows the second assumption of the ABCD method to be satisfied – the number of b-tagged jets and the reconstructed quantity $\langle\Delta\phi(b,W)\rangle$ are largely uncorrelated for background events.

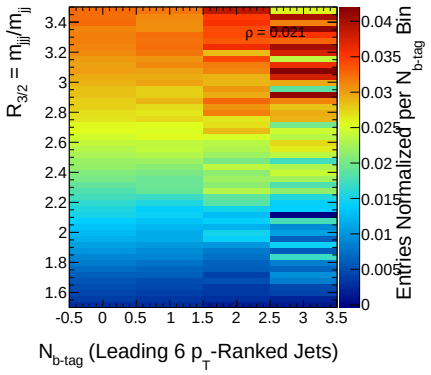

(a) $R_{3/2}$ versus the number of b-tagged jets in an event.

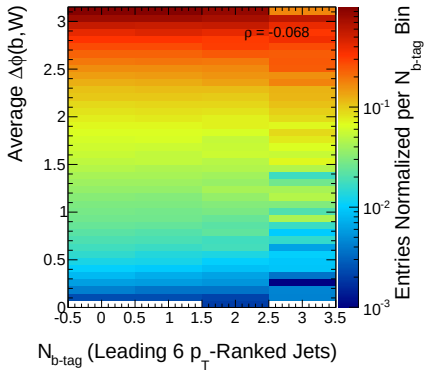

(b) Average $\Delta\phi(b, W)$ versus the number of b-tagged jets in an event.

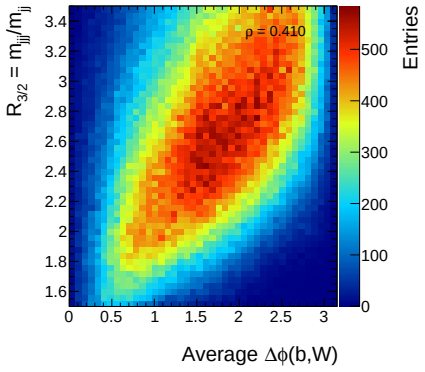

(c) $R_{3/2}$ versus average $\Delta\phi(b, W)$.

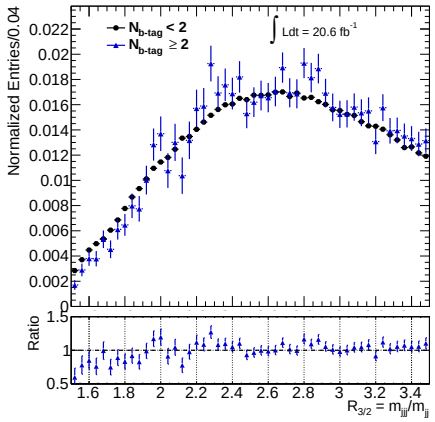

(d) Normalized shapes of the expected shape of the $R_{3/2}$ distribution for QCD events for different values of the number of b-tagged jets in an event.

Figure 9.3: Two-dimensional histograms used to check for correlations between the $R_{3/2}$ observable and the two observables used in the data-driven QCD background-extraction method in (a) and (b), as well as the correlation between the two observables themselves in (c). Data events passing all but the final two event selection cuts are used to fill the distributions. The final plot in (d) shows the normalized data-minus-signal shape for the $R_{3/2}$ observable for two different b-tag multiplicity bins.

The third plot, shown in Figure 9.3(c), was also produced similarly and shows a two-dimensional distributions of the reconstructed $R_{3/2}$ observable as a function of the the quantity $\langle \Delta\phi(b, W) \rangle$. Here it can be noted that the level of correlation is considerable. This fact is however both to be expected and is not of concern in the context of the ABCD method[5]; it is sufficient that the other two correlations be sufficiently small, as is seen to be the case.

Finally the plot in Figure 9.3(d) shows a one-dimensional distribution of data-minus-signal for the $R_{3/2}$ observable. Two normalized distributions are shown together: those for the merged regions A and B, and those for the merged regions C and D. This plot further demonstrates that within statistical fluctuations the shapes are consistent, and that the level of correlation between $R_{3/2}$ and the b-tag multiplicity in QCD events is small.

Such distributions should be produced for any observable for which one is hoping to estimate the QCD background distribution. It should be noted that the same data events as were used in Figure 9.1 were used to fill the histograms in Figures 9.3, *i.e.* data events which necessarily satisfy all but the final two event selection cuts.

In what follows the estimated number of signal entries from Monte Carlo[6] in bin i of control region A (CR A) will be expressed as $\mu_{s,i}^{CR\ A}$. Similarly the number of background entries is denoted $\mu_{b,i}^{CR\ A}$ and data entries $n_i^{CR\ A}$. Analogous terms exist for the three remaining control and signal regions. These numbers of entries are meant to represent the bin contents for a generic variable x, where x can represent for example the $R_{3/2}$ observable introduced in the preceding chapter, the n^{th} leading jet p_{T}, or some other quantity of interest. This generic variable x is implied in the expressions that follow but it is not written explicitly.

Provided the two ABCD observables shown are truly uncorrelated for QCD multi-jet events, one can say that:

$$\frac{N_b^{CR\ C}}{N_b^{CR\ A}} = \frac{N_b^{SR\ D}}{N_b^{CR\ B}} \tag{9.1}$$

where $N_b^{CR\ A}$, $N_b^{CR\ B}$, $N_b^{CR\ C}$, and $N_b^{SR\ D}$ are the total numbers of expected QCD entries in regions A, B, C, and D, respectively[7]. For control region A, the number of expected QCD

[5]The shapes of the background $R_{3/2}$ distribution are expected to differ between regions A and C compared with B and D. However as will be described in the equations that follow no cross terms exist between individual columns in the ABCD method – control regions A and C relate to the evaluation of the background normalization and control region B sets the background shape. Pictorially the equations relate quantities in an up-and-down manner rather than in a left-to-right manner. Moreover, as will be explained in the summary at the end of this chapter, it is only the shape of the $R_{3/2}$ distribution, and not the overall normalization, which is to be subsequently used in the final measurement of the top quark mass.

[6]In the case of the estimated numbers of signal entries, terms such as $\mu_{s,i}^{CR\ A}$ are in all cases taken to be scaled to their theoretical production cross-sections times branching ratio together with the known integrated luminosity of the 2012 $\sqrt{s} = 8$ TeV dataset considered for the analysis. This scaling is described in Appendix B.3.

[7]The total number of background entries in control region A for example is given by $N_b^{CR\ A} = \sum_{i=0}^{N_{bins}+1} \mu_{b,i}^{CR\ A}$. The normalizations for the signal and data entries are determined analogously. It is im-

entries is simply the number of entries observed in data minus the expected contributions from all-hadronic $t\bar{t}$ events, *i.e.*.

$$N_b^{CR\ A} = \sum_{i=0}^{N_{bins}+1} \left(n_i^{CR\ A} - \mu_{s,i}^{CR\ A} \right) = N_d^{CR\ A} - N_s^{CR\ A} \tag{9.2}$$

and similarly for regions B and C. Note that in the above the total number of data entries ($N_d^{CR\ A}$) and estimated signal entries ($N_s^{CR\ A}$) in control region A have been expressed similarly to the analogous term for the multi-jet background.

The value of $N_b^{SR\ D}$, which could also in principle be evaluated in an analogous fashion, is left as an unknown. It is precisely the desired QCD multi-jet normalization for the final signal region D which is to be determined solely from events in the other regions.

In a similar vein, the shape of the $R_{3/2}$ distribution for QCD entries – the bin-by-bin contents – can be estimated from the shape of the QCD distribution in region B alone; one expects that the normalized shape of the QCD distribution should not differ in moving from region $B \to D$. This is a reiteration of the first of the assumptions above for the ABCD method. Analogously to Equation 9.2, the number of estimated QCD multi-jet entries in bin i of region B for a generic variable is given by:

$$\mu_{b,i}^{CR\ B} = n_i^{CR\ B} - \mu_{s,i}^{CR\ B} \tag{9.3}$$

The fact that the normalized shapes of the QCD multi-jet background are assumed to be identical between regions B and D can be written mathematically as:

$$\left(\frac{1}{N_b^{CR\ B}} \right) \mu_{b,i}^{CR\ B} = \left(\frac{1}{N_b^{SR\ D}} \right) \mu_{b,i}^{SR\ D} \tag{9.4}$$

Using the expression for the unknown normalization N_D^{QCD} from Equation 9.1, one can therefore estimate the bin contents of the QCD distribution in the signal region D as:

$$\mu_{b,i}^{SR\ D} = \left(\frac{N_b^{CR\ C}}{N_b^{CR\ A}} \right) \mu_{b,i}^{CR\ B} \tag{9.5}$$

In the above equation, one can see that the bin-by-bin contents of the QCD distribution in the final region of interest can therefore be estimated using signal and data events exclusively from other regions, *i.e.* the QCD bin contents are estimated bin-by-bin without using any data events from the signal region D. The right-hand side of Equation 9.5 may be written using data

portant to emphasize that such sums are performed over all bins for the chosen variable and include underflow (bin 0) and overflow (bin $N_{bins} + 1$) contents – the bin contents for bins outside the plotting range shown. The limits in the sum highlight this fact. Furthermore the normalizations in each region are irrespective of the variable to be drawn.

and simulated signal terms only, though the expression is identical:

$$\mu_{b,i}^{SR\ D} = \left(\frac{\sum_{j=0}^{N_{bins}+1} \left(n_j^{CR\ C} - \mu_{s,j}^{CR\ C} \right)}{\sum_{j=0}^{N_{bins}+1} \left(n_j^{CR\ A} - \mu_{s,j}^{CR\ A} \right)} \right) \left(n_i^{CR\ B} - \mu_{s,i}^{CR\ B} \right) \tag{9.6}$$

It should be noted that while the relative contribution of signal $t\bar{t}$ entries in regions A and B are quite small as compared with data, the signal contribution is of course non-zero, and it is sizeable in region C. As a result, one can speak of the so-called signal contamination – the presence of signal entries in control regions when estimating the QCD bin contents in the final region – which could bias the final result. This is particularly important in the shape extraction from region B; here a looser overall event selection would allow for a minimal amount of signal contribution, but one would necessarily have a larger relative fraction of QCD multi-jet entries in the final signal region. Studies were performed to strike a good balance between these two opposing demands – yielding a sufficiently low signal contamination in the control regions (A,B, and C) while maintaining a sufficiently high signal fraction in the final signal region (D). The potential bias effect introduced by the larger contribution in control region C, though it appears problematic, will be mitigated by allowing the background normalization to float in the final fit to extract the measured value of m_{top}.

9.2 Control Plots of Event Kinematic Variables

To validate the process described in the previous section, the shape of the QCD multi-jet background is derived for several key variables in a series of control plots shown in Figures 9.4, 9.5, and 9.6. Each of these plots represents the final signal region D for a particular observable, where the estimated QCD multi-jet background (shown in grey) is determined bin-by-bin *via* the ABCD method in the form of Equation 9.5. The contributions from all-hadronic $t\bar{t}$ signal entries, scaled to their theoretical cross-section, are represented by the blue histograms. The black $\sqrt{s} = 8$ TeV data points are superimposed on top of the histograms, and a ratio is shown below comparing the number of data entries in a given bin to the total number of estimated entries – both signal and background contributions combined. Shaded regions in both the primary and the ratio plots below correspond to the sum – in quadrature and evaluated bin-by-bin – of statistical and systematic uncertainties. The systematic uncertainties will be described in detail in Chapter 11. Though these sources of systematic uncertainty are quantified primarily in the context of the measurement of m_{top}, the same prescription is adopted in setting the total uncertainty bands in the overall data-estimation control plots to be presented in this chapter.

9.2.1 Agreement in Control Plots

There are several possible reasons that could explain the disagreement between the number of data entries and the sum of Monte Carlo signal and estimated QCD multi-jet background entries in a given distribution. Broadly speaking the causes fall into two categories: those relating to the distributions of the all-hadronic $t\bar{t}$ signal, and those relating to the estimated QCD multi-jet background. In both of these cases either the normalization, the shape of a given distribution, or some combination of the two could be affected[8].

In the case of any disagreement it is at times difficult to disentangle the effects, though comparison of normalized distributions such as that shown in Figure 9.3(d) can help to identify when the primary cause of the disagreement is from a failure of the assumptions used in the ABCD method to estimate the background in the final signal region.

The primary sources leading to an overall data-estimation disagreement are as follows:

1. **Monte Carlo**: Mismodelling in the production of the Monte Carlo dataset at any of the several stages – from the generation of the hard-scatter events at the matrix-element level to simulations of particles with the various levels of the ATLAS detector. Effects could also arise due to the incorrect overall normalization which comes from theoretical values of the $t\bar{t}$ production cross-section and branching ratios together with the measured integrated luminosity over the 2012 data-collection period.

2. **Value of m_{top}**: The value of the true top quark mass in data differs from that in the simulated dataset; this is expected to affect predominantly those variables most sensitive to the value of m_{top}. Checks for any potential m_{top}-dependent biases introduced in performing the measurement are included through a series of closure tests (Section 11.2).

3. **ABCD Method Assumptions**: Correlations in the ABCD method which result in differences between the normalized shapes of the variable of interest in the combined regions A & B, compared with those in regions C & D, thereby resulting in a misestimated normalized shape. Since the two variables selected to define the control and signal regions in the ABCD were themselves shown to be uncorrelated, this effect is expected to arise predominantly in cases where for QCD multi-jet events the variable to be drawn is correlated with the number of b-tagged jets in the event. Even with no dependence on the top quark mass, small kinematic differences between QCD multi-jet events with high *vs.* low b-jet multiplicity can be expected to be exist with a modest level of correlation.

4. **Statistical Fluctuation**: Standard statistical fluctuations. These are expected to be encompassed by the final statistical uncertainty bands.

[8]Note that these effects are of course not independent and that a moderate amount of correlation would be expected to exist between the two for certain cases – an incorrect value of the top quark mass for the simulated events will result an overall normalization issue as well as local variations in the shapes of m_{top}-sensitive variables.

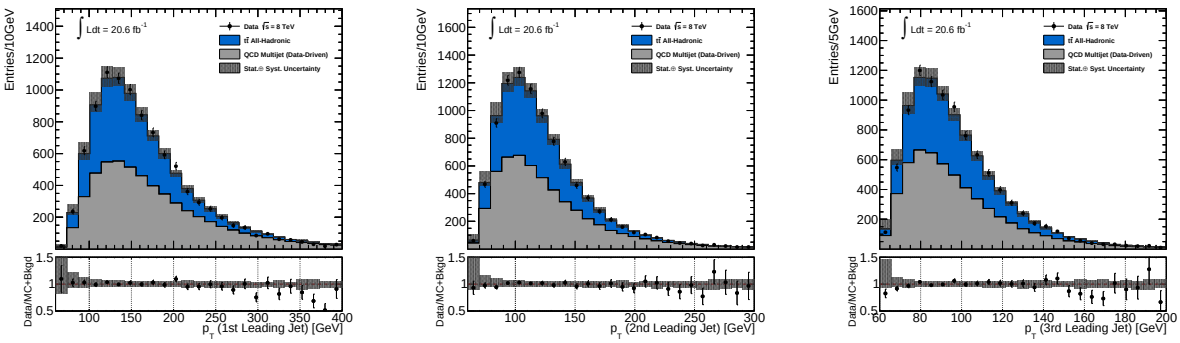

(a) Leading jet p_{T} (b) 2nd-leading jet p_{T} (c) 3rd-leading jet p_{T}

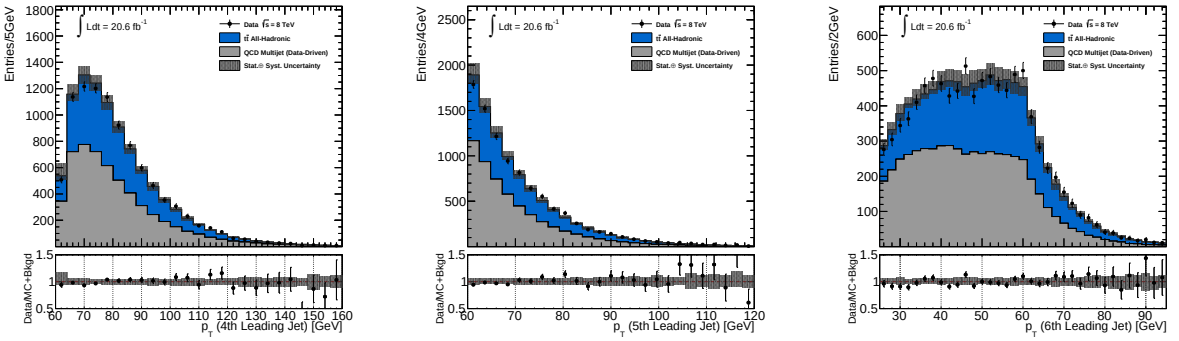

(d) 4th-leading jet p_{T} (e) 5th-leading jet p_{T} (f) 6th-leading jet p_{T}

Figure 9.4: Six leading jet p_{T} distributions, shown for data (solid points) together with simulated all-hadronic signal, simulated non all-hadronic background, and the estimated QCD multi-jet background from the ABCD method. Ratio plots comparing data to simulation plus estimated background are shown below each figure. Note the different horizontal ranges.

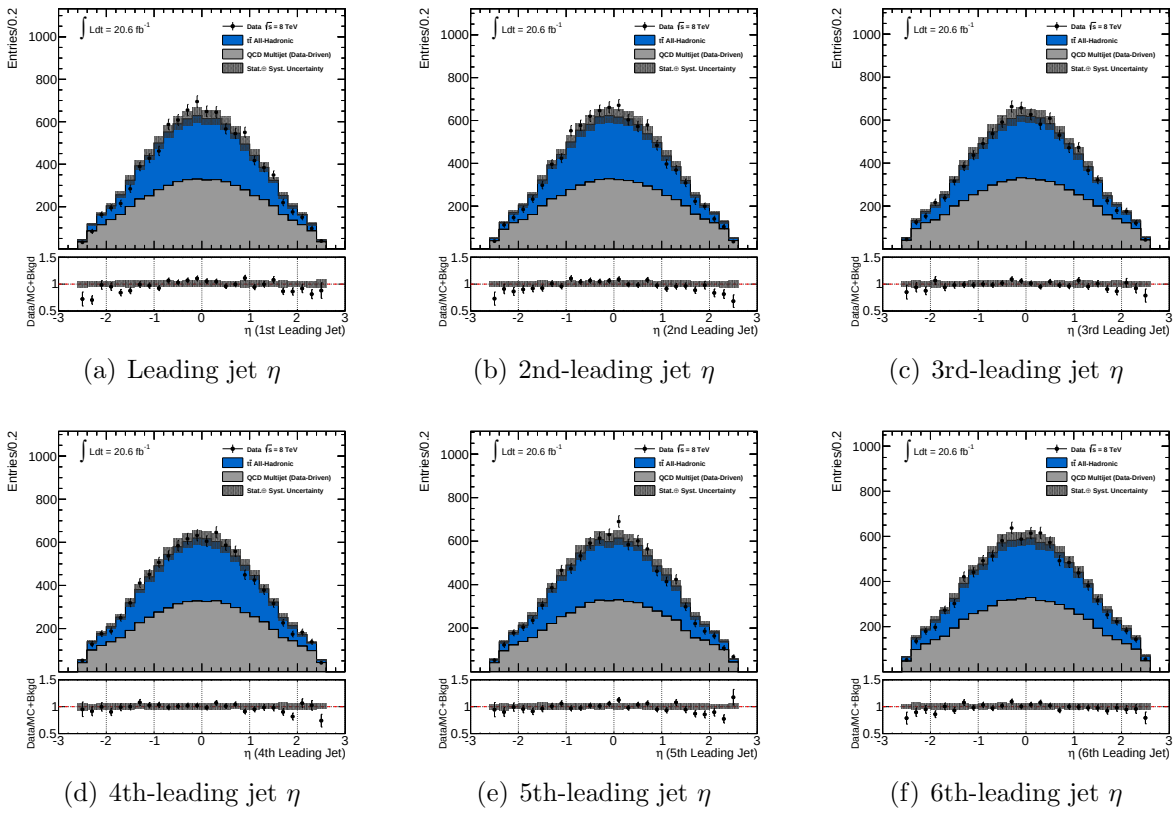

(a) Leading jet η (b) 2nd-leading jet η (c) 3rd-leading jet η

(d) 4th-leading jet η (e) 5th-leading jet η (f) 6th-leading jet η

Figure 9.5: Six leading jet η distributions, shown for data (solid points) together with simulated all-hadronic signal, simulated non all-hadronic background, and the estimated QCD multi-jet background from the ABCD method. Ratio plots comparing data to simulation plus estimated background are shown below each figure. Jets are ranked in order of p_{T}.

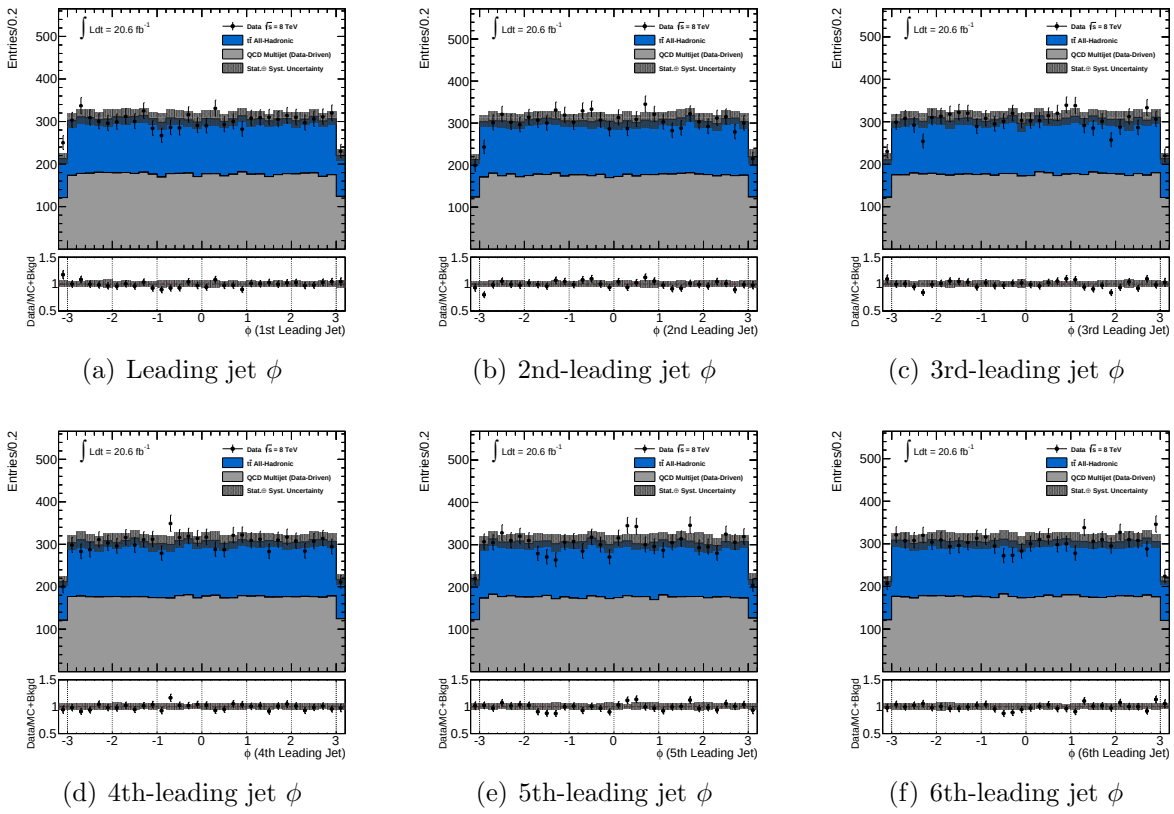

(a) Leading jet ϕ (b) 2nd-leading jet ϕ (c) 3rd-leading jet ϕ

(d) 4th-leading jet ϕ (e) 5th-leading jet ϕ (f) 6th-leading jet ϕ

Figure 9.6: Six leading jet ϕ distributions, shown for data (solid points) together with simulated all-hadronic signal, simulated non all-hadronic background, and the estimated QCD multi-jet background from the ABCD method. Ratio plots comparing data to simulation plus estimated background are shown below each figure. Jets are ranked in order of p_{T}.

The control plots in Figure 9.4 show transverse momentum distributions of the leading six jets. Very good overall agreement can be observed between data and estimation – the sum of the simulated $t\bar{t}$ and estimated QCD multi-jet contributions. The shape of the sixth-jet p_{T} distribution is noticeably different from the others – an artifact of the five-jet trigger and the corresponding offline p_{T} cut employed in the analysis.

Figures 9.5 and 9.6 show the pseudorapidity and azimuthal distributions, respectively, also ordered by jet transverse momentum. Again, good agreement is observed, save the small discrepancies in the η distributions. These are the result of a failure, in the case of this particular observable, of one of the primary assumptions made at the beginning of this section: the normalized η shapes for differing b-tag multiplicities in background events are simply not the same, which translates to a correlation between the number of b-tagged jets and the η of the jets. In QCD multi-jet background events with a higher b-tag multiplicities, the jets are on average more central than in events with zero or one b-tagged jet[9]. Consequently when taking the background shape from control region B this results in an underestimation in signal region D of the background in the central region and an overestimate at high $|\eta|$ values. The same effect was observed in the 7 TeV all-hadronic $t\bar{t}$ top quark mass measurement and it was demonstrated that this failure to correctly model the η distributions had no significant effect on the agreement of the $R_{3/2}$ distribution, nor the measurement of m_{top} itself [79]. It should be emphasized then that this disagreement therefore does not indicate a mismodelling of the simulated events, but is rather a reflection of the fact that the ABCD method, as is, simply cannot be employed in the case of the jet η distributions.

Figure 9.7(a) shows the invariant two-jet mass m_{jj}, *i.e.* the invariant mass of the four-vector object produced by means of a sum of the two associated jets forming each reconstructed W boson candidate. Figure 9.7(b) shows the invariant tri-jet mass m_{jjj}, which is the analogous invariant mass of the three-jet system corresponding to each reconstructed top quark candidate. Each of these two distributions are filled twice per event. The lack of a high-mass tail in the m_{jj} distribution is a result of the cut on the goodness-of-fit P_{gof} from the χ^2 reconstruction method; it should be recalled that permutations of jets yielding m_{jj} values which differ greatly from the reference m_W value are suppressed, whereas no such analogous suppression exists for the tri-jet mass term m_{jjj}. In all cases a good level of agreement between data and prediction is observed.

As the m_{jjj} observable in particular is very sensitive to the true top quark mass, good agreement in the m_{jjj} distribution would only be expected in the case that the input value of m_{top} from the generation of the simulated signal events is close to the true value. Scrutiny of the ratio plot of Figure 9.7(b) suggests that while the true value of m_{top} cannot be expected to differ too greatly from 172.5 GeV – the value used in the generation of the simulated Monte

[9]This could arise due to flavour differences: it is expected that there are more charm-flavoured jets in QCD events when two b-tagged jets are required. These flavour differences could give rise to slightly different kinematic properties which affect the pseudorapdity distributions of the jets in an event.

Carlo sample – it is expected to be slightly larger than this value[10].

Indeed, as mentioned above, for any observable sensitive to the top quark mass m_{top}, it should be pointed out that even in the case of an ideal set of simulated events, one cannot hope to have perfect agreement between data and prediction if the input or generator m_{top} value used differs from the true value of m_{top}.

Four final control plots are shown in Figure 9.8. The first is the jet multiplicity – the number of reconstructed jets in each event. The second plot shows the average p_{T} of the jets – the scalar p_{T} sum over all jets in an event (often referred to as H_T) divided by the number of jets.

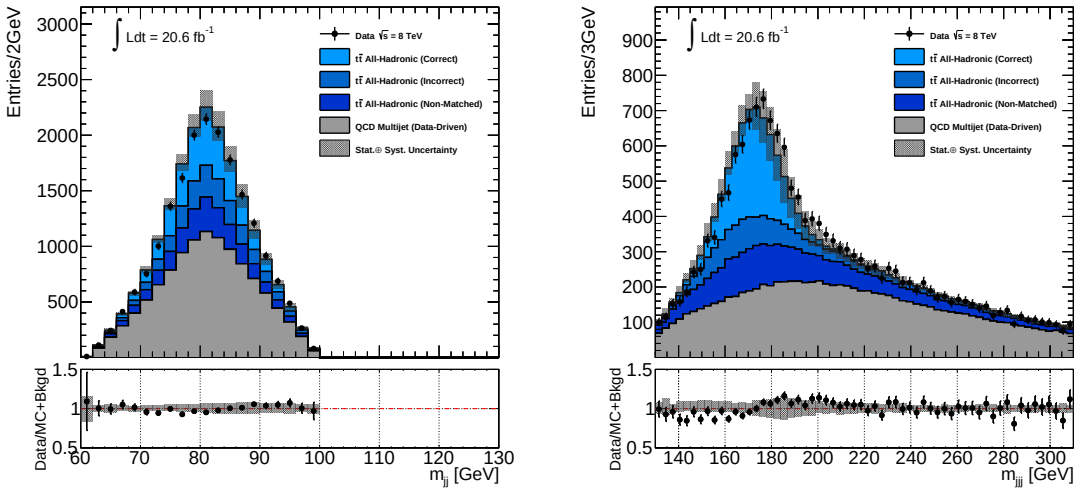

(a) Reconstructed W boson mass

(b) Reconstructed top quark mass

Figure 9.7: Additional control plots of reconstructed invariant mass distributions (a) m_{jj} and (b) m_{jjj}. Distributions were filled twice for each event passing the full event selection.

The third and fourth of these plots correspond to the minimum χ^2 returned from the selected permutation of jets from the top quark reconstruction and its associated P_{gof} value, respectively. In these distributions different shades of blue correspond to the different permutation classifactions based on the reconstructed top quark and W boson candidates[11]. The fourth permutation category, shown in the lightest shade of blue, arises from the fact these distributions are filled only once per event and it can be useful to distinguish between cases where both, only one, or neither of the reconstructed top quarks have the correct jet-quark assignments. The second-

[10]This statement is made under the assumption that the difference in the measured from the true value of m_{top} is the dominant source of the disagreement.

[11]Refer to Section 6.3 for descriptions of how the permutation classification is determined for a given event.

lightest shade of blue therefore corresponds to cases where strictly one of the two top quark candidates has the correct jet-quark associations.

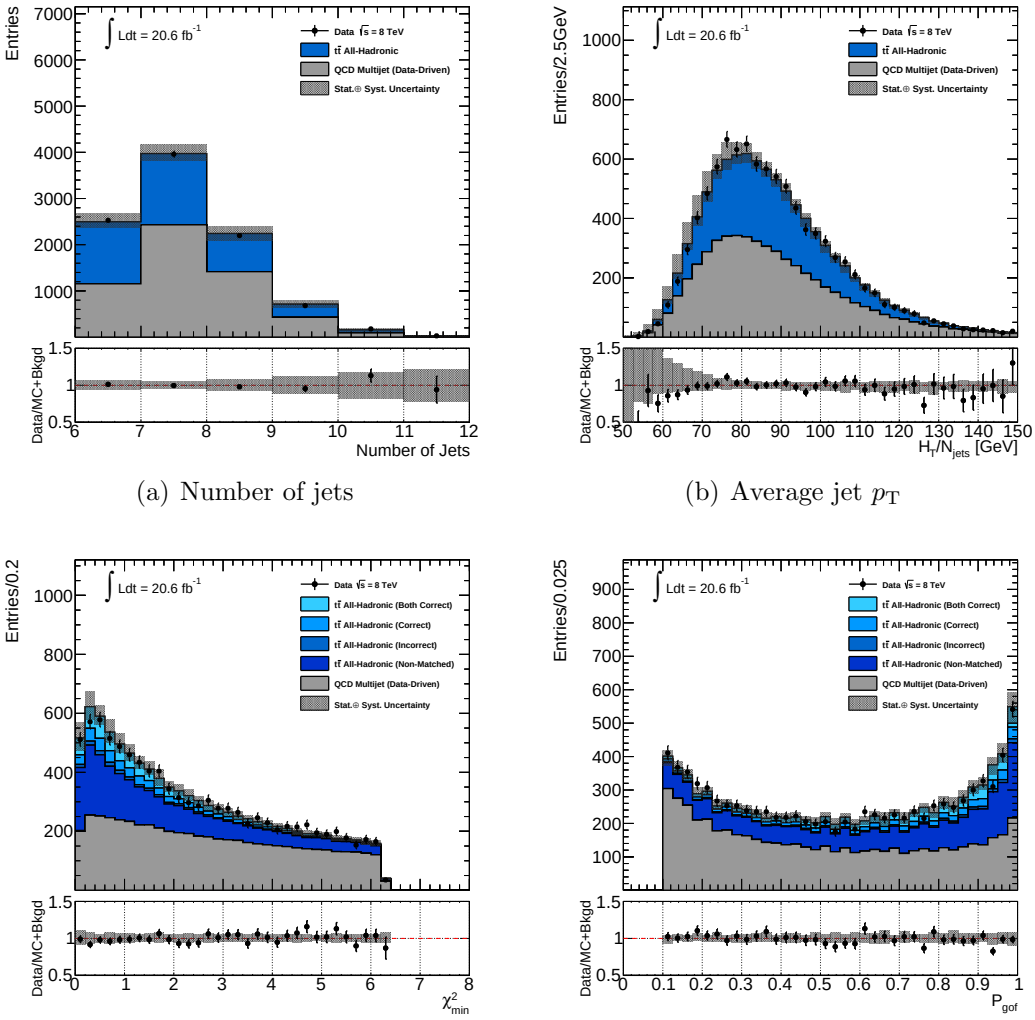

(a) Number of jets

(b) Average jet p_{T}

(c) Minimum reconstruction χ^2

(d) Associated goodness-of-fit P_{gof}

Figure 9.8: Control plots showing the distributions of (a) jet multiplicity, (b) the average jet p_{T} evaluated as the scalar sum of all jet transverse momenta (H_T) divided by the jet multiplicity, as well as the reconstruction (c) χ^2_{min} and (d) P_{gof}. Plots show data (black data points) together with stacked distributions of simulated all-hadronic signal, simulated non all-hadronic background, and the estimated QCD multi-jet background from the ABCD method. Ratio plots which compare the overall data to prediction values are shown below each distribution.

9.3 Estimated QCD Background for the $R_{3/2}$ Observable

It has been shown that there is a negligible correlation between $R_{3/2}$ and the number of b-tagged jets in the event. As such, one should expect relatively good agreement between data and prediction for the $R_{3/2}$ distribution, again under the assumption that the top quark mass is relatively close to the value of 172.5 GeV. Figure 9.9 shows the $R_{3/2}$ distributions in all four ABCD regions in order to compare the predicted QCD background shapes. Plotted are the data points in black and the estimated QCD multi-jet distributions in grey. The latter are evaluated *via* Equation 9.3 in the case of control regions A,B, and C (making the obvious substitutions from $B \to C$ or $B \to A$, where appropriate), and Equation 9.5 in the case of signal region D. One can note the striking difference in shape between the distributions in regions A & C and those in regions B & D. This is due to the topological cut on $\langle \Delta\phi(W, b) \rangle$ which is made on reconstructed quantities and which, as has been shown, is correlated with the $R_{3/2}$ observable (with correlation coefficient $\rho \approx 0.41$).

The final data distribution for the $R_{3/2}$ observable is shown, together with the predicted signal and background distributions in the form of a stacked histogram, in Figure 9.10(a). As in the case of the m_{jjj} and m_{jj} observables, good agreement is achieved, including in the region of the signal peak. Table 9.2 shows the final number of estimated signal and background entries – a mix of simulation for the signal and the data-driven ABCD method for the QCD multi-jet entries – compared with the total number of entries observed in data. In addition to the good agreement over the full range of the distribution, an overall comparison of the number of data to estimated entries is found to be 1.01 ± 0.01. It should be noted that the background fraction term F_{bkgd} differs from what one might expect from the associated signal fraction term shown, (*i.e.* one can observe that $F_{bkgd} \neq 1 - \frac{S}{S+B}$). This is due to the fact that in the evaluation of F_{bkgd} the contributions from the underflow and overflow bins are not included. The reason for this distinction is that in the final measurement of the top quark mass, both m_{top} and this F_{bkgd} term are extracted, where the overflow and underflow bin contributions are explicitly neglected. Adopting this definition of F_{bkgd} allows for a direct comparison with the final fit result.

The extracted QCD multi-jet background bin contents for the $R_{3/2}$ observable – the same bin contents as in the stacked histogram in Figure 9.10(a) – are plotted separately in Figure 9.10(b). It was found that the sum of a Gauss and Landau distribution provides a reasonably good parameterization of this shape. There are a total of five parameters, labelled as the set $\{\mathbf{q}\}$, required to describe this shape as well as a sixth overall normalization parameter which is not subsequently used. The parameters are analogous to those enumerated in the previous chapter for the case of the signal shape of the $R_{3/2}$ distribution. The explicit background probability distribution for the background is therefore expressed, analogously to Equation 8.3, in terms of the sum of the normalized probability distributions for the Gauss and Landau functions (P_G and P_L, respectively[12]):

[12]Refer to Section 8.3.

Table 9.2: Final number of entries in the $R_{3/2}$ distribution in signal region D. All numbers include entries in the underflow and overflow bins of the $R_{3/2}$ distribution with the exception of the expected background fraction F_{bkgd}, in order that it be comparable to the final measured value from data.

	Number of Entries
$t\bar{t}$ All-hadronic	8150 ± 90
QCD multi-jet	11070 ± 100
Total Estimated	19230 ± 130
Data	19150 ± 130
Estimated S/(S+B) [%]	42.6 ± 0.8
Estimated F_{bkgd} [%]	51.9 ± 0.7
Overall Data/Estimation	1.00 ± 0.01

$$\mu_b\left(x \mid \mathbf{q}\right) = q_5\left(1-q_2\right)P_G(x \mid q_0, q_1) + q_5 \cdot q_2 P_L(x \mid q_0 \cdot q_3, q_1 \cdot q_4) \tag{9.7}$$

A least-squares or χ^2 fit is performed and the resulting fit shape is overlayed on the same plot based on the extracted fit parameters. These fitted parameters are summarized in Table 9.3.

The shape of the QCD multi-jet background is assumed to be independent of the value of top quark mass m_{top}, though it is recognized that a modest amount of non all-hadronic $t\bar{t}$ background has been neglected which would have some m_{top}-dependence. The contribution from the non all-hadronic background in the final signal region was found to be below the 3% level and it was decided not to include it in the final distributions. The impact of this choice is treated as a source of systematic uncertainty and is further discussed in Section 11.6.3.

The uncertainties on and correlations between each of QCD background shape parameters will subsequently be incorporated into the final m_{top} measurement, as will be detailed in the following chapter.

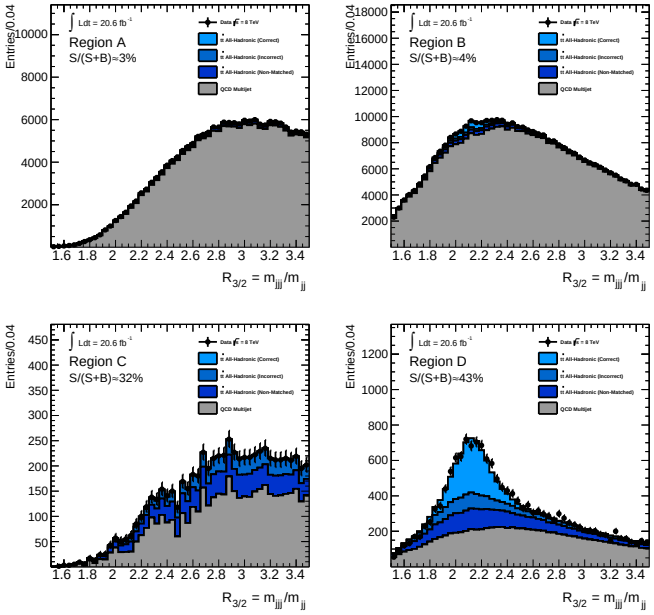

Figure 9.9: The $R_{3/2}$ distributions in each of the control regions (A,B and C) used to estimate the final QCD multi-jet bin contents in the final signal region (D). The black markers denote the data entries, and the grey shaded region the estimated QCD multi-jet background. The all-hadronic $t\bar{t}$ contributions, derived from simulation and decomposed into permutation classifications, are shown in the various shades of blue. Also indicated is the expected signal fraction for each region which includes contributions from overflow and underflow bins.

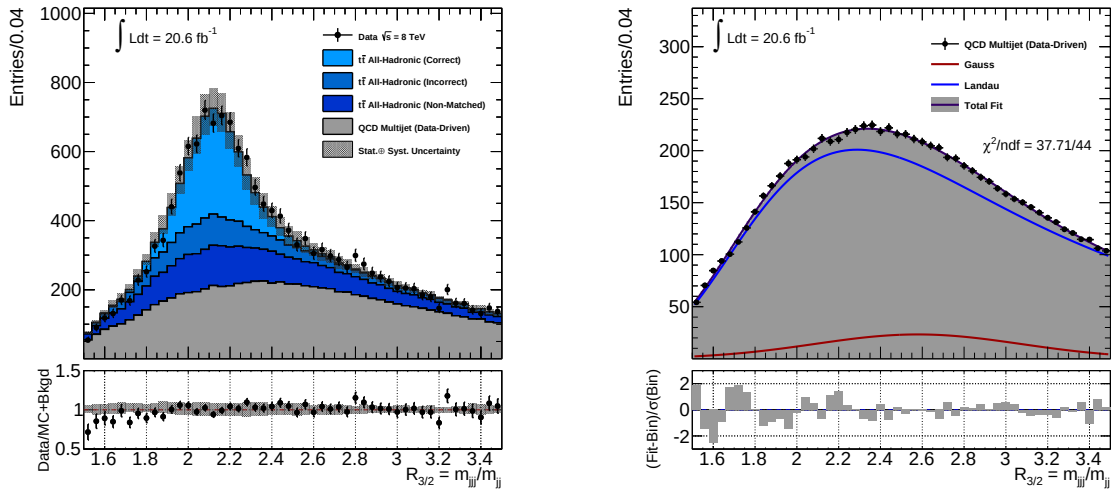

(a) (b)

Figure 9.10: (a) Final $R_{3/2}$ distribution showing agreement between data (black markers) and estimated signal plus background, and (b) the estimated QCD multi-jet background distribution alone (black markers), together with the final overlaid Gauss + Landau fit used to describe the background shape. The QCD bin contents are those derived from the ABCD method.

9.4 Use of the Estimated QCD Multi-Jet Background

The following chapter outlines the procedure used to extract a measurement of the top quark mass from the $R_{3/2}$ bin contents of the distribution from the measured data. In order to do this the estimated QCD multi-jet distribution for the $R_{3/2}$ observable in the final signal region D, as evaluated in this chapter, is used to describe the background shape alone. The estimated background normalization, evaluated in part using data and simulated signal events control regions A and C, is not used in the final m_{top} extraction procedure. The final background normalization is left as a free parameter F_{bkgd} in the final least-squares fit. Only the background shape parameters $\{\mathbf{q}\}$, together with their associated covariance matrix, are used for the purposes of the final measurement.

Table 9.3: Extracted fit parameters of the background template shape of the $R_{3/2}$ observable. The parameterization used is the sum of a Gauss and a Landau function. The fitted distribution corresponds to the estimated QCD multi-jet distribution from the ABCD method in the final signal region D.

Parameter	Description	Extracted Parameter Value
q_0	Gauss Mean μ	2.58 ± 0.12
q_1	Gauss Width σ	0.49 ± 0.12
q_2	Landau Fraction f_L	0.94 ± 0.04
q_3	Landau MPV (Relative) μ_R	0.93 ± 0.05
q_4	Landau Width (Relative) σ_R	0.90 ± 0.22

Chapter 10

Top Quark Mass Determination

10.1 χ^2 Minimization and Linear Algebra Framework

This chapter presents the method by which an estimate of m_{top} is determined from the binned data entries of the $R_{3/2}$ distribution as shown in Figure 9.10(a) in the previous chapter. It should be recalled that the $R_{3/2}$ observable was selected due to its strong dependence on m_{top} and suppressed sensitivity, relative to the m_{jjj} observable itself, to the uncertainties in the Jet Energy Scale (JES)[1].

Chapters 8 and 9 presented the way in which normalized shapes, or probability density functions, of the $R_{3/2}$ observable were extracted for both the all-hadronic $t\bar{t}$ signal and background processes, respectively. Together with the extracted values of the shape parameters – expressed as a function of m_{top} in the case of the signal shape – all of the necessary tools are at hand to be able to perform either a binned or unbinned log likelihood fit or a least-squares fit, in order to measure the quantity of interest: the top quark mass m_{top}. The background fraction F_{bkgd} introduced in the previous chapter is also to be extracted simultaneously.

In this section a slight variation on a standard minimum χ^2 or least-squares approach is presented[2]. In a typical minimum χ^2 fit such as those employed in building the signal templates in Chapter 8, the bin contents of the distribution of a particular observable are known, as is the functional form of a probability density function which depends on a particular number of parameters. In general any number of these parameters are then to be estimated. A χ^2 variable is constructed *via* the sum of squared differences between each of the bin contents and the estimated number of entries in that bin for the given choice of the parameters. Each squared term in the sum is weighted by the reciprocal of the number of events in the corresponding bin

[1] Refer to the plots shown previously in Figure 8.2

[2] For a concise summary of a standard least-squares minimization see [82]. For additional information on numerical methods used to motivate some of the strategies adopted for the minimization procedure summarized in this chapter see [83].

based on poisson statistics. It is generally assumed that there is no uncertainty attributed to the choice of the parameterization itself – an assumption which may not always prove to be appropriate – and furthermore that no correlation exists between the bin contents.

In such a setup, under the assumption that one has N_{bins} bins, and that n_i and μ_i represent the measured and estimated number of events[3] in bin i, respectively, the chi-squared variable is defined as:

$$\chi^2 = \sum_{bin\ i}^{N_{bins}} \sum_{bin\ j}^{N_{bins}} (n_i - \mu_i)\,(n_j - \mu_j)\,[\mathbf{V}]^{-1}_{ij} = \sum_{bin\ i}^{N_{bins}} \frac{(n_i - \mu_i)^2}{n_i} \tag{10.1}$$

The first expression involving a double sum is the more general form of the χ^2 variable, for a general $N_{bins} \times N_{bins}$ covariance matrix $\mathbf{V}$. For a typical chi-squared minimization procedure, $\mathbf{V}$ represents a diagonal matrix with entries $V_{ij} = \delta_{ij} n_j$, where δ_{ij} is the kroenecker delta, which thus collapses the double sum and leaves the more familiar, right-most form of Equation 10.1.

In vector notation the above may be written more succinctly as:

$$\chi^2 = (\vec{n} - \vec{\mu})\,\mathbf{V}^{-1}\,(\vec{n} - \vec{\mu})^T \tag{10.2}$$

where $\vec{n}$ and $\vec{\mu}$ are recognizably the same measured and estimated number of bin entries, but where each is written in the form of a $1 \times N_{bins}$ row vector. The superscript T denotes a transpose. Here $\mathbf{V}$ could in general be any $N_{bins} \times N_{bins}$ covariance matrix with diagonal as well as off-diagonal terms – off-diagonal in the case that some correlation between bin entries exists. For the present analysis, it was desired to have the correlations between signal and background shape parameters propagated to correlations between the estimated number of entries in different bins [83, 84]. In other words, it was desired to incorporate the parameterization uncertainties into the fitting procedure, whereas in a typical chi-squared minimization such uncertainties and correlations are zero and the only uncertainty is assumed to be from the measured bin contents.

The modified form of the χ^2 variable is therefore written as:

$$\chi^2 = \sum_{bin\ i}^{N_{bins}} \sum_{bin\ j}^{N_{bins}} (n_i - \mu_i)\,(n_j - \mu_j)\,[\mathbf{V(d)} + \mathbf{V(s)} + \mathbf{V(b)}]^{-1}_{ij} \tag{10.3}$$

Here the $\mathbf{V(d)}$ term is the same diagonal matrix with entries $V_{ij} = \delta_{ij} n_j$ from before, corresponding to the set of uncertainties in the numbers of measured data entries in bin i which is given by $\sqrt{n_i}$. The other two matrices $\mathbf{V(s)}$ and $\mathbf{V(b)}$, which must also be of dimension $N_{bins} \times N_{bins}$, correspond to the signal and background shape parameterization and are to be determined in what follows.

[3] In this case μ_j corresponds to the sum of signal and background events, *i.e.* $\mu_j = \mu_{s,j} + \mu_{b,j}$. The superscript indicating the ABCD region is dropped – in this section the only region considered is the final signal region D.

Prior to doing so, it is advantageous to replace the single $\vec{\mu}$ vector, representing the expected number of events in each bin, by the sum of entries due to the signal and background contributions separately, namely: $\vec{\mu} = \vec{\mu_s} + \vec{\mu_b}$. For a given observable x, where presently $x = R_{3/2}$, it has been shown that a given value of m_{top} determines the value of all signal shape parameters since each such shape parameter was assumed to depend linearly on m_{top}. The combined background shape was assumed to have no m_{top} dependence and was thus considered fixed. If however the fraction of background entries[4] is introduced as an additional unknown parameter F_{bkgd}, which has yet to be measured, then given a bin width of w_{bin} for the distribution of observable x with total number of data entries N_d, the number of estimated entries in bin i can be expressed as:

$$\mu_i(m_{top},\ F_{bkgd}) = w_{bin} N_d \left[(1 - F_{bkgd})\, P_S(x_i \mid m_{top}) + F_{bkgd} P_B(x_i)\right] \tag{10.4}$$

Here P_S and P_B are the probability density functions for the signal and background, respectively. This means that one can re-write the total row vector $\vec{\mu}$ as:

$$\vec{\mu}(m_{top},\ F_{bkgd}) = \vec{\mu}_s(m_{top}, F_{bkgd}) + \vec{\mu}_b(F_{bkgd}) \tag{10.5}$$

where specifically:

$$\mu_{s,i}(m_{top}, F_{bkgd}) = w_{bin} N_d\, (1 - F_{bkgd})\, P_S(x_i \mid m_{top}) \tag{10.6}$$

and

$$\mu_{b,i}(F_{bkgd}) = w_{bin} N_d F_{bkgd} P_B(x_i) \tag{10.7}$$

10.2 Propagation of $R_{3/2}$ Shape Uncertainties

Based on the previous two equations and using the extracted signal and background parameter values shown in the previous chapters, one can construct distributions of the estimated number of signal and background entries for the $R_{3/2}$ observable. The plots in Figure 10.1 show such distributions both for signal entries in Figure 10.1(a) and for background entries in Figure 10.1(b). In the case of the signal entries, a two-dimensional distribution is shown for a range of m_{top} values from 160 - 190 GeV. Here a clear translation of the peak to higher $R_{3/2}$ values can be observed in moving from the left to the right portion of the plot, thereby demonstrating the strong sensitivity of $R_{3/2}$ to m_{top}. For both plots, the F_{bkgd} and $(1 - F_{bkgd})$ terms, as appropriate, have been factored out for the reason that they act only as multiplicative factors in what

[4]The background fraction parameter F_{bkgd} in this context is taken to be within the plot range of the $R_{3/2}$ distribution since this is the value relevant in the χ^2 minimization procedure. In particular such a definition neglects the contribution from the overflow region of the $R_{3/2}$ distribution where, notably, the QCD multi-jet background has a larger tail.

follows, and since the value of F_{bkgd} is yet to be determined.

The covariance matrices $\mathbf{V(s)}$ and $\mathbf{V(b)}$ to be introduced in the next section arise from the uncertainties in and correlations between signal and background parameters, respectively; they aim to address, in a quantitative fashion, the effect on the values in the plots in Figure 10.1 due to these uncertainties and correlations.

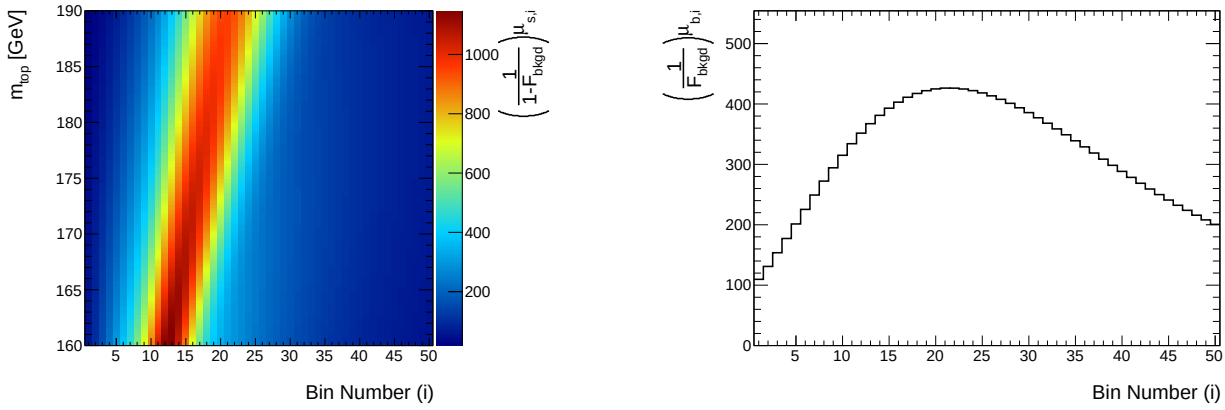

(a) (b)

Figure 10.1: (a) Estimated number of signal $R_{3/2}$ entries in a given bin shown as a function of the input top quark mass and the $R_{3/2}$ bin number and, similarly, (b) the estimated number of QCD multi-jet background bin entries as a function simply of the bin number. The F_{bkgd}-related terms in each plot have been factored out as they represent overall multiplicative factors only.

10.2.1 Correlations in Signal and Background Shape Parameters

Thus far only the extracted signal and background parameters themselves, together with their uncertainties, have been shown in Tables 8.1 and 9.3, respectively. The plots in Figure 10.2 show the associated correlation matrices for these parameters for the $R_{3/2}$ observable. In the case of the signal parameters, the values clearly correspond to the results of the global fit, in which all of the 10 parameters $\{\mathbf{a}\}$ were determined simultaneously[5].

[5]Refer to Section 8.4.

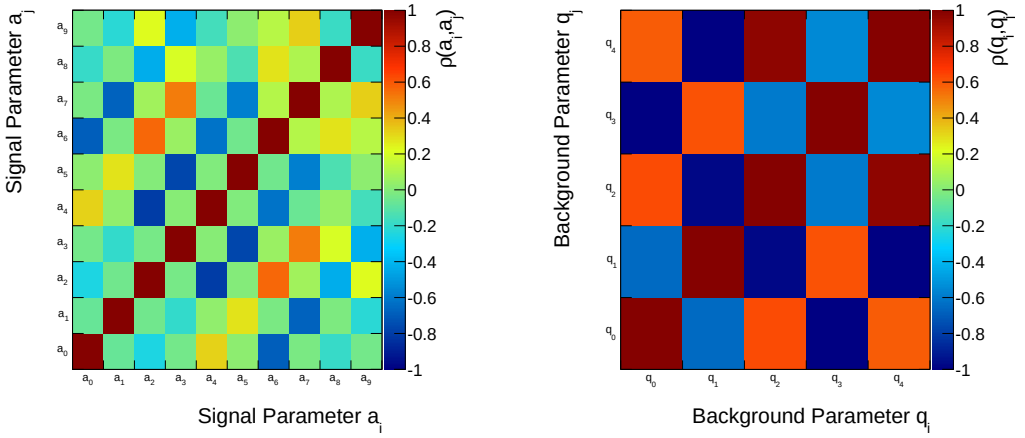

(a) Signal correlation matrix (10×10) (b) Background correlation matrix (5×5)

Figure 10.2: Correlation matrices for the extracted (a) signal and (b) background shape parameters. In the case of the signal parameters, the values are derived from the global fit using the bin contents of the $R_{3/2}$ distributions from all seven mass variation samples.

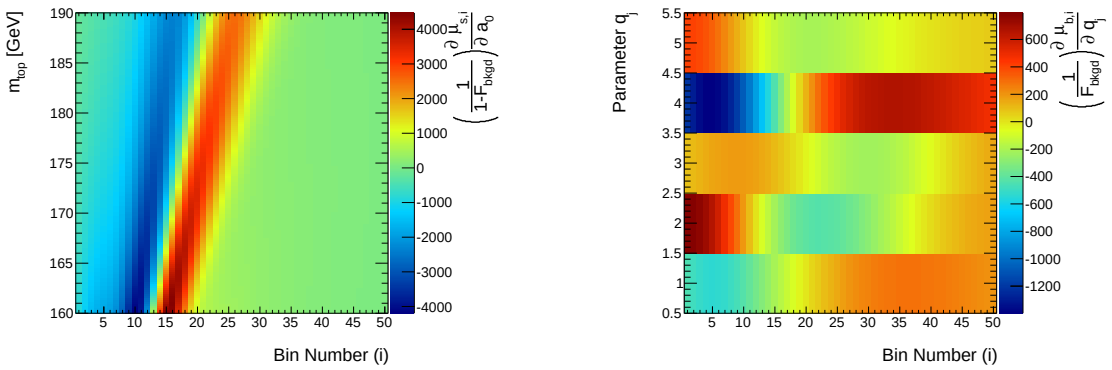

(a) (b)

Figure 10.3: Rates of change of the estimated number of (a) signal and (b) background events with respect to a small change in one of the shape parameters. The instantaneous rates of change are determined bin-by-bin and evaluated at the bin centres. As was the case in Figure 10.1, the F_{bkgd}-related terms in each plot have been factored out. In the case of (a), the rate of change with respect to a single parameter (a_0) is shown as a function of the value of m_{top}. In the case of (b), the rates of change with respect to all five background parameters are summarized in a single plot, where the parameter q_j is shown on the vertical axis.

The 10×10 covariance matrix $\mathbf{V(a)}$ which corresponds to the correlation matrix shown in Figure 10.2(a), can be transformed into the $N_{bins} \times N_{bins}$ covariance matrix $\mathbf{V(s)}$ required for the chi-squared minimization from Equation 10.3 by means of the Jacobian transoformation:

$$\mathbf{V}(\mathbf{s}) = \left(\frac{\partial \mu_s}{\partial \mathbf{a}}\right) \mathbf{V}(\mathbf{a}) \left(\frac{\partial \mu_s}{\partial \mathbf{a}}\right)^T \tag{10.8}$$

or equivalently, written out in component form:

$$V_{ij}(\mathbf{s}) = \sum_{k=0}^{9} \sum_{\ell=0}^{9} \left(\frac{\partial \mu_{s,i}}{\partial a_k}\right) V_{k\ell}(\mathbf{a}) \left(\frac{\partial \mu_{s,j}}{\partial a_\ell}\right) \tag{10.9}$$

Here it can be recognized from dimensional inspection that $\left(\frac{\partial \mu_s}{\partial \mathbf{a}}\right)$ must represent an $N_{bins} \times 10$ matrix; each of its components represents the expected change in a particular bin's estimated number of $R_{3/2}$ entries with respect to an infinitesimal change of a particular signal shape parameter. A complication arises in the fact that each of the terms in such a matrix are themselves a function of the parameter m_{top}.

A two-dimensional histogram can therefore be constructed such as the one in Figure 10.3(a), showing the **rate of change** of the bin contents shown in the plot in Figure 10.1(a), as a function of both the m_{top} parameter, and the bin number i, where the rate of change is with respect to a small change in the signal parameter a_0 – the intercept term corresponding to the mean of the Gaussian function. Nine other such plots are similarly produced for rates of change with respect to the other signal shape parameters, though the plot for a_0 is shown for the reason that it is easiest to interpret: a small increase in the Gauss mean's intercept *vs.* m_{top} would shift the peak to higher $R_{3/2}$ values, and a corresponding rise in the number of expected signal events above the original peak, as well as a drop in the expected number of signal events below it, would be observed. This can be seen to be the case. Bins far from the peak are less affected as can be expected. The analogous plots for the remaining parameters are shown in Appendix C.1.

Derivatives are all evaluated numerically by introducing a *per mil*-level increase to the particular parameter of interest and noting the change in the number of expected signal entries in each bin. For technical reasons a one-dimensional graph, as opposed to a two-dimensional histogram, must be produced for each of the $N_{bins} \times 10$ components of the $\left(\frac{\partial \mu_s}{\partial \mathbf{a}}\right)$ matrix – 500 in total. Each such graph then shows the change in that particular component as a function of m_{top}, such that a value can be interpolated for a specified value of m_{top}. In the same way, 50 one-dimensional graphs are produced from the two-dimensional histogram in Figure 10.1(a) such that the estimated signal entries themselves for a chosen value of m_{top} are able to be determined.

In the case of the $\mathbf{V(b)}$ covariance matrix associated with the background parameter uncertainties, the same steps follow, with the crucial difference that the background shape parameters are taken to be m_{top}-independent, and furthermore that there are only five relevant parameters. This means that a single two-dimensional histogram can be constructed which will remain fixed

for all values of m_{top}, and which shows the rate of change of the estimated number of background entries in a given bin with respect to a small change in one of the background shape parameters. This two-dimensional histogram is displayed in Figure 10.3(b).

Ultimately a total of 550 such look-up graphs for the signal entries are produced which are to be interpolated for each choice of m_{top} in the minimization procedure, as well as two, two-dimensional histograms for the background entries. The F_{bkgd} factors are to be subsequently applied to all signal and background entries as appropriate during each iteration of the minimization step.

For a given choice of the parameters m_{top} and F_{bkgd} then, the components in each of the Jacobian matrices become fixed and all of the components of the larger $N_{bins} \times N_{bins}$ covariance matrices can be computed *via* Equation 10.9. The uncertainties in the signal and background shape parameters propagate to small relative uncertainties in and correlations between the final $R_{3/2}$ bin contents, compared with the diagonal $\mathbf{V(d)}$ matrix itself. Their inclusion in the form of the $\mathbf{V(s)}$ and $\mathbf{V(b)}$ covariance matrices are nonetheless important in yielding an accurate value of the final measured parameters, and in the estimation of a statistical uncertainty on each of such parameters.

The individual covariance matrices $\mathbf{V(s)}$ and $\mathbf{V(b)}$ are displayed in Figures 10.4(a) and 10.4(b), respectively. The matrix components as shown are those evaluated at the final measured values of m_{top} and F_{bkgd} from data, yet to be presented, and they are meant to be illustrative only, recognizing that their particular values are continually changing throughout the minimization procedure.

Finally, Figure 10.4(c) shows the correlation matrix corresponding to the sum of all matrices: $\mathbf{V(d)}$, $\mathbf{V(s)}$, and $\mathbf{V(b)}$. Its components are displayed on a pseudo-log scale, whereby each component's correlation value ρ is transformed *via*:

$$\tilde{\log}_{10}(\rho) = \begin{cases} \log_{10}(\rho) & \text{if } \rho > 0 \\ 0 & \text{if } \rho = 0 \\ -\log_{10}(-\rho) & \text{if } \rho < 0 \end{cases} \tag{10.10}$$

Clearly small, but non-insignificant off-diagonal contributions from the addition of the signal and background terms are seen to exist. This is most noticeable in the tails of the $R_{3/2}$ distribution, but non-zero correlations are in general present and most apparent for nearest-neighbouring bins.

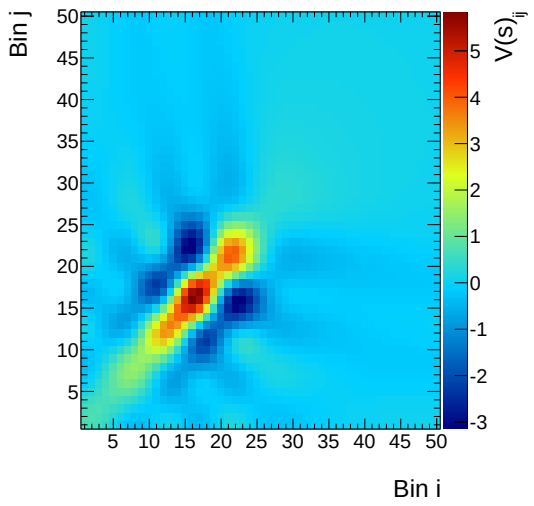

(a) Signal covariance matrix $\mathbf{V(s)}$.

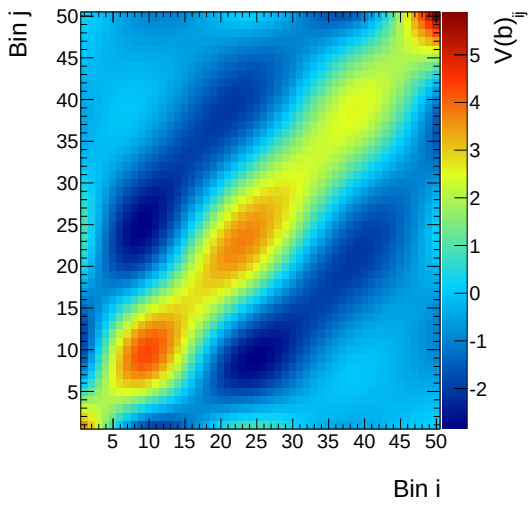

(b) Background covariance matrix $\mathbf{V(b)}$.

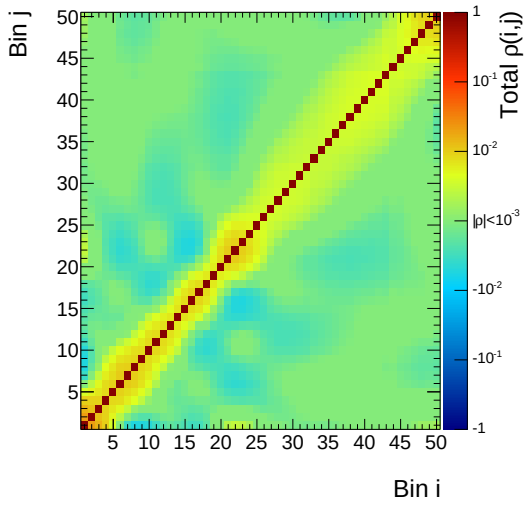

(c) Total correlation matrix as determined from the combined $\mathbf{V(d)}$+$\mathbf{V(s)}$+$\mathbf{V(b)}$ matrices.

Figure 10.4: Final 50 x 50 covariance matrices propagated from the (a) signal and (b) background shape uncertainties, and (c) the total correlation matrix. The horizontal and vertical axes correspond to the 50 bins of the $R_{3/2}$ distribution.

10.3 Extracting the Measured Top Quark Mass

A minimization package TMinuit from the ROOT framework is employed to minimize the χ^2 variable from Equation 10.3. The two unknown parameters varied throughout the minimization and extracted following convergence are the top quark mass m_{top}, and the background fraction F_{bkgd}. Figure 10.5(a) shows the final data distribution of the $R_{3/2}$ observable. Overlaid are the signal and combined background probability density functions, normalized to the total number of data entries N_d, and evaluated at the final extracted measured values of m_{top} and F_{bkgd}.

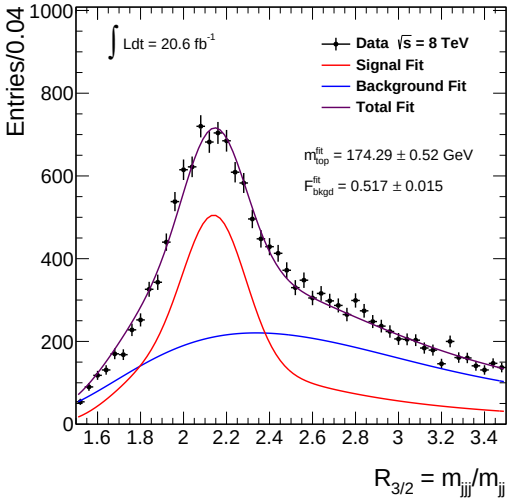

(a) Final data $R_{3/2}$ distribution with resulting signal and background templates overlaid from the results of the χ^2 minimization.

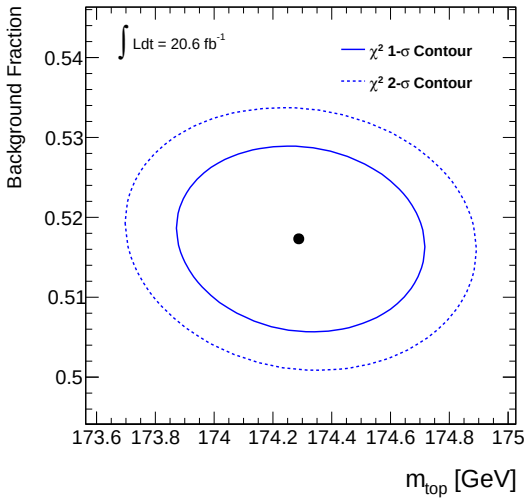

(b) 1- and 2-σ contours from the χ^2 minimization shown as a function of F_{bkgd} and m_{top}.

Figure 10.5: (a) Final data distribution of the $R_{3/2}$ observable together with fits and (b) 1- and 2-σ contour plots from the χ^2 minimization procedure used to extract the measured values of m_{top} and F_{bkgd}. The uncertainties on the measured values quoted in the figure are corrected for the level of correlation between pairs of $R_{3/2}$ values per event – to be described in Section 10.3.1. The contribution associated with the signal and background parameterization is also subtracted in quadrature from the extracted uncertainty as will be explained in the following chapter, such that the uncertainty shown here agrees with the final quoted statistical uncertainty.

Figure 10.5(b) shows one- and two-sigma contour regions around the final measured values of m_{top} and F_{bkgd}, depicted as the single black data point. Such one- and two-sigma contour regions correspond to contours in m_{top}-F_{bkgd} space at which $\chi^2 = \chi^2_{min} + 1$ and $\chi^2 = \chi^2_{min} + 2$, respectively. The one-sigma contour defines the statistical uncertainty on each measured values.

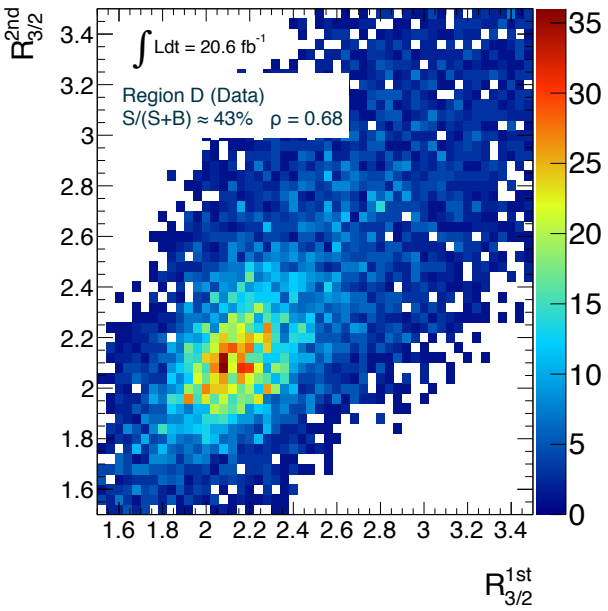

Figure 10.6: Two-dimensional histogram showing the level of correlation between pairs of reconstructed $R_{3/2}$ values from data events in the final signal region.

10.3.1 Accounting for Correlation Between $R_{3/2}$ Values

The final minimization outlined above makes use of the bin contents of one-dimensional distributions of the $R_{3/2}$ observable, where the total number of entries corresponds to exactly twice the number of events passing all of the event selection cuts. The analytic χ^2 method described in Chapter 6 and employed to reconstruct the two top quark candidates per event should however be expected to introduce some non-zero level of correlation between the two values of $R_{3/2}$. The subsequent event selection cuts will have further modified this correlation.

Figure 10.6 shows a two-dimensional distribution of the two reconstructed $R_{3/2}$ values from each event in order to highlight their correlation. Only data events following all event selection cuts were used to fill the histogram. The distribution shown is the two-dimensional equivalent of that from Figure 10.5(a) which shows the $R_{3/2}$ bin contents from data together with the overlayed final fits. The two values of $R_{3/2}$ are designated $R^{1st}_{3/2}$ and $R^{2nd}_{3/2}$ and are selected impartially for each event by drawing a random number from a uniform distribution. The linear correlation factor obtained from the distribution was found to be $\rho = 0.678 \pm 0.006$.

In order to properly correct for the correlation between the two $R_{3/2}$ values, the statistical uncertainty returned from the final minimization of the χ^2 variable in Equation 10.3 must be scaled up by a factor $\sqrt{1+\rho} \approx 1.30$. This correction factor $\sqrt{1+\rho}$ is justified in Appendix C.4.

The same linear correlation factor was determined analogously from the nominal set of simulated all-hadronic $t\bar{t}$ events at the central $m_{top} = 172.5$ GeV point. It was found to have a value of $\rho = 0.675 \pm 0.005$. In this case the level of correlation could also be expected to

have some potential dependence on the top quark mass[6]. A similar level of correlation was observed in the multijet background – a modification to the ABCD method was required in order to produce the analogous two-dimensional $R_{3/2}$ distribution in this case[7]. Although the individual ρ values from the data, the simulated signal and the estimated background are very similar, ultimately it is the value of $\rho = 0.678$ from data events which is of primary importance and which is used to correct the statistical uncertainty on the final measurement; it reflects the correlation present in the final sample used to perform the m_{top} extraction.

10.3.2 Extracted Values of m_{top} and F_{bkgd}

The values of each of the parameters, together with their corrected statistical uncertainties, were measured to be:

$$m_{top} = 174.29 \ \pm \ 0.52 \ \ \text{GeV}$$

and

$$F_{bkgd} = 0.517 \ \pm \ 0.015$$

A number of systematic uncertainties have thus far been neglected in the nominal measurement and must be included for a proper treatment of the total uncertainties in the measurement. The following chapter itemizes each of these systematic uncertainties in turn.

[6]It was found that the correlation factor between $R_{3/2}$ values $\rho\left(R_{3/2}^{1st}, R_{3/2}^{2nd}\right)$ decreases roughly linearly with increasing m_{top}. As no residual bias was observed in the tests of the method closure to be shown in Section 11.2, it was determined that the potential bias on the m_{top} measurement from this dependence was negligible.

[7]As an alternative approach one could build signal and background templates of the 2D distributions of $R_{3/2}$, where no such correction factor would be required. This was deemed more complicated with no expected gain in sensitivity. See Section C.3 however for a description of how the $R_{3/2}$ distribution could be obtained for the QCD multijet background using a modified 2D method analogous to the ABCD method presented in Chapter 9.

Chapter 11

Sources of Systematic Uncertainty

11.1 Introduction

This chapter outlines the various sources of uncertainty on the parameters m_{top} and F_{bkgd}, measured from data by means of the minimization procedure described in the preceding chapter.

The uncertainties on the final extracted parameters, both of statistical and systematic nature, are summarized in Table 11.1. Individual contributions are treated as symmeterized and the total is taken as a quadratic sum of all contributions, treating all sources independently. The fractional uncertainties on each measured parameter are also quoted.

Depending on the nature of the source of uncertainty there are two potential choices for the reference value of m_{top} appearing in both the difference (Δm_{top}) and the denominator of the fractional uncertainty ($\frac{\Delta m_{top}}{m_{top}}$). In the case that the simulated dataset used for calculating a particular systematic uncertainty consists of the identical events as those in the reference nominal sample, but subject to some systematic change, the events are 100% statistically correlated. In this case it makes sense to quote reference m_{top} value above to be the average m_{top} value as measured in the pseudo-experiments – to be described below – based on the original nominal sample. The JES uncertainty, to be described later in this chapter, is an example of such a case: the same nominal signal events are used with and without the JES uncertainty propagated to the jet four-vectors, so a direct comparison to the nominal result provides an appropriate measure of the true effect of this source of uncertainty.

In other cases a set of statistically independent events were simulated, and the average m_{top} value as determined from the closure tests – to be described in Section 11.2 – is used as the reference value, in order not to double-count effects arising from statistical fluctuations. The same cases apply to the quoted values of the background fraction parameter F_{bkgd}.

Table 11.1: Summary of all quoted sources of statistical and systematic uncertainties on the measured values of the top quark mass and background fraction. The various subcomponents for those entries denoted by the symbol † or ‡ are shown in Tables 11.3 and 11.4, respectively. Totals are evaluated by means of a quadratic sum and under the assumption that all contributions are uncorrelated. The uncertainties are subdivided into three categories: theoretical uncertainties, method-related uncertainties, and calibration- or detector-related uncertainties. The expected statistical uncertainties on the quoted values of Δm_{top} are also shown where applicable, but have no further bearing on the analysis.

Uncertainty	$\Delta m_{top}/m_{top}$ [%]	Δm_{top} [GeV]	$\Delta F_{bkgd}/F_{bkgd}$ [%]	ΔF_{bkgd}
Monte Carlo Generator	0.04	0.07 ± 0.27	6.45	0.033
Hadronization Modelling	0.25	0.44 ± 0.20	1.44	0.007
Parton Distribution Functions	0.02	0.03	1.21	0.006
Initial/Final-State Radiation	0.13	0.22 ± 0.43	7.44	0.038
Underlying Event	0.17	0.29 ± 0.22	0.86	0.004
Colour Reconnection	0.12	0.22 ± 0.22	1.99	0.010
Template Method Non-Closure	0.06	0.10	0.36	0.002
Signal and Bkgd Parameterization	0.06	0.10	0.56	0.003
Non All-Hadronic $t\bar{t}$ Contribution	0.03	0.06 ± 0.18	1.54	0.008
ABCD *vs.* ABCDEF	0.09	0.15 ± 0.19	0.69	0.003
Trigger Efficiency	0.05	0.08 ± 0.19	2.32	0.012
Pile-Up Dependence	0.13	0.22 ± 0.31	1.47	0.007
Pile-Up Reweighting	0.01	0.01 ± 0.19	0.50	0.003
Lepton/$E_{\mathrm{T}}^{\mathrm{miss}}$ Calibration‡	0.01	0.02	1.31	0.007
b-Tagging Scale Factors‡	0.01	0.02	6.72	0.034
Jet Energy Scale (JES)†	0.38	0.65	5.11	0.026
b-Jet Energy Scale (bJES)‡	0.22	0.37	1.04	0.005
Jet Energy Resolution	0.06	0.11 ± 0.19	5.00	0.025
Jet Reconstruction Efficiency	0.00	0.00 ± 0.19	0.55	0.003
Total Systematic	0.60	1.03	14.65	0.075
Total Statistical	0.30	0.52	2.89	0.015
Total Uncertainty	0.67	1.15	14.94	0.076

In what follows, a brief description is provided for the evaluation of each of the sources of systematic uncertainty. These are broken down into three categories. The first category, **theory- and modelling-related uncertainties**, is associated with the simulation of the signal Monte Carlo events. The second, **method-related uncertainties**, involve uncertainties in the way that the analysis has been performed, including the choice of a template method, the background modelling, and the final m_{top} extraction procedure. Finally a third category, **calibration- and detector-related uncertainties** involves uncertainties arising from the standard calibrations of physics objects in ATLAS.

Often it is the top quark mass parameter m_{top} which is of primary interest in the evaluation of systematic uncertainties, but the same prescriptions are employed for evaluating systematic uncertainties in the background fraction parameter F_{bkgd}. This is to be implied even if it is only m_{top} which is mentioned in a given context.

Prior to introducing each of the various sources in turn, a description is presented for the way in which the closure is evaluated for the analysis. The method closure is a test of the final m_{top} extraction machinery which is carried out by performing the standard minimization procedure as outlined in Chapter 10 on distributions of $R_{3/2}$. In performing closure tests these distributions are produced from simulated events for which the input value of m_{top} is known. The method is said to be closed when the difference between the average value of m_{top} returned from the fits and the true input m_{top} value is zero within statistical uncertainties. The general approach to performing closure tests is *via* so-called **pseudo experiments** [85]. As pseudo experiments are also used in order to quantify the uncertainty associated with each of the systematic sources, the adopted procedure is presented in detail here.

11.2 Template Method Closure

In an effort to validate the method employed to extract the top quark mass from the $R_{3/2}$ distribution from data and to check for any potential bias, a series of pseudo experiments were performed. For each of the seven m_{top} samples a total of 2500 pseudo distributions of the $R_{3/2}$ variable were produced[1]. The total number of events to be drawn for each pseudo experiment to generate these distributions is taken from a random number following a Poisson distribution with a mean parameter given by the total number of expected events – both signal and background combined – normalized to the integrated luminosity and cross-section for the samples in question. Two separate scenarios are investigated: in the first, events are drawn from the histograms of interest using the **TH1::GetRandom** function[2]; in the second scenario events are rather drawn

[1] This value of 2500 is also used when performing pseudo experiments to evaluate the systematic uncertainties.

[2] In this case the events are drawn from one-dimensional distributions of the $R_{3/2}$ observable, either from the nominal background or from the distributions from the respective m_{top} sample template shapes. A study was performed to validate this approach by drawing from two-dimensional $R_{3/2}$ distributions initially believed to be necessary to account for the correlation between pairs of $R_{3/2}$ values. See Section C.3.

directly from the parameterized signal or background shapes themselves[3], similarly using the **TF1::GetRandom** function[4]. In all cases the nominal values of all signal and background shape parameters are used[5], and therefore only the two parameters, m_{top} and F_{bkgd}, are left as parameters to be returned from the minimization procedure, as in the case of the nominal fit performed to the data distribution. For all seven top quark mass samples the same QCD background distribution is used for drawing pseudo background events.

Figure 11.1 shows a sample $R_{3/2}$ distribution drawn from the 165 GeV m_{top} histogram, together with the resulting fit. For each of the remaining 2499 pseudo experiments performed at this 165 GeV top mass point a similar, but not identical[6] distribution is produced by similarly drawing from the same signal and background histograms, or parameterized functions, as the case may be. For each of these distributions a fit is then performed returning a value of m_{top} and F_{bkgd}. The same process is then repeated for the remaining six m_{top} points.

The extracted values of m_{top} and F_{bkgd} from each pseudo experiment are then used to fill distributions of the difference in the fitted top quark mass value, m_{top}^{fit}, from the true generator-level top quark mass, m_{top}^{gen}, and similarly for F_{bkgd}. The true value of F_{bgkd}, labelled as F_{bkgd}^{histo}, is taken from the pseudo distribution bin contents themselves. Figure 11.2 shows such difference distributions (Δm_{top} and ΔF_{bkgd}), both for the case where events are drawn from the histograms and those where the events are drawn from the PDFs directly.

For each of the distributions of Δm_{top} and ΔF_{bkgd} in Figure 11.2 a single Gaussian fit is performed *via* a standard χ^2 minimization procedure, resulting in an estimator for the Gaussian mean and width parameters, each with their respective uncertainties: $\hat{\mu} \pm \delta\hat{\mu}$ and $\hat{\sigma} \pm \delta\hat{\sigma}$. These distributions can be seen to be very Gaussian in shape, and the uncertainties on the mean and width parameters can be expected to be very small. Visibly however one can note rather large deviations in the mean values of these distributions from the expected central position, particularly for the distributions corresponding to the cases where the pseudo events were drawn from the template histograms themselves. These deviations are the result of generating a large number (2500) of pseudo distributions by continually drawing from the same base template distributions which were themselves produced from Monte Carlo samples with a finite number of events, and which are consequently susceptible to statistical fluctuations[7]. In order to com-

[3]These shapes are the functional probability distribution functions (PDFs) from Equations 8.3 and 9.7.

[4]The functions referred to are functions associated with C++ classes in the ROOT analysis package. They allow random numbers to be drawn according to a probability distribution function defined by the bin contents of a given histogram (TH1) or from an analytic function (TF1) itself. TH1 and TF1 refer to the class names.

[5]That is, the values used are those corresponding to the global fit quoted in Table 8.1 for the signal parameters and the values in Table 9.3 for the background parameters.

[6]The same histograms or parameterized functions are used for drawing the events, but the difference arise due to different randomly generated numbers.

[7]Recall that black markers shown in the plots of Figure 8.7, corresponding to the signal shape parameters in each of the seven m_{top} samples, did not lie perfectly on the fitted lines associated with the global fit values. Since the same template distributions which led to these points were also used when drawing pseudodata for

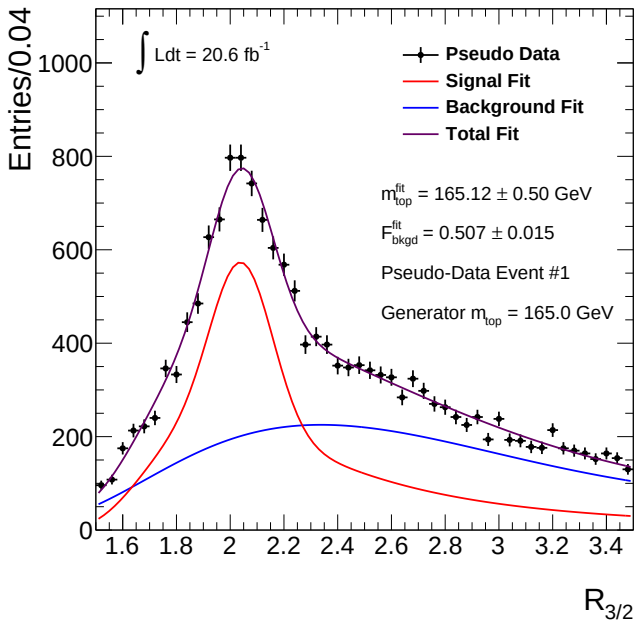

Figure 11.1: A sample pseudo $R_{3/2}$ distribution drawn from the 165 GeV m_{top} signal and the nominal background histograms. Also shown is the result of the corresponding total fit (magenta) as well as its decomposition into signal (red) and background (blue) components.

pensate for this oversampling effect, the error on the Gaussian mean parameter is corrected[8], in the case of each m_{top} sample, *via*:

$$\delta\hat{\mu}_{corr} = \delta\hat{\mu}\sqrt{1 + (N_{\psi} - 1)\,\rho} \tag{11.1}$$

In the above expression N_{ψ} is the number of pseudo experiments performed (2500) and ρ is representative of the probability that the same event will be redrawn from the same given distribution with replacement. The number of times that the same event will be chosen follows a Poisson distribution with mean $\lambda = n_s/N_{us}$, where n_s is the expected number of events in a given $R_{3/2}$ distribution normalized to the theoretical cross-section times integrated luminosity, and N_{us} the total number of Monte Carlo events generated, prior to the distributions being scaled[9]. The correction to the Gauss mean parameter *via* Equation 11.1 aims to account for the oversampling of individual, repeatedly sampled events due to the finite Monte Carlo statistics

each m_{top} point, similar deviations are to be expected in the fits to the pseudo distributions. An arbitrarily large number of pseudo experiments can be performed, but care must then be taken to correct for the fact that the precision cannot become arbitrarily good since one is often redrawing the same event; at some value of N_{ψ} there is no further gain achieved by performing additional pseudo experiments.

[8]See reference [86] for an explanation of the correction factors due to oversampling from a finite number of Monte Carlo events in this technique referred to as **bootstrapping**.

[9]As will be explained in the following pages the value of $\lambda = n_s/N_{us}$ will be used in order to calculate an expected value of ρ.

despite the fact that the values $R_{3/2}$ are already in the form of a binned histogram.

Since there are N_ψ pseudo experiments performed, the value of ρ must account for the probability of an event being drawn multiple times and in multiple pseudo experiments. The value of ρ can be taken as $\rho \approx 1 - e^{-n_s/N_{us}}$, which is an approximation to the true value given by the following expression – the one employed in the analysis [86]:

$$\rho_k = 1 - P(0) - \frac{P(1)}{2}P(1) - \frac{P(2)}{3}\left(P(2) + 2P(1)\right) - \ldots - \frac{P(k-1)}{k}\left(\sum_{i=1}^{k-1}(k-i)\,P(i)\right) \quad (11.2)$$

In the above the term $P(j)$ is a shorthand for $P(j|\lambda)$, the Poisson probability of selecting a value j given a mean parameter $\lambda = n_s/N_{us}$. Using the fact that $P(j|\lambda) = \frac{\lambda^j e^{-\lambda}}{j!}$, the full expression can rather be expressed as:

$$\rho_k = 1 \; - \; e^{-\lambda} - \; \sum_{\ell=2}^{k} \frac{P(\ell-1)}{\ell}\left(\sum_{i=1}^{\ell-1}(\ell-i)\,P(i)\right) \quad (11.3)$$

or more explicitly:

$$\rho_k = 1 \; - \; e^{-\lambda} \; - \; \sum_{\ell=2}^{k} \frac{\lambda^{\ell-1}e^{-\lambda}}{\ell!}\left(\sum_{i=1}^{\ell-1}(\ell-i)\,\frac{\lambda^i e^{-\lambda}}{i!}\right) \quad (11.4)$$

where in all cases[10] it is necessary that $k \geq 2$.

The value of ρ_k in the above equations quickly converges for increasing k, such that in the machinery of the program it is sufficient to continue to add terms to the series only until such time as $|\rho_k - \rho_{k+1}| < 0.001$ at which point the value of ρ is deemed to have sufficiently converged.

It should be noted that the quantity n_s/N_{us} becomes unity in the case that the number of simulated Monte Carlo signal events is equal to the expected number of signal events in data. For the central $m_{top} = 172.5$ GeV sample with 10M simulated events, the ratio n_s/N_{us} has a value of approximately 0.39 for signal only (neglecting the background), meaning that final distributions produced from this simulated sample were required to be scaled down by roughly a factor of 2.5 in order to compare the distributions with those from data. In the case of the remaining m_{top} samples, each with 4M generated events, this value lies in the range of 0.66 to 0.86, with the range due to the cross-section values which depend on the value of m_{top}. In an extreme case where $N_{us} \gg n_s$ (in which case the size of the simulated dataset far exceeds the expected number of events in data – not the case at present), then $\rho \approx 0$ and no such oversampling correction would be required.

In the above expressions it is assumed that there is only one relevant value of n_s/N_{us}, but

[10] Note that the $k = 1$ case is simply $\rho_1 = 1 - e^{-\lambda}$.

in reality the template distribution of $R_{3/2}$ used for drawing pseudo events for each generator m_{top} value comes from the sum of two individual pseudo distributions – one for each the signal and the background – which have separate effective scaling factors n_s/N_{us}. The scale for the QCD distribution comes directly from the evaluation of the QCD multi-jet normalization in the ABCD method *via* Equation 9.1. This means that the value of n_s/N_{us} for the background is therefore given by $\frac{N_b^{CR\ C}}{N_b^{CR\ A}}$. Since the same background distribution is used for drawing the pseudo background events from all m_{top} samples, this ratio is the same in all cases. The effective value of ρ must however take into account the appropriate fractional contribution from the signal and background. Here we let the n_s/N_{us} terms for the signal (for a given mass sample) and the background be represented by λ_s and λ_b, respectively. The appropriate value of ρ to use then will be given by:

$$\begin{aligned}\rho_k \;=\; 1 \;-\; (1 - F_{bkgd}) \left[e^{-\lambda_s} \;+\; \sum_{\ell=2}^{k} \frac{\lambda_s^{\ell-1} e^{-\lambda_s}}{\ell!} \left(\sum_{i=1}^{\ell-1} (\ell - i) \frac{\lambda_s^i e^{-\lambda_s}}{i!} \right) \right] \\ -\; F_{bkgd} \left[e^{-\lambda_b} \;+\; \sum_{\ell=2}^{k} \frac{\lambda_b^{\ell-1} e^{-\lambda_b}}{\ell!} \left(\sum_{i=1}^{\ell-1} (\ell - i) \frac{\lambda_b^i e^{-\lambda_b}}{i!} \right) \right] \end{aligned} \tag{11.5}$$

The value of the background fraction F_{bkgd} is evaluated for all m_{top} samples analogously to the way in which the value shown in Table 9.2 was determined. This value is based only on the plotted range of the $R_{3/2}$ distribution without the inclusion of overflow or underflow bins.

Table 11.2 summarizes the values relevant to the oversampling corrections for the 7 top quark mass samples in building the $R_{3/2}$ distributions used for performing the template closure tests. In particular the final column shows the final value of $\delta\hat{\mu}_{corr}/\delta\hat{\mu}$ – the value by which the Gaussian mean error is scaled up due to oversampling.

For the Gaussian width parameter no such correction was initially applied due to the oversampling from finite Monte Carlo statistics; the value of $\delta\hat{\sigma}$ returned from the fit was used directly in setting the corresponding uncertainty.

However, an final residual correction was subsequently applied to both the Gaussian mean and width parameter. This residual correction will be described shortly.

Pull distributions, similar to the difference distributions (Δm_{top} and ΔF_{bkgd}) described above and shown in Figure 11.2, were constructed in an analogous fashion. The pull [82] is defined as:

$$Pull = \left(m_{top}^{fit} - m_{top}^{gen} \right) / \delta m_{top} \tag{11.6}$$

In the above, δm_{top} is the statistical uncertainty on the m_{top} parameter returned following each minimization. The quantity $\left\langle \left(m_{top}^{fit} - m_{top}^{gen} \right) / \delta m_{top} \right\rangle$, referred to as the **pull mean**, corresponds

Table 11.2: The relevant quantities used in order to derive the oversampling correction factor to scale up the fitted Gauss mean parameter, $\delta\hat{\mu}_{corr}/\delta\hat{\mu}$, based on the numbers of events in the signal and background distributions of the $R_{3/2}$ observable before and after scaling the distributions. The terms λ_s and λ_b as well as the probability ρ are described in the text.

Mass Sample m_{top} [GeV]	F_{bkgd}	λ_s	λ_b	ρ	$\delta\hat{\mu}_{corr}/\delta\hat{\mu}$
165.0	0.509	0.859	0.024	0.230	23.981
167.5	0.505	0.822	0.024	0.227	23.828
170.0	0.499	0.785	0.024	0.224	23.685
172.5	0.491	0.389	0.024	0.152	19.523
175.0	0.501	0.716	0.024	0.213	23.105
177.5	0.517	0.687	0.024	0.203	22.543
180.0	0.522	0.660	0.024	0.197	22.201

to the value of the fitted Gaussian mean parameter for each top quark mass point[11], and these values are shown as a function of the input m_{top}^{gen} value in Figure 11.3(a). Figure 11.3(b) shows the analogous Gaussian width parameter σ, referred to as the **pull width**, as a function of the generator top quark mass. The error bars in each case are the uncertainties $\delta\hat{\mu}_{corr}$ and $\delta\hat{\sigma}$, respectively, each multiplied by a residual factor which will be described now.

In the case of each of the plots in Figure 11.3 a zeroth-order polynomial fit was initially performed to the solid black markers. This resulted in an average pull mean consistent with zero and an average pull width consistent with one, though the level of scatter of the data points suggested that the oversampling correction applied was smaller than necessary – the χ^2 value returned from the minimization divided by the **number of degrees of freedom** (ndf) was too large. In such cases a common technique is to scale up the size of the error bars by a factor $\sqrt{\chi^2/\text{ndf}}$ such that the final χ^2/ndf from the sum of the residuals is unity by construction[12]. It should be emphasized that this residual correction has no effect on the final measured values of m_{top}, F_{bkgd}, nor on their quoted uncertainties; it serves solely to increase the sizes of the error bars of the points in the Figures 11.3 (as well as similarly constructed plots shown in the appendix) in order to reflect the fact that a larger oversampling correction was required compared with those quoted in the final column of Table 11.2.

[11]It should be highlighted that while it is referred to as the pull mean, it is evaluated not as a true arithmetic mean but as the Gaussian mean parameter from a least-squares fit.

[12]Such a procedure is used in [87] and referenced in the introductory section of [3].

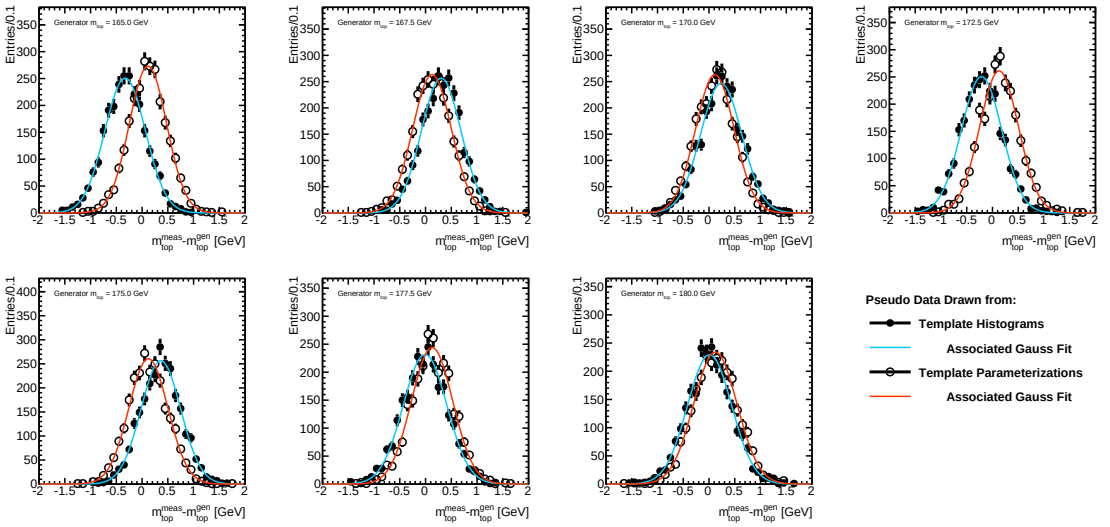

(a)

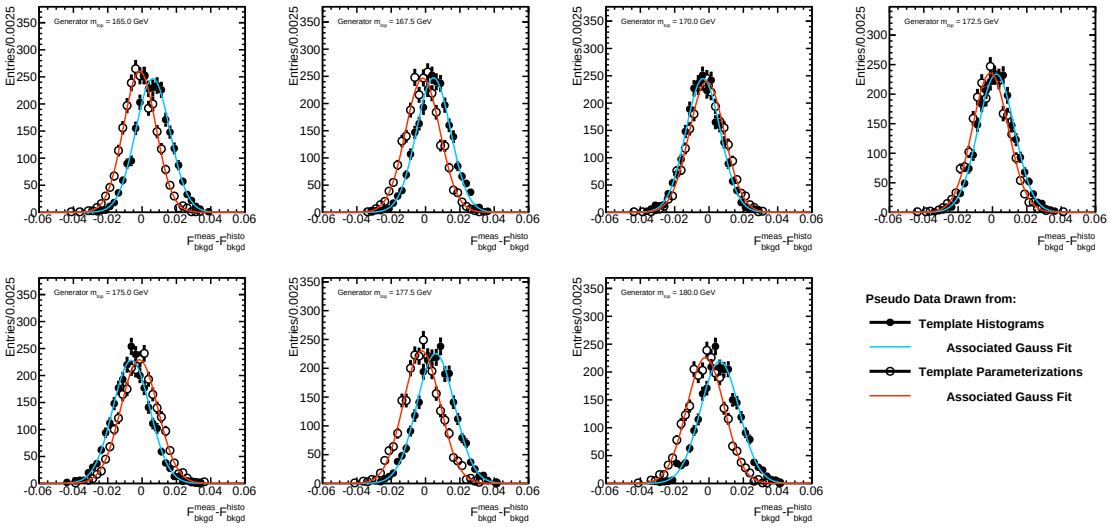

(b)

Figure 11.2: Distributions from pseudo experiments for each of the seven fast-simulation top mass samples in the range of m_{top} from 165 to 180 GeV. Plotted are the difference in the (a) m_{top} and the (b) background fraction F_{bkgd} from the reference value. The solid black markers correspond to cases where the pseudo events were drawn from the $R_{3/2}$ histograms, and the open markers where pseudo events were drawn from the parameterizations themselves. In either case a single Gaussian fit is performed by means of a standard least-squares minimization.

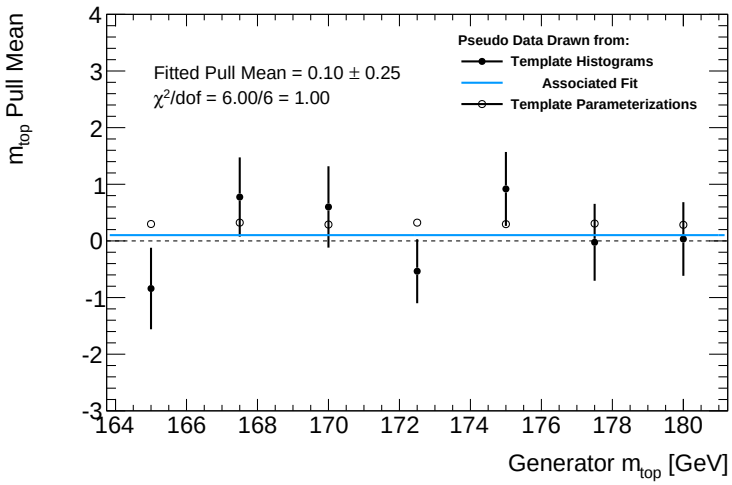

(a)

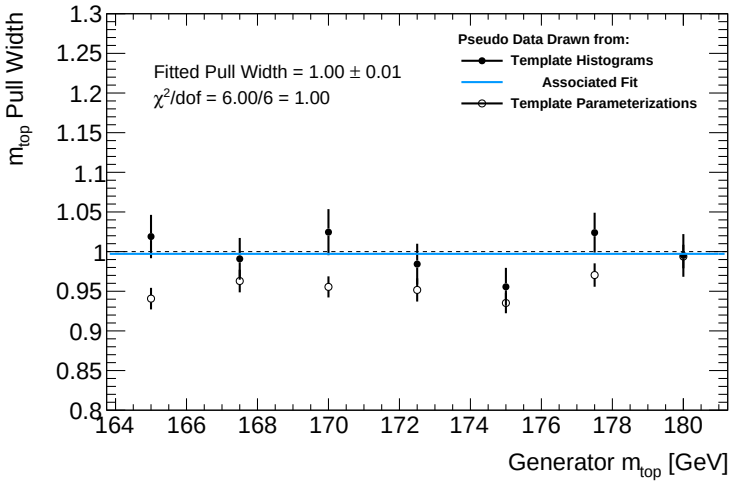

(b)

Figure 11.3: The (a) mean and (b) width parameters from the m_{top} pull distributions, $\left(m_{top}^{fit} - m_{top}^{gen}\right)/\delta m_{top}$, based on the results of a single Gaussian fit to distributions analogous to those from Figure 11.2(a). The solid black markers correspond to cases where the pseudo events were drawn from the $R_{3/2}$ histograms, and the open markers where pseudo events were drawn from the parameterizations themselves. The solid blue line corresponds to a zeroth-order polynomial fit performed based on the seven black markers and their corrected uncertainties (including the residual corrections) as described in the text.

Ultimately in Figure 11.3(a) the pull mean can be seen to be consistent with zero within

statistical uncertainties, and in Figure 11.3(b) the pull width is also seen to be consistent with one. The method is therefore shown to be closed, within statistical uncertainties, and no residual m_{top}-dependent bias is observed.

11.3 Statistical Component of Systematic Uncertainties

The machinery described in the previous section for performing pseudo experiments is used not only for the closure tests, but also for quantifying the systematic uncertainties for a variety of effects. The various simulated datasets used to check the effect of a given systematic sample also consist of a finite number of simulated Monte Carlo events. For certain systematic sources the same signal samples are used for both the nominal reference case as well as the modified systematic case. In other cases an entirely different set of simulated Monte Carlo events are produced. For all cases a total of 2500 pseudo distributions of the $R_{3/2}$ observable are produced and a Gauss fit is performed based on the resulting values of m_{top} and F_{bkgd}. The fitted Gauss mean parameter based on the results of all 2500 pseudo experiments is taken to be the value of m_{top} (or F_{bkgd}) associated with that given systematic or reference sample. The uncertainty on this value is scaled up, in all cases, by the oversampling correction factor given by Equation 11.1 multiplied by the residual correction described earlier. The values of λ_s and λ_b as well as the resulting value of ρ in each particular case (evaluated using Equation 11.5) are used to determine the original oversampling correction factor (without the residual correction). It should be noted that this factor will be largest in the case that the number of simulated Monte Carlo events is small. The residual correction factor, as described at the end of Section 11.2, is subsequently applied.

For cases where a systematic uncertainty is quoted as a difference between the results of pseudo experiments using that systematic sample and those using the nominal sample, the statistical uncertainty on the systematic value quoted in Table 11.1 is the sum in quadrature of the two uncertainties on the corresponding Gauss mean terms, each corrected for oversampling. This reflects the fact that the two samples are treated as statistically independent.

It should be highlighted that the level of statistical uncertainty on individual sources of systematic uncertainty has no bearing on any subsequent stages of the analysis; the values are merely quoted to provide a level of the expected precision on the sources of systematic uncertainty. It is recognized that increased Monte Carlo statistics would allow the statistical components of the systematic uncertainties to be reduced – in the case that an arbitrarily high number of simulated events were produced, any differences in the average m_{top} value from that obtained in the nominal case would be expected to be the result of a true systematic shift alone.

11.4 Optimization of Event Selection Cuts

A variety of studies have been performed over the course of the analysis in order to select the optimal cut values to be employed in helping to identify signal events from the data. In the earlier stages of the analysis these cut values, and the choice of the variables themselves, were motivated from normalized distributions such as those presented in Figure 7.4, in addition to selection cuts employed in previous ATLAS analyses[13]. These optimization studies involved making comparisons, for varying choices of the cut values, of the signal efficiency[14] (ε_{signal}), the top reconstruction purity[15] ($\mathcal{P}_{reco}$), the signal fraction relative to the combined number of estimated signal and background events (S/(S+B)), and the statistical uncertainty on the measured value of m_{top}[16]. Following the introduction of the various sources of systematic uncertainty in what will be described below, the optimization criteria were reinterpreted to correspond to the set of cut values yielding the smallest total uncertainty on the measured value of m_{top} – the sum in quadrature of all statistical and systematic uncertainties. A number of different regions of phase space were explored for comparisons of the final sensitivity of the measurement. Some of the choices included modifications of p_{T} thresholds, the introduction of upper limits on the jet multiplicity (N_{jet}), and an adjustment of angular separation (ΔR or $\Delta\phi$) cuts to modify the suppresion of contributions from backgrounds processes. The precision of the final measurement was shown to be largely impervious to such changes. The values ultimately adopted for the event selection cuts reflect the values leading to the optimal precision as determined from these studies.

11.5 Theory- and Modelling-Related Uncertainties

11.5.1 Monte Carlo Generator

In order to assess the impact on the m_{top} measurement due to the choice of MC generator, the results of pseudo experiments using two different simulated samples are compared: one sample produced using Powheg as the MC generator and a second sample using MC@NLO [89]. Both samples use Herwig with the AUET2 tune as the choice of hadronization model [90], in contrast with the nominal signal MC where Pythia is used. The absolute difference in the resulting average m_{top} parameter returned from the fits based on the pseudo experiements is quoted as the symmeterized uncertainty.

[13] See for example the analogous top quark mass measurement in the all-hadronic $t\bar{t}$ decay channel performed by the ATLAS collaboration at a centre of mass energy of $\sqrt{s} = 7$ TeV [79], as well as study on the prospects for a mass measurement based on simulated events [88].

[14] Refer to Section 7.3 for a definition of the signal efficiency.

[15] Refer to Section 6.2 for a definition of the reconstruction purity.

[16] Note that the statistical uncertainty on the measurement is strongly anti-correlated with the signal efficiency.

11.5.2 Hadronization Modelling

To quantify the expected difference in the measured m_{top} value as a choice of hadronization model, pseudo experiments were performed for two independent datasets both employing Powheg to generate the all-hadronic $t\bar{t}$ events but differing in their choice of hadronization model. In the first case Pythia is used for the parton showering and hadronization model with the Perugia 2011C tune [69]. The results from this are compared to those using an independent dataset in which Herwig with the AUET2 tune for the parton showering and hadronization is used. The absolute difference between the average m_{top} value obtained in the two cases is quoted as the systematic uncertainty due to hadronization modelling.

11.5.3 Proton Parton Distribution Functions

A variety of proton parton distribution function (PDF) sets[17] are investigated in order to assess the impact of the choice of CT10 – the default PDF set used in the nominal measurement – on the measured value of m_{top}. There are a total of 53 distinct sets considered for the CTEQ PDFs. In addition there are 101 distinct NNPDF23 PDF sets and 41 distinct MSTW2008 PDF sets to consider for a total of 195 distinct sets to compare. A single set of simulated Powheg+Herwig events is used for the comparison, and in each case that a different PDF set is used, the events are given a weight which results in a modified initial number of weighted events for scaling the final simulated distributions. For a given PDF set the weight ξ is determined, at leading order, by comparison to the central values *via*:

$$\xi = \frac{x_1 g_i(x_1;\mu^2)}{x_1 f_i(x_1;\mu^2)} \times \frac{x_2 g_i(x_2;\mu^2)}{x_2 f_i(x_2;\mu^2)} \tag{11.7}$$

In the above expression, $x_1 f_i(x_1;\mu^2)$ corresponds to the parton distribution function from Equations 2.3 and 2.4 for the parton with momentum fraction x_1 of incoming proton 1 and using the nominal PDF set. The term $x_1 g_i(x_1;\mu^2)$ corresponds to the analogous term using the modified PDF set. The remaining two terms correspond to both the nominal and modified cases for the oppositely directed proton 2, where the parton carries momentum fraction x_2.

Pseudo experiments are then performed with the modified normalization taken into account, and the resulting average m_{top} values obtained in each of the 195 cases are compared. For the CT10 PDFs, the difference between the up and down variations are added in quadrature, and half the quadratic sum is taken as the total deviation for the CT10 PDF sets. A similar procedure is adopted for the MSTW and NNPDF sets. The final quoted value is evaluated by selecting the largest deviation from the reference value for each type of PDF set with respect to either the up or down variation. This value is quoted as the final proton PDF systematic uncertainty on m_{top}.

[17] Refer to the description of the partonic structure of the protons in Section 2.2.2.

11.5.4 Initial and Final State Radiation

The presence of more or less **initial** and **final state radiation** (ISR and FSR) can have an impact on the number of reconstructed jets in p-p collision events, which in turn can affect the overall measurement of the top quark mass. In order to quantify this sensitivity to ISR/FSR a number of simulated signal events were produced, with the leading-order AcerMC as the Monte Carlo generator [91] and Pythia with the AUET2B tune for the parton showering and hadronization. Differing parton shower strengths are used giving rise to differences in the amount of radiation present in the simulated all-hadronic $t\bar{t}$ events. Half the absolute difference between the average measured m_{top} values from the pseudo experiments is quoted as the corresponding systematic uncertainty[18].

11.5.5 Underlying Event

Additional semi-hard **multiple parton interactions** (MPI) present in the hard-scattering process can lead to differences in the resulting kinematics of the underlying event – additional activity attributed to the interactions from the partonic remnants of the protons other than those two involved in the primary hard-scatter interaction of interest. The amount of such additional semi-hard MPI present is a tunable parameter in Pythia – the choice of model for the parton showering and hadronization [69]. Simulated signal $t\bar{t}$ events were produced using a generator-level top quark mass of 172.5 GeV but with an increased amount of semi-hard MPI in order to assess the potential impact on the final measurement. The absolute difference between the results of these pseudo experiments and the average non-closure is quoted as the corresponding systematic uncertainty.

11.5.6 Colour Reconnection

Simulated signal $t\bar{t}$ events using Pythia for the parton shower and hadronization modelling have a tunable parameter associated with the colour reconnection strength due to the colour flow along parton lines in the strong-interaction hard-scattering process. A number of simulated signal $t\bar{t}$ events were produced with the Pythia P2012loCR tune which offers a reduced colour reconnection strength. The motivation for the introduction of such a tunable parameter in the simulation process stems from measurements of average charged particle p_{T} as a function of track multiplicity (N_{ch}) in results from the CDF experiment [69]. The absolute difference between the results of pseudo experiments with the suppressed colour reconnection and the average non-closure is quoted as the systematic uncertainty.

[18] At the time of writing the ISR and FSR systematic samples used to evaluate this source of systematic uncertainty consist of a smaller number of generated events (1.2M for each ISR and FSR). Consequently the statistical component on the quoted systematic uncertainty – not the systematic uncertainty itself – is the largest of all systematic sources due to this limited number of simulated events.

11.6 Method-Dependent Uncertainties

11.6.1 Non-Closure of Template Method

Based on the results of the closure tests, no bias was observed in the case of the pull mean[19]. A zeroth-order polynomial fit is also performed for the associated difference plot $(m_{top}^{fit} - m_{top}^{gen})$ as a function of m_{top}^{gen} and based on the results of the fit the larger of either the fitted parameter or its uncertainty is quoted for the non-closure systematic uncertainty on the value of m_{top}.

11.6.2 Signal and Background Parameterization

As described in the previous chapter in Section 10.1, the uncertainties in the shape parameters of the $R_{3/2}$ observable for both signal and background contributions are propagated into $N_{bins} \times N_{bins}$ covariance matrices $\mathbf{V(s)}$ and $\mathbf{V(b)}$, respectively, which are then included in the minimization of the final χ^2 variable in order to extract the top quark mass parameter m_{top}. Omitting these contributions would yield a simplified definition of the χ^2 variable such that Equation 10.3 would become:

$$\chi^2 = \sum_{bin\ i}^{N_{bins}} \sum_{bin\ j}^{N_{bins}} (n_i - \mu_i)\,(n_j - \mu_j)\,[\mathbf{V(d)}]^{-1}_{ij} = \sum_{bin\ i}^{N_{bins}} \frac{(n_i - \mu_i)^2}{n_i} \tag{11.8}$$

which can be recognized to be identical to the form given in Equation 10.1. The fit to the data distribution is repeated using this simplified definition of the χ^2 variable. This results in a slightly modified value of the m_{top} parameter being returned, and a smaller statistical uncertainty. The quadratic difference between the final statistical uncertainty returned from the original minimization and this modified value is quoted as the uncertainty attributed to uncertainties in the signal and background parameterization alone. The value of the original statistical uncertainty is consequently modified in Table 11.1 to reflect the fact that this decomposition has been performed.

11.6.3 Inclusion of Non All-Hadronic $t\bar{t}$ Background

A number of event selection requirements, such as the lepton veto and the requirement that the missing transverse energy satisfy $E_{\mathrm{T}}^{\mathrm{miss}} < 60$ GeV, results in a large suppression of the potential background contributions arising from non all-hadronic $t\bar{t}$ events. The estimated fractional

[19]The open markers in the plots of Figure 11.3 which show the pull mean and width as a function of the generator m_{top} value indicate that when drawing pseudo events from the template parameterizations themselves a small potential m_{top}-independent bias exists. This is not corrected for in the final measurement.

contribution from such events in the final signal region is below 3%[20].

The implicit assumption made by not including the non all-hadronic $t\bar{t}$ contribution in the background is that the normalized shapes of the $R_{3/2}$ distributions for both the QCD and non all-hadronic $t\bar{t}$ do not differ. This assumption is incorrect, but provided the discrepancies are small, the resulting differences between the estimated and the true QCD multi-jet shape should be minimal. By not including the non all-hadronic $t\bar{t}$ contribution implicitly, the shape and normalization of the QCD distribution in the final signal region is inferred using data and all-hadronic $t\bar{t}$ signal events alone, and the ABCD method presented in Chapter 9 reinterprets all signal-subtracted data distributions to be reflective of QCD multi-jets events. As a consequence the non all-hadronic $t\bar{t}$ contributions are in a way effectively absorbed by the estimated QCD multi-jet shape, but it is recognized that a small effect due to true non all-hadronic $t\bar{t}$ events will remain.

The advantages of neglecting the non all-hadronic $t\bar{t}$ contribution in the nominal measurement are largely technical: including the non all-hadronic $t\bar{t}$ into the machinery of the extraction procedure would invalidate the assumption that the background shape and normalization are independent of the m_{top} parameter – there are true top quarks in such events so there should be some dependence on the shape, however small, due to the choice of m_{top}. In addition, a necessary amount of undesireable complexity would be added to the program framework in the evaluation of systematic uncertainties: evaluating any of the other systematic uncertainties on m_{top} would require modified simulated datasets not only for signal all-hadronic $t\bar{t}$ events but also non all-hadronic events. This would have the effect of doubling the amount of work required for large parts of the systematic uncertainty evaluations.

The impact of such a choice must however be evaluated as a consequence. To this end the nominal measurement was repeated, this time allowing for the contribution from non all-hadronic $t\bar{t}$ events separately, in order to validate the choice of neglecting its contribution in the final analysis, and to assign a corresponding systematic uncertainty to this choice.

Equation 9.2 used for estimating the normalization of the QCD shape in control region A, for example, is modified to become:

$$N_b^{CR\ A} = \sum_{i=0}^{N_{bins}+1} \left(n_i^{CR\ A} - \mu_{s,i}^{CR\ A} - \mu_{\ell,i}^{CR\ A} \right) \tag{11.9}$$

where $\mu_{\ell,i}^{CR\ A}$ represents the estimated number of non all-hadronic $t\bar{t}$ events. The equations for estimating the QCD bin contents, as well as those for the other control regions, are adjusted analogously. The resulting final distribution for the $R_{3/2}$ observable with these modifications can

[20]The value of 3% was evaluated by producing distributions of all key variables, including $R_{3/2}$, using simulated $t\bar{t}$ events in which at least one of the W bosons decays leptonically. The distributions were normalized to their theoretical cross-section times branching ratio and the integrated luminosity considered. This was then compared to the total number of data events observed in the final signal region.

be seen in Figure 11.4(b) where the non all-hadronic $t\bar{t}$ contribution is shown explicitly in orange. Similarly to the nominal case, good agreement between data and simulation is observed. Pseudo experiments were subsequently performed by drawing events from the nominal signal distribution but from the modified background, now consisting of both QCD and non all-hadronic $t\bar{t}$. The absolute difference between the average m_{top} value obtained in this way and that from the nominal case is quoted as a systematic uncertainty.

For the purpose of comparison, the pie charts showing the fractional contribution for each process in the various signal and control regions, analgous to those shown in Figure 9.2 but with the specific inclusion of non all-hadronic $t\bar{t}$ events, are shown in Figure 11.4(a). As in the case of the nominal pie charts, the quoted values are estimated using a mix of data and simulation.

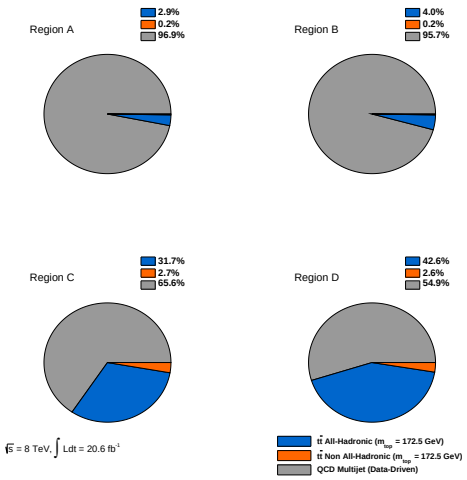

(a) Estimated fractional contributions from each, evaluated using both data and simulated events in the final control and signal regions of the $R_{3/2}$ observable.

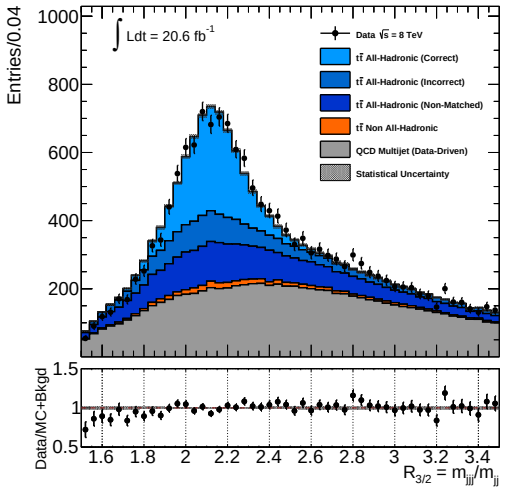

(b) Final comparison of data and simulation for the $R_{3/2}$ observable in the case that the non all-hadronic $t\bar{t}$ contribution is included explicitly prior to evaluating the QCD multi-jet bin contents *via* the ABCD method.

Figure 11.4: Systematic plots associated with the inclusion of the non all-hadronic $t\bar{t}$.

11.6.4 Variation in the Number of Control Regions

A variation on the background estimation procedure was considered in which six distinct regions, rather than four, were considered for the ABCD method used to estimate the QCD background. This was done by allowing for three different cases for the value of observable one, such that for a given event N_{b-tag} can have values of 0, 1, or greater than 1. Events can then be separated

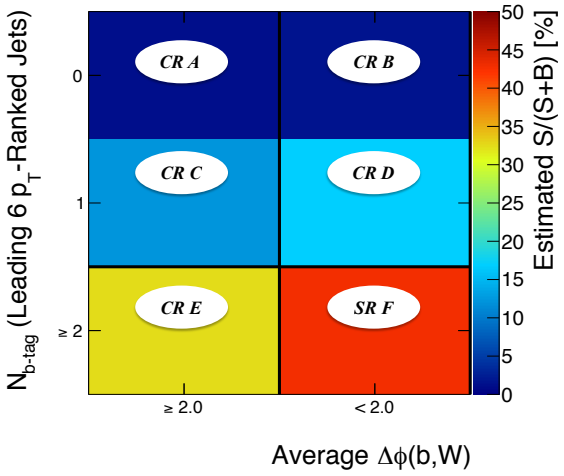

Figure 11.5: Two-dimensional plot of the estimated signal fraction, shown as a percent, as a function of the two final event selection cut variables, which are used to classify the five control regions (CR) and final signal region (SR) for the modified ABCDEF method. The plot is produced in an identical way to that shown for the nominal ABCD method in Figure 9.1.

into the six differing control regions as was done in the nominal analysis. In the nominal case of four ABCD regions, the regions with 0 and 1 b-tagged jet can effectively be thought of as having been merged together. As in the nominal case the number of b-tagged jets in an event considers only the leading six jets, ordered in p_{T}. The values of the second ABCD variable, $\langle \Delta\phi(b, W) \rangle$, are unchanged from the nominal case.

One reason for considering this alternative is that the inclusion of a larger number of control regions could potentially provide sensitivity to different physics processes – the relative contribution of some backgrounds could be larger in the 0-tagged jet compared with the 1-tagged jet bin. Additionally the overall contribution to a systematic uncertainty on the measured value of m_{top} arising from uncertainties in the b-tagging scale factors could differ between these methods.

With a total of six rather than four regions the machinery of the background estimation technique remains similar to that described in Section 9.1. The final signal region is labelled F rather than D; region D now, together with region B, is used to predict the shape of of the QCD multi-jet background in region F, whereas regions A, C, and E set the QCD normalization. For the purposes of the normalization, regions C and E are given equal weight, and similarly for the two contributions to the QCD multi-jet shape equal weight is given to the shapes in regions B and D. The six regions, together with the estimated signal fraction in each region as determined from both data and simulation, are shown in Figure 11.5.

Equation 9.5 which describes the estimated number of QCD multi-jet background events for region F in bin i would transform to the following:

$$\mu_{b,i}^{SR\ F} = \left(\frac{N_b^{CR\ E}}{2}\right)\left[\left(\frac{1}{N_b^{CR\ A}}\right)\mu_{b,i}^{CR\ B} + \left(\frac{1}{N_b^{CR\ C}}\right)\mu_{b,i}^{CR\ D}\right] \tag{11.10}$$

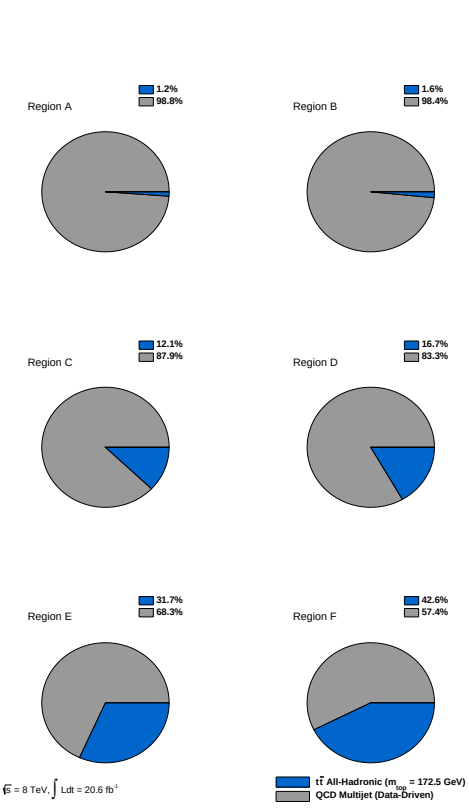

(a) Estimated signal fractions in the six different ABCDEF regions, evaluated using both data and the nominal all-hadronic $t\bar{t}$ Monte Carlo events.

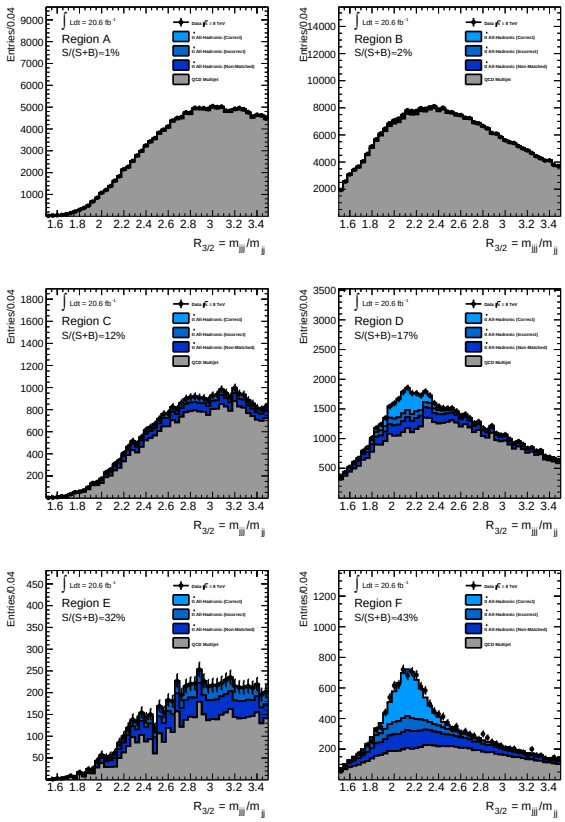

(b) The $R_{3/2}$ distributions in all six regions used for the modified background estimation method. Black points correspond to the data entries, and grey distributions to the estimated QCD multi-jet bin contents.

Figure 11.6: Systematic plots associated with the choice of the number of control regions of the QCD background estimation method.

Pseudo experiments were performed by drawing background events from the modified QCD multi-jet distribution in the final signal region. The differences between the final results using either four or six regions are small. The absolute difference between this and the nominal case is quoted as the systematic uncertainty[21].

[21] A further approach which yields the smallest amount of signal contamination in the estimation of the background shape is to use the originaly four ABCD regions but to ignore any events for which $N_{b-tag} = 1$. In such a case control regions A and B consist only of events with exactly zero b-tagged jets. The overall result is a slightly smoother QCD multi-jet background shape, but since the improvement in the overall precision is negligible, the standard ABCD signal and control region definitions were kept.

Figures 11.6(a) and 11.6(b) were produced using the standard ABCD method machinery, but with the modified definition of the control and signal regions. These are analogous to Figures 9.2 and 9.9 presented for the nominal analysis, respectively.

11.7 Calibration- and Detector-Related Uncertainties

11.7.1 Trigger Efficiency

The trigger efficiency plot produced using simulated signal events and shown in Section 7.4.3 shows the fraction of events passing the trigger used for the analysis as a function of the p_{T} of the fifth-leading jet[22]. In a measurement of the inclusive $t\bar{t}$ production cross-section in the all-hadronic decay channel using ATLAS $\sqrt{s} = 8$ TeV data an identical plot was produced for the jets in real data events using the same trigger item [75]. When comparing the trigger efficiency curve in data to that for the simulated $t\bar{t}$ events a discrepancy was observed.

This difference can be seen in Figure 11.7(a) for the full range from $0 \leq p_{\mathrm{T}}^{5th} \leq 100$ GeV. Figure 11.7(b) shows the same plot expanded in the region near the choice of the offline p_{T} cut on the 5^{th} jet. Both of the plots were produced using the nominal set of simulated signal events and the full 2012 dataset, though strictly only events passing an analogous four-jet trigger (**4j55**) were used. In addition the jets were required to be well isolated by means of the same isolation cut introduced in Section 7.4.4, requiring no pair of jets within $\Delta R \leq 0.6$.

As the data in this case are expected to consist primarily of QCD multi-jet events, it is expected that some true kinematic differences could give rise to the different turn-on curves. In order to yield a conservative uncertainty on m_{top} as a result of this difference however it is assumed that the discrepancies represent an inherent difference in the trigger between data and simulation.

[22] As a reminder, the fifth-leading jet in this context corresponds to the jet in a given event with the fifth-highest p_{T} of all reconstruction-level jets.

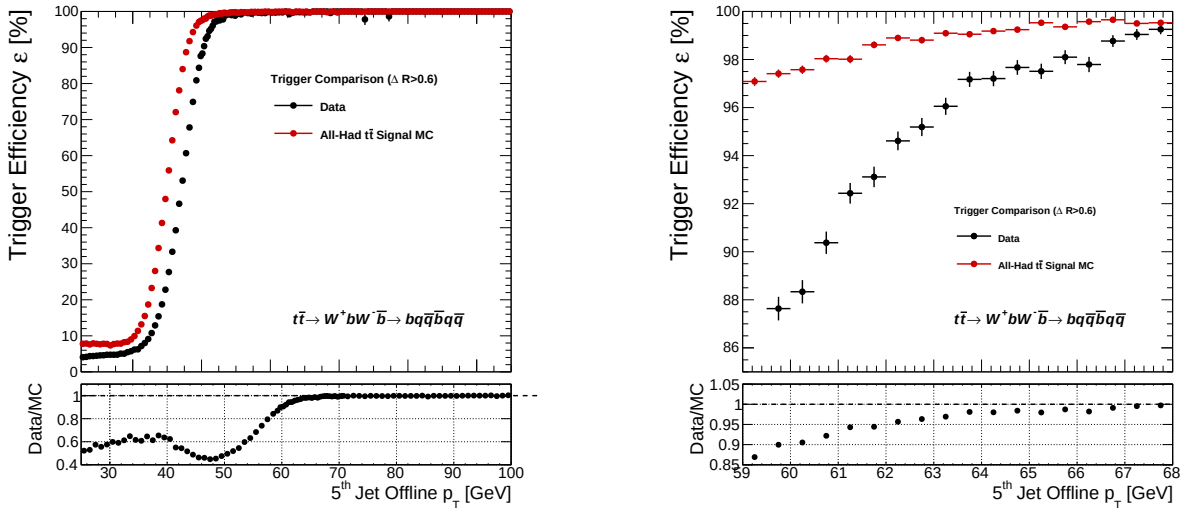

(a) (b)

Figure 11.7: Comparison of the measured trigger efficiency as a function of the transverse momentum of the 5^{th} jet, ordered in p_{T}, showed for both simulated signal and data events. All events used to produce the distributions were required to have at least five reconstructed and isolated jets, requiring $\Delta R > 0.6$ between any pair of jets. Events were further required to pass the analogous 4-jet trigger with an offline p_{T} cut of 55 GeV before being considered. The plot in (a) shows the full range from $0 \leq p_{\mathrm{T}}^{5th} \leq 100$ GeV. Figure (b) shows an enlarged view of the critical region between 59 and 68 GeV for comparison. The values for the plots were provided by an analysis group performing a measurement of the inclusive $t\bar{t}$ production cross-section using all-hadronic events at $\sqrt{s} = 8$ TeV using the same dataset and simulated samples [75].

The simulated signal events were assigned a p_{T}-dependent **trigger efficiency scale factor** (SF), defined according to the values in the plot in order that the Monte Carlo be made to agree with the data. Based on the ratio plots shown in the plots in Figure 11.7 the simulated events necessarily receive a scale factor strictly less than unity and most impactful at low values of the fifth jet p_{T}. Only very small differences in the normalized shape of the $R_{3/2}$ observable were observed when such p_{T}-dependent scale factors were applied[23]. Pseudo experiments were performed by drawing signal events from the modified $R_{3/2}$ distribution with the trigger SFs applied, and the absolute difference compared to the nominal case is quoted as a conservative uncertainty due to the trigger efficiency.

[23]The trigger SF applied for a particular event is evaluated *via* linear interpolation based on the p_{T} of the fifth jet in the event. In events with fewer than five reconstruction-level jets no such trigger SF was applied.

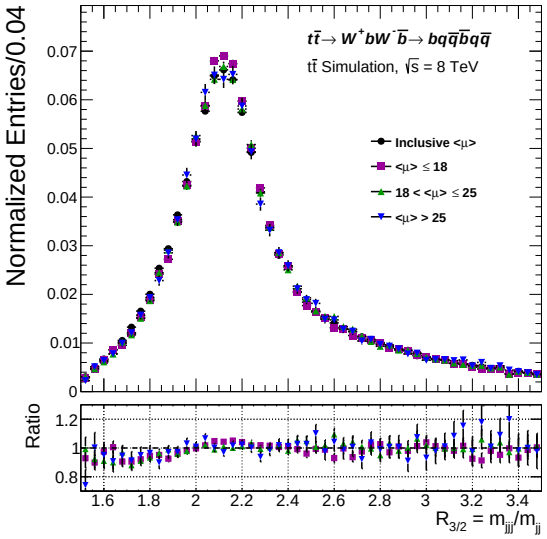

Figure 11.8: Normalized distributions of the $R_{3/2}$ observable from simulated all-hadronic $t\bar{t}$ events. The inclusive distribution includes all events passing the full event selection. The same events are further divided into different bins of a quantity referred to as the average number of interactions per bunch crossing, $\langle\mu\rangle$, an observable chosen characterize the amount of pile-up activity in the detector. The bin contents of each of the distributions corresponding to a particular $\langle\mu\rangle$ interval are also shown in the ratio plot relative to the bin contents in the inclusive distribution.

11.7.2 Fast *vs.* Full-Simulation for Monte Carlo Signal Samples

The nominal signal shape parameters for the $R_{3/2}$ observable used in the final minimization procedure are obtained using the seven simulated m_{top} variation samples which were produced using so-called **fast simulation** for some levels of particle interactions within the ATLAS detector – fast as compared with the standard **full-simulation** approach. This allowed the simulated samples to be produced with a reduced CPU time, but with some expected degradation in performance[24]. In order to be able to neglect an overall systematic uncertainty on m_{top} due to the use of fast simulation datasets, an additional set of mass-variation samples with higher statistics were produced using the full simulation[25]. At the time of writing these full-simulation samples have been produced and the closure tests as outlined in Section 11.2 repeated. The method was again shown to be closed and consequently no residual uncertainty is quoted due to the difference between fast and full simulation. It is expected that the full-simulation mass variation samples will likely replace the fast-simulation samples for the nominal analysis.

[24]For more information on the differences between fast- *vs.* full-simulation, see [71].

[25]These full-simulation samples were produced similarly to the fast-simulation mass-variation samples with the exception that only a total of five mass variation samples were used – the 165 and 180 GeV generator m_{top} points were omitted. The justification for producing five rather than seven m_{top} samples was the reduction in the computing resources together with the fact that the current precision on the top quark mass does not warrant such a large range of generator m_{top} points.

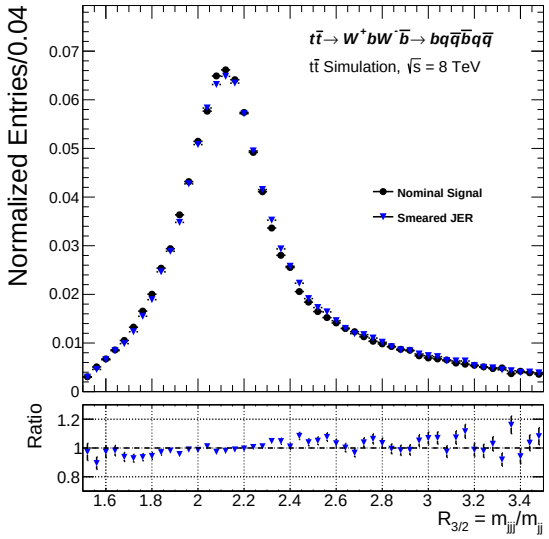

Figure 11.9: Normalized distributions of the $R_{3/2}$ observable from simulated all-hadronic $t\bar{t}$ events. Shown is a comparison between the nominal signal events and those for which the jet energy resolution (JER) has been smeared. This smearing has the effect of degrading the jet energy resolution which translates to a broadening of invariant mass distributions and consequently the broadening of the $R_{3/2}$ distribution as shown here.

11.7.3 Pile-up Reweighting Scale

The distribution of the average number of interactions per bunch crossing, denoted as $\langle\mu\rangle$, is known to differ between data and simulation. This is due to the strong dependence of $\langle\mu\rangle$ on the instantaneous luminosity of the LHC, and to the production of the simulated datasets prior to the completion of the data-taking period. Simulated events are reweighted in order that the value of $\langle\mu\rangle$ be equal between data and simulation[26]. In order to assess the impact this has on the final result, pseudo experiments are performed using the simulated signal Monte Carlo dataset in which the reweighting scale is shifted up and down according to its uncertainty, and the fit procedure is repeated. The maximum deviation is quoted as the symmeterized uncertainty.

11.7.4 Dependence on Pile-Up Activity

In addition to a systematic uncertainty associated to the pile-up reweighting outlined above, a residual bias could exist in the form of a sensitivity of the $R_{3/2}$ observable to the amount of pile-up activity in a given event. As a means to check for such a potential bias, simulated signal events were split into three separate regions based on their average number of interactions per bunch crossing, $\langle\mu\rangle$, and were subsequently used to fill distributions of the $R_{3/2}$ observable. The variable $\langle\mu\rangle$ was selected as it is customarily employed to characterize the amount of pile-up in the detector. The three regions were selected in order that they each contain roughly equal numbers of events following the event selection cuts: $\langle\mu\rangle \leq 18$, $18 < \langle\mu\rangle \leq 25$, and $\langle\mu\rangle > 25$.

Figure 11.8 shows the normalized $R_{3/2}$ distributions for the three regions separately as well

[26]Refer to Appendix B.2 for a description of the various weights applied to simulated events.

as that for the inclusive case. A ratio plot for the distributions in each of the three regions relative to the inclusive distribution is also shown in the lower portion of the figure. In all cases the distributions were filled only for those events passing the full set of event selection cuts. No clear dependence on the amount of pile-up is observed between the distributions.

Pseudo experiments were then performed using each of the distributions from the three $\langle\mu\rangle$ regions in turn in order to draw random pseudo events. The distributions were first scaled to their theoretical cross-section times branching ratio for the all-hadronic $t\bar{t}$ process. The nominal QCD background distribution was used for drawing background events. The average values of m_{top} from all three cases were consistent with the inclusive result. The maximum of half the absolute difference between any pair of average values is quoted as a conservative systematic uncertainty on m_{top} corresponding to the pile-up dependence.

It should be noted that the systematic uncertainty value quoted in this case is itself more prone to statistical fluctuations than several of the other systematic errors on m_{top}; in effect only roughly a third of the total number of simulated events are present in the $R_{3/2}$ distributions from which events are drawn for the pseudo experiments. Making use of Equation 11.1 with values for the nominal signal sample used for this study, decreasing the value of N_{us} *via* $N_{us} \rightarrow N'_{us} = N_{us}/3$ results in a corrected statistical uncertainty on the Gauss mean parameter larger than in the nominal case.

11.7.5 Lepton and $E_{\mathrm{T}}^{\mathrm{miss}}$ Soft Term Calibrations

Uncertainties in the calibration scales and resolutions of the lepton (e/μ) four-vector objects can potentially lead to very small differences in the results of the event selection or the jet-quark assignment in the top reconstruction algorithm, which can in turn affect the final measured result. Similarly, a small uncertainty can be expected due to miscalibrations of the $E_{\mathrm{T}}^{\mathrm{miss}}$ soft term[27] and uncertainties in its resolution. Each of the associated terms are scaled up and down, where appropriate, by their uncertainties and pseudo experiments are performed with the modified simulated signal events. In the case of the muon-related uncertainties Gaussian smearing is performed to assess the impact this has on the final result. The maximum absolute deviation from the reference m_{top} value from the full-simulation sample in the nominal case is taken as the uncertainty in each case, and these are added in quadrature. This sum in quadrature is then quoted as the total systematic uncertainty all lepton- and $E_{\mathrm{T}}^{\mathrm{miss}}$-related scale and resolution uncertainties, with the final value quoted in Table 11.1. The values of the individual contributions are listed in Table 11.4.

[27]The soft term of the $E_{\mathrm{T}}^{\mathrm{miss}}$ involves calorimeter energy deposits not associated with other reconstructed objects such as electrons, muons, photons or jets. These energy clusters are calibrated at the LC scale similarly to the clusters used to reconstruct the jet four-vector objects as described in Chapter 4.

11.7.6 b-Tagging Scale Factors

To identify the number of jets in an event initiated by bottom-type quarks, the MV1c b-tagging algorithm was used for this analysis. In the validation of the MV1c and other such b-tagging algorithms, the differences between data and simulation are corrected by means of applying **b-tagging factors** (b-tag SF) to the simulated events. The scale factor is taken as the product of all factors associated with each reconstructed jet in a given event. The uncertainties on the b-tagging SF values are made available for a standard selection of discrete working points based on the measured efficiencies in a reference $t\bar{t}$ sample. In order to propagate the uncertainty on these SFs to the final measurement, pseudo experiments are performed where the SFs are modified by a 1-σ up or down variation. The uncertainties are calculated separately for the b-tagging SFs, the c-tagging SFs and the overall mistag SFs. For each contribution, half the absolute difference between the result of the up and down variations is quoted as the corresponding uncertainty. When deviations are in the same direction the maximum absolute deviation is quoted. Although a modest level of correlation is to be expected between these sources, they are treated as independent in order to yield a conservative estimate on the overall uncertainty quoted in Table 11.1. The three contributions are quoted separately in Table 11.4.

11.7.7 Jet Energy Scale (JES)

The standard prescription for ATLAS analyses is to quote the contributions to the total JES uncertainty individually [63]. These are presented in Table 11.3. Uncertainties in the JES components were evaluated by a dedicated combined performance group in ATLAS, which used both data and simulation to validate the results.

For each component the resulting differences between the up and down variations, corresponding to 1-σ deviations relative to the nominal JES, are quoted separately. The total uncertainty for each contribution is taken as half the absolute difference between the up and down variation. In the case that both the up and down variations result in a change in the estimated parameter in the same direction, the largest absolute difference is taken as the symmeterized uncertainty. The total JES uncertainty is taken as the quadratic sum of all of these sub-contributions. This includes all but the bJES contribution which is quoted separately.

Table 11.3: Breakdown of the standard components for the jet energy scale (JES) uncertainties on the measured values of the top quark mass and background fraction. Contributions include all but that associated with the bJES uncertainty. The totals correspond to the quadratic sum of all entries in a given column. Both the up and down variations are listed for each contribution as well as a combined value, evaluated as half the absolute difference between the up and down variation, in order to yield a symmeterized overall uncertainty. The absolute maximum deviation from the nominal case is quoted for the combined value when both the up and down variations result in a shift in the same direction.

	Δm_{top} [GeV]			ΔF_{bkgd}		
Uncertainty Component	up	down	combined	up	down	combined
JES Effective Stat1	0.05	-0.03	±0.04	-0.000	0.005	±0.003
JES Effective Stat2	0.02	-0.02	±0.02	0.002	0.003	±0.003
JES Effective Stat3	-0.10	0.10	±0.10	0.005	0.000	±0.005
JES Effective Stat4	0.10	-0.07	±0.09	0.001	0.003	±0.003
JES Effective Model1	0.37	-0.41	±0.39	-0.009	0.016	±0.013
JES Effective Model2	0.03	-0.02	±0.02	0.003	0.002	±0.003
JES Effective Model3	-0.07	0.09	±0.08	0.004	0.001	±0.004
JES Effective Model4	0.06	-0.03	±0.05	0.002	0.002	±0.002
JES Effective Det1	0.29	-0.29	±0.29	0.001	0.005	±0.005
JES Effective Det2	-0.01	0.02	±0.01	0.002	0.003	±0.003
JES Effective Det3	0.03	-0.02	±0.03	0.002	0.003	±0.003
JES Effective Mix1	0.22	-0.23	±0.22	-0.000	0.005	±0.003
JES Effective Mix2	-0.02	0.03	±0.03	0.004	0.001	±0.004
JES Effective Mix3	-0.08	0.10	±0.09	0.003	0.002	±0.003
JES Effective Mix4	0.01	0.00	±0.01	0.002	0.003	±0.003
η Intercalibration Model	0.08	-0.08	±0.08	0.001	0.005	±0.005
η Intercalibration Statistical	0.11	-0.09	±0.10	0.000	0.005	±0.005
Single Particle	0.01	0.01	±0.01	0.003	0.003	±0.003
Pileup Offset (μ)	-0.00	0.02	±0.01	0.004	0.002	±0.004
Pileup Offset (NPV)	-0.11	0.10	±0.11	0.007	-0.002	±0.005
Pileup p_{T}	-0.02	-0.00	±0.02	0.003	0.002	±0.003
Pileup Energy Density ρ	0.24	-0.30	±0.27	-0.005	0.011	±0.008
Jet Flavour Component	-0.01	-0.02	±0.02	-0.007	0.015	±0.011
Jet Flavour Response	-0.03	-0.01	±0.03	0.012	-0.004	±0.008
Total JES	+0.64	−0.68	±0.65	+0.022	−0.029	±0.026

11.7.8 b-Jet Energy Scale (bJES)

The four-vector quantities of the reconstructed top quark candidates are very sensitive to the energy scale of jets initiated by bottom-type quarks, particularly as a result of choices in the parton fragmentation modelling. Based on the uncertainties associated with the bJES, a similar up-and-down variation procedure is performed using pseudo experiments and half the absolute difference between the two is quoted as the systematic uncertainty. The corresponding entry, together with the results for the up and down variations shown separately, is shown in Table 11.4.

The bJES-related systematic uncertainty is particularly large, as expected, since the choice of $R_{3/2}$ as the m_{top}-sensitive observable was made due to the roughly equal sensitivity expected in the numerator and denominator to uncertainties in the JES, whereas uncertainties in the bJES are expected to affect primarily the numerator in the definition of $R_{3/2}$ (m_{jjj}/m_{jj}). The overall bJES systematic uncertainty is comparable to the largest individual component of the JES (as listed in Table 11.3), though smaller than the overall JES systematic uncertainty as it involves a number of sub-contributions.

11.7.9 Jet Energy Resolution

The uncertainty in the jet energy resolution can be propagated to a systematic uncertainty on m_{top} by comparing the results of pseudo experiments performed in two separate cases, both of which make use of the same simulated $t\bar{t}$ signal events. In the first case the default jet four-vectors are used. In the second case the energies of the reconstructed jets are smeared by a Gaussian function based on the corresponding uncertainty. The resolution, and the resulting smearing, depends on the jet transverse momentum and pseudorapidity. The full event selection and top reconstruction are performed, ultimately yielding a modified signal $R_{3/2}$ distribution which is used for drawing the pseudo events. The absolute difference in the average measured m_{top} values in the two cases is quoted as the systematic uncertainty. The effect of the smearing of the jet energies on the $R_{3/2}$ observable can be seen from the plot in Figure 11.9, produced using all-hadronic $t\bar{t}$ signal events. The plot shows the comparison of normalized signal shapes between the nominal case and that for which the same jets have had their energies smeared.

11.7.10 Jet Reconstruction Efficiency

A small difference between the measured jet reconstruction efficiency in data and simulation was observed in the 8 TeV dataset by a dedicated ATLAS performance group, and this difference has the ability to affect the final measured m_{top} value. A set of pseudo experiments was therefore performed whereby jets from simulated events were removed at random by a frequency selected in order that the effect of this overall disparity between data and simulation in the jet reconstruction efficiency is removed. Following this procedure the analysis is repeated: the event selection is performed, the top quark candidates reconstructed and a modified signal $R_{3/2}$ distribution

produced which is used for drawing the pseudo events. The small differences observed are quoted for the corresponding systematic uncertainties on m_{top} and F_{bkgd}.

Table 11.4: Breakdown of additional sources of systematic uncertainty arising from the b-jet energy scale (bJES) and flavour tagging uncertainties, as well as uncertainties related to lepton and missing E_{T} ($E_{\mathrm{T}}^{\mathrm{miss}}$) energy scales and resolution, as well as lepton ID. Both the up and down variations are listed for each contribution as well as a combined value, evaluated as half the absolute difference of between the up and down variation, in order to yield a symmeterized overall uncertainty. The absolute maximum deviation from the nominal case is quoted for the combined value when both the up and down variations result in a shift in the same direction.

	Δm_{top} [GeV]			ΔF_{bkgd}		
Uncertainty Component	up	down	combined	up	down	combined
b-Jet Energy Scale (bJES)	0.39	-0.36	±0.37	0.001	0.005	±0.005
Jet b-Tagging SF	-0.01	0.03	±0.02	-0.030	0.037	±0.034
Jet c-Tagging SF	-0.01	0.01	±0.01	0.001	0.004	±0.004
Jet Mistagging SF	-0.00	0.00	±0.00	0.002	0.003	±0.003
Total Jet Flavour-Tagging SF	+0.02	−0.03	±0.02	+0.030	−0.038	±0.034
Electron Energy Scale	0.00	0.00	±0.00	0.002	0.003	±0.003
Electron Energy Resolution	0.01	0.00	±0.01	0.003	0.002	±0.003
$E_{\mathrm{T}}^{\mathrm{miss}}$ Soft Term Scale	0.01	0.00	±0.01	0.003	0.002	±0.003
$E_{\mathrm{T}}^{\mathrm{miss}}$ Soft Term Resolution	0.02	-0.00	±0.01	0.003	0.003	±0.003
Muon Momentum Smearing			±0.01			±0.003
Muon ID Resolution			±0.01			±0.003
Total Lepton/$E_{\mathrm{T}}^{\mathrm{miss}}$ Calibration	+0.02	−0.01	±0.02	+0.007	−0.006	±0.007

Chapter 12

Results & Conclusions

Based on the results of the extracted value of m_{top} from the data and the sources of systematic uncertainty presented in Chapter 11, the top quark mass was measured to have a value:

$$m_{top} = 174.29 \pm 0.52 \text{ (stat)} \pm 1.03 \text{ (syst) GeV}$$

This value of m_{top} is consistent with both the current world average value and all previous ATLAS measurements of the top quark mass[1].

For comparison the summary of some of the most recent top quark mass measurements previously shown in Figure 2.13 is shown again below in Figure 12.1.

The top quark mass analysis presented in this thesis will soon lead to a published result. It will also serve to bolster previous ATLAS measurements of the top quark mass at centre-of-mass energies of $\sqrt{s} = 7$ and 8 TeV through its inclusion in future combinations. These are expected to include combinations of ATLAS measurements, combinations of LHC measurements (both ATLAS and CMS in this case), and world combinations (adding together the results from the Tevatron experiments). It is important to note that the event selections between this and other $t\bar{t}$ decay channels at $\sqrt{s} = 8$ TeV are completely orthogonal and consequently no statistical correlation exists between this measurement and previous ATLAS measurements.

The precision of the m_{top} measurement presented in this analysis rivals that of the best of the individual measurements highlighted in the table in Figure 12.1, though a number of $\sqrt{s} = 8$ TeV measurements from the two leading LHC experiments in differing $t\bar{t}$ decay channels remain to be finalized; consequently they have yet to be included in the table. It should be mentioned that reaching an m_{top} precision comparable to that obtained in the semileptonic and dileptonic $t\bar{t}$ decay channels is a feat given that the relative contribution from background processes – both QCD multi-jet but also combinatorial – in the all-hadronic channel far exceeds that from the

[1]For $\sqrt{s} = 7$ TeV ATLAS results, see references [79], [35], and [36]. A world combination of top quark mass measurements can be seen here [40].

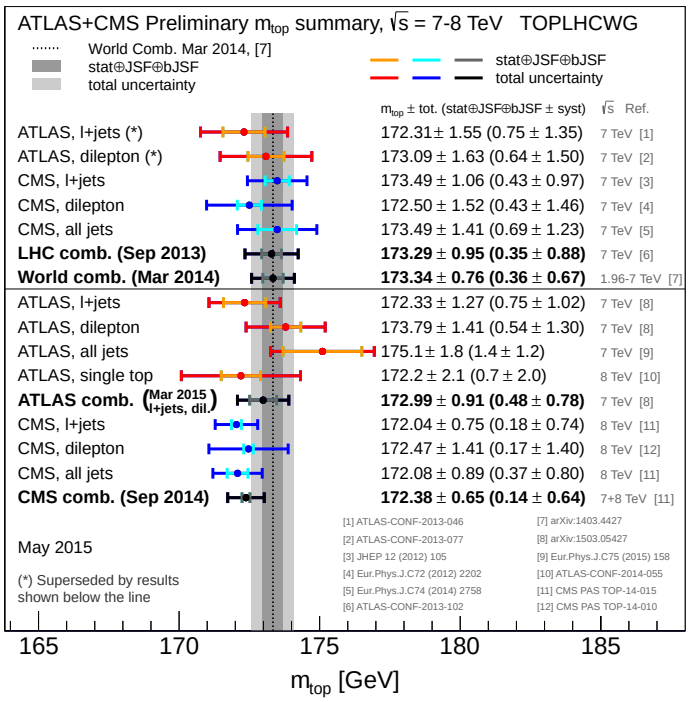

Figure 12.1: A summary plot of some of the more recent top quark mass measurements performed at the two LHC experiments ATLAS and CMS. The current world average combination from 2014 is also listed [40].

background processes in the non all-hadronic channels.

Ultimately the additional precision on the measured value of the top quark mass provided by this measurement could aid in the refinement of Monte Carlo models, which can in turn help particle physicists carry out searches for new physics with both an improved sensitivity and a clearer sense of where to focus their efforts.

12.1 Potential for Improved Precision

The use of b-tagging to reduce the number of possible permutations in the top reconstruction was demonstrated clearly in Chapter 6[2]. With far fewer possible jet-quark permutations to consider for the reconstruction of two top quark candidates per event, it becomes correspondingly difficult to yield a low reconstruction χ^2 quantity by combining the jets from QCD multi-jet events – events for which there are no true top quarks. Consequently it is more difficult for QCD background events to fake a signal event and pass the full set of event selection cuts.

It is tempting to apply a veto in the top reconstruction whereby permutations in which a non-tagged jet plays the role of one of the bottom-flavoured quarks are neglected. The performance

[2]This is particularly reflected in the values shown in Table 6.1.

on simulated signal events is striking as can be seen by comparing the plots in Figure 12.2. The plots were filled as they were for the standard analysis, where the vertical scale shows the number of weighted entries following the full set of event selection cuts. The left plot corresponds to the nominal analysis with no b-tagging veto, whereas in the right plot the b-tagging veto is applied. The fraction of correctly reconstructed top quark candidates increases significantly, and the resolution is improved; the latter can be seen by comparing the peak values in the inset figures for the correct cases in each plot. Also noticeable is the fact that the total number of signal events does not seem to decrease significantly in the vicinity of the peak, whereas the upper tail region is substantially diminished.

A similar procedure can be employed when running the full analysis on both data and simulation by applying a requirement that the highest MV1c-valued jets in a given event must strictly be selected to play the role of the two bottom-type quarks. This will be referred to in the following as a *soft* b-tagging requirement. This requirement, rather than the strict b-tagging veto mentioned above, is necessary in light of the fact that some of the control regions used for estimating the QCD multi-jet background have fewer than two b-tagged jets; a common definition must exist for all regions, as was the case for the event selection cut introduced to minimize the contribution from gluon-splitting ($g \to b\bar{b}$) events. All subsequent stages of the analysis, including the building of a set of m_{top}-dependent signal templates[3], perform well with the soft b-tagging requirement, though crucially there arises one notable exception: the ABCD method is no longer able to accurately estimate the shape of the QCD multi-jet background for a number of variables, including, regrettably, the variables m_{jj}, m_{jjj}, and $R_{3/2}$. The b-tagging efficiency, as evaluated in signal events and with values shown in Figure 4.5, can be seen to have a dependence on the jet pseudorapidity; similar plots exist showing a dependence on the jet energy and p_{T}. These dependences introduce correlations which invalidate the primary assumptions of the ABCD method outlined in Chapter 9. Unfortunately the number of alternative variables – those which satisfy both of these assumptions for the ABCD method while at the same time offering a strong discriminating power to separate signal from background events – are few.

In order to gauge the level of overall improvement one might expect by applying such a soft b-tagging requirement, the standard analysis was re-run over all simulated and data events with the requirement in place, and the final $R_{3/2}$ distribution showing both data, simulated signal, and estimated background, was produced in order that it might be compared with that from the nominal analysis. The resulting distribution is shown in Figure 12.3 by means of a stacked plot similar to those presented in Chapter 9. One can note the poor level of agreement between data and prediction – a consequence of the fact that the normalized shape of the data-minus-signal $R_{3/2}$ distribution in control region B differs from that in signal region D due to the correlations introduced *via* the b-tagging efficiencies[4].

[3]Note that the signal shape parameters $\{\mathbf{a}_i\}$ and background shape parameters $\{\mathbf{q}_i\}$ will be expected to differ from those in the nominal analysis.

[4]The level of disagreement varied for different variables. Both primary assumptions of the ABCD method

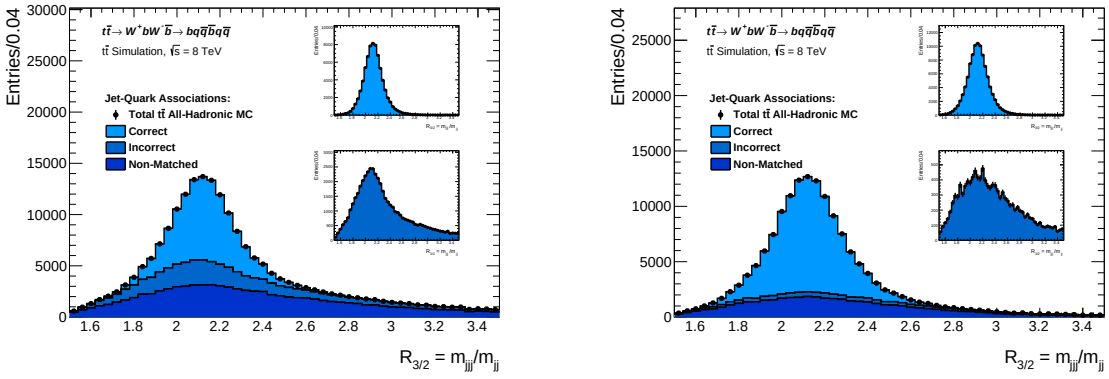

Figure 12.2: Distributions of the reconstructed $R_{3/2}$ values for the 60M fast-simulation m_{top}= 172.5 GeV signal events, where the top quarks and W bosons are reconstructed from jets based on the χ^2 event reconstruction. The plots show the results (a) without and (b) with the requirement that the jets in the b-quark positions be tagged by the MV1c b-tagging variable. In both cases the full set of event selection cuts were applied. The plot in (a) corresponds to the case used for the nominal analysis; it is identical to that shown previously in Figure 8.4(a). The distributions shown in the inset figures allow for a comparison of the individual shapes in the stacked distributions; in all cases the axis labels and horizontal range are unmodified from those in the main figure.

The level of disagreement between data and prediction notwithstanding, the resulting event yields from the distribution shown in Figure 12.3 allow for a rough estimate of the expected relative contributions of signal and background in this modified scenario. The estimated signal fraction, as well as other important quantities for evaluating the comparative performance with the inclusion of a soft b-tagging requirement, are summarized in Table 12.1. These values show a significant improvement in the signal fraction and top reconstructon purity, as well as a slight increase in the estimated number of correctly reconstructed top quarks. The final number of data entries can be seen to drop by roughly a factor of two. With such an improvement in the signal fraction however, it is recognized that if such a soft b-tagging requirement were adopted a number of the other event selection cuts could be loosened in order to increase the final event yields, thereby reducing the statistical uncertainty.

The ultimate gains in the attainable precision on the final measurement would be speculative in light of the fact that the background cannot be modelled correctly. However, as the resolution of the signal peak is shown to be improved, the most m_{top}-sensitive signal shape parameter – the Gauss mean – can be known more precisely. An overall reduction of the statistical uncertainty

became invalid with the soft b-tagging requirement. The level of correlation between N_{b-tag} and $\langle \Delta\phi(b, W) \rangle$ affects the level of agreement for all variables; for a subset of variables, with the regretable inclusion of m_{jj}, m_{jjj}, and $R_{3/2}$, an additional heightened correlation is present between the variable itself and N_{b-tag}.

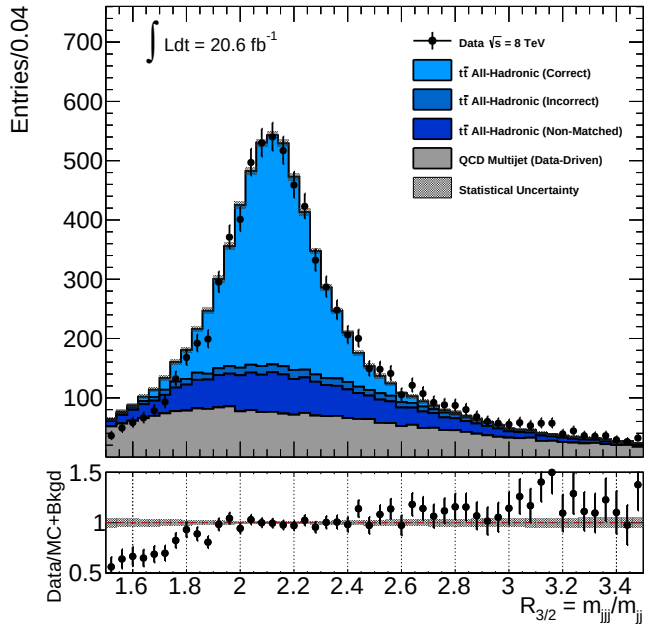

Figure 12.3: Distribution of reconstructed $R_{3/2}$ values for data (black markers) together with the simulated signal and estimated QCD multi-jet distributions. A soft b-tagging requirement was employed in the top reconstruction algorithm to consider only permutations in which the highest MV1c-valued jets are in the two bottom-quark positions. The QCD multi-jet shape and normalization is evaluated using the standard ABCD method, which performs poorly due to correlations as described in the text. The distribution was produced in order to assess the potential for improvement by using b-tagging information in the top reconstruction algorithm.

Table 12.1: A summary of selected benchmark quantities highlighting the expected gains in performance by employing a soft b-tagging requirement in the top reconstruction. Values are approximate and are quoted without uncertainties. The numbers of entries in all cases are those from the final signal region D from the $R_{3/2}$ distribution. They correspond therefore to twice the final event yields in each case. For the estimated signal entries only the correct and incorrect entries are listed as well as the total – the non-matched candidates are not shown separately. The value of P_{reco} is that of the reconstructed top quark candidates as opposed to W boson candidates.

	Estimated Signal $\left(N_s^{SR\ D}\right)$			Data $\left(N_d^{SR\ D}\right)$	Signal Fraction & Reco Purity	
	Correct	Incorrect	Total (S)	Total (S+B)	S/(S+B) [%]	P_{reco} [%]
(1) w/ b-tagging	3760	424	5797	8878	65.3	89.9
(2) w/o b-tagging	2746	1883	8152	19152	42.6	59.3
Ratio (1) / (2)	1.37	0.23	0.71	0.46	1.53	1.52

on the measurement of m_{top} would be expected as a consequence, and indeed early results, in which the QCD multi-jet distribution from the ABCD was taken at face value, showed an improvement on the order of 100 MeV in the statistical precision on m_{top}. It is expected that the improvement in the systematic uncertainty associated with the JES would not be nearly as significant, though some sensitivity to the JES was observed in previous studies simply by restricting some of the permutations in the top reconstruction method.

Ultimately it is expected that the use of b-tagging in the top reconstruction would offer a substantial improvement in the final measured result. Its inclusion would however require an alternate background-estimation technique which would require a significant amount of additional development and validation work not deemed feasible given the timeline of the current analysis.

12.2 Future Top Quark Mass Measurements

At the time of writing it is not clear whether there will be significant efforts during Run II of the LHC to perform similar top quark mass measurements at the two leading experiments in the standard $t\bar{t}$ decay topologies as were made during Run I at $\sqrt{s} = 7$ and 8 TeV. Over the course of the Run II data-collecting period both ATLAS and CMS will be afforded the luxury of vast numbers of statistics, thereby allowing for the use of tighter cuts which consequently yield larger signal-to-background ratios. The presence of additional unwanted pile-up activity in the detectors due to the LHC running conditions may however introduce a variety of countervailing effects[5] such as to render such measurements less viable in the end.

Proposals for an e^+-e^- collider, the **International Linear Collider** (ILC) [92], operating at centre-of-mass energies very near to the $t\bar{t}$ production threshold for e^+-e^- collisions, would allow for a so-called threshold-scan type of top quark mass measurement: the $t\bar{t}$ production cross-section can be measured for a number of values of $\sqrt{s}$ in the vicinity of the production threshold for top-antitop quark pairs. In this case it would be in the range of 350-400 GeV. Since the cross-section is dependent on the value of m_{top}, this would allow the shape of the cross-section as a function of $\sqrt{s}$ to be used to probe this sensitivity and extract a best-fit value of m_{top} from the data.

Threshold-scans are precluded in hadron colliders such as the LHC since it is the quantity $\sqrt{\hat{s}}$ from the partonic hard-scattering process which dictates the possible final states in a given interaction, and the relevant centre-of-mass energy in an individual partonic interaction at the LHC is unknown. In contrast, the clean environment offered by an e^+-e^- collider allows the value of $\sqrt{s}$ to be tuned precisely. It is also worth noting that in e^+-e^- collisions the dominant

[5] One example of such an effect is the fact that the trigger p_{T} thresholds would necessarily need to be raised in order to have un-prescaled triggers; such an increase in threshold would impact the signal efficiency, ultimately diminishing the final number of candidate events which could be used for the final measurement.

production mechanism will be *via* electroweak production rather than the strongly produced $t\bar{t}$ pairs at ATLAS. This is important to study in its own right but also in light of the potential role the top quark may play in electroweak symmetry breaking.

The level of precision attainable from a threshold scan measurement of m_{top} at the ILC from the production mechanism $e^+e^- \to t\bar{t}$ is expected to be on the order of a few hundred MeV [92], far exceeding the level of precision reachable at the LHC experiments. Nonetheless the high-precision measurements of m_{top} from the LHC and Tevatron experiments, together with their combinations, can help evaluate the prospects and set the strategies for such measurements.

Appendix A

Personal Contributions to the Analysis

The top quark mass measurement presented in this thesis was performed on behalf of the ATLAS collaboration as a whole[1]. ATLAS members from two institutes, Carleton University in Ottawa and the Max Planck Institute for Physics in Munich, carried out the bulk of the analysis using the full $\sqrt{s} = 8$ TeV p-p collision dataset collected in 2012. A large number of common analysis tools, simulated datasets, distributed computing networks and software packages available to the entire ATLAS collaboration were employed in the analysis. These datasets were used to produce all of the analysis-specific plots presented in this thesis[2].

This appendix is meant to summarize my personal contributions to the analysis effort based on my role as primary analyzer. One of the advantages of working in a small analysis group within a very large collaboration such as ATLAS is the ability to be involved in all aspects of the analysis, thereby gaining a holistic and global view of the analysis as a whole.

There were no major elements of the analysis presented here for which I was not involved.

The members from the two institutes involved in this top quark mass measurement include:

Max Planck Institute for Physics[3]:
Dr. Teresa Barillari, Dr. Sven Menke, Dr. Martin Nagel, Dr. Horst Oberlack, Dr. Denis Salihagic, Dr. Peter Schacht, Fabian Spettel & Dr. Andreas Wildauer

Carleton University:
Thomas McCarthy & Dr. Gerald Oakham

[1]Note however that the analysis as presented remains to be approved by the collaboration at the time of writing; the analysis is currently at the editorial board stage where a number of additional validation checks are being performed prior to a request for a publication.

[2]A number of C++ packages from a data analysis framework **ROOT** were used to produce all analysis plots.

[3]Max-Planck-Institut für Physik (Werner-Heisenberg-Institut), Föhringer Ring 6, 80805 München, Germany

The details of my personal contributions to the analysis effort are summarized below:

- **Package Development and Implementation of Various Elements of the Analysis**
  - Top quark reconstruction: development, testing, and implementation of the standard χ^2 reconstruction algorithm into the program framework and comparisons with several alternative top reconstruction algorithms
  - All output plots and summary tables: layout, design and incorporation into final program framework for their use in this thesis, in the internal documentation and in all presentations
  - Building of 1D templates: development of the $R_{3/2}$ template shapes to parameterize both the signal and background including studies of several alternative parameterizations
  - Background modelling: incorporation of the background modelling (ABCD method) into the program framework with extensive testing with a variety of possible observables
  - Final χ^2 minimization: development through meetings with Dr. Menke for the matrix-algebra machinery and implementation into program framework
  - In-situ jet energy correction: development of an iterative in-situ method to use the known W boson mass to correct jet energies (not ultimately adopted for the final analysis)
  - Optimization and automation: execution of a number of additional studies in order to validate many parts of the analysis, in addition to the development of several custom-made optimization tools allowing other analyzers to be able to perform the analysis using a number of different selection cuts
  - Final m_{top} Measurement: Use of developed software to measure the top quark mass together with its associated statistical and systematic uncertainties; this included a blinding of the final numerical value, followed by an unblinding in the mature stages of the analysis
- **Dataset Cataloguing**
  - Ensuring local datasets (both data and simulation) are complete and program references refer to the appropriate datasets paths maintained as older datasets are replaced in the case of any modifications (roughly once every two months).

- **Presentations to the ATLAS Community**
  - Making regular presentations (roughly once per month in later stages of the analysis) to the 'Top Quark Mass' group within the ATLAS physics community which involved the preparation and delivery of 20-30 slides highlighting recent progress, addressing any concerns, and reporting back on any additional studies which were requested in previous meetings
  - Providing regular updates, in the form of presentations, of ongoing studies as requested from the Editorial Board members as we move towards producing a public result for the ATLAS collaboration
- **Documentation**
  - Provide feedback to Dr. Barillari in writing the bulk of the internal documentation as well as responding to and addressing feedback from ATLAS members
  - Write the sections on the method closure and evaluation of systematic uncertainties for the internal documentation
- **Systematic Uncertainties**
  - Final calculation of quoted uncertainties from combination of all sources of uncertainty
  - Method closure and check for m_{top}-dependent bias
  - Monte Carlo generator uncertainty
  - Hadronization modelling uncertainty
  - Initial/final state radiation uncertainty
  - Colour reconnection uncertainty
  - ABCD vs ABCDEF uncertainty
  - Non all-hadronic $t\bar{t}$ inclusion uncertainty
  - Trigger efficiency uncertainty
  - Pile-up sensitivity uncertainty

Appendix B

Summary of Simulated Datasets and Monte Carlo Event Weights

B.1 Monte Carlo Samples

This analysis makes use of a number of simulated Monte Carlo samples, both for all-hadronic signal events and, in the case of the corresponding systematic uncertainty, non all-hadronic $t\bar{t}$ background events. The relevant samples are outlined in Table B.1 below. The shapes and normalization of the QCD multi-jet background are entirely data-driven[1], and consequently no simulated samples for QCD events are listed.

The values of the theoretical cross-sections and branching ratios for the various samples are used, together with the total integrated luminosity, to normalize the number of events in the final distributions when comparing to data. In addition, a number of weights are applied on a per-event level to simulated events based on standard prescriptions for all ATLAS analyses using the 2012 $\sqrt{s} = 8$ TeV dataset. These weights will be explained further in Section B.2. The K-Factor shown in the table is the ratio of the next-to-leading-order (NLO) cross-section to the leading-order cross-section (LO), such that the effective theoretical production cross-section used in the normalization of events from a given dataset is found by taking the product of $\sigma\times$ K-Factor $\times BR$.

In the table the DSID corresponds to the ID of the particular dataset and is listed as an internal ATLAS reference only. Some additional acronyms are listed with the names of some datasets to qualify some of the choices of tunable parameters in the production of the simulated datasets. Samples produced using a full simulation (FS) are to be distinguished from those employing a fast simulation in some of the reconstruction modelling (AFII) [71].

[1]It should be recognized however that simulated all-hadronic $t\bar{t}$ signal contributions are also partly used to estimate the QCD multi-jet background as described in the machinery of the ABCD method in Chapter 9.

A second table, Table B.2, lists the identical datasets with an additional description to highlight their role in the analysis.

B.2 Monte Carlo Event Weights

Any differences exhibited between data and simulation for a number of known quantities can be corrected for by means of **weights** which are to be applied to simulated events prior to any calculations or to the filling of histograms. For analyses involving the 2012 dataset collected at a centre-of-mass energy $\sqrt{s} = 8$ TeV, key differences were observed to exist between data and the corresponding simulated Monte Carlo which arose from four main causes. This required the use of four weights derived in order to improve the agreement between simulation and data: a **generator weight**, a **pile-up weight**, a **z-vertex weight**, and a **b-tagging weight** or **scale factor**[2].

Each simulated event i is assigned a total weight w_i^{MC} according to the product of four individual weight terms, all of which are standardized for all ATLAS analyses employing the $\sqrt{s} = 8$ TeV dataset. The total weight for event i is thus given by:

$$w_i^{MC} = w_i^{gen} \times w_i^{pile-up} \times w_i^{z-vertex} \times w_i^{b-tag} \tag{B.1}$$

where: w_i^{gen} coresponds to the Monte Carlo generator[3] of the simulated sample and has a value of ± 1; $w_i^{pile-up}$ is a decimal value derived as a function of the average number of interactions per bunch crossing[4]; $w_i^{z-vertex}$ is a term to correct for the fact that the spread of primary vertices in the $z-$direction was found to differ nominally between data and simulation; finally w_i^{b-tag} is a term to correct for observed differences in the b-tagging efficiencies between data and simulation.

The final of these four weights, the b-tagging weight or scale factor, is itself the product of weights applied to all reconstructed jets in the event. The value of w_i^{b-tag} for a particular event i with N_{jet} reconstructed jets, each with weight $w_{i,j}^{b-tag}$ is given by:

[2]It should be noted that to some extent such differences between data and simulation were to be expected: some of the simulated datasets were produced prior to the completion of the data-collecting period, and consequently the exact pile-up conditions and z-vertex distributions in data were not known *a priori*. In other cases, such as the b-tagging scale factors, corrections were applied to simulated events based on the observed differences in measured b-tagging efficiencies between data and simulation.

[3]The term w_i^{gen} only applies to certain Monte Carlo generators such as MC@NLO. For simulated samples produced with other generators this weight is assigned a value of $+1$ for all events and consequently has no effect. The negative weights arise due to presence of interference phenomena in the hard-scattering process in the way that the MC@NLO events were generated.

[4]The average number of interactions per bunch crossing, $\langle\mu\rangle$, is a quantity corresponding to LHC beam conditions as well as those of the ATLAS detector; it thus differs depending on the particular data collection period to which the simulated event corresponds.

Table B.1: A summary of all Monte Carlo samples used in the analysis, both for the nominal measurement and for systematic uncertainty studies. All samples use a generator-level value of m_{top}= 172.5 GeV for the top quark mass except when otherwise indicated. N_{evts} refers to the total number of simulated events in a given sample. The six non-central mass variation samples employed for the purposes of building a signal template shape are denoted by the symbol †. For the central mass point with m_{top} = 172.5 a total of 10M events were produced. For the remaining six mass points a total of 4M events were produced per mass point. The dataset ID number (DSID) for these samples ranges from 117835 - 117845.

Monte Carlo Sample	DSID	N_{evts}	$\sigma\times$ BR [pb]	K-Factor
Nominal Samples – All-Hadronic $t\bar{t}$ Signal				
Powheg+Pythia OTF with P2012 tune (mc12b, AFII)	110351	50M	96.343	1.1996
Powheg+Pythia with P2012 tune (mc12b, AFII)	117427	10M	96.346	1.1995
Powheg+Pythia with P2011C tune (mc12a, AFII)†	varies	4M	varies	varies
Systematic Samples – All-Hadronic $t\bar{t}$ Signal				
Powheg+Pythia with P2011C tune (mc12a, FS)	117049	10M	96.346	1.1995
Powheg+Pythia with P2012C tune (mc12a, AFII)	117049	10M	96.346	1.1995
Powheg+Herwig OTF with AUET2 tune (mc12b, AFII)	110360	60M	96.346	1.1995
MC@NLO+Herwig with AUET2 tune (mc12b, AFII)	105204	10M	95.197	1.2140
AcerMC+Pythia with AUET2B tune MorePS (mc12a, AFII)	117211	1.2M	50.066	2.3084
AcerMC+Pythia with AUET2B tune LessPS (mc12a, AFII)	117212	1.2M	50.065	2.3084
Powheg+Pythia with P2012loCR tune (mc12b, AFII)	117416	10M	96.346	1.1995
Powheg+Pythia OTF with P2012loCR tune (mc12b, AFII)	110352	20M	96.333	1.1997
Powheg+Pythia with P2012mpiHi tune (mc12b, AFII)	117418	10M	96.337	1.1997
Powheg+Pythia OTF with P2012mpiHi tune (mc12b, AFII)	110353	20M	96.335	1.1997
Systematic Samples – Non All-Hadronic $t\bar{t}$ Background				
Powheg+Pythia with 2011C tune (mc12a, FS)	110750	15M	114.49	1.1994

Table B.2: A summary of all Monte Carlo samples used in the analysis with entries identical to those shown Table B.1, but identifying the function served by each of the samples. As in the previous table, the six non-central mass variation samples are denoted by the symbol †.

Monte Carlo Sample	Description
Nominal Samples – All-Hadronic $t\bar{t}$ Signal	
Powheg+Pythia OTF with P2012 tune (mc12b, AFII)	Nominal Signal Events
Powheg+Pythia with P2012 tune (mc12b, AFII)	Additional Nominal Signal Events
Powheg+Pythia with P2011C tune (mc12a, AFII)†	Mass Variation Samples (6 m_{top} Samples)
Systematic Samples – All-Hadronic $t\bar{t}$ Signal	
Powheg+Pythia with P2011C tune (mc12a, FS)	Full-Simulation Signal Samples
Powheg+Pythia with P2012C tune (mc12a, AFII)	Central Mass Variation Sample
Powheg+Herwig OTF with AUET2 tune (mc12b, AFII)	Hadronization Modelling
MC@NLO+Herwig with AUET2 tune (mc12b, AFII)	Monte Carlo Generator
AcerMC+Pythia with AUET2B tune MorePS (mc12a, AFII)	ISR/FSR
AcerMC+Pythia with AUET2B tune LessPS (mc12a, AFII)	ISR/FSR
Powheg+Pythia with P2012loCR tune (mc12b, AFII)	Colour Reconnection
Powheg+Pythia OTF with P2012loCR tune (mc12b, AFII)	Colour Reconnection
Powheg+Pythia with P2012mpiHi tune (mc12b, AFII)	Underlying Event
Powheg+Pythia OTF with P2012mpiHi tune (mc12b, AFII)	Underlying Event
Systematic Samples – Non All-Hadronic $t\bar{t}$ Background	
Powheg+Pythia with 2011C tune (mc12a, FS)	Non All-Hadronic $t\bar{t}$ Contribution

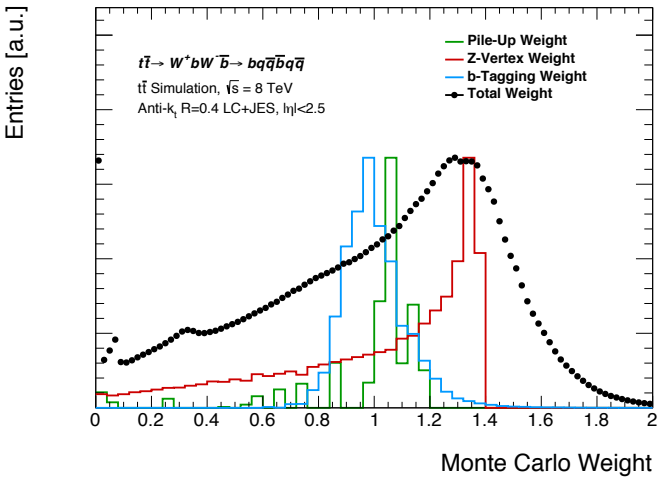

Figure B.1: One-dimensional distributions showing the range of possible values for the various Monte Carlo weights from events in the nominal simulated all-hadronic $t\bar{t}$ dataset. The black markers show the range of values of the total weight, evaluated as the product of all other weights *via* Equation B.1. Not shown is the Monte Carlo generator weight; in the case of the nominal signal sample these all have a value of one. For a given simulated event the total weight is applied when filling histograms.

$$w_i^{b-tag} = \prod_{j=1}^{N_{jet}} w_{i,j}^{b-tag} \tag{B.2}$$

It is the total number of weighted events, $N_{evts}^{weighted}$, rather than the total number of generated events, N_{evts}, which is the important quantity with regards to the normalization of simulated distributions to the number of expected events in the measured data. The relationship between N_{evts} and $N_{evts}^{weighted}$ is[5]:

$$N_{evts}^{weighted} = \sum_{i=1}^{N_{evts}} w_i^{MC} \tag{B.3}$$

Figure B.1 shows distributions of the various Monte Carlo weights for the full set of 60M signal events prior to the application of any event selection cuts. Shown is the range of possible values for each of the weights as well as the overall weight given by Equation B.1.

[5]In the case of the b-tagging weight, the per-event weight is indeed given by Equation B.1, though the terms w_i^{b-tag} are not included in the expression for w_i^{MC} in determining the initial number of weighted events. This was due to technical limitations but it should result in only having a small effect on the overall normalization given that the average value of w_i^{b-tag} from simulated signal events has an average value of one.

B.3 Normalization of Simulated Distributions

Separately from the weights applied on a per-event basis when filling histograms, the various distributions produced using simulated events must be scaled to the integrated luminosity and cross-section before they can be compared with those from data. Consider a generic variable x, for which a histogram with N_{bins} is filled using all simulated events satisfying some base selection criteria. Let x_i representing the number of entries in bin i for the histogram of the variable x, weighted event-by-event as described in the preceding section. The normalization for the distribution will be given by:

$$\mathcal{N} = \sum_{i=1}^{N_{bins}} x_i \tag{B.4}$$

In order to be able to compare to data, the distribution must be scaled by a factor $\mathcal{A}$, where:

$$\mathcal{A} = \frac{\int Ldt \times \sigma_{t\bar{t}} \times \text{K-Factor} \times BR}{N_{evts}^{weighted}} \tag{B.5}$$

Here $\int Ldt$ is the total integrated luminosity considered from the 2012 dataset, $\sigma_{t\bar{t}}\times$ K-Factor is the total theoretical $t\bar{t}$ production cross-section at the LHC at a centre of mass energy of $\sqrt{s} = 8$ TeV, and BR corresponds to the branching ratio for the process – $t\bar{t} \to W^+bW^-\bar{b} \to q\bar{q}bq\bar{q}\bar{b}$ in the case of all-hadronic $t\bar{t}$ events. The total normalization therefore becomes $\mathcal{N} \to \mathcal{N}' = \mathcal{N}\mathcal{A}$. It should be noted that distributions filled with data events, as opposed to those from simulation, are left unscaled; all events can be thought of as having a weight of unity.

Appendix C

Additional Analysis Plots and Studies

C.1 Signal Shape Jacobian Transformation Matrices

The minimization procedure to extract the measured values of m_{top} and F_{bkgd} was presented in Chapter 10, where a two-dimensional plot was displayed in Figure 10.3(a) showing the rate of change in the estimated number of signal entries with respect to a_0, where a_0 corresponds to the Gaussian mean parameter in the parameterization of the $R_{3/2}$ observable and based on a global fit to the seven top quark mass variation samples. This two-dimensional plot is shown as a function of both the generator top quark mass, and the bin number i.

The analogous two-dimensional distributions for the remaining nine $\{\mathbf{a}\}$ parameters are shown in Figure C.1. Throughout the minimization process, values from these distributions are interpolated for a given value of the parameters m_{top} and F_{bkgd} in order to yield the m_{top}- and F_{bkgd}-dependent components of the 50×50 covariance matrix $V_{ij}(\mathbf{s})$ *via* the Jacobian transformation in Equation 10.9.

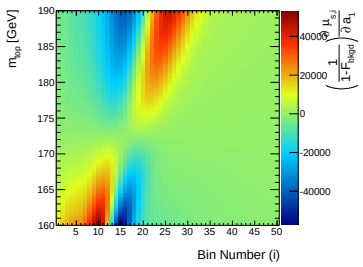

(a) a_1: Gauss mean (slope)

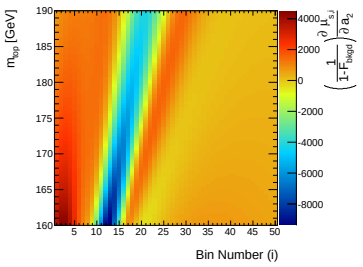

(b) a_2: Gauss width (intercept)

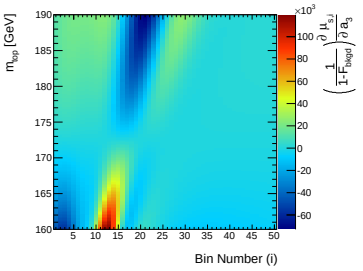

(c) a_3: Gauss width (slope)

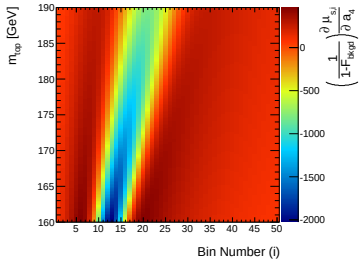

(d) a_4: Landau mean (intercept)

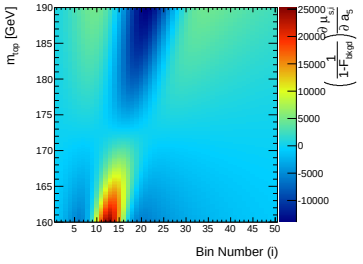

(e) a_5: Landau mean (slope)

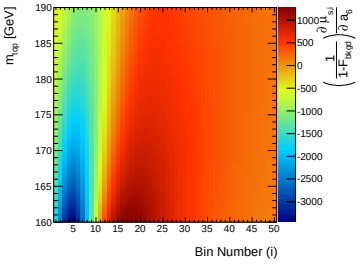

(f) a_6: Landau width (intercept)

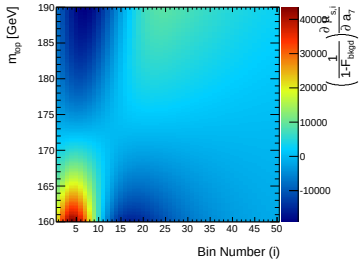

(g) a_7: Landau width (slope)

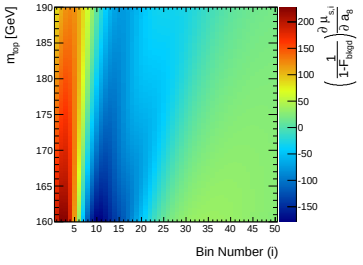

(h) a_8: Landau fraction (intercept)

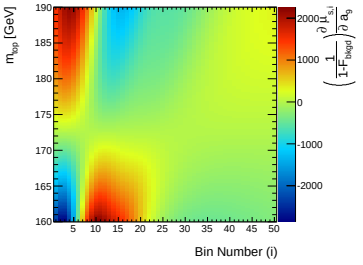

(i) a_9: Landau fraction (slope)

Figure C.1: Additional Jacobian matrices used to produce the final 50 × 50 covariance matrix in the final top mass quark extraction. Shown are the change in the number of expected signal bin contents of the $R_{3/2}$ distribution with respect to a small change of a given parameter a_i as a function of both m_{top} and the $R_{3/2}$ bin number. The background fraction term has been factored out for simplicity but is included in the final transformation.

C.2 Additional Template Method Closure Plots

The figures below show additional plots associated with the closure tests described in Section 11.2. The plot shown in Figure C.2(a) is identical to that shown in Figure 11.2(b), and the Gauss mean parameter from the resulting fits are plotted as a function of the generator top quark mass in Figure C.2(b). The error bars on the Gauss mean parameters returned from the single Gaussian fit are corrected for oversampling based on Equation 11.1 as well as the residual correction described in the text. Note that the true values for F_{bkgd} are taken to be those obtained from the reference histogram bin contents themselves.

Similarly to the distributions from Figure 11.2(a) showing the difference quantity $\left(m_{top}^{fit} - m_{top}^{gen}\right)$, the distributions in Figure C.3(a) are filled with the extracted statistical uncertainty on the m_{top} parameter, δm_{top}, for each of the 2500 pseudo experiments per top quark mass point[1]. The mean parameter of a single-Gaussian fit to each of these distributions, again with error bars corrected for oversampling from finite Monte Carlo statistics, is plotted as a function of the generator-level m_{top} value in Figure C.3(b). The clear increase in statistical uncertainty as a function of m_{top} is to be expected given the dependence of the total $t\bar{t}$ production cross-section on the top quark mass value – at higher values of m_{top} the production cross-section of top-antitop quark pairs decreases at the LHC[2], and fewer events in the final distribution gives rise to a larger statistical uncertainty. A second-order effect is that the top quark width parameter Γ_{top} also increases with the value of m_{top}, and this broadening of the signal peak will also degrade the statistical precision with which a measurement of m_{top} can be made.

[1]Note that the statistical uncertainty on m_{top} here is not corrected by the factor $\sqrt{1+\rho}$ arising from the correlation between the two reconstructed $R_{3/2}$ values; it is simply the value returned from the χ^2 minimization.

[2]Refer to Section 2.2.2

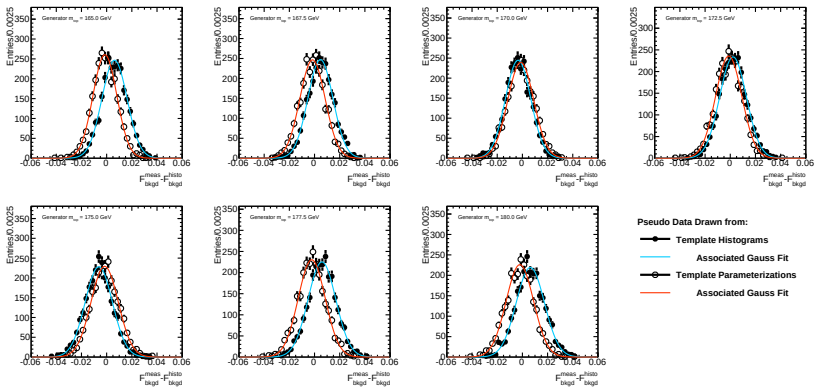

(a)

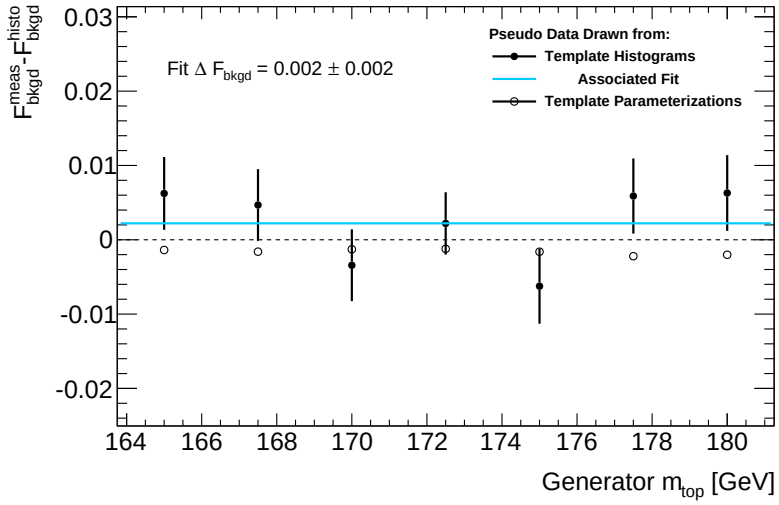

(b)

Figure C.2: (a) Distributions of the measured difference $\left(F_{bkgd}^{fit} - F_{bkgd}^{histo}\right)$ in each of the 2500 pseudo experiments per top mass point together with their single-Gaussian fits, and (b) the fitted Gauss mean parameter from each difference plot as a function of the input top quark mass, shown for the range of m_{top} values from 165 to 180 GeV. The solid black markers correspond to cases where the pseudo events were drawn from the $R_{3/2}$ histograms, and the open circular markers where pseudo events were drawn from the parameterizations themselves. The blue horizontal line in (b) corresponds to a zeroth-order polynomial fit to the black points, showing there to be no bias in the measurement of the background fraction parameter F_{bkgd}.

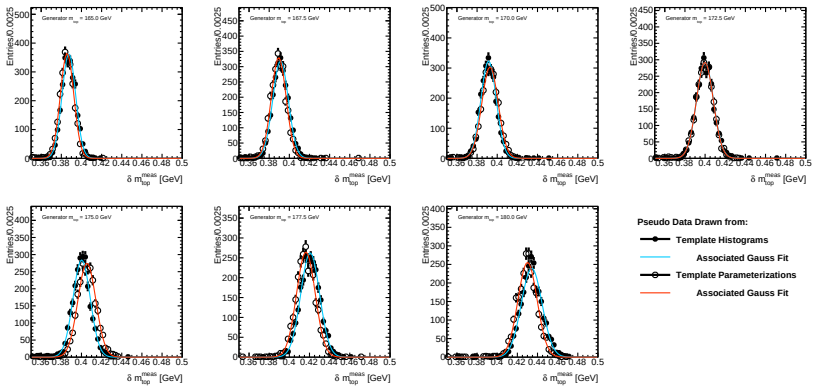

(a)

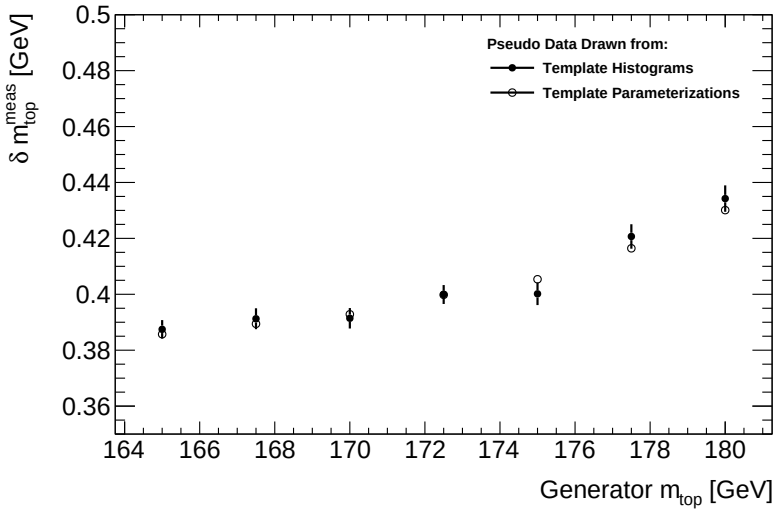

(b)

Figure C.3: (a) Distributions of the measured statistical uncertainty on the m_{top} parameter in each of the 2500 pseudo experiments per top mass point together with their single Gaussian fits, and (b) the Gaussian mean parameter extracted by means of a fit to each of the plots in (a) as a function of the input top quark mass, and shown for the range of m_{top} values from 165 to 180 GeV. The solid black markers correspond to cases where the pseudo events were drawn from the $R_{3/2}$ histograms, and the open circular markers where pseudo events were drawn from the parameterizations themselves. The statistical uncertainties are not corrected for the correlation between the two $R_{3/2}$ values.

C.3 Drawing Pseudo Events from 2D Distributions

In performing the pseudo experiments based on the approach outlined in Section 11.2, the pseudo events were drawn from one-dimensional distributions of the $R_{3/2}$ observable, both in the case of the signal and the background events. As mentioned in Section 10.3, the two $R_{3/2}$ values reconstructed per event have a level of correlation of approxiately 68% following the full event selection, and the statistical uncertainties on m_{top} and F_{bkgd} quoted in the Table 11.1 include a factor to correct for this level of correlation.

In principle it should be possible to determine the requisite correction by producing pull mean and width plots shown as a function of the generator m_{top} value similar to those shown in Figure 11.3, but where entries for the pseudo $R_{3/2}$ distributions were drawn from two-, rather than the one-dimensional distributions as was the case in the nominal analysis.

Obtaining such two-dimensional $R_{3/2}$ distributions for signal events for each of the seven mass points is straightforward: two-dimensional histograms are filled in an identical fashion to their analogous one-dimensional histograms by running over all simulated signal events. The integral of the 2D histograms will be exactly twice that for the 1D case.

In order to produce the analogous two-dimensional distributions of $R_{3/2}$ for the background, it is necessary to modify the ABCD method from Chapter 9 somewhat. Equations 9.2 through 9.5 can be altered simply by the addition of a secondary index j, and the ABCD method performed in an analogous fashion. The final $R_{3/2}$ distributions produced in this way, both for the signal and QCD background, remained unchanged from the standard distribution – the result is identical to the final plot shown in Figure 9.10(a) once the 2D distribution is transformed back to a 1D distribution.

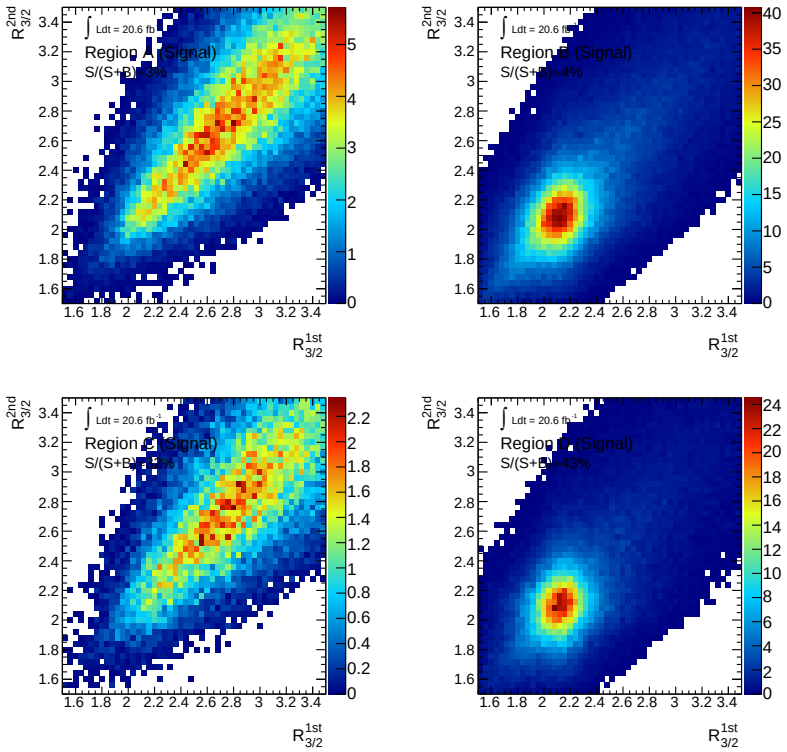

Figure C.4: Two-dimensional signal distributions of the $R_{3/2}$ observable in the four ABCD regions analogous to the one-dimensional distributions presented in Figure 9.9. In this case the entries are not subdivided into the three separate permutation categories as they are in the one-dimensional cases.

The difference in performing a two-dimensional ABCD method is that one obtains two dimensional $R_{3/2}$ distributions from which the pseudo data can be drawn. An analogous 2D function to draw events at random following a probablity distribution function described by the normalized bin contents of each 2D $R_{3/2}$ distribution is used. Drawing a single random value from the two-dimensional distribution returns two values of $R_{3/2}$, and the correlation can be taken into account directly; for a given event it is more probable to draw a second $R_{3/2}$ value more similar to the first based on the correlation factor $\rho(R^{1st}_{3/2}, R^{2nd}_{3/2}) \approx 0.69$.

The two-dimensional distributions for each of the four ABCD regions are shown, in the case of signal events at the central mass point, in the plots in Figure C.4. The analogous background distributions obtained by performing the two-dimensional ABCD method are shown in Figure C.5.

The limited statistics in the analysis as a result of the tight event selection cuts cause some bins, particularly in the tails, to have zero or negative bin contents in the two-dimensional distributions; the bins with zero bin content occur for both the signal and the background 2D

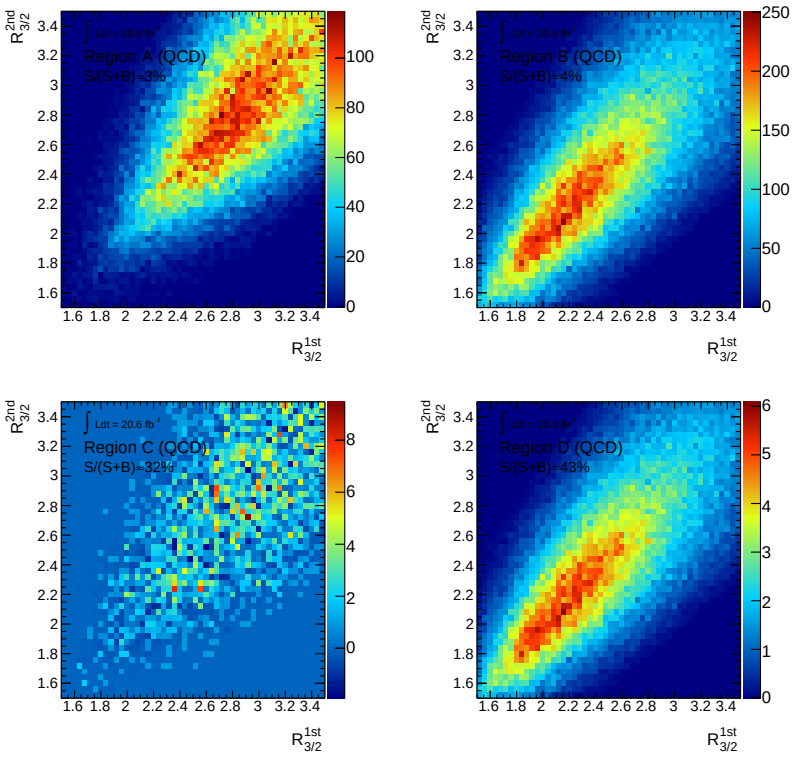

Figure C.5: Two-dimensional QCD multi-jet distributions of the $R_{3/2}$ observable in the four ABCD regions analogous to the one-dimensional distributions presented in Figure 9.9.

distributions. In the case of the background, the negative bins for the background arise in the regions where there are negligible numbers of entries in control region B where the bin contents are determined *via* the two-dimensional equivalent form of Equation 9.3, namely:

$$\mu_{b,ij}^{CR\ B} = n_{ij}^{CR\ B} - \mu_{s,ij}^{CR\ B} \tag{C.1}$$

In the case that in a particular bin with indices ij there are more estimated signal than data entries, *i.e.* $\mu_{s,ij}^{CR\ B} > n_{ij}^{CR\ B}$, the associated estimated background bin content will have a negative number of entries. Consequently the same will be true for the corresponding bin in signal region D since its bin contents are determined by scaling those from control region B.

Studies have shown that it is due to this fact, and not to the inherent effect from the correlation, that the normalized shapes of the one-dimensional pseudo distributions produced by means of two-dimensional template distributions differ from the nominal one-dimensional template distributions themselves. This is particularly problematic for the case of the background.

The function used to draw events at random from a 2D distribution rely on positive, non-zero bin contents only; neither a global shift of the bin contents, nor the setting of any bins with negative contents to zero in order to mitigate the effect of negative bins, results in the correct shapes of the one-dimensional $R_{3/2}$ pseudo distributions[3]. Loosening the cuts would ensure larger statistics in the high-$R_{3/2}$ tails of the distributions which would ensure $\mu_{b,ij}^{CR\ D} > 0$ for all i and j. In such a case it would be possible to repeat the closure tests drawing from two- rather than one-dimensional $R_{3/2}$ distributions. The result would show that the statistical uncertainty must be corrected by a factor $\sqrt{1+\rho}$ as quoted in Section 10.3.

C.4 Correction to the Statistical Uncertainty

The correction to the statistical uncertainty on m_{top} and F_{bkgd} can be explained by considering the simple scenario in which two measurements, m_1 and m_2, are made of the same physical quantity M. Here M is taken to be a generic quantity unrelated to the present analysis. Assuming the uncertainty on both measurements m_1 and m_2 to be equal and to have a value σ_m, but a level of correlation to exist between the measurements with correlation factor ρ, a standard χ^2 variable can be defined as:

$$\chi^2 = \left(\vec{m} - \vec{M}\right) V^{-1} \left(\vec{m} - \vec{M}\right)^T \tag{C.2}$$

In the above the row vectors $\vec{m}$ and $\vec{M}$ represent the difference between each of the two measurements and the true physical value, namely $\vec{m} - \vec{M} = (m_1 - M,\ m_2 - M)$. The 2×2 covariance matrix V, based on the information above, is given by:

$$V = \sigma_m^2 \begin{bmatrix} 1 & \rho \\ \rho & 1 \end{bmatrix} \tag{C.3}$$

One can then minimize the χ^2 variable in order to yield an estimate $\hat{m}$ of the quantity M. In such an idealized case the minimization can be performed analytically. The estimated uncertainty on this measured parameter, determined as a result of the χ^2 minimization, is a factor $\sqrt{1+\rho}$ larger than in the case in which the correlation is neglected (by setting $\rho = 0$). In practice, the correlation can initially be neglected, and the resulting uncertainty on a chosen parameter scaled up by the factor $\sqrt{1+\rho}$ in order to properly take into account the correlation effect.

In order to demonstrate the validity of this assumption in a less trivial case, a toy Monte Carlo study was performed whereby events were generated using random numbers drawn from a Gaussian probability density function with a mean parameter 170 and a width parameter 20. Two independent values (x_1 and x_2) were drawn for 2500 events. A user-defined value of ρ (in

[3] A smoothing procedure could however be used in order to strictly ensure non-negative bin contents.

this particular example it is chosen to have a value $\rho = 0.7$) was then selected in order to build an additional variable z, correlated to x_1 by the pre-designated amount ρ [93] and defined by:

$$z = \rho \cdot x_1 + \sqrt{1-\rho^2} \cdot x_2 \tag{C.4}$$

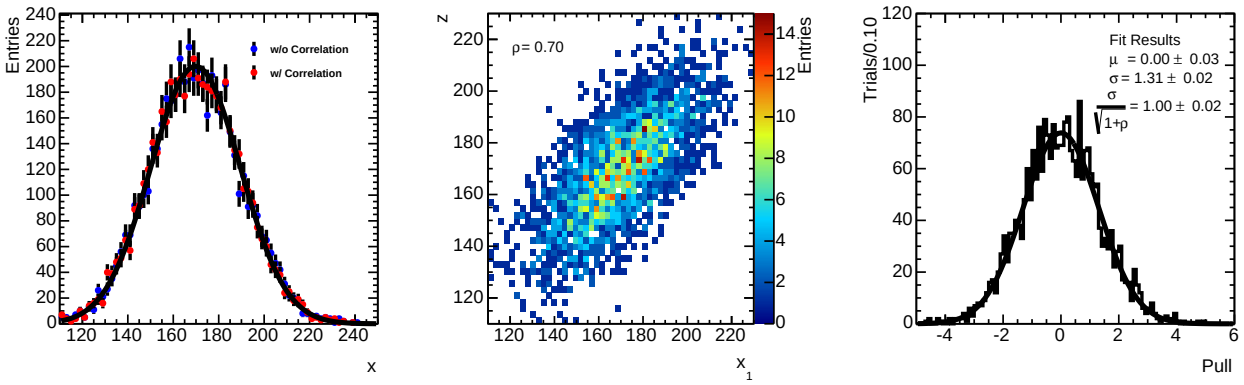

Figure C.6: Plots motivating the need for a correction factor $\sqrt{1+\rho}$ applied to correct the final statistical uncertainty on the measured parameters m_{top} and F_{bkgd} due to the correlation between the two reconstructed $R_{3/2}$ values per event.

The left-most distributions in Figure C.6 were filled using these 5000 randomly drawn values: in the first case (blue markers) by filling separately the uncorrelated values x_1 and x_2 for each event, and in the second case (red markers) by filling the values x_1 and z. The one-dimensional distributions in each case of the general variable x (where here $x = x_1, x_2$ or z) are similar; the effect from this sizeable correlation is difficult to discern by eye. A standard least-squares fit was then performed to the two distributions separately using a single Gaussian function for the parameterization and two fitted parameters of primary interest were returned: the Gaussian mean and width. The distributions with red markers (filled using x_1 and z) in the left-most plot were then cleared and the 5000 entries re-drawn 2499 additional times[4], each time using independently drawn random events. In each case the pull, defined as the ratio of the Gaussian mean parameter to its associated uncertainty from the least-squares fit, was used to fill the right-most distribution in Figure C.6.

A final least-squares fit is performed to the right-most distribution in Figure C.6 of the pull quantity. Assuming the correct statistical approach has been taken, it should be expected that the resulting pull mean (the Gaussian mean parameter μ) would be consistent with zero and the

[4]To avoid any possible confusion, the value of 2500 was selected both for the number of events for each distribution as well as the number of trials. Since two values are drawn for each event, the total number of entries for each distribution is doubled from 2500 events to 5000.

pull width (σ) consistent with one. While the former can be seen to be true based on the values returned from the fit and shown in the figure, the latter is shown only to be satisfied by making a correction by the factor $\frac{1}{\sqrt{1+\rho}}$. Here it should be recognized that in the actual analysis, the correlation is initially neglected; the returned statistical uncertainties on m_{top} and F_{bkgd} must consequently be scaled up by $\sqrt{1+\rho}$ in order to yield the correct overall uncertainty[5].

The central, two-dimensional distribution shown in Figure C.6 corresponds to the first set of 2500 randomly drawn events. It is filled using the identical values to the distribution in the left-most plot (in the case of the red markers) based on the values of x_1 and z. The value of $\rho = 0.7$ printed in the figure is that evaluated from the distribution's bin contents themselves, showing it to be equal to the input value as expected.

C.5 Top Reconstruction Performance

Several additional studies were carried out during the development of the top reconstruction algorithm introduced in Chapter 6, and re-explored in the later stages of the analysis following the inclusion of the systematic uncertainties.

Presented here are a series of plots highlighting the performance of the χ^2 reconstruction algorithm, and in particular the dependence of its performance on the jet multiplicity. The two-dimensional plots in Figure C.7 (a) through (d) show the outcome of the reconstruction algorithm for four selected and representative simulated signal events. These events correspond to the first simulated events encountered with N_{jet}=6, 7, 8 and 9 reconstructed jets, respectively. The vertical and horizontal axes show the average reconstructed top quark and W boson candidate invariant masses, respectively, based on the given jet-quark association. The distributions are filled for all possible unique permutations.

The total number of permutations based on the jet multiplicity was given in Equation 6.1. These values are identical to those quoted in Table 6.1 when no b-tagging is used to designate which jets are to be associated with the bottom-flavoured quarks. The prominent vertical gap structure is an effect of the fixed reference value for the reconstructed W boson mass in the definition of the χ^2 variable; for the reconstructed top quark masses the difference term Δm_{jjj} allows for more of a continuum of reconstructed m_{jjj} values.

In the case that $N_{jet} = 9$, there are a total of 7560 distinct permutations possible. As a consequence a large region of the phase space can be covered by the various permutations.

[5]It should be highlighted that in the analysis the correlation is neglected since each of the $R_{3/2}$ distributions for the 7 generated m_{top} samples is a one-dimensional distribution. The template closure tests described in Section 11.2 begin with these distributions for the pseudo experiments, so any effect from this intrinsic correlation will not manifest itself in the width of the pull distributions. The above correction must nevertheless be made to account for the fact that one does not strictly have twice the number of data events in performing the final measurement – the effective number of entries in the $R_{3/2}$ distribution must be suppressed by a factor $(1+\rho)$.

In light of this it should be recognized that for high jet multiplicities it will often be the case that the incorrect jet-quark permutation will be selected by the algorithm, but the average m_{jjj} and m_{jj} values will be close to the expected values[6]. Despite this fact the algorithm employed, as it is, does not rely on any truth information, and the linearity of the signal shape parameters for the $R_{3/2}$ variable demonstrates that the outcome of the top reconstruction behaves as required for a template method for the range of m_{top} values.

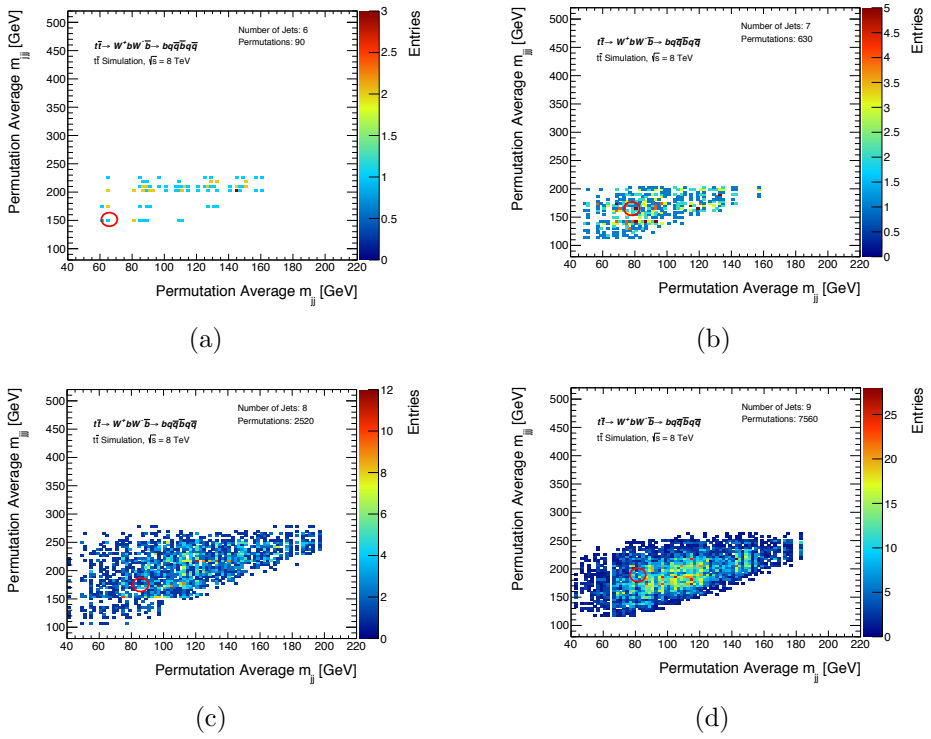

Figure C.7: Two-dimensional histograms showing the proliferation of the number of possible permutations to consider as the number of reconstructed jets increases. Shown are sample simulated signal events consisting of a total of (a) six to (d) nine reconstructed jets. The average invariant masses of the two reconstructed top-W pairs are plotted for every possible permutation in each given event, where the total number of permutations agrees with Equation 6.1. Each permutation results in a particular χ^2 value based on Equation 6.5. The values of the average reconstructed masses associated with the minimum χ^2 value in each case are circled; these correpond to the permutation that would be selected by the algorithm.

[6]Recognizably if one of the constituent jets of a top quark candidate is a low-energy jet it will not have as large an effect on the overall reconstructed three- or two-jet mass, so even if the reconstruction is officially incorrect, it could be only incorrect due to one jet which could have a small effect on the overall value of m_{jj} or m_{jjj}.

Figure C.8(a) shows the fraction of top quark candidates which were correctly or incorrectly reconstructed as a function of the jet multiplicity. In this case the two-dimensional distribution was filled using only events passing the full set of event selection cuts. Only simulated signal events were used. Non-matched cases were not included.

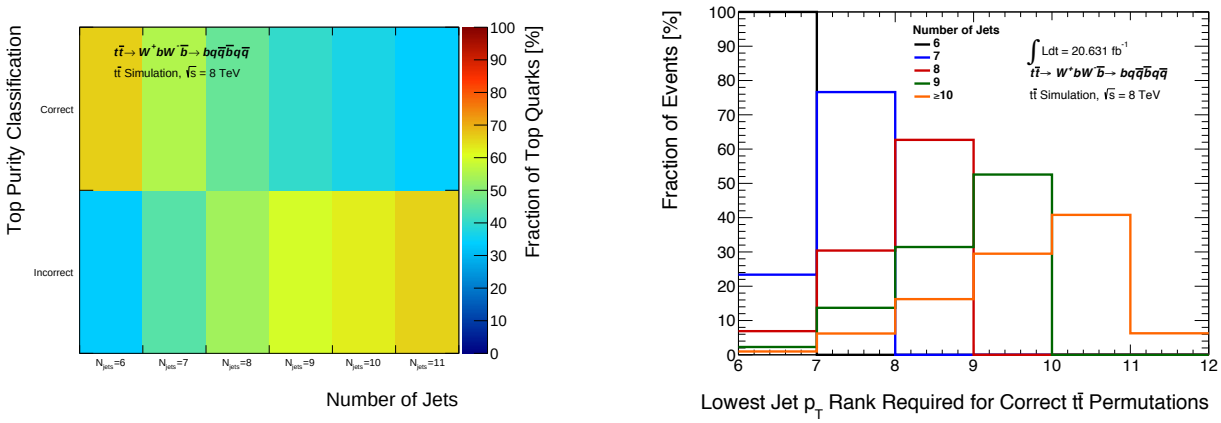

(a) (b)

Figure C.8: Figure (a) shows the reconstructed top quark purity classification for correct and incorrect cases based on the reconstruction purity, $\mathcal{P}_{reco}$, defined in Equation 6.2. This classification is shown as a function of the jet multiplicity. Events used to produce the plot in (a) were required to pass the full set of event selection cuts. Figure (b) shows the rank, ordered in p_{T}, of the lowest-ranked jet in each event which is matched to one of the truth-record quarks from the top quark decay, and consequently needed in order to select the correct permutation. No event selection cuts were applied in order to produce the plot in Figure (b), though only events with matchable top quark candidates were considered. The nominal set of simulated signal events were used to produce both plots.

Figure C.8(b) was produced similarly, using simulated signal events but with no event selection applied. Only events with two matchable top quarks were considered – those for which there are six unique reconstructed jets matched to each of the true hard-scatter quarks from the $t\bar{t}$ decays based on the truth-record information. The histograms show the p_{T} rank corresponding to the lowest-ranked p_{T} jet which is matched to one of the quarks for a given event. In essence this allows one to see how many jets must necessarily be considered in order for the top reconstruction algorithm to have a non-zero possibility of having the correct combination for both top quark candidates. The different coloured lines correspond to differing jet multiplicities. Each distribution is normalized to unity and expressed as a percent. This plot was produced to see if one could expect a better χ^2 reconstruction performance either by cutting events with higher jet multiplicities or by only allowing the χ^2 reconstruction algorithm to create permutations for a fixed number of jets regardless of the overall jet multiplicity. In the case of the former a cut on the jet multiplicity would result in the loss of a large number of statistics; this would consequently give rise to a greater statistical uncertainty on the measurement of m_{top}.

Restricting the number of jets considered by the top reconstruction algorithm would result in a modified shapes of the $R_{3/2}$ distributions. This would impact not only the signal shape – the correct, incorrect and non-matched shapes would all be expected to change – but also the QCD multi-jet shape.

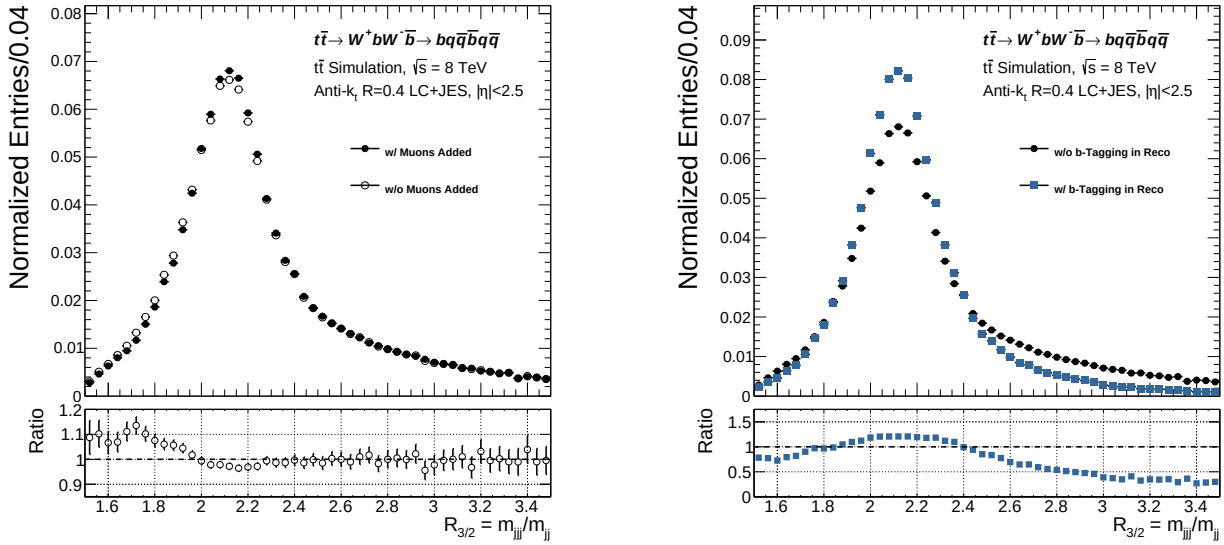

Figure C.9: Comparisons of normalized $R_{3/2}$ shapes in simulated signal events for two scenarios which differ from the defaults used in the nominal analysis: (a) the jet four-vectors without the addition of match muon four-vectors and (b) the requirement in the top reconstruction stage that the jets in the b-quark positions necessarily be the two highest MV1c-valued jets in the event. The distributions in each of the two sub-figures shown as the solid black markers are identical and correspond to the choices used in the nominal analysis. In all cases events were required to satisfy the full set of event selection cuts prior to filling the histograms.

C.6 Normalized $R_{3/2}$ Shape Comparisons

Figure C.9 compares the normalized shapes of the $R_{3/2}$ observable in simulated signal events for alternate choices compared with those used in the nominal analysis. Figure C.9(a) compares the $R_{3/2}$ shape in the default case that muon four-vectors matched to reconstruction-level jets are added to the jet four-vectors as described in Section 4.5.3 compared with the scenario in which they are not added. Figure C.9(b) shows the expected improvement in resolution through the use of a b-tagging requirement in the top reconstruction algorithm[7].

C.7 Comparison of b-Tagging Working Points

The values shown in Table C.1 provide a comparison in the performance of the five standard and recommended b-tagging working points for ATLAS analysis with the $\sqrt{s} = 8$ TeV dataset. The table lists, for each b-tagging variable and working point, the overall signal fraction and the signal efficiency relative to the nominal choice of MV1@57. The values were evaluated from both data and simulation for events in the final signal region D, identically to the way such numbers were derived for the nominal analysis. In all cases only the b-tagging variable and working point were modified – all remaining aspects of the analysis were identical to the nominal case.

The MV1c variable at the 57% efficiency working point was ultimately selected for the analysis as it was demonstrated to offer the best compromise between maintaining a low contribution from QCD multi-jet events in the final region while at the same time retaining a large number of final candidate events with which to perform the final measurement of m_{top}.

Table C.1: Comparison of performance for various choices of b-tagging variables and working points as described in the text. All values quoted were evaluated using simulated signal and data events following all event selection requirements.

Variable and Working Point	$S/(S+B)$ [%]	$\varepsilon_{signal}/\varepsilon_{signal}^{MV1c@57}$
MV1@80	19.3	2.35
MV1@70	41.2	1.29
MV1@60	47.9	0.35
MV1c@57	42.9	1.00
MV1c@50	44.6	0.78

[7]The improved resolution and its potential to improve precision on m_{top} was described in Section 12.1.

Appendix D

Additional Jet Energy Response and Resolution Plots

The jet energy response and resolution plots from Section 4.5, shown for various jet flavours, were produced from the results of the fits to the distributions which will be shown in Sections D.1, D.2 and D.3. All reconstructed jets from a subset of the nominal 60M simulated all-hadronic $t\bar{t}$ signal events were considered – this includes only those events passing a base set of preselection cuts[1]. The association of jets to truth-level jets or quarks from the hard-scatter process, as the case may be, was made by means of ΔR matching. In all cases a match required a separation $\Delta R < 0.3$ between the two objects. Non-matched reconstructed jets were not considered.

For comparisons between the energy or p_{T} of reconstructed jet and quark, the only further selection requirement is that the pseudorapidity of a given truth-record quark must satisfy $|\eta| < 2.5$ and its energy be at least 35 GeV. In the case of comparisons between reconstruction-level and truth-level jets, the same η requirement is used while the truth-jet energy threshold is set at 30 GeV. The reason for the cuts on the quark or truth-jet quantities is to be able to draw meaningful results from the fits. The minimum reconstruction-level jet p_{T} – strongly correlated with the energy – considered is 25 GeV; if a minimum quark energy threshold of 25 GeV were selected as opposed to 35 GeV (corresponding to the term in the denominator), there would be an artificially diminished number of entries in distributions of E^{reco}/E^{quark} below unity, and fits to such distributions would return distorted results. In light of this fact, it should be highlighted that the results of the response and resolution plots presented here, though quantitative, have no bearing on the final result and are meant to be illustrative only. Their primary purpose is to estimate the energy and p_{T} response of the reconstructed jets from simulated all-hadronic $t\bar{t}$ signal samples; these are expected to differ somewhat from the average response in the samples of events used to derive the standard jet calibrations such as the JES as will be described in Section D.4.

[1] These preselection cuts correspond exactly to those described in Section 7.4.2.

Before filling the distributions, the reconstructed jets from simulated events are separated into bins of energy[2] based on the energy of their associated truth-record object – either a truth-level jet or a quark as the case may be. The bin boundaries are selected in order that roughly equal numbers of truth-record quarks fall into each energy bin. This is accomplished by filling a two-dimensional $|\eta|$-E distribution for the quarks (or truth jets) and setting the boundaries such that the integrated number of objects in each region are approximately equal[3].

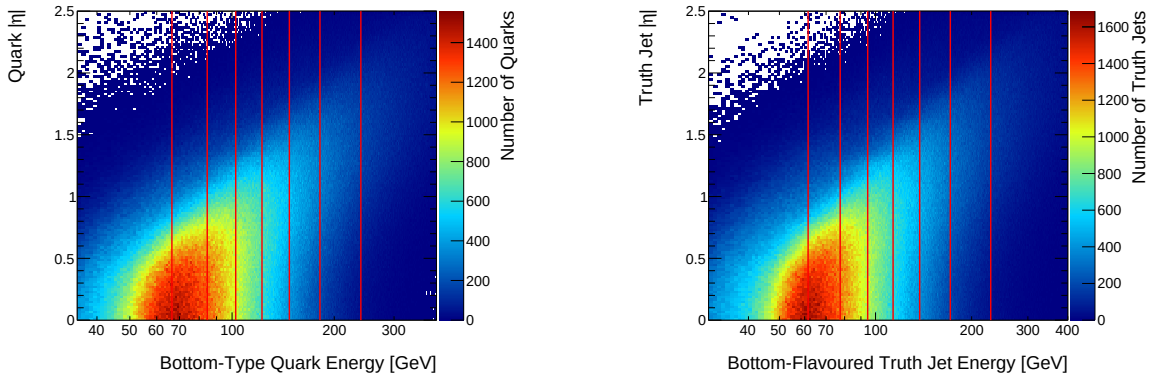

(a) Bottom-flavoured quarks

(b) Bottom-flavoured truth jets

Figure D.1: Binning regions selected to produce the jet energy response and resolution plots. The distributions were produced using simulated all-hadronic $t\bar{t}$ events. The binning was evaluated separately for two types of truth-record objects: (a) bottom-flavoured quarks from the top quark decay and (b) truth-level jets which themselves are matched to bottom-flavoured quarks. In all cases the objects are matched to a unique reconstructed jet.

A total of eight energy bins were selected for quark or truth-jet energies in the range $0 \leq E \leq 400$ GeV for the plots shown in this appendix. The two-dimensional histograms in Figures D.1(a) and D.1(b) show distributions of bottom-flavoured quarks and truth jets, respectively. Red lines correspond to the bin boundaries.

It should be recognized that there is a unique reconstruction-level jet associated with every quark or truth-level jet used to fill the above distributions. Reconstructed jets matched to truth-level jets but not to one of the six quarks from the hard-scatter event are assumed to be gluon-initiated jets, though it is recognized that there could exist other quarks leading to a truth-level jet in an event where the quark does not originate from the decay of one of the top

[2]Bins of pseudorapidity p_{T} may alternatively be used.

[3]Two-dimensional distributions were produced since the response is more generally meant to be evaluated as a function of both energy and pseudorapidity. For simplicity and since the response is not subsequently used to correct the jets in the analysis, a single $|\eta|$ bin was used.

quarks[4]. Since the truth-record information was not made available for the gluon four-vector quantities, only the response relative to truth-level jets was possible for these jets.

Plots analogous to those in Figures D.1(a) and D.1(b) were produced for other jet flavours in order to determine the bin ranges separately for each flavour but are not shown here.

D.1 Energy Response Relative to Quarks

In Figure D.2 distributions of the quantity E^{reco}/E^{quark} were filled using pairs of reconstruction-level jets and their associated quarks. Separate distributions were filled for jets matched to bottom-flavoured quarks (Figure D.2(a)) and lighter-flavoured (u/d/s/c) quarks (Figure D.2(b)), due to differences in the decay properties of the hadrons produced as a result of the parton shower. In either case a double Gaussian fit is performed in order to account for the low-energy tails present and due primarily to the undetected energies of the neutrinos and muons which were produced in the partonic showering process.

The significant fraction of energy carried away by the undetected particles is enhanced in the low-response tail of the bottom-flavoured distributions; bottom-type quarks (or rather hadrons containing bottom-type quarks) typically decay semileptonically *via* a virtual W boson leading to the process *i.e.* $b \to W^* \to q\ell\bar{\nu}_\ell$, where $q = u, c$ and $\ell = e, \mu, \tau$. The subsequent decay of the charm-type quark can lead to so-called **cascading decays** of the form $b \to W^* \to c\,(\to W^* q\ell^+\nu_\ell)\,\ell^-\bar{\nu}_\ell$ where now $q = s, d$. It should be recognized that the flavour of the two final-state (anti-)lepton and (anti-)lepton neutrinos in such cases, ℓ and ν_ℓ need not be the same. Cascading decays of this type can result in a larger fraction of unmeasured energy due to the presence of two final-state neutrinos.

Double-Gaussian fits were performed to each of the above distributions based on a standard χ^2 minimization procedure. The mean (μ) and width (σ) parameters of the higher-response Gaussian returned from the fit are the values shown in the jet energy response and resolutions plots shown in Figure 4.7(a) and Figure 4.7(c), respectively. In this case both the response and resolution of bottom-flavoured jets can be seen to be better than light-quark-flavoured jets, though in these plots one does not see information regarding the relative normalizations of the two Gaussians – the relative contribution of the lower-response Gaussian does not feature in the response and resolution plots.

The figures nonetheless highlight the flavour-dependent differences in the energy response and resolution of reconstructed jets.

[4]The quark could for instance come from the underlying event – interactions from partons from the colliding protons aside from those involved in the initial hard scatter.

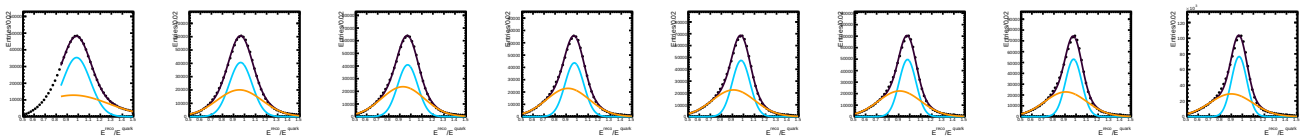

(a) Distributions of E^{reco}/E^{quark} for jets matched to bottom-flavoured quarks.

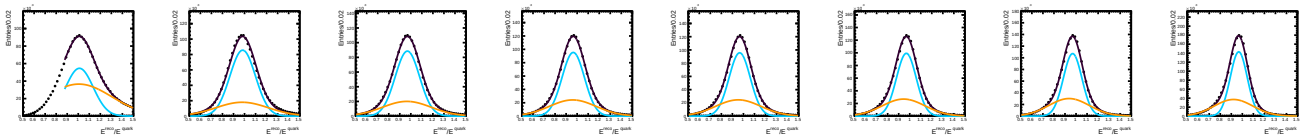

(b) Distributions of E^{reco}/E^{quark} for jets matched to light-flavoured quarks

Figure D.2: Distributions of the quantity E^{reco}/E^{quark} used to determine the jet energy response and resolution of reconstructed jets relative to the associated quark energies. Shown are the distributions for jets matched to (a) bottom-flavoured quarks and (b) light-flavoured (u/d/s/c) quarks. The lower- and higher-response double-Gaussian fit results are shown separately for each distribution in orange and blue, respectively. The plots are ordered from left to right in terms of the quark energy, based on the divisions shown in Figure D.1(a) in the case of the bottom-flavoured jets, and an analogous plot (not shown) for the light-flavoured-quark jets.

D.2 Energy Response of b-Flavoured Jets

In Section 4.5.3 the response and resolution of bottom-flavoured jets were shown separately for three cases, based on the presence of reconstructed muons matched to these reconstructed jets: bottom-flavoured jets with no matched muon; bottom-flavoured jets with a muon matched within $\Delta R(\mu, \text{jet}) < 0.3$; and the latter case in which the highest-energy matched muon four-vector is added back to that of the matched jet.

The plots shown in Figure D.3 show the base distributions of the quantity E^{reco}/E^{quark} for these three cases. The response and resolution from the plots in Figure 4.8 come from the double-Gaussian fits to these distributions identically to the procedure described above in Section D.1.

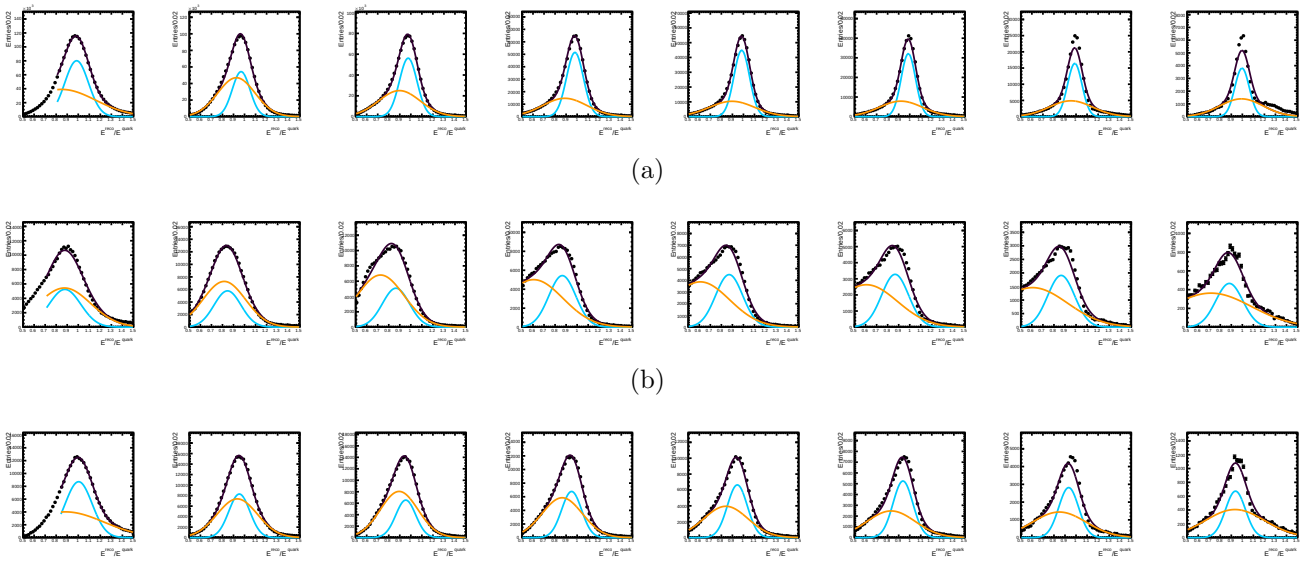

(a)

(b)

(c)

Figure D.3: Distributions of the quantity E^{reco}/E^{quark} used to determine the jet energy response and resolution of reconstructed jets relative to the associated quark energies. Shown are the distributions for jets matched to bottom-flavoured quarks and separated into three categories, based on potential matches between muons and each reconstructed jet: (a) no μ matched to reco-level jet, (b) μ matched to reco-level jet, (c) μ matched and added to reco-level jet four-vector. Overlayed on the distributions are the results from the double Gaussian fit, performed separately for each individual distribution.

D.3 Energy Response Relative to Truth Jets

Distributions of the quantity E^{reco}/E^{truth} are shown in Figure D.4 and separated into three jet flavour categories based on matches to truth-level jets: bottom-flavoured jets, light-quark-flavoured jets, and gluon-initiated jets. The third category, gluon-initiated jets, as described in the text, are labelled as such when no ΔR match is made between a given truth-level jet and one of the initial hard-scatter quarks from the top quark decay based on the Monte Carlo truth record.

The values of the parameters returned from the χ^2 minimization and based on the double-Gaussian parameterization were used to set the values of the points in the plots Figures 4.7(b) and 4.7(d).

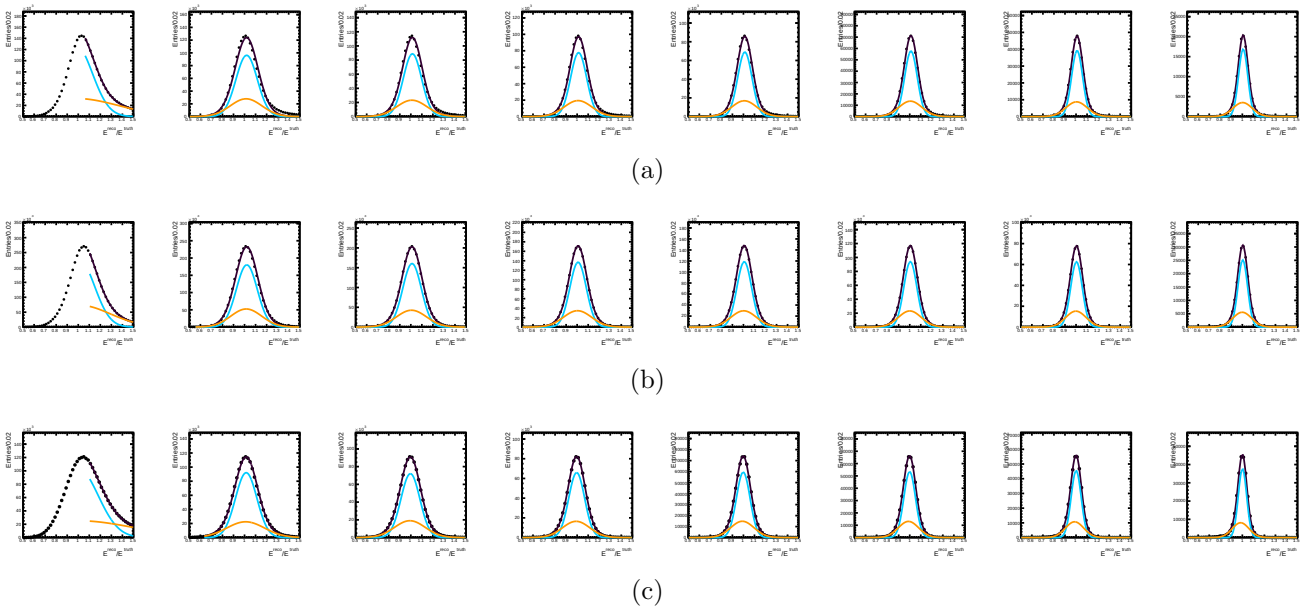

(a)

(b)

(c)

Figure D.4: Distributions of the quantity E^{reco}/E^{truth} used to determine the jet energy response and resolution of reconstructed jets relative to the associated truth jet energies. Shown are the distributions for jets matched to (a) bottom-flavoured quarks, (b) light-flavoured (u/d/s/c) quarks, and (c) those in which the jets are not matched to one of the quarks from the hard-scattering process – predominantly expected to be composed of gluon-initiated jets. Overlayed on the distributions are the results from the double Gaussian fit, performed separately for each individual distribution.

D.4 Flavour Fractions and Average Response

The plots in Figures D.5 (a) through (c) show the estimated flavour fractions of jets, evaluated from simulation, for the reconstruction-level jets in all-hadronic $t\bar{t}$ events. The same simulated events were used to produce these plots as those throughout this appendix. Figure D.5(d) shows the resulting two-dimensional plot of the average p_{T} response of jets, where the responses of each individual flavour of jet is weighted by its corresponding flavour fraction. The non-uniformity of the response in Figure D.5(d), and in particular the deviations from unity, are an artifact of the samples of events used to derive the JES corrections having had a different flavour composition to those in all-hadronic $t\bar{t}$ events.

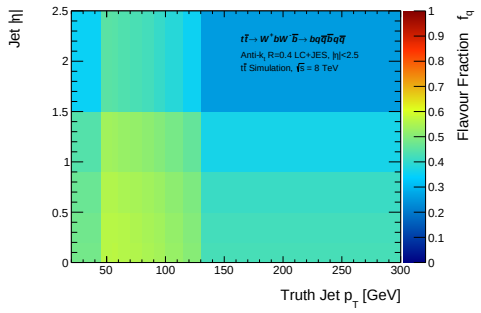

(a) Fraction of light-quark flavoured jets

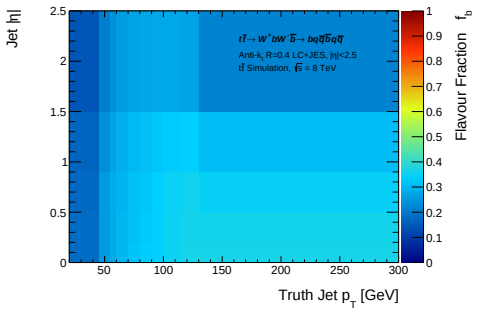

(b) Fraction of bottom-quark flavoured jets

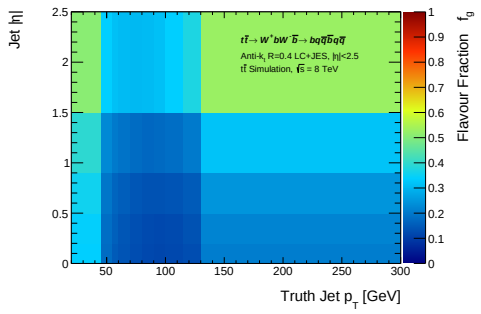

(c) Fraction of gluon flavoured jets

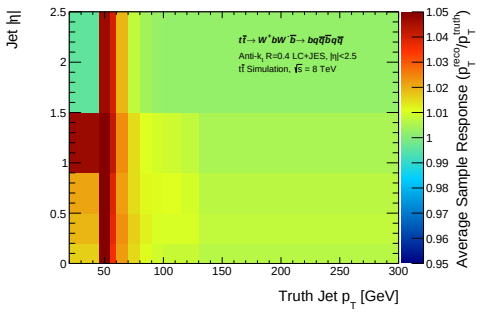

(d) Average flavour-weighted jet p_{T} response

Figure D.5: The fractions of reconstructed jets in simulated all-hadronic $t\bar{t}$ signal events identified as (a) light-quark, (b) bottom-quark, and (c) gluon flavoured jets. Jets are deemed to be gluon flavoured when no ΔR match is made to one of the six truth-record quarks from the initial hard-scatter process. Figure (d) shows the overall p_{T} response (rather than energy response) of jets relative to truth-level jets where the individual responses are weighted by their respective flavour fractions.

Appendix E

Parton-Level Jet Energy Correction

This appendix outlines an alternative approach to the one used in this analysis to derive a set of energy- and η-dependent correction factors for reconstructed jets by means of an iterative *in situ* approach[1]. The method works by exploiting the correlations between kinematic quantities from pairs of reconstructed jets which were produced as a result of hadronic W decays, together with the known W boson mass. Since the correction relates the energy of a reconstructed jet to that of a truth-record quark (a parton), it is referred to as a **parton-level correction** (PLC).

Although the method can be shown to work successfully when relying on truth-level quantities, closure of the method cannot be demonstrated when using only reconstruction-level quantities[2]; the method therefore remains a simulation-based correction. As such, employing such a technique in any analysis, given the method's reliance on truth-level quantities, would require a number of additional validation studies as well as the inclusion of a series of systematic uncertainties similar to those evaluated for the standard Jet Energy Scale (JES) corrections commonly used in ATLAS analyses. Such studies would require a significant amount of additional time, therefore rendering such an approach unfeasible due to timeline constraints. The parton-level correction method presented in this appendix was consequently not employed in the present analysis. It nevertheless remains a valid method and is included here as an appendix

[1] It is alternatively possible to derive p_{T}- and η-dependent correction factors. For the purposes of this appendix, it is the jet energy, rather than the jet p_{T}, which will be used, though the approach using the transverse momentum is identical. The method is referred to as an *in situ* approach in the case that no truth-level information were to be used, since in principle the correction could then be derived using data events alone. Note however that the method as described in this appendix, and based on the plots shown, is not used in this way.

[2] This failure to show method closure is due primarily to an effect known as bin migration: the energy response, as described in Section 4.5, of jets at the electromagnetic (EM) scale, is intrinsically a function of the energy or p_{T} of truth-level jets or quarks themselves. Consider a low-energy reconstruction-level jet: without relying on truth-level information, it is not possible to know *a priori* if the physical particle responsible for initiating the jet truly was a low-energy particle, or if it was rather a high-energy particle with a significant fraction of its energy lost due to non- or weakly interacting particles in the detector.

for documentation purposes.

It should be highlighted that in future $t\bar{t}$ analyses at the LHC the statistical limitations of the method may be overcome. In such a case the method could be revisited. Were it to be shown to work successfully without the use of truth-level quantities to derive the corrections, it would result in a significant reduction in the JES uncertainty for precision top quark analyses such as a measurement of the top quark mass.

This work is motivated by earlier studies carried out in 2009 using simulated semileptonic $t\bar{t}$ events in ATLAS at a centre-of-mass energy of $\sqrt{s} = 10$ TeV. In this study it was shown that employing such a technique could reduce the uncertainty on a top quark mass measurement due to uncertainties in the Jet Energy Scale (JES) [94][3].

E.1 Theoretical Motivation

As previously shown[4] the invariant mass of an object reconstructed *via* the four-vector sum of two jets with four-momenta p_1 and p_2 can be determined *via* the following relation:

$$m_{1,2}^2 = (p_1^\mu + p_2^\mu) \cdot (p_{1\mu} + p_{2\mu}) = m_1^2 + m_2^2 + E_1 E_2 - \vec{p_1} \cdot \vec{p_2} \tag{E.1}$$

where E_1, m_1, and $\vec{p_1}$ denote the energy, invariant mass and momentum of the first jet, and E_2, m_2 and $\vec{p_2}$ the corresponding values of the second jet. Using the rapidity y and transverse energy E_T of each object, and letting $\beta_T = p_\mathrm{T}/E_\mathrm{T}$, the alternate expression for the invariant mass quoted in Equation 3.6 may be used:

$$m_{1,2}^2 = m_1^2 + m_2^2 + 2E_{T_1}E_{T_2}\left(\cosh\Delta y - \beta_{T_1}\beta_{T_2}\cos\Delta\phi\right) \tag{E.2}$$

where Δy and $\Delta\phi$ represent the jet separations in rapidity and azimuthal angle, respectively.

The purpose of this appendix is to investigate the effect on the above invariant mass relation following the application of a parton-level correction, to be determined, to both the energy and momentum of the reconstruction-level jets. Here it can be assumed that such a correction factor, $f\,(E, \eta)$, is a function of a jet's energy and pseudorapidity without explicitly proposing its exact functional form. An underlying reason that such a correction would be required arises from the potential mis-measurement of the jet energies. This could be due to the nonlinear energy response of the calorimeter, to the presence of additional non-sampling detector material, or simply to some overall mis-calibration. Some of these effects could also be expected to vary non-negligibly with η. The presence of a potential cross-term associated with the product $E \cdot \eta$ is neglected in the derivation of the correction factors themselves.

[3]The BaBar Collaboration employed a similar iterative method to calibrate their electromagnetic calorimeter using the invariant mass of reconstructed neutral pions decaying *via* $\pi^0 \to \gamma\gamma$. See [95] for more information.

[4]Refer to Section 3.2.1 for a reminder of the definitions of several of the quantities used in this appendix.

A jet with original energy and transverse momentum E and p_{T}, upon application of such a correction factor, will have a corrected energy and transverse momentum E' and p'_{T} given by:

$$E \to E' = f\left(E,\eta\right)E \quad \text{and} \quad p_{\mathrm{T}} \to p'_{\mathrm{T}} = f\left(E,\eta\right)p_{\mathrm{T}} \tag{E.3}$$

whereas its angular angular position, in terms of the quantities η, ϕ and also the rapidity y, will remain unmodified. In other words, a given jet's four-vector transforms *via*:

$$p^{\mu} = (p_{\mathrm{T}},\eta,\phi,E) \to p'^{\mu} = (fp_{\mathrm{T}},\eta,\phi,fE) \tag{E.4}$$

Using the definition of the transverse energy it can be shown that E_{T} transforms in an identical manner to E and p_{T}, namely:

$$E_{\mathrm{T}} \to E'_{\mathrm{T}} = \sqrt{E'^2 - p'^2_z} = \sqrt{E'^2 - p'^2\cos^2\theta} = \sqrt{f^2E^2 - f^2p^2\cos^2\theta} = f\left(E,\eta\right)E_{\mathrm{T}} \tag{E.5}$$

Consider a large sample of hadronically decaying W boson candidates[5], where each candidate has been reconstructed by means of the four-momentum addition of two reconstruction-level jets. The jets in this case must both be uniquely ΔR-matched to two truth-record quarks from the hadronic W boson decay[6]. It would be expected that if the appropriate correction factors were to be applied to each of the jets as described by the process above, that the distribution of the invariant mass, $m_{1,2}$, should have its peak near the true mass of the W boson. The true mass of each W boson is taken to be the invariant mass of its truth-record decay products, $q\bar{q}$. It should be noted that the distribution $m_{q\bar{q}}$ can be described by a Breit-Wigner function[7]. The mean parameter from a Breit-Wigner fit to this distribution was seen to be consistent with the best-measured m_W value from the PDG, and this becomes the most sensible reference point.

[5]Although the same simulated all-hadronic signal events are used here as in the nominal analysis, in principle *any* sample of W bosons which decay *via* $W \to q\bar{q}$ may be employed for the purpose of deriving these parton-level corrections. One must then ensure that the kinematics and energy response of the jets in the sample for which the corrections were derived do not differ greatly from those in the analysis for which the correction factors are to be subsequently applied. In particular, semileptonic $t\bar{t}$ events could be used to derive the corrections using the standard tag-and-probe technique which allows the reconstruction of one hadronically and one leptonically decaying W boson. This would take advantage of the comparatively suppressed background in semileptonic $t\bar{t}$ analyses. The derived correction factors could then be applied to the jets in all-hadronic $t\bar{t}$ analyses. This would further avoid the issue of statistical correlation introduced by using the same events to derive the calibration as those used in the final analysis.

[6]In other words, the correct jets have always been used in the reconstruction of the W boson candidates. In practice such truth-level information is not available in data events. The best one can hope for is to employ a high-purity reconstruction algorithm similar to that described in Chapter 6 in order to assign the jets to the quarks. Provided the fractional number of incorrectly reconstructed W bosons remains small, the invariant $m_{1,2}$ distribution will take on a near-Gaussian shape, aside perhaps from the presence of a broad, secondary tail due to non-interacting particles in the detector.

[7]See the distribution of $m_{q\bar{q}}$ in Figure 6.2(b).

The value of m_W^{PDG} is adopted in order to perform an absolute calibration based on this best-measured value of the W boson mass. On a per-event basis however it should not be expected that the invariant mass of any particular reconstructed W boson should be equal to m_W^{PDG} itself.

Mathematically, the values of the correction factors $f(E,\eta)$ for a given energy and $|\eta|$ range can be selected such that the position of the peak of the $m_{1,2}$ distribution satisfies:

$$\frac{m_{q\bar{q}}}{m_{1,2}} = \left[\frac{m_1'^2 + m_2'^2 + 2E'_{T_1}E'_{T_2}\left(\cosh\Delta y - \beta_{T_1}\beta_{T_2}\cos\Delta\phi\right)}{m_1^2 + m_2^2 + 2E_{T_1}E_{T_2}\left(\cosh\Delta y - \beta_{T_1}\beta_{T_2}\cos\Delta\phi\right)}\right]^{\frac{1}{2}} \tag{E.6}$$

or alternatively, by making use of Equation E.3, that:

$$\frac{m_{q\bar{q}}}{m_{1,2}} = \left[\frac{f^2\left(E_1,\eta_1\right)m_1^2 + f^2\left(E_2,\eta_2\right)m_2^2 + 2f\left(E_1,\eta_1\right)f\left(E_2,\eta_2\right)E_{T_1}E_{T_2}\left[\cosh\Delta y - \beta_{T_1}\beta_{T_2}\cos\Delta\phi\right]}{m_1^2 + m_2^2 + 2E_{T_1}E_{T_2}\left(\cosh\Delta y - \beta_{T_1}\beta_{T_2}\cos\Delta\phi\right)}\right]^{\frac{1}{2}} \tag{E.7}$$

Provided the energies and pseudorapidities of the two quarks in a given $q\bar{q}$ pair are highly correlated, one can then say that the correction factors for each of the two jets associated to these quarks should be approximately equal to the correction factors based on the average values of quark energy or jet $|\eta|$. In other words, here the assumption is made that:

$$f\left(E_{1(2)},\eta_{1(2)}\right) \approx f\left(\frac{E_1+E_2}{2},\frac{\eta_1+\eta_2}{2}\right) \tag{E.8}$$

In practice, the strength of such a correlation will vary depending on the kinematics of a particular sample. In some cases it might be necessary to artificially construct a correlated sample, or enhance the correlation in the case that it is small. This could be done – at the cost of diminished statistics and potential kinematic biases – by removing any W boson candidates for which the difference in energy between the two constituent quarks is larger than some allowed tolerance. For the present case such a requirement is indeed enforced by requiring that for each W candidate the energies of their two constituent quarks are allowed to differ by no greater than 25 GeV (*i.e.* the two quarks must satisfy $|E_{q1} - E_{q2}| \leq 25$ GeV). Candidate W bosons failing this requirement are not considered.

Provided the approximation given in Equations E.8 is satisfied – that the level of correlation between the relevant quantities is large – then, making use of Equation E.7, one can say that:

$$\frac{m_{q\bar{q}}}{m_{1,2}} \approx f\left(\frac{E_1+E_2}{2},\frac{\eta_1+\eta_2}{2}\right) \tag{E.9}$$

Distributions of invariant dijet masses ($m_{1,2}$) of the full sample of reconstructed W bosons can therefore be produced by filling different histograms of the inverse of the left-hand side of Equation E.9, ($m_{1,2}/m_{q\bar{q}}$). Each of the distributions will correspond to different quark energy and jet $|\eta|$ ranges in order to probe the structure of this correction function $f\left(E,\eta\right)$. The value

($m_{1,2}$) of each dijet pair is used to fill two separate histograms: the first based on the energy of the first quark (and $|\eta|$ of the corresponding jet), and the second based on the energy of the second quark (and $|\eta|$ of its corresponding jet). For a total of N_E unique energy bins and N_η unique bins of $|\eta|$, there will be a total of $N_E \times N_\eta$ such distributions.

At this point it is important to highlight the fact that in the binning procedure is performed based on the energy of the quarks as opposed to their corresponding reconstructed jets. This is a standard practice in deriving a simulation-based correction, employing a technique referred to as **numerical inversion**[8]. The correction factors are first derived as a function of the quark energies, and are subsequently transformed in order to yield correction factors to be applied as a function of the reconstruction-level quantities. Such a procedure results in distributions which are more Gaussian for the purposes of performing the fits. In contrast to the energy, which can differ greatly between a reconstructed jet and its associated truth-record quark, the pseudorapidity of the two objects are quite similar; for this reason the binning in $|\eta|$ employs the reconstruction-level jet $|\eta|$ values rather than those of their associated quark.

A standard least-squares fit can then be performed to each individual distribution of the quantity $m_{1,2}/m_{q\bar{q}}$ based on a double-Gaussian parameterization. The second Gaussian reflects the asymmetric nature of the $m_{1,2}$ which arises primarily due to non-interacting neutrinos and muons. If any calibration was performed upstream, such as a calibration of the energy of the jets or their constituent clusters, then this broader tail will not necessarily be a low-mass tail. It should be highlighted that a large number of parallels exist between fits performed here and those for evaluating the energy response and resolution of jets[9].

The assumption made in Equation E.8 is not exact. This can be compensated for by repeating the above procedure iteratively. For all iterations the bin corresponding to a particular jet is based on its quark energy and initial $|\eta|$ value – a jet's bin remains constant throughout the entire procedure. The strength of this method therefore comes from the correlations between the energies and pseudorapidities of pairs of quarks, which allow for such an iterative one-dimensional approach as opposed to a non-iterative, two-dimensional approach[10].

For a given iteration n, a correction factor $f_n^{ij}(E,\eta)$ for quarks in a particular energy bin i and $|\eta|$ bin j can be derived, and the product of such correction factors over all iterations represents the final correction factor to be applied to the jets in the analysis, i.e.:

$$f^{ij} = \prod_{n=1}^{N} f_n^{ij}(E,\eta) \tag{E.10}$$

It should be noted that the correction factor applied to a jet at a given iteration is the product of all factors up to the immediately preceding iteration. Since the exact functional form is neither

[8] For more information on this technique used for deriving a general jet energy correction see [96].

[9] Refer to Section 4.5 as well as Appendix D.

[10] Using a one-dimensional iterative approach allows for a far greater number of statistics in each bin.

known, nor evaluated[11], the particular correction factor applied to the given jet is evaluated by means of a linear interpolation from the graph (for a fixed $|\eta|$ region) of the values of $f_n(E,\eta)$ as a function of energy[12].

A series of tests were performed in order to validate the performance of this iterative method. Initially the four-vector quantities for the truth-record quarks themselves – rather than those of the reconstruction-level jets – were used as the input to the method, but with modified energy and transverse momentum. These modified values were produced by means of applying some global (or energy-dependent) shift to the energy and p_{T} of the input quarks, or by applying Gaussian smearing to degrade their energy or p_{T} resolution. This allowed for an effective user-controlled energy response and resolution for the input objects; the iterative method was then performed and the resulting correction factors compared with the known form of the shifts.

E.2 Derived Corrections from Simulated Signal Events

In what follows, a set of PLC factors were derived from simulated all-hadronic $t\bar{t}$ signal events. Although ultimately the decision was made not to apply PLCs to the jets in the present analysis due to the additional validation and systematic studies that would have been required, the derivation serves as an example of the machinery of the method. As this method could in principle be used in the place of the standard JES and jet corrections[13], the initial jet four-vectors correspond to their uncorrected values – the energy and momentum are based on the four-vector sum of all energy clusters selected by the anti-k_T jet reconstruction algorithm[14] with cluster energies at the LCW scale.

Figure E.1 shows a two-dimensional distribution of all quarks considered for the PLC derivation. The distribution is filled using truth-record quarks from the hard-scatter process $t\bar{t} \to W^+bW^-\bar{b} \to q\bar{q}bq\bar{q}\bar{b}$, though strictly only those resulting from hadronic W boson decays ($W \to q\bar{q}$), and only those for which each $q\bar{q}$ pair has a corresponding pair of reconstructed jets and with a unique jet-quark match for each quark. Only W candidates for which both quarks have an energy of at least 35 GeV are considered[15], and as mentioned above the energy of each pair of quarks must satisfy the constraint $|\Delta E| \leq 25$ GeV. Events in which *any* two reconstructed jets fail to pass an isolation cut ($\Delta R(j_1, j_2) < 0.6$) are not considered[16]. A total of

[11] An alternative approach would be to parameterize the functional form of the correction factors $f_n(E,\eta)$ and perform a least-squares fit at each step in the iteration.

[12] In this case the interpolation is performed in energy alone; a bilinear interpolation, performed using a two-dimensional graph of the evaluated correction factors *versus* both the energy and pseudorapidity could alternatively be performed.

[13] Refer to Section 4.6 on the corrections applied to reconstruction-level jets.

[14] Refer to Section 4.2.

[15] This minimum energy cut is employed for the same reason as that described in Appendix D.

[16] The application of this cut is made in order to ensure a unique jet-quark match exists for all quarks considered,

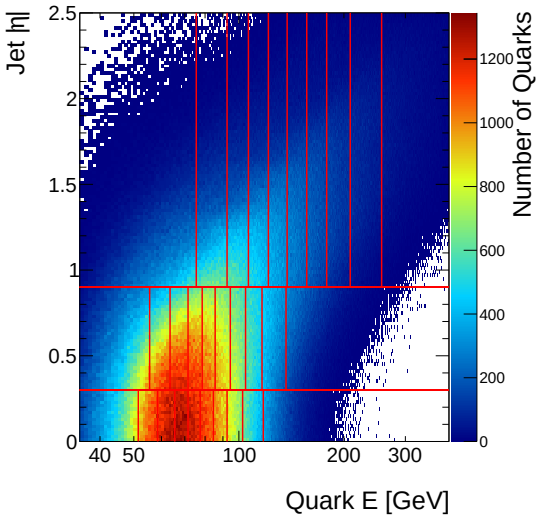

Figure E.1: Distribution of quarks in the simulated all-hadronic $t\bar{t}$ sample used to derive parton-level correction factors. Solid red lines correspond to the bin boundaries; these were selected in order to have a roughly equal number of quarks in each bin in the two-dimensional histogram.

$N_E \times N_\eta = 10 \times 3 = 30$ distinct bins were used, with bin regions selected in order to have roughly equal numbers of quarks in each bin.

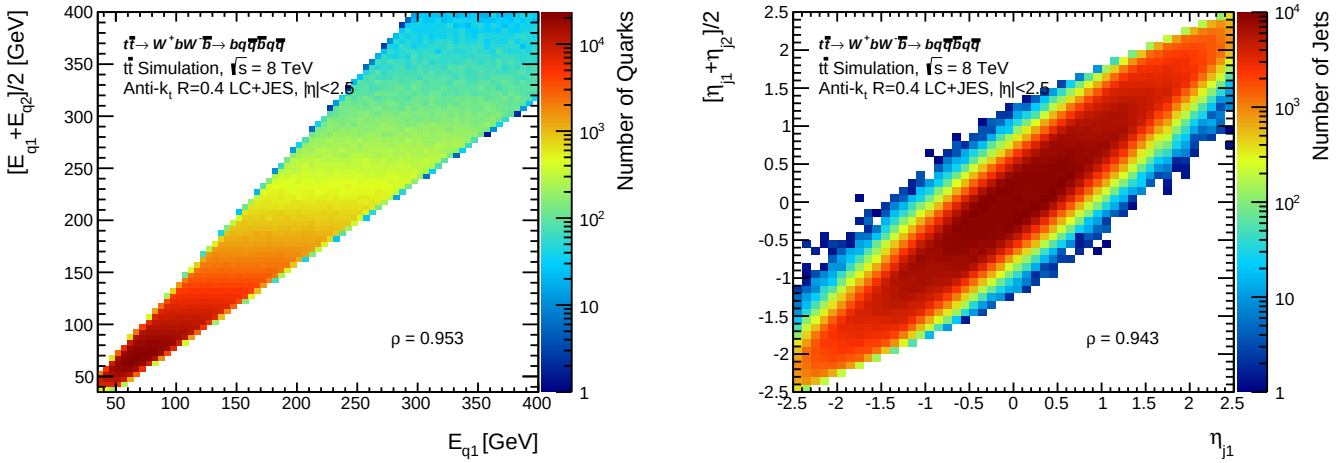

Figure E.2: Two-dimensional histograms produced using all-hadronic $t\bar{t}$ events. The left-hand plot shows the correlation between the energy of one of the quarks and the average of the two quarks forming each W. The right-hand plot simlarly shows the correlation between the η of one of the jets and the average η of the two jets forming the W candidate. Such plots motivate the assumption made in Equation E.8.

The assumption made in Equation E.8, that the energy of a given quark and the average energy of the two quarks are highly correlated (and similarly that the η of one jet in the dijet pair

and due to the fact that such an event selection cut is enforced in the analysis.

is correlated to the average jet η), is validated by the plots shown in Figure E.2. The designation of quark 1 and quark 2 is performed impartially by means of drawing from a uniform U(0,1) distribution; a similar process is used for the reconstructed jets for the purposes of the plots. The high level of correlation between the energies and pseudorapidities of a single object (quark or jet as the case may be) and the average value should be expected – highly boosted W bosons from the top quark decays will result in higher boosts of both daughter quarks. In contrast the relative fractions of the W boson energy for each of the two quarks (*i.e.* the quantities $E_1/E_{1,2}$ and $E_2/E_{1,2}$) are 100% anti-correlated. The constraint mentioned above, requiring $|\Delta E| \leq 25$ GeV for the energies of the quarks, serves to strengthen the desired correlations.

Figures E.3(a) and E.3(b) show representative distributions of the quantity $m_{1,2}/m_{q\bar{q}}$ for two subsets of quarks – those in the energy range [35-52] or [118-400] GeV and with their associated jets in the $|\eta|$ range [0,0.3]. The distributions were filled based on jet four-vector quantities at the first iteration of the procedure and using the form of the invariant mass $m_{1,2}$ from Equation E.1 (or equivalently Equation E.2). One can note in both distributions the presence of a primary signal, as well as a secondary, broader tail encapsulated by the second Gaussian. This plot is analogous to those in Figure 4.6 used to derive the jet energy response and resolution of b-flavoured jets.

The inverse value of the primary Gauss mean parameter, extracted as a result of a standard χ^2 minimization procedure, sets the correction factor for that bin for the subsequent iteration. Its value also appears at the corresponding point in the plot shown in Figure E.5(a), which shows all of the derived correction factors as a function of quark energy following the first iteration.

The plot in Figure E.4(a) offers an alternate perspective of the extracted PLC factors following the first iteration; it shows a two-dimensional plot of the derived PLC values as a function of jet $|\eta|$ and quark energy. The coloured values of the PLC factors are equivalent to the values shown in the plot in Figure E.5(a).

In the subsequent iterations, jets for which the associated quark falls in this E and $|\eta|$ bin have their energy and p_{T} corrected *via* Equation E.9, based on the PLC factor interpolated from this plot. The process is subsequently repeated for the next iteration. The PLC factors following the first, the third, and the fifth and final iteration are shown in Figure E.5. The various markers in Figure E.5 correspond to different jet $|\eta|$ ranges. The right-hand plots in all cases correspond to the cumulative values based on Equations E.10. The power of the iterative procedure is made clear from the fact that the PLC factors derived in later iterations, and for all E and $|\eta|$ bins, approach unity; smaller and smaller corrections are required for each subsequent iteration. The fifth iteration, with results shown in Figure E.5(c) is the final iteration performed. In general the iterative process was made to terminate when the PLC factor in all bins was smaller than 1% – a condition satisfied following five iterations for the present case. The analogous two-dimensional plots following the fifth iteration, as well as the cumulative values, are shown in Figures E.4(b) and E.4(c), respectively.

The final result is that a maximum correction of up to roughly 8% must be applied to the

jet energies and p_{T} in order to yield the proper, calibrated, invariant mass value $m_{q\bar{q}}$. It should be noted that this is recognizably for uncalibrated jets, and is illustrative only. In some cases the jet energies and p_{T} must be scaled down. The final cumulative PLC factors are shown in the right-hand plot of Figure E.5(c). The process of numerical inversion can subsequently be performed in order to transform the plot of $f(E, |\eta|)$ *vs.* the quark energy (as currently shown in the right-hand plot of Figure E.5(c)) to a plot of $f(E, |\eta|)$ *vs.* reconstruction-level jet energy[17].

Overall the method described provides a means to correct to the energy scale of jets to the original quark energies using a one-dimensional iterative approach. It is recognizably a topology-dependent correction, appropriate only for $t\bar{t}$ events with a certain quark-gluon flavour fraction. Moreover the kinematics of quark-initiated jets from other processes could differ. Ultimately the true strength of such a method would lie in the ability to perform the binning of jets with no reliance on truth-record information; should it prove possible to do so in the future, this method would allow for an *in situ* or data-driven correction resulting in a great reduction in the JES uncertainty. The systematic uncertainties arising from uncertainties in the bJES[18] however would be expected to remain unaffected, as the correction described here targets primarily light-quark-initiated jets from the $W \to q\bar{q}$ decays.

In future linear e^{+}-e^{-} colliders the all-hadronic $t\bar{t}$ channel will not be expected to suffer from a dominant QCD multi-jet background as in the case of a p-p collider. This would allow for an analogous two-step correction scheme to be employed using the known W boson and top quark mass to correct quark- and bottom-quark-initiated jets, respectively. At centre-of-mass energies far above the $t\bar{t}$ threshold energy, the majority of top quarks would be produced with a significant boost. In such a regime, a single, large-R-parameter jet[19] could be used, together with some of the current tools utilized by the ATLAS collaboration to investigate jet substructure, in order to determine a jet energy calibration scheme.

[17] In effect the process of numerical inversion keeps the vertical positions of the points fixed while adjusting the bin ranges (and therefore the horizontal positions of the points) of the energy based on the measured energy response relating quark to jet energies.

[18] Refer to the b-Jet Energy Scale (bJES) systematic uncertainty in Section 11.7.8.

[19] Such jets are conventionally referred to as fat jets. Refer to the anti-k_T jet reconstruction algorithm described in Section 4.2 for a reminder of how the R parameter is used to reconstruct jets from calorimeter energy clusters.

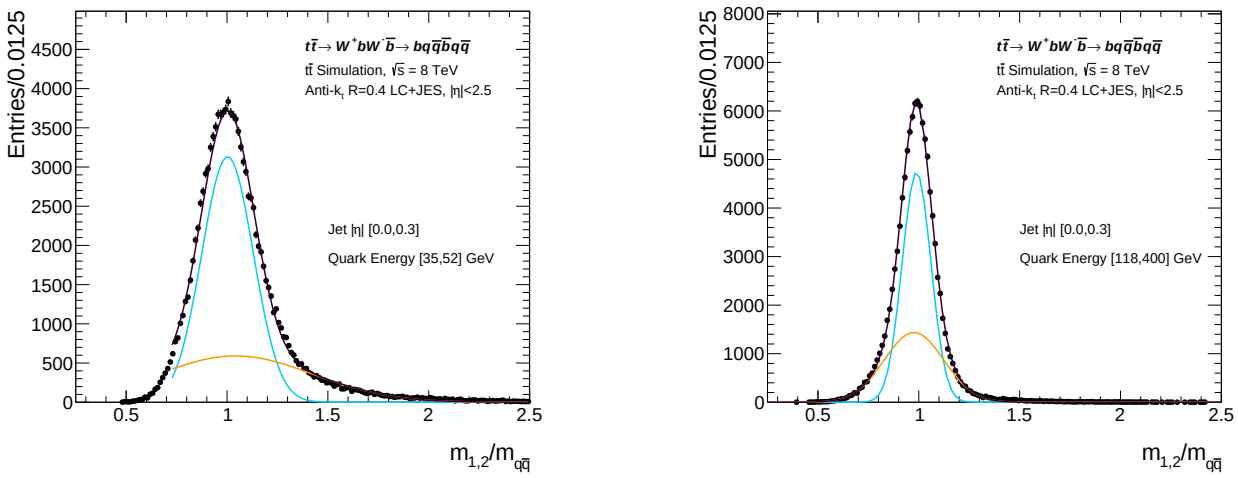

(a) (b)

Figure E.3: Sample but representative distributions of the quantity $m_{1,2}/m_{q\bar{q}}$ for two subsets of quark energies in (a) and (b), where the result of the double-Gaussian fit to each distribution is used to derive the PLC factor for that bin.

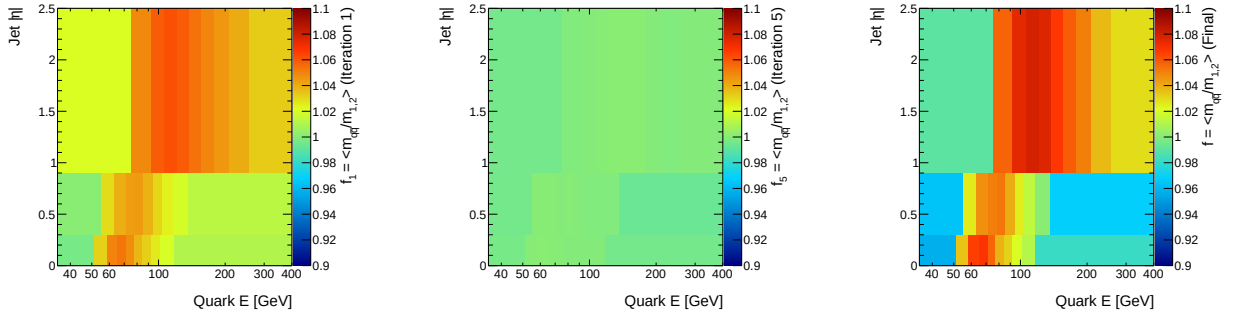

(a) (b) (c)

Figure E.4: Two-dimensional plots of the derived PLC factors, shown as a function of both the jet pseudorapidity and the corresponding quark energy. The values are shown following (a) the first iteration, (b) the fifth and final iteration, and (c) the cumulative values following all iterations based on the expression from Equation E.10.

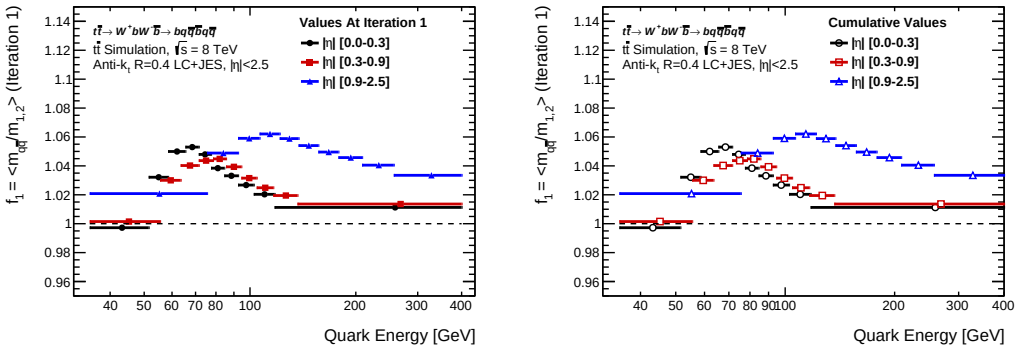

(a)

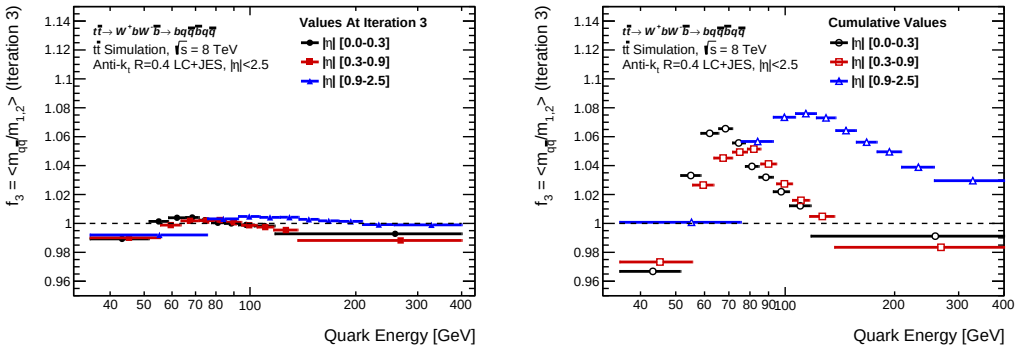

(b)

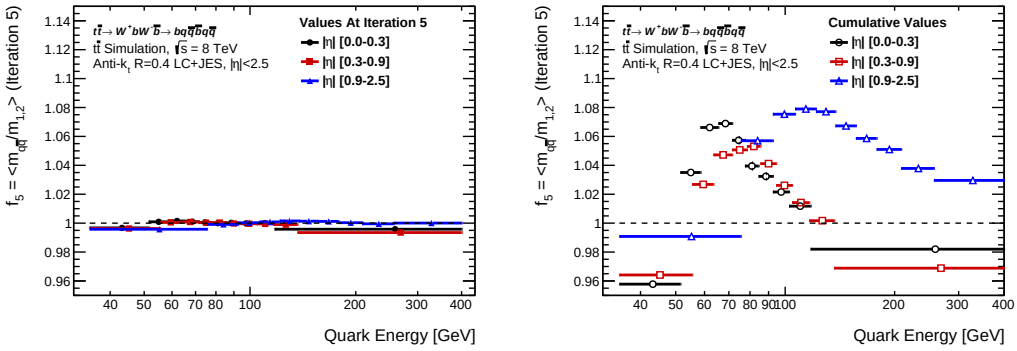

(c)

Figure E.5: Derived PLC factors after the 1st, the 3rd and the 5th and final iteration. The individual values following each iteration are shown (left-hand plots) as well as their cumulative values (right-hand plots).

References

[1] ATLAS Collaboration. *Observation of a new particle in the search for the Standard Model Higgs boson with the ATLAS detector at the LHC.* Phys. Lett. B, **716**:1–29, (2012).

[2] G. Degrassi et al. *Higgs mass and vacuum stability in the Standard Model at NNLO.* JHEP, **1208**:35, (2012).

[3] K.A. Olive et al. *Review of Particle Physics.* Chin.Phys., **C38**:090001, (2014).

[4] ATLAS and CMS Collaborations. *Combined Measurement of the Higgs Boson Mass in pp Collisions at $\sqrt{s}$ = 7 and 8 TeV with the ATLAS and CMS Experiments.* Phys. Rev. Lett., **114**:191803, (2015). [arXiv:1503.07589].

[5] S.W. Herb et al. *Observation of a Dimuon Resonance at 9.5-GeV in 400-GeV Proton-Nucleus Collisions.* Phys. Rev. Lett., **39**, 252, (1977).

[6] H. Harari. *A New Quark Model for Hadrons.* Phys. Lett. B., **57B, 3**, (1975).

[7] S.Abachi et al. *Observation of the Top Quark.* Phys. Rev. Lett., **74**, 2632, (1995). [hep-ex/9503003] (D0 Collaboration).

[8] F.Abe et al. *Observation of Top Quark Production in $p\bar{p}$ Collisions.* Phys. Rev. Lett., **74**, 2626, (1995). [hep-ex/9503002] (CDF Collaboration).

[9] D. Gillberg. *Discovery of Single Top Quark Production.* PhD Thesis, Simon Fraser University, (2009). (D0 Collaboration).

[10] T. Aaltonen et al. *First Observation of Electroweak Single Top Quark Production.* Phys. Rev. Lett., **Vol. 103**, (2009). [arXiv:0903.0885v3] (CDF Collaboration).

[11] V.M. Abazov et al. *Observation of Single Top Quark Production.* Phys. Rev. Lett., **103**, (2009). [arXiv:0903.0850v2] (D0 Collaboration).

[12] M.E.Peskin and D.V.Schroeder. *An Introduction to Quantum Field Theory.* Westview Press, (1995).

[13] *ATLAS Luminosity Public Results.* https://twiki.cern.ch/twiki/bin/view/AtlasPublic/LuminosityPublicResults.

[14] I.J.R.Aitchison and A.J.G.Hey. *Gaus Theories in Particle Physics, Volume I: From Relativistic Quantum Mechanics to QED.* Taylor and Francis Group, 3rd edition, (2003).

[15] J. Pumplin et al. *New Generation of Parton Distributions with Uncertainties from Global QCD Analysis.* JHEP, (2012). [arXiv:hep-ph/0201195].

[16] H. Lai et al. *New parton distributions for collider physics.* Phys. Rev. D., **82**, (2010). [074024].

[17] N. Kidonakis and B. Pecjak. *Top-quark production and QCD.* Eur. Phys. J., **C72 2084**, (2011). [arXiv:1108.6063].

[18] ATLAS Collaboration. *Measurement of the $t\bar{t}$ production cross-section using $e\mu$ events with b-tagged jets in pp collisions at $\sqrt{s} = 7$ and 8 TeV with the ATLAS detector.* Eur.Phys.J., **C74**:3109, (2014). [arXiv:1406.5375v2].

[19] M. Cacciari et al. *Top-pair production at hadron colliders with next-to-next-to-leading logarithmic soft-gluon resummation.* Phys. Lett. B., **B710 612**, (2012). [arXiv:1111.5869].

[20] P. Baernreuther et al. *Percent Level Precision Physics at the Tevatron: First Genuine NNLO QCD Corrections to $q\bar{q} \rightarrow t\bar{t}$.* Phys. Rev. Lett., **109 132001**, (2012). [arXiv:1204.5201].

[21] M. Czakon and A. Mitov. *NNLO corrections to top pair production at hadron colliders: the quark-gluon reaction.* JHEP, **1301 080**, (2013). [arXiv:1210.6832].

[22] M. Czakon et al. *The total top quark pair production cross-section at hadron colliders through $\mathcal{O}(\alpha_s^4)$.* Phys. Rev. Lett., **110 252004**, (2013). [arXiv:1303.6254].

[23] A. Quadt. *Top quark physics at hadron colliders*. Eur. Phys. J., **48**, (2008).

[24] ATLAS Collaboration. *Determination of the Top-Quark Mass from the $t\bar{t}$ Cross Section Measurement in pp Collisions at $\sqrt{s} = 7$ TeV with the ATLAS detector*. (2011). [ATLAS-CONF-2011-054].

[25] *ATLAS Standard Model Public Results*. https://twiki.cern.ch/twiki/bin/view/AtlasPublic/StandardModelPublicResults.

[26] ATLAS Collaboration. *Differential top-antitop cross-section measurements as a function of observables constructed from final-state particles using pp collisions at $\sqrt{s} = 7$ TeV in the ATLAS detector*. JHEP, (Submitted 2015).

[27] *ATLAS Top Quark Public Results*. https://twiki.cern.ch/twiki/bin/view/AtlasPublic/TopPublicResults.

[28] V. Boisvert. *Top quarks objects definition and performance at ATLAS*. Journal of Physics: Conference Series 452, (2013). [012012] (Top2012 Workshop, On behalf of the ATLAS Collaboration).

[29] V.M. Abazov et al. *Precision Measurement of the Top Quark Mass in Lepton + Jets Final States*. Phys. Rev. Lett., **Vol. 113**:032002, (2014). (D0 Collaboration).

[30] G. Panchieri et al. *Precise measurement of the toponium mass from the observation of its two-photon decay at the LHC*. Phys. Lett. B., **Vol. 277**:518–523, (1992).

[31] ATLAS Collaboration. *Measurement of the W boson polarization in top quark decays with the ATLAS detector*. Phys. Lett. B., **1206**:088, (2012).

[32] ATLAS Collaboration. *Observation of spin correlation in ttbar events from pp collisions at $\sqrt{s} = 7$ TeV using the ATLAS detector*. Phys. Rev. Lett., **108**:212001, (2012).

[33] ATLAS Collaboration. *Measurement of the mass difference between top and anti-top quarks in pp collisions at $\sqrt{s} = 7$ TeV using the ATLAS detector*. Phys. Lett. B., **728**:363–379, (2013).

[34] ATLAS Collaboration. *Measurement of the top quark charge in pp collisions at $\sqrt{s} = 7$ TeV with the ATLAS detector.* JHEP, **11**:031, (2013).

[35] ATLAS Collaboration. *Measurement of the Top Quark Mass with the Template Method in the $t\bar{t} \rightarrow$ lepton+jets Channel using ATLAS data.* Eur. Phys. J., **C72**:2046, (2012).

[36] ATLAS Collaboration. *Measurement of the Top Quark Mass in Dileptonic Top Quark Pair Decays with $\sqrt{s} = 7$ TeV ATLAS data.* (2013). [ATLAS-CONF-2013-077].

[37] ATLAS Collaboration. *Measurement of the top quark mass in topologies enhanced with single top quarks produced in the t-channel at $\sqrt{s} = 8$ TeV using the ATLAS experiment.* (2014). [ATLAS-CONF-2014-055].

[38] ATLAS Collaboration. *Determination of the top-quark pole mass using $t\bar{t} + 1$-jet events collected with the ATLAS experiment in 7 TeV pp collisions.* (2014). [ATLAS-CONF-2014-053].

[39] M.C. Smith and S.S. Willenbrock. *Top-quark pole mass.* Phys. Rev. Lett., **79**:3825–3828, (1997). [hep-ph/9612329].

[40] ATLAS, CDF, CMS and D0 Collaborations. *First combination of Tevatron and LHC measurements of the top-quark mass.* (2014). [ATLAS-CONF-2014-008].

[41] R. Nisius. *A ROOT class to combine a number of correlated estimates of one or more observables using the Best Linear Unbiased Estimate method.* Software version 1.8.0, http://blue.hepforge.org/.

[42] L. Evans and P. Bryant. *LHC Machine.* J. Inst., **3**, (2008). (S08001).

[43] G. Aad et al. *The ATLAS Experiment at the CERN Large Hadron Collider.* J. Inst., **3**, (2008). (S08003).

[44] R. Fernow. *Introduction to experimental particle physics.* Cambridge University Press, (1986).

[45] R. Wigmans. *Calorimetry: Energy Measurement in Particle Physics.* Oxford Science Publications, (2000).

[46] ATLAS Collaboration. *Alignment of the ATLAS Inner Detector and its Performance in 2012*. (2014). [ATLAS-CONF-2014-047].

[47] N. Nikiforou. *Performance of the ATLAS Liquid Argon Calorimeter after Three Years of LHC Operation and Plans for a Future Upgrade*. (Proceedings of talk presented in "Advancement in Nuclear Instrumentation Measurement Methods and their Applications", Marseille), (2013). (On behalf of the ATLAS Collaboration).

[48] W. Lampl et al. *Calorimeter Clustering Algorithms: Description and Performance*. ATLAS Note, (2008). (ATL-LARG-PUB-2008-002).

[49] P. Strizenec and A. Minaenko (for the ATLAS LAr Endcap Group). *Performance of the ATLAS Liquid Argon Endcap Calorimeter in Beam Tests*. J. Phys. Conference Series, **160**, (2009). [012078].

[50] J.P. Archambault et al. *Energy calibration of the ATLAS Liquid Argon Forward Calorimeter*. J. Inst., **3**, (2008). [JINST 3 P02002].

[51] J.C. Armitage et al. *Electron signals in the Forward Calorimeter prototype for ATLAS*. J. Inst., **2**, (2007). [JINST 2 P11001].

[52] J. Artamonov et al. *The ATLAS Forward Calorimeters*. J. Inst., **3**, (2008). [JINST 3 P02010].

[53] G. Pospelov and others (On behalf of the ATLAS hadronic calibration group). *The overview of the ATLAS local hadronic calibration*. J. Phys., **Conf. Ser. 160**, (2009). [012079].

[54] ATLAS Collaboration. *Performance of Missing Transverse Momentum Reconstruction in ATLAS studied in Proton-Proton Collisions recorded in 2012 at* $\sqrt{s} = 8$ *TeV*. (2013). [ATLAS-CONF-2013-082].

[55] C. Gabaldon (On behalf of the ATLAS Collaboration). *Performance of the ATLAS Trigger System*. J. Inst., **7**, (2012). C01092.

[56] ATLAS Collaboration. *Improved luminosity determination in pp collisions at* $\sqrt{s} = 7$ *TeV using the ATLAS detector at the LHC*. Eur. Phys. J., **C73**:2518, (2013). [arXiv:1302.4393].

[57] ATLAS Collaboration. *Updated results and measurements of properties of the new Higgs-like particle in the four lepton decay channel with the ATLAS detector.* (2012). [ATLAS-CONF-2012-169].

[58] The ATLAS Collaboration. *Light-quark and gluon jet discrimination in pp collisions at $\sqrt{s} = 7$ TeV with the ATLAS detector.* Eur. Phys. J. C., **74**:3023, (2014). [arXiv:1405.6583].

[59] M. Cacciari et al. *The anti-k_T jet clustering algorithm.* JHEP, **0804**:063, (2008). [arXiv:0802.1189v2].

[60] ATLAS Collaboration. *Calibration of b-tagging using dileptonic top pair events in a combinatorial likelihood approach with the ATLAS experiment.* (2014). [ATLAS-CONF-2014-004].

[61] ATLAS Collaboration. *Calibration of the performance of b-tagging for c and light-flavour jets in the 2012 ATLAS data.* (2014). [ATLAS-CONF-2014-046].

[62] The ATLAS Collaboration. *Jet energy measurement with the ATLAS detector in proton-proton collisions at $\sqrt{s} = 7$ TeV.* Eur. Phys. J. C., **73**:2304, (2013). [DOI 10.1140/epjc/s10052-013-2304-2].

[63] The ATLAS Collaboration. *Jet energy measurement and its systematic uncertainty in proton-proton collisions at $\sqrt{s} = 7$ TeV.* Eur. Phys. J. C., **75**:17, (2015). [arXiv:1406.0076].

[64] M. Cacciari et al. *Pileup subtraction using jet areas.* Phys. Lett., **B659**:119–126, (2008). [arXiv:0802.1188].

[65] ATLAS Collaboration. *Jet global sequential corrections with the ATLAS detector in proton-proton collisions at $\sqrt{s} = 8$ TeV.* (2015). [ATLAS-CONF-2015-002].

[66] S. Frixione et al. *Matching NLO QCD computations with Parton Shower simulations: the POWHEG method.* JHEP, **0711**, (2007). [arXiv:0709.2092].

[67] S. Mrenna T. Sjostrand and P. Z. Skands. *PYTHIA 6.4 Physics and Manual.* JHEP, **0605**:026, (2006). [hep-ph/0603175].

[68] P. Nason. *A New Method for Combining NLO QCD with Shower Monte Carlo Algorithms.* JHEP, **11**, (2004). [arXiv:hep-ph/0409146v1].

[69] P. Z. Skands. *Tuning Monte Carlo Generator: The Perugia Tunes.* Phys.Rev.D., (2014). [arXiv:1005.3457v5].

[70] GEANT4 Collaboration. *A Simulation Toolkit.* Nucl. Inst. Meth., **A506**:250–303, (2003).

[71] D. Cavalli et al. *Performance of the ATLAS fast simulation ATLFAST.* (Internal Collaboration Note). [ATLAS-COM-PHYS-2007-012].

[72] ATLAS Collaboration. *The ATLAS Simulation Infrastructure.* Eur. Phys. J., **C70**:823–874, (2010).

[73] W. Pauli. *Niels Bohr and the Development of Physics.* (1955).

[74] K. Kroeninger J. Erdmann, S. Guindon et al. *A likelihood-based reconstruction algorithm for top-quark pairs and the KLFitter framework.* Nucl. Instr. Meth., **A 748**:18–25, (2014). [arXiv:1312.5595v2].

[75] ATLAS Collaboration. *Measurement of the inclusive $t\bar{t}$ cross section in p-p collisions at $\sqrt{s}$ = 8 TeV with ATLAS data using the hadronic decays of the top quark pairs.* (Internal collaboration note only at time of writing). [ATLAS-COM-PHYS-2014-783].

[76] ATLAS Collaboration. *Measurement of the top quark mass in the $t\bar{t}$ →lepton+jets and $t\bar{t}$ →dilepton channels using $\sqrt{s}$ = 7 TeV ATLAS data.* Submitted to Eur. Phys. J. C., (2015). [arXiv:1503.05427].

[77] ATLAS Collaboration. *Characterisation and mitigation of beam-induced backgrounds observed in the ATLAS detector during the 2011 proton-proton run.* J. Inst., **8**, (2013). [P07004].

[78] ATLAS Collaboration. *Selection of jets produced in proton-proton collisions with the ATLAS detector using 2011 data.* (2012). [ATLAS-CONF-2012-020].

[79] ATLAS Collaboration. *Measurement of the Top Quark Mass using a Template Method in the Fully Hadronic Decay Channel from ATLAS Data at $\sqrt{s}$ = 7 TeV.* Eur. Phys. J. C., (Pending Publication - Submitted 2014).

[80] K.S.Koelbig and B.Schorr. *A Program Package for the Landau Distribution.* Computer Physics Communications, **31**:97–111, (1983).

[81] ATLAS Collaboration. *Observation of $W \to \tau\nu$ Decays with the ATLAS Experiment.* (2010). [ATLAS-CONF-2010-097].

[82] G. Cowan. *Statistical Data Analysis.* Oxford Science Publications, (1998).

[83] V. Blobel and E. Lohrmann. *Statistische und numerische Methoden der Datenanalyse.* (2012).

[84] S. Menke. Private communication.

[85] L. Demortier. *Constructing Ensembles of Pseudo-Experiments.* Conference on Statistical Problems in Particle Physics, Astrophysics and Cosmology, (2003). [arXiv:physics/0312100v2].

[86] R. Barlow. *Application of the bootstrap resampling technique to particle physics experiments.* (1999). [MAN/HEP/99/4].

[87] A.H. Rosenfeld. *The particle data group: growth and operations – eighteen years of particle physics.* Ann. Rev. Nucl. Sci., **25**:555, (1975).

[88] P. Giovannini. *Studies on the top quark mass measurement in the all-hadronic $t\bar{t}$ decay channel with ATLAS.* Ph.D. Thesis, (2011). [CERN-THESIS-2011-069].

[89] S. Frixione and B.R. Webber. *Matching NLO QCD computations and parton shower simulations.* JHEP, **0206**:029, (2002). [arXiv:hep-ph/0204244v2].

[90] G. Corcella et al. *HERWIG 6.5: an event generator for Hadron Emission Reactions with Interfering Gluons (including supersymmetric processes).* JHEP, **0101**:010, (2001). [arXiv:hep-ph/0011363v3].

[91] B.P. Kersevan and E. Richter-Was. *The Monte Carlo Event Generator AcerMC 2.0 with Interfaces to PYTHIA 6.2 and HERWIG 6.5.* High Energy Physics - Phenomenology, **TPJU-6**, (2004). [arXiv:hep-ph/0405247v3].

[92] H. Baer et al. *The International Linear Collider Technical Design Report – Volume 2: Physics*. High Energy Physics - Phenomenology, (2013). [arXiv:1306.6352v1].

[93] J. Wang et al. *Generating Multivariante Mixture of Normal Distributions Using a Modified Cholesky Decomposition*. Proceedings of the 2006 Winter Simulation Conference, (2006).

[94] E. Rauter. *Top Quark Mass Measurement: Prospects of Commissioning Studies for Early LHC Data in the ATLAS Detector*. Ph.D. Dissertation, (2009). [CERN-THESIS-2009-000].

[95] S. Menke. *Calibration of the BaBar Electromagnetic Calorimeter with $\pi^0 s$*. Collaboration Note, (2000). [BaBar Note 528].

[96] E.W. Hughes D. Lopez Mateos and A. Schwartzman. *A Simple p_{T}- and η-Dependent Monte Carlo-Based Jet Calibration*. (2009). [ATLAS-COM-2009-076].